Structure–Property Relations of Polyampholyte Hydrogels, Graphene Composites, and Biodegradable Elastomers and Their Applications in Energy Generation and Storage Devices

By

Xinda Li

A thesis submitted in partial fulfillment of the requirements for the degree of

Doctor of Philosophy

In

MATERIALS ENGINEERING

Department of Chemical and Materials Engineering
University of Alberta

Abstract

A polyampholyte is a polyelectrolyte which is composed of macromolecules that contains both cationic and anionic ionisable groups. Understanding the structure of polymer chains in polyampholyte hydrogels and its effect on the phase behavior of the contained water is a challenging problem that has a broad impact on diverse applications, such as gel electrolytes, lubrication layers, and anti-biofouling coatings. In this dissertation, we have investigated the structure of a charge-balanced polyampholyte, poly(4-vinylbenzenesulfonate-*co*-[3-(methacryloylamino) propyl] trimethylammonium chloride). The polymer structure was probed by variable-temperature small-angle X-ray scattering (SAXS); highly hydrated globules with a radius of gyration of 2 ~ 2.5 nm formed a network structure in the charge-balanced polyampholyte hydrogels, whereas the size and the clustering are dependent on synthesis parameters. These highly hydrated network globules formed percolated polymer-rich domains while sub-micron, slush-like ice crystals formed from water-rich domains, resulting in ion-conducting channels that are rich in amorphous water molecules at low temperatures. Solid-state nuclear magnetic resonance (NMR) spectroscopy confirmed the mobility of these amorphous water molecules at temperatures as low as –54 °C. We also visualized the globular structure of polyampholyte hydrogel with scanning electron microscopy (SEM) and scanning transmission electron microscopy (STEM) for the first time. Differential scanning calorimetry (DSC) was used to estimate water states in the polyampholyte hydrogel.

Based on the understanding of temperature-dependent structure evolution of polyampholyte hydrogel, we fabricated two devices using polyampholyte hydrogel. First, we found that the upper critical solution temperature (UCST) for the phase separation between water-

rich and polymer-rich phases in the polyampholyte hydrogel can be finely raised (~ +40 °C) by substituting a small number of cationic monomers (~ 0.5 wt%) to slightly more hydrophobic ones during the random copolymerization process. By harnessing this scientific observation, we developed a smart coating that becomes opaque to both visible and mid-infrared radiation at room temperature to achieve privacy and heat retention in cold night weather. Second, a flexible and self-healing supercapacitor with high energy density in low-temperature operation was fabricated using the polyampholyte hydrogel as a gel electrolyte. The resulting supercapacitor device showed a high energy density of 30 Wh/kg, and a capacitance retention of ~90% after 5000 charge–discharge cycles. At low temperature (−30 °C), the supercapacitor had an energy density of 10.5 Wh/kg at a power density of 500 W/kg.

Inspired by the new graphene chemistry we developed for the aforementioned supercapacitor electrodes, we also devised a self-reinforcing conductive coating strategy where graphene nanoflakes (GNF) were wrapped by self-assembling reduced graphene oxide (RGO) for electrical conductivity and mechanical integrity. The conductivity of the GNF-RGO coating reached 4.47×10^4 S/m. The coating was then applied on 3D printed porous elastomers, resulting in flexible radio frequency (RF) antennas and strain sensors with arbitrary shapes for internet-of-things (IoTs) applications. The same conductive coating strategy also converted a commercial polyurethane (PU) sponge into electricity generators, where zinc oxide (ZnO) nanowires were hydrothermally grown on top of the three-dimensional graphene networks coated on the inner wall of the PU sponge. The nanogenerator yielded an open circuit voltage of ~0.5 V and short circuit current density of ~2 μA/cm^2, while the output was found to be consistent after ~3000 cycles.

Finally, we studied the synthesis of poly (glycerol sebacate) (PGS), a synthetic biocompatible elastomer developed as a template for cardiac cells, to establish criteria for quick

and consistent synthesis for tailored mechanical properties. Here, we suggested that the degree of esterification (DE) could be used to predict precisely the physical status, the mechanical properties, and the degradation of PGS. Young's modulus was shown to linearly increase with DE, which was in agreement with an entropic spring theory of rubbers. To provide a processing guideline for researchers, we also provided a physical status map as a function of curing temperature and time. The amount of glycerol loss, obtainable by monitoring the evolution of the total mass loss and the DE during synthesis, was shown to make the predictions even more precise. Quick synthesis could be achieved by employing a microwave oven instead of convection heating for prepolymerization, but microwave heating led to severe mismatch between monomeric units by uncontrolled evaporation of glycerol, leading to an inconsistency in mechanical properties.

Preface

A part of Chapter 4 and subsection 1.2.1 of this thesis has been published as "Xinda Li, Hemant Charaya, Guy M. Bernard, Janet A.W. Elliott, Vladimir K. Michaelis, Byeongdu Lee*, Hyun-Joong Chung*. Low-Temperature Ionic Conductivity Enhanced by Disrupted Ice Formation in Polyampholyte Hydrogels. *Macromolecules*, 51 (7), 2723–2731 (2018)". Xinda Li and Dr. Hyun-Joong Chung conceived ideas. Xinda Li and Hemant Charaya prepared and characterized hydrogels. Dr. Janet A.W. Elliott provided critical insights in solution thermodynamics and ice formation. Dr. Guy M. Bernard and Dr. Vladimir K. Michaelis performed, analyzed, and interpreted solid-state NMR experiments. Dr. Byeongdu Lee performed, analyzed, and interpreted the SAXS and WAXS experiments. Xinda Li and Dr. Hyun-Joong Chung developed the model to explain the structure-property relations in polyampholyte hydrogels. Xinda Li, Dr. Janet A.W. Elliott, Dr. Guy M. Bernard, Dr. Vladimir K. Michaelis, Dr. Byeongdu Lee, and Dr. Hyun-Joong Chung wrote the manuscript. Dr. Jae-Young Cho performed, analyzed, and interpreted the additional FE-SEM and STEM experiments to visualize globular structure.

Chapter 5 of this thesis will be submitted as "Xinda Li, Sambit Banik, Guy M. Bernard, Janet A.W. Elliott, Vladimir K. Michaelis, Hyun-Joong Chung*. (The author order is not finalized) Water States in Salt-Containing Polyampholyte Hydrogels". Xinda Li and Dr. Hyun-Joong Chung conceived ideas. Xinda Li and prepared and characterized hydrogels. Xinda Li, Dr. Janet A.W. Elliott and Dr. Hyun-Joong Chung designed and interpreted DSC experiments. Dr. Guy M. Bernard and Dr. Vladimir K. Michaelis performed, analyzed, and interpreted solid-state NMR experiments. Xinda Li, Dr. Janet A.W. Elliott, Dr. Guy M. Bernard, Dr. Vladimir K. Michaelis, and Dr. Hyun-Joong Chung wrote the manuscript.

A part of Chapter 6 and subsection 1.2.2.1 of this thesis has been published as "Thanh-Giang La[†], Xinda Li[†], Amit Kumar, Yiyang Fu, Shu Yang, Hyun-Joong Chung*. Highly Flexible, Multipixelated Thermosensitive Smart Windows Made of Tough Hydrogels. *ACS Applied Materials & Interfaces*, 9(38), 33100-33106 (2017)". Xinda Li, Dr. Thanh-Giang La and Dr. Hyun-Joong Chung conceived ideas. Xinda Li and Yiyang Fu prepared and characterized

* Corresponding Author
[†] Equal Contribution

hydrogels. Amit Kumar fabricated the ink and heater. Dr. Thanh-Giang La assembled the device. Xinda Li, Dr. Thanh-Giang La, Dr. Shu Yang, and Dr. Hyun-Joong Chung wrote the manuscript.

A part of Chapter 7, subsection 1.2.2.2, and subsection 1.2.3.1 of this thesis has been published as "Xinda Li, Li Liu, Xianzong Wang, Yong-Sik Ok, Janet A.W. Elliott, Scott X. Chang, Hyun-Joong Chung*. Flexible and Self-Healing Aqueous Supercapacitors for Low Temperature Applications: Polyampholyte Gel Electrolytes with Biochar Electrodes. *Scientific Reports*, 7, 1685 (2017)". Xinda Li and Dr. Hyun-Joong Chung conceived ideas. Dr. Yong-Sik Ok and Dr. Scott X. Chang provided the pristine biochar. Dr. Janet A.W. Elliott contributed in developing the hydrogel electrolyte. Xinda Li fabricated the electrode, the hydrogel electrolyte, and the supercapacitor device. Xinda Li, Liu Li and Xianzong Wang characterized the materials and the device. Xinda Li and Dr. Hyun-Joong Chung drafted the manuscript. Dr. Janet A.W. Elliott, Dr. Yong-Sik Ok and Dr. Scott X. Chang provided critical revisions of the manuscript.

A part of Chapter 8 and subsection 1.2.3.2 of this thesis has been published as "Xinda Li, Mohammad Mahdi Honari, Yiyang Fu, Amit Kumar, Hossein Saghlatoon, Pedram Mousavi*, Hyun-Joong Chung*. Self-Reinforcing Graphene Coatings on 3D Printed Elastomers for Flexible Radio Frequency Antennas and Strain Sensors. *Flexible and Printed Electronics*, 2, 035001 (2017)". Xinda Li conceived of the idea presented in this paper with guidance from Dr. Hyun-Joong Chung; Xinda Li and Yiyang Fu designed and performed the material preparation and characterization; Mohammad Mahdi Honari and Hossein Saghlatoon designed the antenna structure and characterized its performance; Amit Kumar designed and fabricated the 3D printed substrate; Xinda Li, Yiyang Fu, and Amit Kumar designed and performed the strain sensor; Xinda Li, Mohammad Mahdi Honari, Amit Kumar and Yiyang Fu wrote the paper with feedback provided by Dr. Pedram Mousavi and Dr. Hyun-Joong Chung.

A part of Chapter 9 and subsection 1.2.3.3 of this thesis has been published as "Xinda Li, Yi Chen, Amit Kumar, Ahmed Mahmoud, John A. Nychka, Hyun-Joong Chung*. Sponge-Templated Macroporous Graphene Network for Piezoelectric ZnO Nanogenerator. *ACS Applied Materials & Interfaces*, 7, 20753-20760 (2015)". Xinda Li and Dr. Hyun-Joong Chung conceived ideas. Xinda Li, Dr. Yi Chen, and Amit Kumar performed experiments. Dr. Yi Chen, Dr. John A. Nychka and Dr. Hyun-Joong Chung established ZnO nanowire array deposition protocols. Ahmed Mahmoud

provided important contributions in material characterization. Xinda Li and Dr. Hyun-Joong Chung wrote the manuscript.

A part of Chapter 10 and subsection 1.2.4 of this thesis has been published as "Xinda Li, Albert T. Hong, Nilanjon Naskar, Hyun-Joong Chung*. Criteria for Quick and Consistent Synthesis of Poly(Glycerol Sebacate) for Tailored Mechanical Properties. *Biomacromolecules*, 16 (5), 1525–1533 (2015)". Xinda Li, Albert T.-L. Hong, and Dr. Hyun-Joong Chung conceived ideas. Xinda Li, Albert T.-L. Hong, and Nilanjon Naskar performed experiments. Xinda Li and Dr. Hyun-Joong Chung wrote the manuscript.

Acknowledgments

I would like to take this opportunity to express my sincerest gratitude to the people around me during my Ph.D. study.

My deepest thanks goes to Professor Hyun-Joong Chung, my Ph.D. thesis advisor and my mentor. Thank you for providing me with the opportunity to study and research in his group. Under his guidance, I not only consolidated my background in polymer science but also learned how to become a rigorous, passionate and inspiring researcher, and educator. When I met difficulties with my projects, Professor Chung always tried to find all the possible recourse for me to solve those problems. His encouragements and advice made my completion of graduate study possible and they will follow me wherever I go in my life. I would like to thank my thesis committee members Professor Janet A.W. Elliott, Professor Hongbo Zeng, Professor Weixing Chen and Professor Jan Genzer (North Carolina State Univ.) for their invaluable advice and discussions on my dissertation.

I also want to express my special gratefulness to Dr. Byeongdu Lee (Argonne National Laboratory). Only with his help on SAXS and WAXS experiments, were we able to make such progress. I was truly impressed by his instant and thorough replies whenever I requested help. It is my fortune to know and work with such an amazing scientist like him. I also would like to thank Professor Janet A.W. Elliott again for her extremely valuable inputs during these years. The meetings with her were excellent. Her sharp insights and wonderful explanations accelerated my research at every stage. I would like to thank Professor Hongbo Zeng. I took his course in my first year here and I learned a lot. He always generously provided his help during my study. I also want to thank Professor Jan Genzer for his kind help as well as traveling to Edmonton to attend my defence. I would like to thank Professor Vladimir K. Michaelis and Dr. Guy M. Bernard from the Department of Chemistry for the rare opportunity of solid-state NMR measurements, and I was motivated by their dedication to science. I also thank Dr. Jae-Young Cho (Nanotechnology Research Centre) for his help with hydrogel imaging. I would like to thank Professor Anastasia Elias for discussions and advice, as well as kindly providing the access to instruments in her lab. I have also benefited from invaluable help from many people, namely (alphabetically), Dr. Matthew Benesch, Professor Michael J. A. Hore (Case Western Reserve Univ.), Dr. Cui Kai (Nanotechnology Research Centre), Professor Karen I. Winey (Univ. of Pennsylvania), Dr. Mike

Xia (Nanotechnology Research Centre), and Dr. Zhimin Yan (Nanotechnology Research Centre). I would like to acknowledge the sponsors of the Natural Sciences and Engineering Research Council of Canada (NSERC) and Alberta Innovates-Technology Futures (now Alberta Innovates) Graduate Scholarship.

I also want to thank my friends in the Soft Material and Device Lab: Dr. Yi Chen, Dr. Thanh Giang La, Dr. Tanushree Ghosh, Hemant Charaya, Amit Kumar, Chungyeon Cho, Li Liu, Shide Qiu, Fanghui Liu, Dinara Zhalmuratova, Wendy Tran, and Lelin Zheng. We walked together all the way along, with both smiles and cries. I am also very thankful to undergraduate researchers: Albert Hong, Rafael R. Sencio, Nilanjon Naskar, Aniket Shah, Sambit Banik, Kun Jiang, Yiyang Fu, Jin Hui Tan, and Nathan Jen. I am also looking forward to seeing you sometime in the future.

Many thanks to the staff of the CME department: Lily Laser, Pritchard Marion, and Kevin Heidebrecht. I always felt delighted after talking with you. I also thank the staff in the nanoFAB: Peng Li, Dr. Anqiang He, Shiau-Yin Wu, Dr. Shihong Xu, and Dr. Nancy Zhang. Your helpfulness and kindness made my experiments smooth and productive.

Four years and eight months ago, I said goodbye to Shanghai and arrived at Edmonton, I can still recollect every detail of that day just like yesterday. Countless things occurred, the love from my mother, father, grandparents and Dr. Guanmin Meng warmed me up in the cold winter. Thank you so much for believing in me and understanding all the decisions I made in these years.

Table of Contents

List of Tables

List of Figures and Illustrations

Chapter 1 Introduction

1.1 Introduction

Hydrogel, a water-containing swollen three-dimensional polymeric network, was first reported from the seminal work of Wichterle and Lim in 1960.[1] In their study, poly(2-hydroxyethyl methacrylate) was developed with particular interests in tissue engineering, leading to commercialization of contact lenses in our daily life. As reviewed by Buwalda *et al*.,[2] the history of hydrogel research can be divided into the following three periods: (i) From 1960 to 1970, hydrogels of chemically crosslinked networks were synthesized with relatively simple stratagem and fundamentals of various hydrogel properties were studied. (ii) Starting in the 1970s, the emerging of hydrogels capable of responding to external stimuli accelerated their applications such as drug releasing matrices instead of passive orthopaedic implants.[3] (iii) Then in the mid-1990s, the focus of hydrogel research shifted to other crosslinking mechanisms (such as ionic interactions, stereocomplexations, *etc*.), which provided an abundant inventory of hydrogel systems with various properties that can be fine-tuned.[4]

After more than a half century of development, the recent trend of hydrogel research is more intensive and diverse, revealing the possibilities for applications, for instance, from the conventional uses, such as scaffolds for tissue engineering,[3] to the contemporary uses, such as smart materials for soft robotics.[5,6,7] On the other hand, the demands for hydrogels with better performances for applications act as the impetus to promote fundamental hydrogel research. As an example, since the mechanical properties of hydrogels are decisive in the recently occurring fields of artificial muscle or soft robotics, a new class of hydrogels with extremely high mechanical strength and tear-resistance, tough hydrogels,[8] were developed by employing double network architectures,[9,10,11] forming nanocomposite hydrogels with inorganic nanoparticles,[12,13,14] and introducing freely movable crosslinks.[15,16] Polyampholyte hydrogel is a class in the family of tough hydrogels,[17] where the polymer networks are associated by ionic bonding between oppositely charged units in their backbone chains. The hydrogel is intrinsically tough, stretchable, and self-healable,[17] and is versatile since the mechanical or physicochemical properties can be finely tuned by changing the monomers with different hydrophobicity or ionic strength.[17,18] However,

fundamental studies on polymer structures in the polyampholyte hydrogel and their relation to the unique properties are seldom reported.

As hydrogels are inherently rich in water content, understanding the structure of the polymer network has important implications for applications where the interaction between polymer and water is determinant, such as ionic conductivity,[19,20] anti-biofouling effects,[21,22,23] lubrication,[21,24] adhesion,[25] and water-retention ability.[22] Using a model system of poly[sodium 4-vinylbenzenesulfonate-*co*-[3-(methacryloylamino)propyl] trimethylammonium chloride], this dissertation sheds light on understanding of the temperature-dependent structure evolution of polyampholyte hydrogel upon cooling–heating cycles, as well as the impacts of the morphological evolution on ice formation and ionic conductivity of the polyampholyte hydrogels. These investigations are supported by experimental results with small-/wide-angle X-ray scattering, solid-state nuclear magnetic resonance, and electron microscopy (Chapter 4) differential scanning calorimetry (Chapter 5) techniques.

The fundamental knowledge on the temperature-dependent evolution of polymer network structures and their relation to the properties of polyampholyte hydrogel lead to device applications. In this dissertation, we showcase two types of devices based on polyampholyte hydrogels. The first device is a thermosensitive smart window since polyampholyte hydrogel exhibits a reversible optical transition from opaqueness to transparency upon heating above the upper critical solution temperature (UCST). At a high temperature (*i.e.,* during daytime), our polyampholyte hydrogel is transparent so that visible light can transmit. At a lower temperature (*i.e.,* at night), our polyampholyte hydrogel blocks the visible light, and the transmittance of mid-infrared radiation. The transition temperature of the hydrogel was finely tuned by introducing a 'molecular doping' strategy, where substituting a trace amount of anionic monomers to the ones with different hydrophobicity changes the UCST in a highly controllable manner (Chapter 6). The second device is a robust and flexible aqueous supercapacitor suitable for cold climates. The enhanced ionic conductivity of electrolytes due to suppression of ice formation resulted in an improvement of electrochemical performance of the supercapacitor at low temperatures (Chapter 7).

In the course of developing supercapacitors (Chapter 7), we developed a protocol to fabricate self-standing electrodes by wrapping powdery conducting materials, such as chemically treated

biochar, with self-wrapping reduced graphene oxide. This protocol enables flexible electrodes with hierarchical porosity distribution ranging from nano- to macro-pores, which are ideal for electrochemical energy storage devices. While reduced graphene oxide wrapping provides a binder to maintain mechanical integrity and a conducting conduit for electrical conductivity, the abundant nanopores in chemically treated biochar play a role as electrochemically active sites. This protocol was further applied to two other application-driven projects. We developed a processing method based on graphene oxide-wrapping and reduction to fabricate a carbonaceous conductive layer coating with an arbitrary shape factor via 3D printing, which can be used as a flexible antenna and strain sensor (Chapter 8). Using the same protocol, we also devised a simple and inexpensive processing pathway to produce a nanogenerator with a 3D structure for enhanced performance and mechanical integrity based on a reduced graphene coated commercially available polyurethane sponge, combined with a one-step hydrothermal method that grows ZnO nanowires (Chapter 9).

Finally, we focused on a problem of achieving a quick and consistent synthesis of a biodegradable elastomer poly(glycerol sebacate) for tailored mechanical properties (Chapter 10). From a literature survey, we found big discrepancies between reported mechanical properties among different research groups while their processing conditions seemed mostly identical. We propose that the degree of esterification is a chemical indicator of the synthesized poly(glycerol sebacate) to determine the physical status, mechanical properties and degradation behaviors in a precise and reproducible way. The effects of adding cross-linking agent, 4,4'-methylene diphenyl diisocyanate, and a commodity class of nanoparticles, fumed silica was also studied.

In summary, this dissertation addresses the following topics, as shown in Figure 1.1:

(i) The temperature-dependent structure evolution of polyampholyte hydrogel (Chapter 4)
(ii) The water-polymer interactions in polyampholyte hydrogel (Chapter 5)
(iii) Thermosensitive smart windows based on polyampholyte hydrogel (Chapter 6)
(iv) Flexible polyampholyte supercapacitors for low temperature (Chapter 7)
(v) Self-reinforcing graphene coatings for flexible antennas and strain sensors (Chapter 8)
(vi) Sponge-templated graphene network for piezoelectric nanogenerator (Chapter 9)
(vii) Criteria for synthesis of poly(glycerol sebacate) for tailored mechanical properties (Chapter 10)

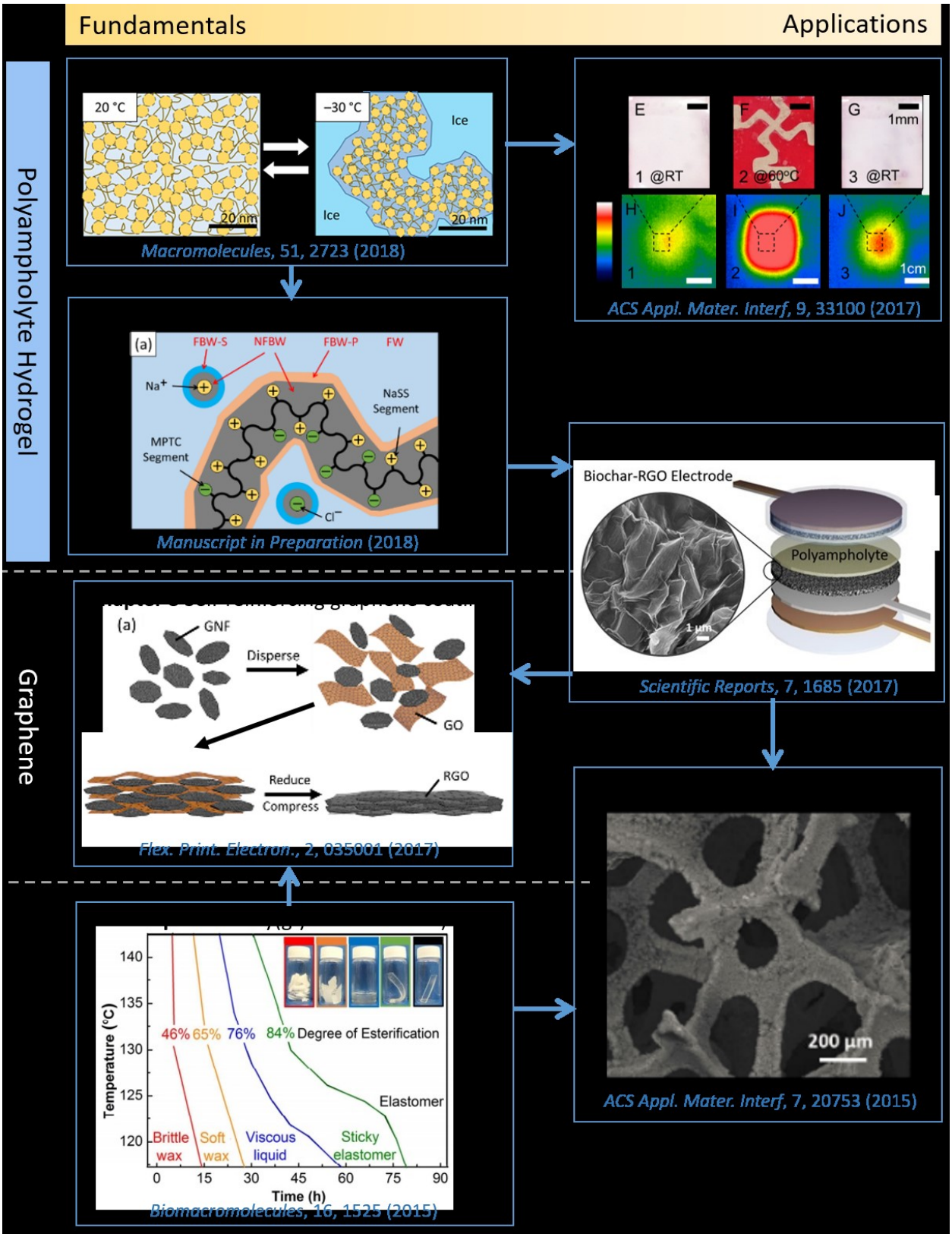

Figure 1.1 Topics covered in this dissertation. The arrows indicate the sequence and relationships between topics.

The remainder of Chapter 1 contains the following subjects. Section 1.2 provides the content for a brief review of each topic and how the current work in this dissertation can advance the relevant research fields. Finally, in section 1.3, the structure of the dissertation is outlined.

1.2 Impacts of Current Work

1.2.1 Fundamental Studies on Polyampholyte Hydrogel (Chapters 4, 5 and 6)

Polyampholyte hydrogels have been used as absorbents in wastewater metal removal,[26] tissue adhesives,[27] electrolyte for supercapacitors,[28] and thermosensitive smart windows.[29] However, experimental studies on the polymer network structure of polyampholytes have been relatively rare. Nisato *et al.* proposed a qualitative description of the globular structure of chains in polyampholyte hydrogels based on light scattering and swelling experiments.[30] However, the details of the globular structures, including size and chain density of each globule and the secondary structures that the globules may produce, have not been explored. Within the polyampholyte family, the hierarchical structure of polyzwitterions, has been studied in detail. Polyzwitterions show a unique property called anti-polyelectrolyte behavior because they are in an isoelectric state — so do any other isoelectric polyampholytes.[31] Whereas ordinary polyelectrolytes undergo a collapse in their chain conformation when the salt concentration increases in the aqueous solution, isoelectric polyampholytes exhibit swelling behavior that leads to an increase of the solution viscosity and the solubility of the macromolecular component.[32,33,34,35] Moreover, the high polymer concentration in the hydrogel leads to electrostatically induced hierarchical self-assembly that defines a multi-scale structural network in the hydrogel.[31] Safinya and coworkers recently investigated the effect of salt on the hierarchical structural formation of neurofilament hydrogel, whose structural assembly is dictated by ionic interactions between polyampholyte sidearm chains. The neurofilament hydrogel (~ 5 wt% neurofilament in salt water) undergoes transitions from liquid-crystalline hydrogel to isotropic gel, and to nematic hydrogel when the background salt concentration increases.[22] However, the study of polyampholyte with randomly distributed charges has not been investigated. Furthermore, the chain conformation of polyampholyte in dilute solution has been theoretically predicted—a charge-balanced polyampholyte chain forms a globular conformation because Debye–Huckel fluctuation induces attraction between charges,[36] and the size of the globule depends on the ionic strength and on the number of repeating units of the polymer.[10,37] But in the practical application

of polyampholyte hydrogel, the concentrations of polymers are much higher than concentrations of dilute solutions. Thus, the investigation on polyampholyte hydrogels with comparable polymer concentration to those for practical application is imperative.

1.2.1.1 Temperature-Dependent Structure Evolution (Chapter 4)

In Chapter 4, we explored a model charge-balanced polyampholyte hydrogel, poly(4-vinylbenzenesulfonate-*co*-[3-(methacryloylamino) propyl] trimethylammonium chloride), whose polymer and water structures were probed by variable-temperature small-/wide-angle X-ray scattering (SAXS/WAXS) and solid-state nuclear magnetic resonance (NMR) spectroscopy. SAXS results indicate a networked globule structure in the charge-balanced polyampholyte hydrogels, at the length scale of ~5 nm, whereas the structure is dependent on synthesis parameters. Variable-temperature SAXS data reveal a temperature-dependent structure evolution of the polyampholyte hydrogel. An interconnected globular network structure of polymer-rich phase at low temperature, observed by electron microscopy, suggests to preserve ion-conducting channels of non-frozen water molecules at low temperatures. This hypothesis is further supported by solid-state ^{1}H NMR spectroscopy that elucidates the mobility of water molecules at low temperatures. Together these findings provide macromolecular- and molecular-level insight to design gel electrolytes for enhanced low-temperature performance.

1.2.1.2 Water States and Ice Formation (Chapter 5)

Since the fixation of water molecules due to their interaction with polymer chains is a deterministic factor that governs the hydrogel's material properties, in Chapter 5, we studied the water–polymer interactions of hydrogels made of a model charge-balanced polyampholyte at various water content and salt concentration, as well as the effect of dialysis and salt reinfusion, using differential scanning calorimetry (DSC). The amount of ice in the hydrogel was quantified.

1.2.2 Applications of Polyampholyte Hydrogel (Chapters 6 and 7)

In this section, we introduced two devices based-on the polyampholyte hydrogel. First, we developed a smart coating that becomes opaque to both visible and mid-infrared radiation at room temperature to achieve privacy and heat retention in cold night weather. Second, a flexible and self-healing supercapacitor with high energy density in low-temperature operation was fabricated

using the polyampholyte hydrogel as a gel electrolyte. Recent research activities on each device were reviewed, and the major progress that advances the related fields are addressed.

1.2.2.1 Thermosensitive Smart Windows (Chapter 6)

Optically switchable materials have the ability to control their light absorption, scattering, and transmission properties as a response to external stimuli.[38,39,40] The switching behavior is typically controlled by the electric field or light intensity.[41] For conventional electrochromic materials, the optical properties of the active layer are modulated by an externally applied electric field, which requires continuous energy input.[42,43] The energy consumption and maintenance issues for long-term operation are not preferred for the energy-saving aspect of building operation.[44] It would be desirable if the material could passively modulate its transparency as a function of the environmental temperature. Metal oxide nanoparticles, such as vanadium oxide (VO_2) that have been utilized in electrochromic smart windows,[44] have been extensively investigated as a potential candidate material for this purpose. Moreover, the thermochromic VO_2-based thin layer can block near-infrared light at temperatures > 40 °C to save energy for air conditioning in hot weather.[45,46] However, since the degree of transparency change and the transition temperature depend on the composition of the VO_2 layer, it is challenging to tune these two at the same time to desired values.[39,47] Another drawback of the VO_2-based smart window is that the active layer is sensitive to the oxygen in the surroundings. A tightly sealing encapsulation layer is necessary to integrate on the window to prevent oxidation from the environment.[48,49,50,51] The sophisticated manufacturing protocol limits the fitting and sizing of such smart windows for different built structures.

Recently, poly(N-isopropylacrylamide) (PNIPAAm) hydrogel has drawn much attention due to its unique combination of stretchability and tunable optical transmittance.[52,53,54,55,56] PNIPAAm hydrogel undergoes a transition from transparency to an opaque state upon heating above the lower critical solution temperature, which is suitable for the smart window application. Compared with the use of light-reflecting liquid crystals,[57, 58] and copolymer solution,[59] the quasi-solid-state of PNIPAAm hydrogel prevents leakage under mechanically induced deformation of the smart window. The rubber-like stretchability of hydrogel can be an added value to the optically switchable material; such materials can be applied to randomly shaped objects with motional and

dimensional changes. Kodak Research Laboratories mixed a small fraction of PNIPAAm as a nanoscopic aggregation in a self-healing hydrogel matrix to achieve rapid switching from transparency to opalescent states within ~30 s.[56] It is noted that most synthetic hydrogels, including PNIPAAm, are intrinsically brittle and the mechanical integrity of such a layer over time is of concern. Therefore, development of a tough hydrogel that can overcome such limitations will allow us to achieve superb tear-resistance, stretchability, and self-healing ability.[12,8,60,61,17] According to the previous study,[62] polyampholyte hydrogel exhibits a reversible optical transition from opaqueness to transparency upon heating above the upper critical solution temperature. This phenomenon provides us with a feasible scenario to fabricate tough hydrogel-based thermosensitive smart coatings.

In Chapter 6, a smart window is designed to control transparency to sunlight (predominantly visible and near-infrared) and/or black-body radiation (mid-infrared) with respect to external stimuli. Using polyampholyte hydrogel, we developed a smart coating that becomes opaque to both visible and mid-infrared radiation at low temperatures to achieve privacy and heat retention in cold night weather. Here, the phase structure of polyampholyte hydrogel governs the transparency for the electromagnetic wave, where the separation between water-rich and polymer-rich phases at low temperature induces scattering of the wave. We fine-tuned the upper critical solution temperature of the hydrogel from 25 to 55 °C by introducing relatively hydrophobic dopant monomers from 0.1 to 0.5 wt%, respectively, during a random copolymerization process. By including an electric heater made of printed elastomeric composite, we developed an active array of stretchable, high-contrast, optically tunable smart windows. The pixelated window demonstrated rapid switching time and stable cyclic operation.

1.2.2.2 Supercapacitors for Low Temperature Applications (Chapter 7)

Improving the low-temperature performance of electrochemical storage devices is crucial in cold climates. For electrochemical capacitors, *i.e.*, supercapacitors, low-temperature operation is established down to −40 ºC, by using organic solvents or ionic liquids with low freezing points,[63,64,65] but they are typically toxic and expensive.[66,67,68,69,70] In order to address the electrolyte leakage induced hazards, aqueous gel electrolytes (sometimes denoted as solid-state electrolytes) are under extensive investigation for energy storage devices, such as lithium ion[71] or sodium ion

batteries,[72] as well as supercapacitors[73] in order to develop safe energy storage devices; however, low-temperature operation has still not been established.

Gel polymer electrolytes are swollen polymers with an electrolyte solution containing proper solvents or plasticizers. They combine good free-standing properties of solid systems with liquid-like transport properties. Compared to liquid electrolytes, gel polymer electrolytes are intrinsically free of leakage problems or the need for separators, reducing the requirement for costly special packaging.[74] Poly(vinyl alcohol) is one of the widely used polymeric frameworks for aqueous gel polymer electrolytes with proton[75,76] or alkaline doping.[77,78] Potassium hydroxide (KOH) doped poly(vinyl alcohol) hydrogels exhibit high ionic conductivities. However, the low-temperature application of aqueous gel electrolytes is limited due to monolithic ice formation. Hydrogels from polyampholytes possess desirable structural properties found in gel polymer electrolytes such as rubber-like elasticity, extreme tear resistance against crack propagation, self-healing ability and self-adjusting adhesion.[17,18,25] In addition, our parallel research showed that polyampholyte hydrogel electrolyte maintains mechanical flexibility at very low temperature by slush-like ice formation; thus we envision making robust, flexible, and eco-friendly aqueous energy storage devices suitable for cold climates.

In Chapter 7, a flexible and self-healing supercapacitor with high energy density in low-temperature operation was fabricated using a combination of biochar-based composite electrodes and a polyampholyte hydrogel electrolyte. The fabricated supercapacitor showed high energy density of 30 Wh/kg with ~90% capacitance retention after 5000 charge–discharge cycles at room temperature at a power density of 50 W/kg. At −30 ºC, the supercapacitor exhibited an energy density of 10.5 Wh/kg at a power density of 500 W/kg. The mechanism of the low-temperature performance excellence is likely to be associated with the concept of non-freezable water near the hydrophilic polymer chains, which can motivate future research on the phase behaviour of water near polyampholyte chains.

1.2.3 Investigations and Applications on Graphene Oxide Wrapping and Reduction (Chapters 7, 8 and 9)

During the fabrication of the electrode materials for the supercapacitor with polyampholyte hydrogel, we developed a protocol, called "graphene oxide wrapping and reduction". By applying this protocol, several applications were achieved, as summarized in the following sections.

1.2.3.1 Biochar-Reduced Graphene Oxide Electrodes for Supercapacitors (Chapter 7)

Carbon-based materials have been of intensive interest as electrodes for energy storage devices. Currently, activated carbon from renewable resources is a gold standard for the supercapacitor industry.[79] Purified coconut shell based activated carbon currently costs $15 per kilogram, which consists of half of the total material price for commercial supercapacitors.[80] More alternative carbon sources with superior surface area per weight, such as carbon nanotube and graphene, have been extensively researched to achieve superior nanostructure for the application.[81,82,83] For industrial applications, however, the key issue for a suitable electrode material has been to find the optimal balance between material production cost and performance, in addition to overcoming technical challenges such as the volumetric energy density issue caused by 'fluffiness' of the alternative carbon sources.[80] Compared to the current gold standard of coconut shell based activated carbon and the heavily researched contenders of carbon nanotube and graphene electrodes, biochar has a potential to establish an economic choice for a renewable energy storage material owing to its mild processing temperature, abundance in nature, and its built-in hierarchical nanostructures. Biochar produced from agriculture waste by slow pyrolysis at low temperature (400~700 °C) has attracted attention for soil fertility improvement, carbon sequestration and water purification.[84,85] Recent studies show possibilities of using biochar in energy storage devices.[86,87,88] Pure biochar is not suitable as an electrode material for three reasons: low specific capacitance, the powdery nature of the material, and low electrical conductivity. Nitric acid treatment and thermal flashing can increase the specific capacitance of exfoliated biochar electrodes from 2.1 to 221.3 F/g.[87] Structural integrity and electrical conductivity are remedied by adding polymeric binders and conductive additives, respectively. These additional components make up a considerable fraction of the weight of electrodes, resulting in lower energy density and higher device cost.[89,90,91]

To provide mechanical integrity and electrical conductivity of binder-free biochar-based electrodes, we developed biochar-reduced graphene oxide composites in Chapter 7. The production started from biochar in a coarse powder form (> 100 μm in size). After milling and acid treatment, the treated biochar exhibited significantly increased specific surface area (increase from ~180 m^2/g to ~410 m^2/g), as experimentally determined by a nitrogen absorption study. The modified biochar, however, was still in powder form and did not exhibit sufficient electrical conductivity to be useful as an electrochemical electrode. Thus, we further modified the material by adding a small amount (~7.5 wt%) of reduced graphene oxide. The reduced graphene oxide played a role as a binder to maintain mechanical integrity and a percolating path for electrical conductivity. The resulting biochar composite material exhibited an enhanced specific surface area that was nearly comparable to commercial activated carbons (~490 m^2/g). Moreover, the composite can be bent and stretched repeatedly without leaving disintegrated powders, enabling the possibility of using the electrode for flexible electronics application. After the fabrication, characterizations of the electrochemical properties, morphology, and surface chemical analysis were performed. At a current density of 0.5 A/g, the specific capacitance of the biochar-reduced graphene oxide electrodes reached 216 F/g. The capacitance value normalized by specific surface area was 44.62 $\mu F/cm^2$ at 0.5 A/g, which is desired for electrochemical energy storage devices.

1.2.3.2 Self-Reinforcing Graphene Coatings for Flexible & Printed Electronics (Chapter 8)

Ink-jet printing of conductive inks has been proven as a feasible method to fabricate flexible and printed electronics at an affordable price.[92] A wide range of materials have been employed as conductive inks. However, most of them require rather harsh post-printing treatments. For example, conductive inks based on metal nanoparticles can achieve high conductivity, but require a sintering process at high temperature or other severe chemical or energetic post treatments to remove stabilizing agents or oxide layers.[92] Such processes have caused compatibility problems to many substrates used for flexible electronics, such as paper, plastic sheet, or elastomer, which may denature upon heat and acid treatments.[93] Noble metals allow rather mild post-treatment conditions, but they are generally expensive.[94] The conductive polymer is another popular choice, but chemical stability, such as oxidation, has been a critical issue that prevents widespread use.[95] Carbon-based conductive inks, especially graphene-based inks, have been suggested as a balanced combination between high conductivity, mild processing, and chemical stability.[96]

Graphene can be dispersed to form ink by two methods: First, graphene powder is directly dispersed in the organic solvent with relatively high viscosity, such as N-Methyl-2-pyrrolidone or dimethylformamide without additives.[97,98] The second scenario is that of employing binder materials, such as ethyl cellulose, as additives to form a suspension.[99,100] Using the former method, Hu *et al.* inkjet printed a binder-free graphene/N-Methyl-2-pyrrolidone suspension on the paper, followed by rolling compression to achieve a conductivity of 4.3×10^4 S/m.[101] However, usually organic solvent is not compatible with the polymer substrates, which may cause swelling or dissolving of polymer substrates for the printing, leading to distortion or fracture of the printed graphene traces that limits the resolution of the printed pattern. In addition, the absence of active chemical binding between the graphene nanoflakes causes poor mechanical integrity that may induce the fracture of the printed graphene traces. The latter method that employs binder material can provide enhanced mechanical integrity by covalent bonding between the graphene flakes, but the binder compromises the conductivity, thus a thermal post-treatment to decompose the material is needed, which is not ideal for flexible substrates. If the binder material itself is electrically conductive, on the other hand, both electrical conductivity and mechanical integrity can be achieved at the same time.

In Chapter 8, we propose a self-reinforcing conductive coating strategy, in which reduced graphene oxide self-assembles to wrap graphene nanoflakes as a conductive binder that can also achieve mechanical integrity. The conductivity of the graphene nanoflakes–reduced graphene oxide coating reaches 4.47×10^4 S/m. To demonstrate the potential applications of the coating, applying the coating on 3D printed porous elastomers enabled flexible radio frequency antennas and strain sensors. The radio frequency antenna shows high radiation efficiency and maintains excellent performance under bending conditions. The coating also produces a strain sensor with a gauge factor of ~13 up to 40% of strain. We foresee that the electrically conductive composite coating can provide versatile functionalization strategy in the flexible electronics and in wearable biomedical devices.

1.2.3.3 Sponge-Templated Graphene Network for Piezoelectric Nanogenerator (Chapter 9)

As the concept of 'Internet of Things (IoT)'—that many living and non-living objects have network connectivity to send and receive data—evolves, power sources are required to be included

in all existing objects to transfer the information between nodes.[102] Energy harvesting by utilizing piezoelectric materials that can convert mechanical motion to electrical energy is suitable for wearable products, where devices can be charged during daily activities.[103,104]

Arrays of zinc oxide (ZnO) nanowires have been utilized as promising electricity generators by the piezoelectric effect in the recent studies by Wang and co-workers.[105,106,107] The piezoelectricity stems from the crystalline structures of the nanowires and their self-rectifying nature at the electrical contact to substrate materials.[108,109,110] Moreover, ZnO arrays on graphene provide an attractive option for nanogenerators due to desirable Schottky barrier properties.[111,112,113,114] However, synthesis of both ZnO and graphene substrate is costly by conventional methods, and consumers do not wish to see an increase in price for inexpensive commodity items due to the power sources. For IoT applications, remaining challenges include a simple and inexpensive synthesis of the nanomaterials and the maximization of the ZnO/graphene area per unit volume for high-density power generation. Recent studies suggested that the former can be achieved by hydrothermal synthesis of ZnO nanowires, which allows a high-density array of ZnO at the maximum processing temperature of ~90°C.[115,116] The latter requires a 3D porous network of graphene with a low-cost fabrication method.[117,118,119]

In Chapter 9, we report a simple approach to fabricate ZnO nanowire-based electricity generators on 3D graphene networks by utilizing a commercial polyurethane sponge as a structural template. Here, a 3D network of graphene oxide is deposited from solution on the template, then is chemically reduced. Following steps of ZnO nanowire growth, polydimethylsiloxane backfilling, and electrode lamination completes the fabrication processes. When compared to conventional generators with 2D planar geometry, the sponge template provides a 3D structure that increases volumetric power density by increasing ZnO nanowire density per unit volume. The modified one-pot ZnO synthesis method allows the whole process to be inexpensive and environmentally benign. The nanogenerator yields an open circuit voltage of ~0.5 V and short circuit current density of ~2 $\mu A/cm^2$, while the output was found to be consistent after ~3000 cycles. Finite element analysis of stress distribution showed that external stress is concentrated to deform ZnO nanowires by four orders of magnitude compared to surrounding polyurethane and polydimethylsiloxane. It is shown that the backfilled polydimethylsiloxane plays a crucial role in the stress concentration, which leads to an efficient electricity generation.

1.2.4 Synthesis of Poly(glycerol sebacate) for Tailored Mechanical Properties (Chapter 10)

Poly (glycerol sebacate) (PGS) and its derivatives make an attractive class of biomaterial owing to their tunable mechanical properties with programmable biodegradability. In practice, however, the application of PGS is often hampered by frequent inconsistency in reproducing process conditions. The inconsistency stems from the volatile nature of glycerol during the esterification process. In this study, we suggest that the degree of esterification (DE) can be used to precisely predict the physical status and the mechanical properties of the PGS materials. The Young's modulus is shown to linearly increase with DE, which is in agreement with an entropic spring theory of rubbers. In order to provide a processing guideline for researchers, we also provide a physical status map as a function of curing temperature and time. The amount of glycerol loss, obtainable by monitoring the evolution of the total mass loss and the DE during synthesis, is shown to make the predictions even more precise. We expect that these strategies can be applicable to different categories of polymers that involve condensation polymerization with the volatility of the reactants. In addition, we demonstrate that microwave-assisted pre-polymerization is a time and energy efficient pathway to obtain PGS. For example, 15 minutes of microwave time is shown to be as efficient as the pre-polymerization in nitrogen atmosphere for 6 hours at 130°C. The quick synthesis method, however, causes a severe evaporation of glycerol, resulting in a large distortion in the monomer ratio between glycerol and sebacic acid. Consequently, more rigid PGS is produced at a similar curing condition compared to the conventional pre-polymerization method. Finally, we demonstrate that the addition of molecularly rigid crosslinking agents and network-structured inorganic nanoparticles are also effective in enhancing the mechanical properties of the PGS derived materials.

1.3 Outline of the Dissertation

The layout of the dissertation is as follows. In Chapter 2, theories that are required to understand this dissertation, including polymer solution, ion solvation, polyampholyte conformation, graphene oxide and its reduction, are briefly reviewed. Chapter 3 describes chosen material systems and their synthesis and characterization techniques. Chapters 4 to 10 cover the main results and discussions in the dissertation. Titles, objectives and major results from each chapter are summarized in Table 1.1. Finally, Chapter 11 provides insights for possible future studies.

Table 1.1 Summary of Chapters 4 to 10

Chapter 4

Title	Low-Temperature Ionic Conductivity Enhanced by Disrupted Ice Formation in Polyampholyte Hydrogels
Major Results	- The SAXS results suggest a network of globule structures in the charge-balanced polyampholyte hydrogels. - The globular network structure results in the increase in amorphous water at −30 °C, as supported by WAXS results. - The interconnected polymer-rich domains result in a slush-like ice formation that allows enhanced ionic conductivity of the hydrogel in ice forming conditions at low temperatures. - The globular structures were directly visualized with SEM for the first time, as supported by scanning transmission electron microscopy.

Chapter 5

Title	Water States in Salt-Containing Polyampholyte Hydrogels
Major Results	- A differentiation of the water–polymer interactions in polyampholyte hydrogel into free water, freezable bound water–polymer, freezable bound water–salt, and nonfreezable bound water through quantitative DSC analysis. - Different synthesis condition may change the ice amount in the polyampholyte hydrogel.

Chapter 6

Title	Highly Flexible, Multipixelated Thermosensitive Smart Windows Made of Tough Hydrogels
Major Results	- A flexible smart window with a polyampholyte hydrogel was fabricated, showing 80% in transmittance contrast from opalescence to transparency. - The phase transition temperature of the polyampholyte hydrogels could be fine-tuned by doping of a small number of hydrophobic monomers into cationic monomers. - By printing a stretchable elastic heater layer onto the hydrogel film, we demonstrated a pixelated array of actively tunable smart windows. - The window is highly robust against large deformation, which could undergo a large deformation (up to 80% strain).

Chapter 7

Title	Flexible and Self-Healing Aqueous Supercapacitors for Low Temperature Applications: Polyampholyte Gel Electrolytes with Biochar Electrodes
Major Results	- A supercapacitor with a high energy density that works at low temperature was fabricated. - Reduced graphene oxide was incorporated with biochar to transform the pyrolyzed waste biomass into high-performance binder-free electrodes for electrochemical energy storage devices. - A symmetric supercapacitor made with biochar composite as the electrode and polyampholyte hydrogel as the electrolyte showed a high energy density of 30 Wh/kg, and a capacitance retention of ~90% after 5000 charge–discharge cycles. - At low temperature (−30 °C), the supercapacitor had an energy density of 10.5 Wh/kg at a power density of 500 W/kg.

Chapter 8

Title	Self-Reinforcing Graphene Coatings on 3D Printed Elastomers for Flexible Radio Frequency Antennas and Strain Sensors
Major Results	- A self-reinforcing nanocomposite of graphene nanoflakes that are enclosed by self-assembled GO particles was developed. - A two-step acid treatment protocol reduced graphene oxide, enhancing the electrical conductivity of the composite coating. - The substrate material was 3D printed porous elastomers prepared from a commercial filament material. The whole process was conducted at a temperature lower than 120 °C without using any organic solvent. - The composite coatings were applied on 3D-printed objects to transform the non-functional elastomers into flexible radio frequency antennas and the strain sensors.

Chapter 9

Title	Sponge-Templated Macroporous Graphene Network for Piezoelectric ZnO Nanogenerator
Major Results	- A low-temperature processing method to fabricate a ZnO nanowire-based electricity generator with a 3D structure templated on a commodity sponge material was demonstrated. - Graphene oxide was dip-coated from aqueous solution on the commodity sponge and reduced, resulting in the transformation of a sponge into a conductive 3D network. - ZnO nanowires were grown by a one-step hydrothermal method in an aqueous solution below 95 °C. - A band diagram shows a Schottky contact at the ZnO/Au interface and ohmic contact at the ZnO/reduced graphene oxide interface. - The nanogenerator yielded an open circuit voltage range up to ~0.5 V and a short circuit current density range up to ~2 $\mu A/cm^2$. In a durability test, degradation in output voltage was not found after ~3000 bending and releasing cycles. - Finite element analysis of stress distribution showed that the stress is localized to the ZnO arrays under operational condition within the presence of polydimethylsiloxane, thus allowing effective electricity generation.

Chapter 10

Title	Criteria for Quick and Consistent Synthesis of Poly(glycerol sebacate) for Tailored Mechanical Properties
Major Results	- The degree of esterification (DE) is shown to be effective in quantitatively predicting physical state and Young's moduli and degradation of PGS. - Loss of glycerol in PGS is shown to cause a deviation from the prediction based on DE. - The effect of microwave time was also studied in terms of DE. The microwave method is shown to be effective to achieve a high-degree of DE in a short time (for less than 30 min), suggesting that it can provide a time- and energy-conserving synthesis pathway compared to a conventional prepolymerization method in a nitrogen oven (for hours to days). - The addition of cross-linking agents with rigid molecular structure can result in a significant increase in Young's modulus without compromising the stretchability. - Nanoparticles, fumed silica in this study, were also shown to be effective in enhancing Young's modulus. - Both cross-linking agents and nanoparticles can significantly decrease the degradation rate by increasing strand density in PGS networks.

Chapter 2 Theoretical Background

2.1 Introduction

Chapter 2 is a brief review of fundamental concepts of polymer physics, covering chain conformation in general polymer solutions, the conformation of polyampholyte chains, and their gelation. Since the concept of the water state is used in the majority of the chapters, a short introduction of ion/polymer solvation effect is included after the polymer physics sections. The results reported in the literature are also discussed in the corresponding parts to provide a better understanding of the following chapters.

2.2 Polymer Solution

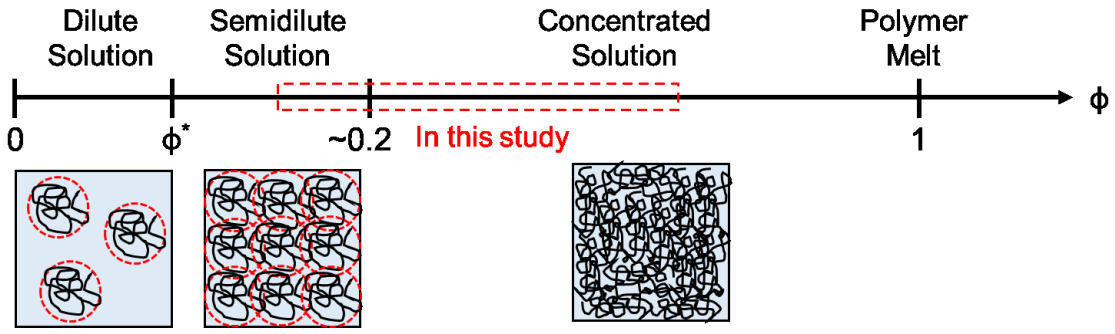

Figure 2.1 The classifications of polymer solution depend on the polymer fraction. Based on the concepts of reference [120].

Before we investigate the chain conformation of polyampholytes, a brief introduction of the general polymer solution is given. In this subsection, ionic interactions between the polymer chains are not considered. Since hydrogel is a polymer network containing large quantities of water,[121] the knowledge of the chain conformations in polymer solution may give us some hints for understanding the chain conformation in the polyampholyte hydrogel. For example, the strongly hydrophobic polyampholytes with a charge-balanced stoichiometry are fully soluble in the concentrated salt solutions and precipitated in solutions with lower salt concentrations.[122,123,124] The presence of salt in the polyampholyte solution can change the solvent quality from poor to good by increasing salt concentration. As shown in Figure 2.1, the polymer volume fractions in

this study are from 0.1 to 0.5, which is in the range from a semidilute solution to concentrated solution.

2.2.1 Theta Solvent

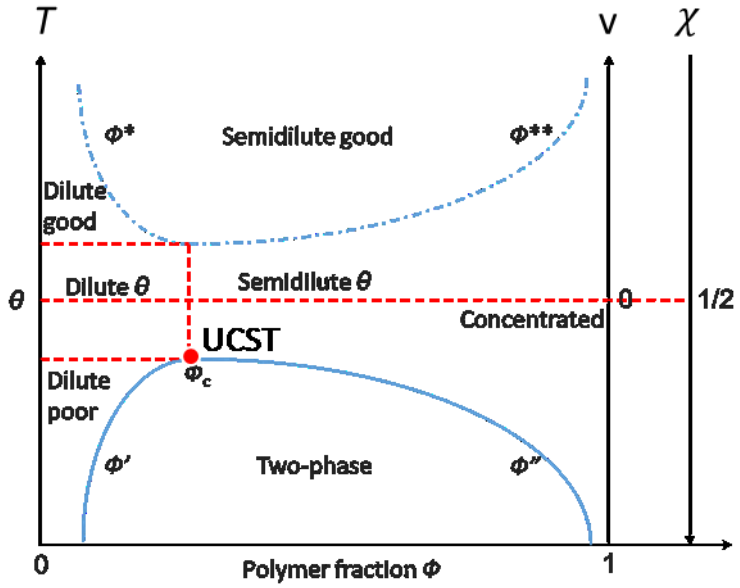

Figure 2.2 Phase diagram for polymer solutions with an upper critical solution temperature (UCST). The solid blue curve donates the binodal and phase separation occurs for polymer solutions with temperature and polymer fraction below the binodal. The dash-dotted blue curve is the low temperature boundary of the semidilute good solvent regime. ϕ' is the polymer volume fraction of dilute supernatant. ϕ'' is the polymer volume fraction of a concentrated sediment. ϕ^* is the polymer volume fraction at which the polymer chains begin to interpenetrate and become a semidilute solution. ϕ^{**} is the polymer volume fraction of the high concentration branch of the semidilute regime. Redrawn from Figure 5.1 in reference[120].

Figure 2.2 shows a not-to-scale schematic phase diagram of a polymer solution with an upper critical solution temperature (UCST). The reason for using this phase diagram is that typical polyampholyte hydrogel has the same behavior. The temperature dependence of the Flory interaction parameter is empirically written as:[120]

$$\chi(T) \cong A + \frac{B}{T} \qquad (2.1)$$

where A is the parameter of the "entropic part", and $\frac{B}{T}$ is the "enthalpic part". The relative magnitude of the enthalpic part is dependent on the relative strength of interactions between the

polymer chains and the solvent, and the relative magnitude of the entropic part depends on the hydrophobic effect of the polymer backbones, and the ordered hydration shell around ionic groups in the polymer backbones.[125,126,127] For polyampholyte hydrogels, as temperature increases, the water molecules breaks the ion–ion interactions between polymer chains and forms ion–dipole interactions between water and polymer chains.[128] Since ion–dipole interactions are weaker than ion–ion interactions,[125] the enthalpic part in the Flory interaction parameter is inversely proportional to the temperature. According to Equation 2.1, the phase behavior of the polymer solution can be tuned by changing either the entropic part or the enthalpic part of the Flory interaction parameter. In Chapter 6, the entropic part is reduced by doping hydrophobic monomers in the polymer backbones. In the regime below the binodal curve, the polymer solution separates into two phases. Because of the difference in the refractive index of the polymer-rich and solvent-rich phases, light is scattered by the polymer solution influences the turbidity.[125] When the phase transition happens in the polymer solution, the turbidity changes sharply, and the transition temperature of turbidity is called the cloud point.[125]

The diagram of the polymer solution is separated by the temperature $T = \theta$, at which the interaction parameter $\chi = 1/2$ and the excluded volume, v = 0, according to:[120]

$$\mathrm{v} = (1 - 2\chi)b^3 = \frac{T-\theta}{T}b^3 \qquad (2.2)$$

where b is the Kuhn length. At the θ-temperature, the polymer chains have nearly ideal conformation. The mean-square end-to-end distance of a linear chain with N Kuhn monomers is:[120]

$$< R^2 >= Nb^2 \qquad (2.3)$$

It is notable that this relationship is valid at all concentrations for polymers in the theta solvent, in which the constant steric repulsion and the solvent-mediated attraction between monomers are exactly cancelled. The polymer chains are far apart and exist as isolated coils in the dilute solution until the polymer fraction reaches the overlap concentration, which equals the polymer fraction inside the pervaded volume (*i.e.*, the volume of solution spanned by the polymer chain in the solution[120]) of the coils. The overlapping concentration of theta solvent is:[120]

$$\phi_\theta^* \approx \frac{1}{\sqrt{N}} \qquad (2.4)$$

The linear chains interpenetrate each other above ϕ_{θ}^{*}. Many solution properties are dependent on the overlapping polymer chains in the solution, even though there are much more solvent molecules.

2.2.2 Poor Solvent

As temperature decreases, the solvent quality decreases for the polymer with an UCST. For charge-balanced polyampholyte chain, the solvent quality also decreases with lower ionic strength in the salt solution. The transition of polyampholyte chain conformation will be mentioned in Section 2.3. Here, a general polymer solution is discussed. In Figure 2.2, the highest point on the binodal curve is the critical point with critical composition $\phi_{\mathrm{c}} \cong \frac{1}{\sqrt{N}}$, critical interaction parameter $\chi_{\mathrm{c}} = \frac{1}{2} + \frac{1}{\sqrt{N}} + \frac{1}{2N}$, and critical temperature:[120]

$$\frac{1}{T_{\mathrm{c}}} = \frac{1}{\theta} + \frac{1}{B}\left(\frac{1}{\sqrt{N}} + \frac{1}{2N}\right) \qquad (2.5)$$

The homogeneous polymer solutions phase separate into two phases below the binodal line: a dilute supernatant of isolated globules (with polymer volume fraction ϕ') and a concentrated sediment (with polymer volume fraction ϕ''). The volume fraction of polymer in the supernatant and the coexisting sediment is:[120]

$$\phi' = \phi'' \exp\left(-\frac{\gamma R_{\mathrm{globule}}^{2}}{kT}\right) \approx \frac{|\mathrm{v}|}{b^{3}} \exp\left(-\frac{|\mathrm{v}|^{4/3}}{b^{3}} N^{2/3}\right) \qquad (2.6)$$

$$\phi'' \approx 2\chi - 1 = -\frac{\mathrm{v}}{b^{3}} \qquad (2.7)$$

where R_{globule} is the size of the globules in the supernatant, and γ is the surface tension of the globules. The globules have the tendency to stick together to form large clusters to reduce their surface energy in the poor solvent. The size of the globule in the supernatant is given by:[120]

$$R_{\mathrm{globule}} \approx \frac{b^{2} N^{1/3}}{|\mathrm{v}|^{1/3}} \qquad (2.8)$$

which is the close packing of the thermal blobs. Once the globules stick to the condensed sediment, the chains are in their ideal conformation, and this condition can be described as the melt of thermal blobs.

2.2.3 Good Solvent

The solvent quality increases as temperature increases, as shown in the upper part of the phase diagram in Figure 2.2. The polyampholyte studied in this dissertation is mostly in the poor or theta solvent (*i.e.*, at the temperature below UCST or in the presence of excessive salt in the solution). In dilute solution, the chain behaves like an isolated real chain with size:[120]

$$R \approx b(\frac{\mathrm{v}}{b^3})^{2\nu-1}N^{\nu} \qquad (2.9)$$

where $\nu \cong 0.588$ is the swelling exponent. At ϕ^*, the polymer chains begin to interpenetrate and become a semidilute solution:[120]

$$\phi^* \approx \frac{Nb^3}{R^3} \approx (\frac{b^3}{\mathrm{v}})^{6\nu-3}N^{1-3\nu} \qquad (2.10)$$

The size of a polymer chain is given by:[120]

$$R \approx \xi(\frac{N}{g})^{1/2} \approx b(\frac{\mathrm{v}}{b^3\phi})^{(\nu-\frac{1}{2})/(3\nu-1)}N^{1/2} \qquad (2.11)$$

where ξ is the correlation length, and g is the number of monomers in a correlation blob. With increasing concentration, the correlation length decreases, until it equals to the size of a thermal blob, $\xi \approx \xi_T$. The high concentration branch of the semidilute regime is:[120]

$$\phi^{**} \approx \frac{\mathrm{v}}{b^3} \qquad (2.12)$$

At and above this concentration, the chains are ideal on all length scales, which follows $R \approx bN^{1/2}$.

2.3 Polyampholyte

Polyampholyte chains carry ionizable functional groups. Under certain conditions, for example, in the aqueous solution, these groups dissociate and leave positively and negatively

charged groups on the polymer chain.[36] In this section, the chain conformation of the charge-balanced polyampholyte in the dilute solution is introduced first. Then, the impacts of charge asymmetry and salt concentration on the chain conformation are mentioned. Finally, the phase behavior of polyampholyte solution and gelation of polyampholyte hydrogel are discussed.

2.3.1 Charge-Balanced Polyampholyte Chains in Dilute Solution

Charge-balanced polyampholyte chains have attracted lots of attention because of their unique property compared with general polyelectrolytes, which is known as "anti-polyelectrolyte" behavior.[129,130,131] For example, the viscosity and coil size increase as salt is added to the charge-balanced polyampholyte solution.[132,133]

A change-balanced polyampholyte hydrogel with the degree of polymerization N has the same numbers of positively and negatively charged groups. The charge asymmetry of a polyampholyte chain is:[36]

$$\delta fN = |f_+N - f_-N| \quad (2.13)$$

where f_+ and f_- are the fractions of positively and negatively charged groups, respectively. The first quantitative theory of the collapse transition of a single polyampholyte chain showed that the charge-balanced polyampholyte chains collapse into a globule due to the Debye–Huckel fluctuation-induced attraction between charges.[37] The fluctuation-induced attraction is dictated by the electrostatic interaction between oppositely charged sections of a chain, so the strength of the fluctuation-induced attraction depends on the ratio of the Debye length of the solution and the polymer chain size, which was observed experimentally.[134] An analogue to the globule consisted of closely packed thermal blobs for a polymer in the supernatant in a poor solvent; the globule of collapsed polyampholyte chain can be considered as a densely packed arrangement of concentration blobs with size ξ and monomer number g. At length scales smaller than ξ, the electrostatic interaction energy and thermal energy are comparable, so electrostatic interactions are not strong enough to perturb the chain conformation. The chain sections within ξ are nearly ideal and obey Gaussian statistics:[36]

$$\xi^2 \approx b^2 g \qquad (2.14)$$

At length scales larger than ξ, each concentration blob is surrounded with a higher probability by oppositely charged blobs by electrostatic attractions that force the chain to collapse into a globule. The cohesive energy of a blob equals to $k_{\mathrm{B}}T$ and is proportional to the energy of electrostatic interactions between two neighboring concentration blobs, which carry opposite excess charges, eq and $-eq$:[36]

$$F_{\mathrm{el}}(g) \approx -k_{\mathrm{B}}T\, l_{\mathrm{B}} q^2/\xi \qquad (2.15)$$

where $l_{\mathrm{B}} \equiv \frac{e^2}{\varepsilon\, k_{\mathrm{B}}T}$ is the Bjerrum length, indicating the distance at which the electrostatic interaction energy between two elementary charges e equals to the thermal energy $k_{\mathrm{B}}T$ in the medium. The average excess charge of blobs can be estimated by $eq = e\sqrt{(f_+ g + f_- g)}$, and Equation 2.15 can be rewritten as:[36]

$$F_{\mathrm{el}}(g) \approx -k_{\mathrm{B}}T\, l_{\mathrm{B}} g f/\xi \qquad (2.16)$$

$$f = f_+ + f_- \qquad (2.17)$$

where f is the total fraction of the charged monomer in a polyampholyte chain. There is a three-body repulsion to balance the electrostatic attraction at the equilibrium state, and it is proportional to the thermal energy $k_{\mathrm{B}}T$ times the probability of three-body contacts,[36]

$$F_{\mathrm{rep}}(g) \approx k_{\mathrm{B}}T g(\rho b^3)^2 \approx F_{\mathrm{el}}(g) \qquad (2.18)$$

where $\rho \approx g/\xi^3$ is the average monomer density inside the globule. According to Equation 2.18, the equilibrium size of the concentration blobs ξ, the number of monomers g in the blobs, and the polymer density inside a globule can be determined by,[36]

$$\xi \approx b/(uf) \qquad (2.19)$$

$$g \approx (uf)^{-2} \qquad (2.20)$$

$$\rho \approx ufb^{-3} \qquad (2.21)$$

where $u = l_{\mathrm{B}}/b$ is the interaction parameter. The size of the globule calculated by monomer density is,[131]

$$R_{\mathrm{gl}} \approx (N/\rho)^{1/3} \approx b(\frac{N}{uf})^{1/3} \quad (2.22)$$

2.3.2 Charge Asymmetry on Chain Conformations

The distribution of charge on the polyampholyte chain affects the chain conformation.[135,131] For the ideal case of a charge-balanced polyampholyte chain, the positive and negative charges are alternating. The polyampholyte chain behaves like a polymer chain only with short-range interaction, and the collapse transition of the chain resembles the coil–globule transition of a neutral polymer, since the Debye–Huckel theory is inapplicable to strictly alternating polyampholytes because large fluctuations of charge density are impossible.[135,136] In practice, the polyampholyte chains are usually prepared by random copolymerizing of anionic and cationic monomers.[17,18,137] During the polymerization, the sequence of the charged monomers is fixed. Due to the fact that the reactivity of anionic and cationic monomers are always different, it is difficult to get the alternating charged groups for synthetic polyampholytes prepared by copolymerization, even starting from a symmetric mixture with equal concentrations of positive and negative monomers in the reaction bath.[17,129] The polyampholyte chains prepared by copolymerization have an excess of charges, resulting in a charge asymmetry distribution, and the width of the charge asymmetry distribution depends on the difference in reaction rate constants between the monomers.

In this dissertation, sodium 4-vinylbenzenesulfonate (NaSS) and [3-(methacryloylamino)propyl]trimethylammonium chloride (MPTC) are the mostly used monomers. Sun *et al*. investigated the reactivity ratios of NaSS and MPTC which were determined by using the integrated form of the copolymerization equation (terminal model) for the three reactions based on in situ quantitative ^{1}H NMR monitoring of monomer consumption.[17,138] At the beginning of copolymerization, NaSS molecules are incorporated with a few MPTC molecules added due to the difference in reactivity ratios. Approximately, a sequence of three NaSS molecules is followed by one MPTC molecules. At total monomer conversion rate of 0.8, a sequence of one NaSS molecule would be followed by five MPTC molecules. When the copolymerization reaches total monomer conversion rate higher than 0.9, most of the remaining monomers are MPTC, so the polyampholyte chains grow with a block sequence of MPTC molecules.[17] Charge asymmetry is introduced in the polyampholyte chains by the copolymerization process.

The charge asymmetry of the polyampholyte chain changes the shape of the globule when the energy of electrostatic interactions between the excess charges, $\delta Q = eN|f_+ - f_-|$, becomes comparable with the surface energy of the globules.[137] The critical net charge of a randomly charged polyampholyte globule is $\delta Q_c = e\sqrt{fN}$. If the charge asymmetry is smaller than δQ_c, the energy of electrostatic interactions between the excess charges is weaker than Debye–Huckel fluctuation-induced attraction, so the collapsed chain maintains a globule shape. If the charge asymmetry is larger than δQ_c, the collapsed chain has to reduce its total energy by lowering the electrostatic interaction energy between excess charges at the expense of increasing polymer–solvent interface, leading to increased surface energy. At low temperature, the polyampholyte chains form a necklace globule to minimize total energy of both electrostatic interaction and surface tension.[36]

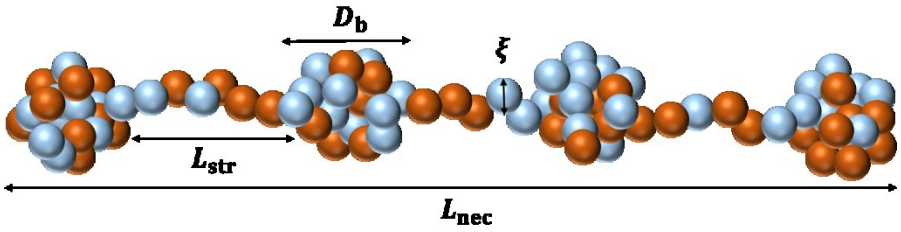

Figure 2.3 Schematic illustration of a necklace globule. The blue blobs are negatively charged, and the brown blobs are positively charged. Redrawn from Figure 5 in reference [36].

A necklace globule conformation of a polyampholyte chain with a large charge asymmetry is shown in Figure 2.3. Beads with diameter D_b are connected by strings with length L_{str}, and the total length of the necklace is L_{nec}. The number of monomers m_b in each bead is determined by Rayleigh's stability condition that the electrostatic energy of a bead is of the order of its surface energy, which is given by:[36]

$$\gamma D_b^2 \approx k_B T (uf)^2 \frac{D_b^2}{b^2} \approx \frac{(e\delta f m_b)^2}{\varepsilon D_b} \qquad (2.23)$$

The size of a beads and monomer number in a bead are given by:[36]

$$D_b \approx (m_b/\rho)^{1/3} \qquad (2.24)$$

$$m_b \approx f/(\delta f)^2 \qquad (2.25)$$

According to Equation 2.25, the number of monomers in the bead decreases as the charge asymmetry of the chain increases. The decreasing bead size increases the number of beads on the necklace, which was observed in Monte Carlo simulations.[139] The equilibrium length of strings between beads is determined by balancing the surface energy of a string with the electrostatic repulsion between two neighboring beads,[36]

$$\gamma\xi L_{\mathrm{str}} \approx k_{\mathrm{B}}T\frac{L_{\mathrm{str}}}{\xi} \approx k_{\mathrm{B}}T(uf)\frac{L_{\mathrm{str}}}{b} \approx \frac{(e\delta f m_{\mathrm{b}})^2}{\varepsilon L_{\mathrm{str}}} \qquad (2.26)$$

Substituting Equation 2.25 into Equation 2.26, L_{str} can be written as,[36]

$$L_{\mathrm{str}} \approx b\sqrt{f}/\delta f \approx b\sqrt{m_{\mathrm{b}}} \qquad (2.27)$$

Comparing Equation 2.25 and Equation 2.27, we can infer that increasing the bead size decreases the length of strings which connect the beads. Since most of the mass of the polymer chain is attributed to the bead, the total length of the globular necklace can be estimated as the total length of the strings,[36]

$$L_{\mathrm{nec}} \approx b\delta f N/\sqrt{f} \qquad (2.28)$$

Based on the previous discussion, the chain conformations of polyampholytes in dilute salt-free solutions in the parameter space of the total fraction of charged monomers and the charge asymmetry can be summarized in Figure 2.4, as a diagram of states.[140] The overall size and shape of the chain are determined by the competition between the following factors.[37,141] Chain entropy tends to keep the polymer configuration to Gaussian statistics, but fluctuation-induced attractions between charges tend to collapse the coil into a globule. The size of the globule is stabilized by short-range three-body monomer–monomer interactions and the size of the chain tends to be elongated by the overall Coulomb repulsion between excess charges.

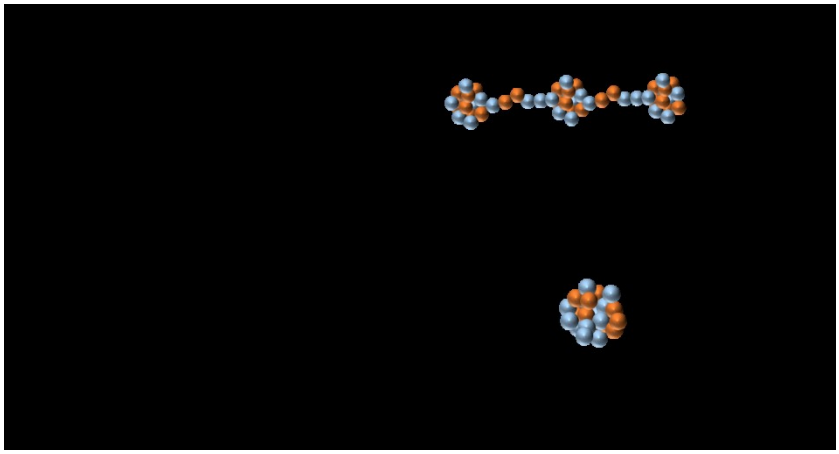

Figure 2.4 Diagram of states of a polyampholyte chain in dilute solution in the parameter space of the total fraction of charged monomers and the charge asymmetry. Redrawn from Figure 7 in reference [36].

2.3.3 Effect of Salt Concentration on Chain Conformation

Polyampholyte solution usually contains salt after polymerization, due to the dissociation of electrolytic monomers. For example, after copolymerization of NaSS and MPTC, counter ions of the monomers were left in the final hydrogel. The existence of NaCl may affect the conformation of polyampholyte chains. Since the origin of interactions between the polyampholyte chains is from the electrostatic force, the salt concentration in the solution can change the interaction strength.[142] For charge-balanced polyampholyte, the size of the chain increases as the salt concentration increases. Salt ions can screen the fluctuation-induced attraction between opposite charges. Without salt ions in dilute polyampholyte solution, the Debye length due to charged groups on the polymer backbone can be rewritten as:[36]

$$\lambda_{\mathrm{D}}^{-2} = 4\pi\, l_{\mathrm{B}} f \rho \approx \xi^{-2} \qquad (2.29)$$

The size of a concentration blob is of the order of the Debye length. Note that Equation 2.29 is only valid for the dilute polyampholyte solution without salt, since the calculation of the Debye length is based on the charges in the polymer backbones. With the presence of foreign ions within the concentration blobs, the Debye length further decreases compared with a salt-free condition, leading to a lower monomer density as well as a larger blob size. Once the salt concentration reaches a critical value, the distance between charged groups on the backbone is

larger than the Debye length, the electrostatic interactions are too weak to perturb the chain conformation.

2.3.4 Phase Behavior of Polyampholyte Solutions

As we discussed in the section 2.3.2, the polyampholytes prepared by random copolymerization usually have a large charge asymmetry.[17] The excess of charges not only affects the single chain conformation, but also affects the phase behavior of polyampholyte solution. The polyampholyte chains with opposite excessive charges form neutral complexes to reduce electrostatic energy, and neutral complexes further aggregate together to reduce their surface energy.[143,144] The aggregates precipitate in the solution, leaving the supernatant to contain charged globules. Molecular dynamics simulations showed that a system of polyampholyte chains with zero net charge phase separated from solution to form a cluster of several chains. For a system of chains with nonzero net charge, a cluster consisting of several chains was also found, but the cluster swelled to minimize the electrostatic repulsion between similarly charged chain segments.[145] The theoretical study also showed the possibility of microphase separation in concentrated polyampholyte solutions, which was caused by the competition between short-range monomer–monomer attractive interactions and the electrostatic interactions between charged groups.[146] Ionic associations formed due to the fluctuations of excessive charges in concentrated polyampholyte solutions serve as the cross-linking between the chains, which facilitate the gelation of polyampholyte.[147,148,149] The gelation of polyampholytes is discussed in the next subsection.

2.3.5 Gelation of Polyampholyte

Cross-linking between polymer chains results in a larger branched polymer. At a certain extent of the cross-linking process, all polymer chains in the solution transform into a network spanning the whole system. This network cannot dissolve in a solvent, but may only swell in it. The transition from a system with only finite branched chains to a system with an infinite molecule is called gelation.[120] There are different types of gelation transitions, which are categorized in Figure 2.5. The gelation transitions can be generally classified into two groups. The first type is chemical gelation that involves the formation of covalent bonds between the polymer chains. For example, polyacrylamide hydrogel is prepared by copolymerizing acrylamide and crosslinker (N, N'-methylenebisacrylamide), which is an ideal matrix for the gel electrophoresis, because the

mesh size of the acrylamide networks is tunable by changing the cross-linking density.[150] The second class of gelation transitions is physical gelation. The gels are formed by physical linking between the polymer chains, such as hydrogen bonding,[151] block copolymer micelles,[152] or ionic associations.[17] Depending on the strength of physical bonds, physical gels can be further divided into weak physical gels and strong (tough) physical gels. The polyampholyte hydrogel investigated in this dissertation is a type of physical gel cross-linked by both ionic interactions between the charged groups and hydrophobic interactions between the polymer backbones.[8,17,148]

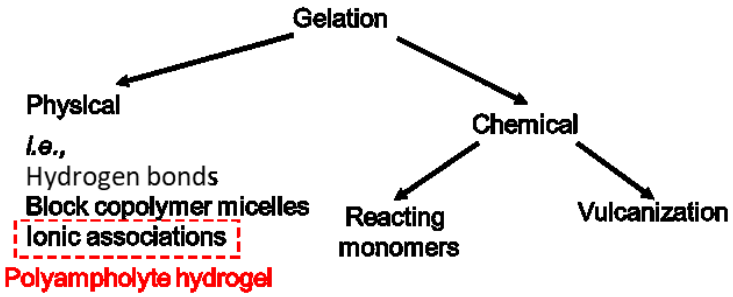

Figure 2.5 Classification of gelation transitions. Redrawn from Figure 6.2 in reference [120].

As we discussed in the section 2.3.2, due to the different reactivity ratios between the monomers, a block sequence of MPTC molecules forms in the copolymerization reactions of poly(NaSS-*co*-MPTC). The block sequences of MPTC increase the charge asymmetry in the polyampholyte chains,[17] and the local nonzero net charge leads to the formation of the ionic associations in concentrated polyampholyte solution.[36] As shown in Figure 2.6, the hydrogel of polyampholyte is formed by the ionic cross-linking between the chains. Since the charge asymmetry is not the same along a polyampholyte chain (*i.e.*, charge asymmetry is low in the middle, and is higher near the ends of the chain), the ionic associations will be formed with different ionic interaction strength. The bottom part of Figure 2.6 illustrates the strong and weak ionic interactions. Strong ionic interactions are formed by NaSS rich segments and MPTC rich segments, while other parts lead to weak ionic associations. Because of the difference in interaction strength, strong and weak ionic associations also have distinguishable properties. Under tensile strain, the strong ionic associations serve as permanent crosslinking points, which keep the shape of the hydrogel. Meanwhile, weak ionic associations act as sacrificial bonds. They break during deformation and dissipate energy. After removing external force, the weak interactions are formed

again.[153] This energy dissipation mechanism makes polyampholyte a class of tough hydrogel.[8,61] The ionic associations are also affected by the salt concentration in the hydrogel. As salt concentration increases, the weaker bonds are dissociated by the screening effect, and all ionic interactions between the polyampholyte chains will be destroyed at high salt concentration.[130] The reversible behavior of ionic interactions in the polyampholyte dedicates to the self-healing ability of the hydrogel. For example, the hydrogel sample broken into two pieces can be stored in a concentrated salt solution and bind together after leaching out the salt.[18,154] Moreover, the UCST of polyampholyte hydrogel can be manipulated by tuning the strength of ionic associations.[125,155] In Chapter 6, the interactions between the polyampholyte chains are enhanced by hydrophobic interactions, by doping the hydrophobic monomers during the copolymerization reaction.[29]

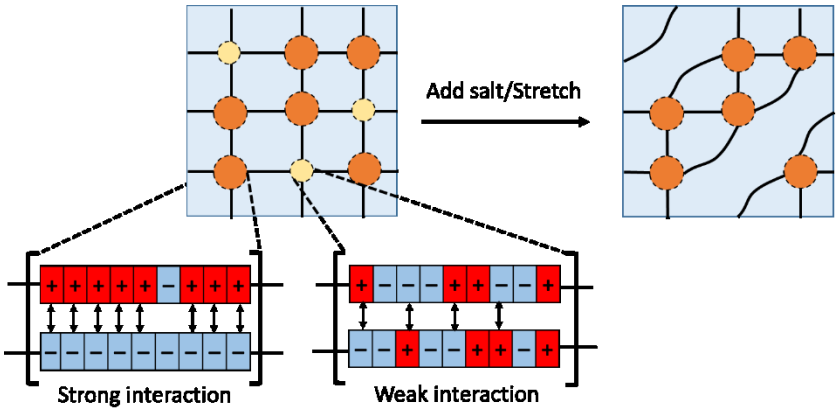

Figure 2.6 Above: an illustration of polyampholyte networks with ionic associations formed by different ionic interaction strengths. Brown circles: strong ionic associations. Yellow circles: weak ionic associations. Below: an illustration of strong and weak interactions with two sequences of charged groups on polyampholyte backbones. Based on the concepts of reference [17].

2.4 Solvation Behavior of Ions and Polymers

A hydrogel is a water-rich system. The properties of water inside the system govern the hydrogel's material properties, such as ionic conductivity and diffusivity.[19,20] The hydration behaviors or solvation effects of solute in the solution are a deterministic factor to consider when researchers design the material to meet various applications, for example, a gel electrolyte.[156,157] In Chapter 5, the water state in the salt-containing polyampholyte hydrogel is investigated. Salt-containing polyampholyte hydrogel is a complicated system, which has both dissociated salt ions

and polyampholyte chains. To simplify the study, the water state of mobile salt ions and that of polyampholyte chains can be considered separately in accordance with the deconvolution criteria in Chapter 5. Basic concepts of solvation behaviors of both simple ions and polymer chains are discussed in the following subsections.

2.4.1 Solvation Behavior of Small Ions

When electrolytes are dissolved in a solvent, they change from the pure state to the dissociated and solvated state in the solution. For strong electrolytes, most ions are dissociated into cations and anions. The presence of these ions gives the change in the solvent structure.[158] In the as-prepared polyampholyte hydrogels, NaCl is dissolved in the water-rich phase. The electrostatic interactions occur between the ions and the water molecules because of the dipolar nature of water. Na^+ ions attract the partial negative charge on the oxygen atom, and Cl^- ions attract the partial positive charge on the hydrogen atom in the water molecules.[159] Apparently, water molecules must reorganize their structure to accommodate these extra interactions. As shown in Figure 2.7, the region of water around the ions can be described by the term solvation shell.[159] The region nearest to the ion is the first solvation shell. Since the water molecules have strong interactions with the ions, water molecules in the first solvation shell are called primary solvation. In most cases, water molecules are coordinated to and move with the ions, so the water in this state is also referred to as bound water, indicating those water molecules have been immobilized and have lost their own translational degrees of freedom.[158] The next nearest layer of water molecules around the ions is called the second solvation shell. Water molecules in this shell are affected by the charge on the ion, which is called secondary solvation. They are not forming a coordination complex, and have certain translational degrees of freedom. However, the water state of secondary solvation is distinguishable from bulk water. The rest of the water molecules are far away from the ions, so the electrostatic interactions between them and the ions are screened by the water molecules in the first and second solvation shells, and cannot feel the existence of the ions. The state of these water molecules is almost the same as that of the bulk water, which can be referred to as non-bound water, or free water. The solvation of ions in the water changes the properties of the ions. For ions, the solvation of ions increases the size of the ions, which changes their ionic activity coefficient or diffusion coefficient.[160] For water, the presence of ions changes the structure of water. For example, the permanent dipoles of water molecules in the vicinity of ions are completely

reorientated in accordance with the dielectric saturation, leading to a decreased permittivity of water.[161] The characterizations of the solvation of small ions focus on measuring their solvation numbers. The solvation number is the number of water molecules in the first solvation shell. The conventional methods include vibrational spectra (IR and Raman), electronic spectra (UV), transport methods (conductance and diffusion), activity measurements, permittivity measurements, NMR measurements, X-ray or neutron diffraction, *etc*.[158,162,163,164] Since the scale of water structures probed by different measurements, the solvation number measured with different methods for the same ion has a large deviation.

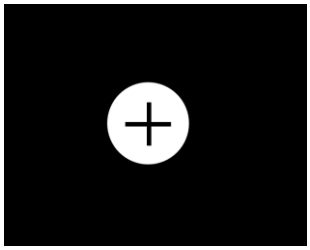

Figure 2.7 Schematic model of the ion solvation with solvation shells. Layer A is the first solvation shell. Layer B is the second solvation shell. The rest of water in regime C is bulk water. Based on the concepts of reference [159]. For monatomic cations and anions, such as Na^+ and Cl^-, six water molecules are normally found in their first solvation shell, and 14 water molecules in a fully hydrogen-bonded second solvation shell.[165,166]

The structure of solvation shells depends on properties of the ion, such as charge and radius. The terms "kosmotrope" and "chaotrope" are used to describe ions' ability to change the structure of surrounding water molecules.[167] A "kosmotrope" means an order-maker, and a "chaotrope" means disorder-maker. Large singly charged ions are chaotropes, because of low charge density, the interactions between ions and water molecules are weaker than water molecules with themselves. Thus, only a few hydrogen bonds of the surrounding water are disturbed. Small multiply-charged ions are kosmotropes, because of high charge density, the interactions between ions and water molecules are stronger than water molecules with themselves. Thus, they are able to break hydrogen bonds among the water molecules. In other words, the water–water hydrogen bonds near ionic kosmotropes are more broken than ionic chaotropes.[168] It has to be pointed out that ionic kosmotropes and chaotropes usually affect the water structure within the solvation shell,[169,170] but in some cases (*e.g.,* certain combinations of ions and counterions, and

concentrations), the effect of ions and counterions on water is interdependent and nonadditive, and extends beyond the water molecules that directly surrounds the ion.[171]

2.4.2 Solvation Behavior of Polymers

The solvation happens when polymer chains absorb water. Water molecules are attached to the polymer chains by hydrogen bonding or dipole–dipole interactions, and act as a part of the polymer chain, and change its properties. For example, water molecules diffuse into the crystalline regions of semicrystalline poly(vinyl alcohol) films, and decrease the mechanical strength of the films.[172] According to the strength of the interactions between polymer chains and water molecules, the states of water can be classified into the following categories.[173,174,175] Firstly, non-freezable bound water corresponds to the water molecules that are strongly bonded to the polymer chains by hydrogen bonding or dipole–dipole interactions. Dipole–dipole interactions are the attraction of two molecular dipoles. Typically, the dissociation energy of dipole–dipole interactions is lower than hydrogen bonding.[176] These water molecules are found to be unfrozen even at –190 ºC.[177] Secondly, freezable bound water corresponds to the water molecules that have secondary interactions with the polymer chains. These water molecules are intensively interacting with the non-freezable bound water by the second-order hydrogen bonding. Since these water molecules are bonded to the polymer chain via other water molecules, the second-order hydrogen bonding is weaker than the first-order hydrogen bonding. However, the activation energy required to rotate the freezable bound water molecules is larger than that required to rotate water molecules without constraint in the event of ice crystal formation. The effects of polymer networks on the ice formation depressions were observed to lower the freezing temperature to between –40 and –65 ºC.[173,178] Thirdly, there are water molecules that are not constrained by the polymer network, and simply occupy the empty space in the polymer network. Because they are unaffected by the presence of polymer chains, these water molecules will freeze at or near 0 ºC.[179] As we discussed in section 2.4.1, the investigations of the solvation behavior of small ions focus on the water structure in the solvation shell. However, it is difficult to get the exact structure of water around the polymer chains, due to the complexity and polydispersity of polymers. Thus, it is reasonable to classify and group the water molecules with the same properties. Moreover, considering the behavior of water molecules as a group (*i.e.,* water state) instead of interaction nanoscale (*i.e.,*

alignment of water molecules near the polymer chains) is convenient to describe the macroscopic properties, such as ionic conductivity, freezing point depression, *etc*.

The water states can be characterized on the basis of group behavior of water molecules in the similar environment. Since the thermodynamics of water molecules are changed in the different states, the behavior of water upon heating and cooling changes. Differential scanning calorimetry (DSC) is one of the most common characterization techniques used to probe the water states. Quantitative analysis on the endothermal peak from a heating scan of DSC can classify the water into distinctive categories.[176,179,180,181] Further details about DSC measurements are discussed in Chapter 3. Nuclear magnetic resonance (NMR) spectroscopy is also the most powerful spectroscopic technique to investigate the water, because shifts in the proton resonance frequency and relaxation time directly indicate the water molecules in different chemical environments.[182] The resolution of NMR spectra are usually limited by the line broadening effect due to the anisotropy of bound water, so solid-state NMR with magic angle spinning is required to resolve water states. For example, different water states were resolved in the poly(N-isopropylacrylamide) gel networks.[183,184] Those investigations found that the water peak was split into two peaks which are attributed to free and bound water. The dielectric permittivity of water was also employed as a fingerprint of water states.[185,186] The results showed the coexistence of liquid-like water with ice structures confined in nanoporous alumina.

2.5 Summary

In this chapter, the basic concepts of the polymer solution, polyampholyte, and solvation behaviors of small ions and polymers are concisely reviewed. In section 2.2, the conformation of general polymer chains in the solvents with different qualities is introduced. In section 2.3, the single chain conformation, phase behavior, gelation of polyampholyte are discussed. In section 2.4, a brief introduction is given of solvation behavior of both small ions and polymer chains. These enumerated theories are the key concepts to understand the structure and water states in the polyampholyte hydrogel in the rest of the dissertation.

Chapter 3 Experimental Techniques

3.1 Introduction

This chapter describes the material system and major techniques used in this dissertation. The synthesis of four materials is discussed, which are polyampholyte hydrogel, reduced graphene oxide composite, zinc oxide nanorods, and poly(glycerol sebacate) and its derivatives. After that, the chapter concludes with two mostly used characterization techniques in the dissertation.

3.2 Synthesis of Polyampholyte Hydrogel

Chapters 4 to 7 are based on polyampholyte hydrogel. The synthesis of polyampholyte hydrogel followed the one-step random copolymerization protocol developed by Gong *et al.*[17] Figure 3.1 shows the typical synthesis procedure. The monomers, NaCl, and photoinitiator were mixed in deionized water with desired concentrations to prepare a precursor solution. Then, the precursor solution was degassed and injected into the gap between two glass plates, where the gap was separated by a spacer (thickness 0.5 mm). A 4 to 8 h irradiation with a UV lamp (22 mW/cm^2 broadband light with a maximum peak at 365 nm; Jelight, US) transforms the precursor solution into the polyampholyte hydrogel. After the polymerization, the hydrogel was peeled off from the glass plate. For some applications, such as gel electrolyte,[154] the hydrogel was further dialyzed in the DIW or KOH solution for one week to exchange ions inside the polyampholyte hydrogel and extract the unreacted monomers. In each chapter, polyampholyte hydrogels with different synthesis conditions were prepared to meet the various demands. Lists of polyampholyte hydrogel prepared with details can be found in the "Experimental Methods" section in the following chapters.

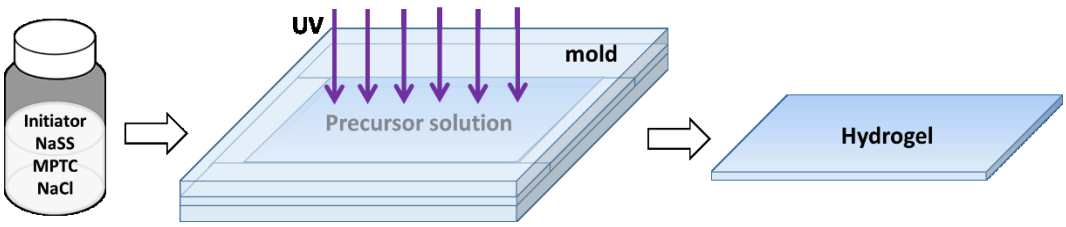

Figure 3.1 The protocol of polyampholyte hydrogel synthesis.

To form polyampholyte hydrogel, electrolytic monomers are needed. Figure 3.2 shows the mostly used monomers. Sodium 4-vinylbenzenesulfonate (NaSS, CAS Number: 2695-37-6) is the anionic monomer, which dissociates and leaves the negatively charged group in the polymer backbone in the aqueous solution. [3-(methacryloylamino)propyl]trimethylammonium chloride (MPTC, CAS Number: 51410-72-1) is the cationic monomer, which dissociates and leaves the positively charged group. In some cases such as the smart window application in Chapter 6, [2-(acryloyloxy)ethyl]trimethylammonium chloride (DMAEA-Q, CAS Number: 44992-01-0) is also used as the cationic monomer, which is a more hydrophilic than MPTC.[29] All chemicals were purchased from Sigma-Aldrich and used as received.

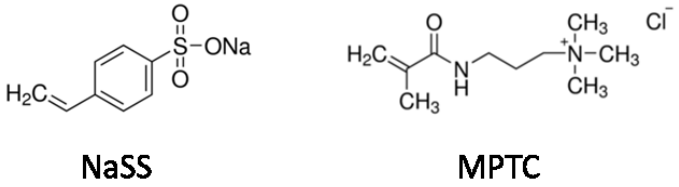

Figure 3.2 The chemical structures of monomers

2-Hydroxy-4'-(2-hydroxyethoxy)-2-methylpropiophenone (Figure 3.3, CAS Number: 106797-53-9) was used as the photoinitiator to initiate the free radical polymerization of monomers. This photoinitiator also has the product name of IRGACURE 2959 (Ciba Specialty Chemicals). It is a highly efficient no-yellowing radical photoinitiator for the UV curing of aqueous systems with unsaturated monomers and prepolymers.[187,188,189] Upon 350 nm excitation, it yields radicals via Norrish-type-I α-cleavage,[190] as shown in Figure 3.3. Once free radicals are generated, a radical polymerization is started. The polymer chain increases its chain length by addition polymerization, until termination happens.[191]

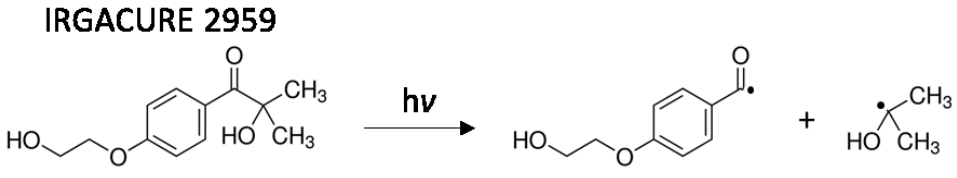

Figure 3.3 The Scheme of IRGACURE 2959 α-cleavage upon UV excitation.

3.3 The Protocol of Reduced Graphene Oxide Composite Fabrication

Figure 3.4 Schematic illustrations that describe the processing of the GNF-RGO coating.

In Chapters 7 to 9, we developed a protocol called "graphene oxide wrapping and reduction" to form a reduced graphene oxide (RGO) composite, as shown in Figure 3.4. Small particles (*e.g.*, biochar, or graphene nanoflakes) are mixed with graphene oxide (GO) solution (4 mg GO/mL, Graphenea, Spain) to form a suspension. The GO in the suspension served as a dispersant to stabilize the small particles owing to its planar 2D structure and hydrophilicity.[192] Then, a thin film of GO composite is formed by evaporation of the water in the suspension. GO sheets are self-assembled into GO papers,[193] and small particles are intercalated between the GO sheets. GO sheets are insulating material because of the disrupted sp^2 bonding networks.[192] The electrical conductivity of GO can be recovered after the reduction, since the π-networks are restored. In this dissertation, self-assembled GO composite film is reduced by chemical reduction to remove labile oxygen-containing functional groups in the GO.[194] Briefly, GO composite film is reduced by an aqueous solution of L-ascorbic acid (Vitamin-C, 8mg/mL, CAS Number: 50-81-7, Sigma-Aldrich, US) with a distillation apparatus in an oil bath at 95 °C. After 4 hours of reaction, the reduced GO (RGO) composite film is dialyzed in deionized water to remove the remaining L-ascorbic acid. Then, the RGO composite film is dried for an hour in a convection oven at 120 °C. In Chapter 8, to achieve higher conductivity for the antenna application, the GO composite film is reduced by a two-step reduction process. The first reduction step is done with a mild reducing agent, L-ascorbic acid, and the second reduction step is carried out with a stronger reducing agent, 50 mM sodium borohydride in water ($NaBH_4$, CAS Number: 16940-66-2, Sigma-Aldrich, US) for 4 h to improve the electrical conductivity.[195]

3.4 Synthesis of Zinc Oxide Nanowires

Zinc oxide (ZnO) nanowires are synthesized for the work reported in Chapter 9 as the piezoelectric material in the nanogenerator. A precursor solution is first prepared by dissolving zinc nitrate hexahydrate (80 mM, CAS Number: 10196-18-6, Sigma-Aldrich, US), hexamethylenetetramine (HMTA, 25 mM, CAS Number: 100-97-0, Sigma-Aldrich, US), polyethylenimine (PEI, 5 mM, CAS Number: 9002-98-6, Sigma-Aldrich, US) and ammonia solution (30%, ACS reagent grade, 5 mL, Sigma-Aldrich, US) in 100 mL DI water. The solution is stirred at room temperature for one hour until it becomes a clear solution.[196] The one-pot synthesis of ZnO nanowire is conducted in a 95 °C solution. The substrate is placed on the liquid surface and the container is closed for 10 minutes. Then, the cover is opened to facilitate precipitation of ZnO seeds due to a sudden vapor pressure drop. A slow agitation of the substrate allows a uniform coating of the ZnO seeds on the surface of the substrate. Subsequently, the sample is submerged in the solution and the cover is closed again for ZnO nanowire growth.[197] The as-grown sample is rinsed with DI water and ethanol and dried for further use.

3.5 Synthesis of Poly(glycerol sebacate) and Its Derivatives

Neat poly(glycerol sebacate) (PGS) is synthesized in two steps. First, a 1:1 molar ratio of glycerol (99%, CAS Number: 56-81-5, Sigma-Aldrich, US) and sebacic acid (SA, 99%, CAS Number: 111-20-6, Sigma-Aldrich, US) are mixed together at room temperature, and placed in a convection oven under nitrogen atmosphere at 120, 130, or 140 °C for 24 h. Then, the prepolymers are dissolved in tetrahydrofuran (THF, 99.9%, CAS Number: 109-99-9, Sigma-Aldrich, US) to form prepolymer/THF solution (0.5 g/mL in THF), and then it is cast into the molds made of aluminum foil (length × width = 10 × 10 cm^2). The prepolymers are placed in a vacuum oven, which is then slowly evacuated to ~1 mTorr. The specimens were cured for 6–66 h at the same temperature as the prepolymerization process. The prepolymerization of PGS may also be carried out in a microwave-assisted process as a time- and energy-efficient alternative by using a microwave oven (Panasonic NN-ST642W) in a chemical hood. The microwave oven is set to provide an output of 600 W to the mixture of glycerol and SA. Although the prepolymerization process sums up to 30 min, the microwave oven is vented by opening the door, and the temperature of the mixture was measured by thermometer every 1 min to prevent overheating of samples and

buildup of produced gas. After completing the microwave step, the prepolymers are allowed to cool and are dissolved in THF at room temperature. The solutions are cast into molds. The specimens are then cured at 130 °C in a vacuum oven for periods of 6–66 h. Two PGS derivatives are prepared. Bis(4-isocyanatophenyl)methane (MDI, 98%, CAS Number: 101-68-8, Sigma-Aldrich, US) and AEROSIL 380 hydrophilic fumed silica (FS, EVONIK, Parsippany, NJ, US) are used as additives to modify the mechanical properties of neat PGS, denoted as PGS-MDI and PGS-FS, respectively. After prepolymerizing in a nitrogen atmosphere at 130 °C for 24 h, the prepolymers were allowed to cool and dissolved with the additives in a cosolvent, THF. For PGS-FS, FS is added into the THF solution, which is bath sonicated for 2 h to achieve a good dispersion. Then, specimens are cured at 130 °C in vacuum for 24 h. The maximum loading of the additives, MDI (7.8 wt %) and FS (10 wt %), is limited by experimental difficulties during the preparation. Namely, both MDI and FS significantly increase the viscosity of the PGS prepolymer solutions. The increased viscosity causes the generation of trapped bubbles in the prepolymer that could not be effectively removed in subsequent processes. After curing, the resulting samples have rough surfaces and trapped bubbles, thus are not suitable for tensile testing.

3.6 Characterization Techniques

Structural characterization of hydrogel requires experimental techniques that can probe nano- to meso-scale information by spectroscopic, microscopic, and chemical methodologies. In this dissertation, we focus on the structure–property relations of polyampholyte hydrogel, so the structure of hydrogel has to be investigated first to elucidate the mechanism of enhanced ionic conductivity at low temperature. In Chapter 4, small angle X-ray scattering (SAXS) is employed to study the as-prepared and dialyzed hydrogel. A model of SAXS theory for clusters was developed for the current projects, and variable-temperature SAXS was used to sense the structure evolution of the polyampholyte hydrogel from room temperature to –40 °C. Moreover, since the changes in water states in the polyampholyte hydrogel have impacts on the phase behavior, and further affect the ice formation, differential scanning calorimetry (DSC) was widely used in the dissertation. The fundamental concepts of the enumerated characterization techniques are briefly discussed in the following subsections. Here, only the most frequently used characterizations are mentioned. There are also other techniques, which can be found in each chapter. The specification of the instruments employed and the general parameters are also provided for data reproduction.

3.6.1 Small Angle X-Ray Scattering (SAXS)

Small angle X-ray scattering (SAXS) is a powerful technique to investigate the structural properties of materials. In contrast to wide-angle X-ray diffraction, SAXS deals with both the diffraction of large lattice spacing and the scattering by structures of amorphous materials.[198] It is capable of observing spatial inhomogeneity of hydrogels to understand their phase behavior and deformation mechanisms.[199,200,201] For example, Mansur *et al*. found nano-ordered disperse phases in the poly(vinyl alcohol) (PVA)/poly(ethylene glycol) hydrogel.[202] Hunt *et al.* observed the ionic domains formed by self-organization of well-defined triblock copolyelectrolytes by SAXS, which enhanced mechanical properties.[203] Chiu *et al.* employed *in situ* SAXS experiments to investigate the pH-responsive nanostructure transformation of hydrophobically-modified chitosan hydrogels.[204]

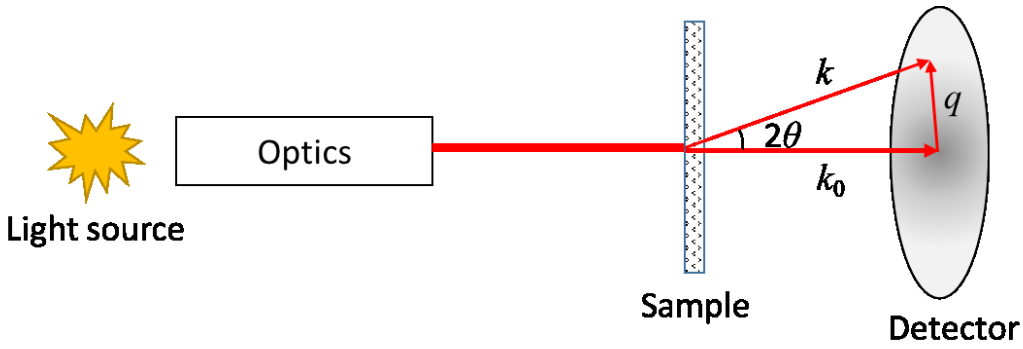

Figure 3.5 Schematic diagram of SAXS experimental setup. Based on the concepts of reference[205].

A schematic diagram of a typical SAXS experimental setup is shown in Figure 3.5. Basically, an experimental setup consists of a light source, optical elements of a collimation system, a sample holder, and detectors.[205] In our experiment, synchrotron X-rays were used as the light source. Compared with conventional X-ray sources (*e.g.,* a copper or molybdenum target), synchrotron X-ray sources have advantages such as small beam divergence, high brilliance, well-defined energy, *etc*.[198] These features allows time-resolved and anomalous SAXS measurements with small samples.[206] A collimation system usually includes pinhole collimators and double crystal monochromators. It offers symmetric beam cross-section, tunability of wavelength and alleviates the smearing effect.[207] The sample holder is the place to put sample capillaries. The sample environment, such as temperature and pressure, can be controlled by the chamber. In

Chapter 4, we carried out variable-temperature SAXS with programmed heating–cooling cycles. To achieve *in-situ* experiments, a unique apparatus is attached to the setups. For example, a stretching system,[208] a shear apparatus,[209] and a fiber drawing apparatus,[210] were integrated into SAXS measurements. The final part is the detector. The detection system converts the X-ray intensity to signal read by the processor. Charge coupled devices (CCDs) are the most popular detectors that can detect X-rays directly in a two-dimension area.[198] A typical SAXS measurement can be described as the following procedures. A monochromatic beam of incident X-rays is collimated and exposed to the sample. The X-rays scattered by electrons are collected as a function of the scattering angle by the detector, revealing fluctuations of electronic densities in the matter. In the following paragraphs, the basics of SAXS are reviewed.

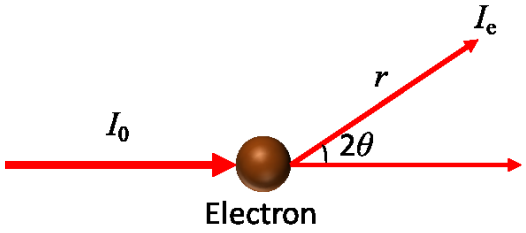

Figure 3.6 Schematic diagram of incident X-ray scattered by an electron. Based on the concepts of reference[205].

Figure 3.6 shows the simplest case in which a beam of incident X-rays is scattered by an electron. The X-ray is described as an electromagnetic wave. The intensity is proportional to the square of its amplitude. Once it is incident on an electron, the electromagnetic wave is spherically scattered and propagated. Scattered X-rays have two major components that are coherent and incoherent, if the incident x-ray beam is monochromatic. Coherent (Thomson) scattering has the same energy as the incident x-rays, and will interact via diffraction, and is the major component considered in SAXS. The incoherent (Compton) component is inelastic scattering in which incident x-rays transfer part of the energy to the electrons. The coherent scattered intensity from a single electron is given by the Thomson formula,[205]

$$I_e = r_0^2 \left(\frac{1+\cos 2\theta}{2}\right) \frac{1}{r^2} I_0 \qquad (3.1)$$

where I_0 is the intensity of incoming X-rays, I_e is the intensity of scattered X-rays, 2θ is the angle of observation, r is the distance of observation, and r_0 is the classical electron radius. This equation is critical for all calculations involving absolute scattering intensities. It is notable that the component in the brackets is referred to as the polarization factor. At the small angle of observation, this term can be neglected.

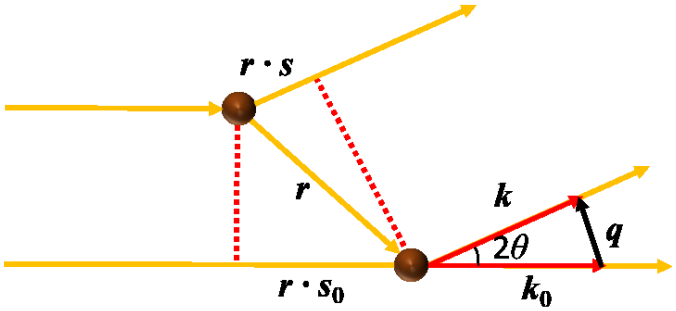

Figure 3.7 Schematic diagram of incident X-ray scattered by two electrons. Based on the concepts of reference [205].

If the incident X-rays are scattered by two electrons, the interference between the coherent scattered X-rays yields a fringe pattern, which contains the information of the position of the scattering centers. Figure 3.7 shows the case in which an incident X-ray beam is scattered by two electrons. Here, $\boldsymbol{r}$ is the position vector, $|\boldsymbol{r}| = r$. The incident wave vector is $\boldsymbol{k}_0 = \frac{2\pi}{\lambda}\boldsymbol{s}_0$, the scattered wave vector is $\boldsymbol{k} = \frac{2\pi}{\lambda}\boldsymbol{s}$, the scattering vector $\boldsymbol{q} = \boldsymbol{k} - \boldsymbol{k}_0$, and the module of $\boldsymbol{q}$ is $q = |\boldsymbol{q}| = \frac{4\pi \sin\theta}{\lambda}$. The total amplitude from two electrons is thus: [205]

$$F(q) = \sum_{i=1}^{2} f_e \exp(\boldsymbol{jq}\cdot\boldsymbol{r}_i) \quad (3.2)$$

where $F(q)$ is the Fourier transform of the spatial distribution of the electrons. Scattering from two electrons can be generalized to N electrons: [205]

$$F(q) = \sum_{i=1}^{N} f_e \exp(\boldsymbol{jq}\cdot\boldsymbol{r}_i) \quad (3.3)$$

where the bold $\boldsymbol{j}$ in this equation and equations hereafter indicates the imaginary component. For an atom with a continuous radial electron density $\rho(r)$ obtained from quantum chemical calculations, Equation 3.3 can be rewritten as the atomic scattering factor: [205]

$$f(q) = \int_0^\infty dr\ \rho(r)\ r^2\ \frac{\sin(qr)}{qr} \qquad (3.4)$$

Since $\lim_{x\to 0}\left(\frac{\sin x}{x}\right) = 1$, $f(0) = Z$, where Z is the nuclear charge of the atom, indicating that atoms with higher Z scatter stronger. Analogously, the form factor (*i.e.,* the scattering amplitude) of an isolated particle with N atoms can be determined as: [205]

$$F(q) = \sum_{i=1}^{N} f_i(q) \exp(\boldsymbol{jq}\cdot\boldsymbol{r}_i) \qquad (3.5)$$

and here $F(q)$ is the Fourier transform of the atomic distribution. The scattered X-ray intensity from this isolated molecule is: [205]

$$I(q) = |F(q)|^2 = \sum_{i=1}^{N}\sum_{j=1}^{N} f_i(q) f_j(q) \exp\left(\boldsymbol{jq}\cdot(\boldsymbol{r}_i - \boldsymbol{r}_j)\right) \quad (3.6)$$

The particles in solution are randomly oriented, thus: [205]

$$\langle \exp\left(i\boldsymbol{q}\cdot(\boldsymbol{r}_i - \boldsymbol{r}_j)\right)\rangle = \frac{\sin(qr_{ij})}{qr_{ij}} \qquad (3.7)$$

Then, Equation 3.6 can be written as: [205]

$$I(q) = |F(q)|^2 = \sum_{i=1}^{N}\sum_{j=1}^{N} f_i(q) f_j(q) \frac{\sin(qr_{ij})}{qr_{ij}} \qquad (3.8)$$

and this is the Debye formula.[211] According to the Debye formula, one can conclude that because of solution averaging, only the distance between atoms is measured, instead of the coordinates of each atom in space.

If particles are concentrated in the solution, the distance between the neighboring particles becomes the same order of magnitude as the particle size. The periodic arrangement of particles will also contribute to the interference pattern on the detector, which is called the structure factor. The scattering intensity is proportional to the product of the form factor and the structure factor, which is presented as:[212]

$$\Delta I(q) \propto N\ I_0\ V^2 (\Delta\rho)^2 F(q) S(q) \qquad (3.9)$$

Here, $\Delta I(q)$ is the difference between the measured intensity and the intensity of the matrix, N is the number of particles, $\Delta\rho$ is the difference in electron density between the particles and the matrix, and $S(q)$ is the structure factor. Moreover, as implied by Equation 3.9, SAXS

measurements require an appropriate background be subtracted. Only with the contrast of electron density between the particles and the matrix (*e.g.,* solvent), the excess scattering from the particles can be obtained. The background level of the scattering pattern will be increased by incoherent scattering from the sample, and coherent and incoherent scattering from the wall of the capillary and the solvent and will have to be considered in the background subtraction process.

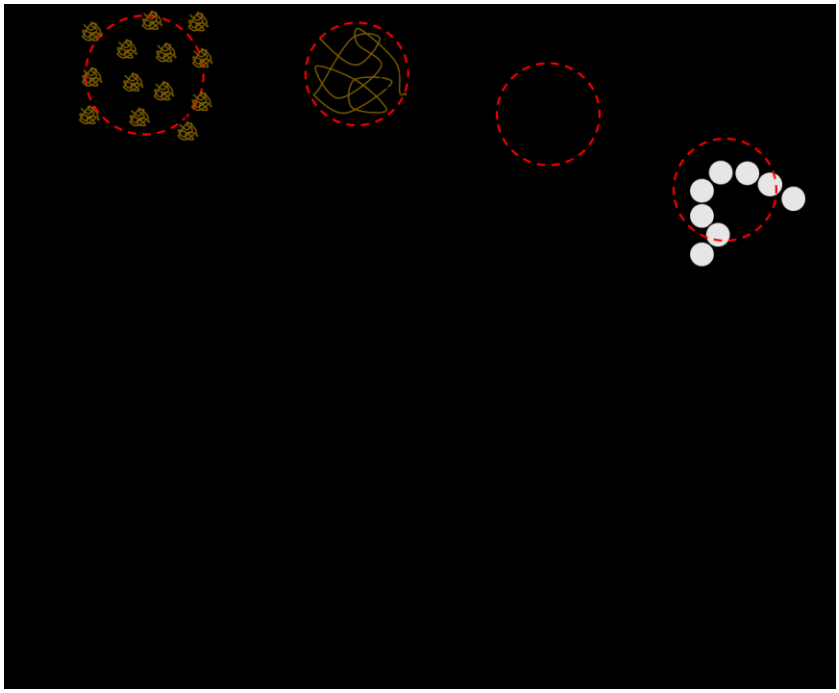

Figure 3.8 Schematic diagram of the transition from inter-chain to intra-chain and finally monomeric scattering. The red circles indicate the range of observation. Based on the concepts of references[120,205].

We conclude the brief review of the basic concepts in SAXS with an example of scattering from the polymer solution. Figure 3.8 is a typical scattering pattern from a dilute polymer solution.[120] The lower limit $q_{\min}$ is because of the presence of the primary beam. It depends on the quality of the alignment of the beam stop and the collimation system. The higher limit $q_{\max}$ is governed by signal-to-noise ratio. At very low q, the observation window is very large. X-ray scattering probes correlations between polymer chains, and the structural order in the solution can be obtained. The trend of $I(q)$ at small q gives information about the interactions between the polymer chains. The decrease in intensity indicates repulsive interaction potentials and an increase implies attractive interaction, such as aggregation.[212] Here, since the solution is dilute, there is no

interaction between the polymer chains, so the scattered intensity is constant in the intermolecular regime. In the Guinier regime, the observation range is about the chain size, and the scattering from correlations of monomers in the same chain is probed, and the downturn occurs near the radius of gyration of the polymer chains. At q that is slightly higher than the reciprocal of the radius of gyration, the scattering intensity scales as $I(q) \sim q^{-d}$, where d is the fractal dimension of the object.[213] At highest q, the Porod scaling dominates the scattering intensity, which is called the Porod regime. Because of the very small observation range, it gives a contrast at the interface between the monomers and the surrounding solvent molecules. This interface can be considered as sharp and smooth, which yields the Porod scaling that $I(q) \sim q^{-4}$.

In this dissertation, the SAXS experiments were performed with the beamline 12-ID-B of the Advanced Photon Source at the Argonne National Laboratory in the US. The 14 keV X-ray beam was exposed to the 1.5 mm diameter capillary sample with an exposure time of typically 0.1 s. Scattered X-ray photons were measured with a Pilatus 2M (Dectris Ltd.) detector located about 2 m downstream of the sample. Ten images per sample were collected and averaged to confirm that no beam damage had occurred and to increase counting statistics. Background scattering from a capillary containing water was subtracted from sample data. In the variable temperature SAXS measurements, the following thermal history was programmed unless otherwise specified: (i) held at 5 °C for 10 min, (ii) cooled from +5 to –40 °C at a rate of 5 °C/min, (iii) held at –40 °C for 10 min, (iv) heated up to 5 °C at a rate of 1 °C/min.

3.6.2 Differential Scanning Calorimetry (DSC)

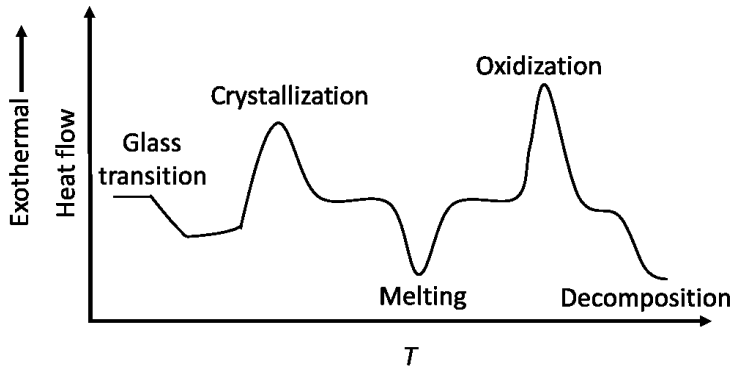

Figure 3.9 Schematic diagram of a typical DSC profile for polymer samples. Based on the concepts of reference[214].

Among the thermal analysis techniques, differential scanning calorimetry (DSC) is the most popular one, especially for the field of polymer research.[214] As ASTM standard E473 states,[215] DSC is a characterization technique in which the sample is controlled by a specified temperature program, while the difference of the heat flow between the sample and the reference is recorded as a function of temperature. DSC has advantages such as easy operation, small sample amount required, and high sensitivity, and is widely employed in the measurement of, for example, latent heat, heat capacity,[216,217] purity,[218,219] and glass transition.[220] As shown in Figure 3.9, temperature and extent of each transition can be extracted and quantitatively analyzed from the DSC profiles to fingerprint the processing history of polymers.

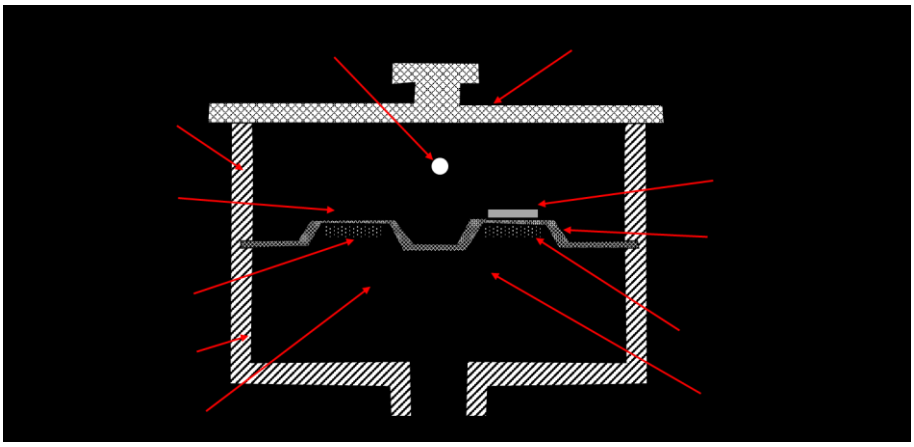

Figure 3.10 Schematic diagram of cross-section of DSC heat flux cell. Redrawn from Figure 2.1 in reference[214].

On the basis of measurement mechanisms, differential scanning calorimeters can be divided into two classes: power compensation DSC and heat flux DSC.[214] In this dissertation, the DSC measurements were done on a DSC-Q1000 from TA Instruments, which is a heat flux DSC, so we put emphasis on the basics and configuration of heat flux DSC in this section. The cross-section of a basic heat flux differential scanning calorimeter is shown in Figure 3.10. The wall of the sample chamber is made of silver for good thermal conductivity and acts as a heating block. It is attached to the furnace and cooling system designed to supply or remove heat at the desired rate. The sample pan and reference pan sit on raised platforms made by constantan. The constantan disk (*i.e.,* heat leak) bridges the two pans and allows a fast transfer of heat between pans and the heating block. Chromel disks attached to constantan disks on the underside of the sample and reference

pans form chromel/constantan thermocouples to monitor the temperature of both pans. Before the experiment starts, sample and reference pan are at the same temperature $T_b = T_s = T_r$, where the subscripts b, s, and r denote the heating block, sample pan, and reference pan, respectively. Once the measurement starts, the temperature of the heating block ramps following the experiment profile, and the heat is supplied or removed from the pan via the constantan disk. Because of the delay in heat transfer, the temperature of both pans always lags behind the block temperature. However, the sample pan contains the sample that has the thermal effect to be probed at the certain temperature. The instrument yields the differential temperature between the sample and reference pans, which gives the sample thermal properties. The heat flow rate between the sample and reference pans can be determined according to a thermal equivalent of Ohm's law:[214]

$$\dot{Q} = \frac{T_s - T_r}{R} \qquad (3.10)$$

where $\dot{Q}$ is the heat flow rate, and R is thermal resistance of the constantan disk.

In this work, the water states in the polyampholyte hydrogel were deduced from the spectra produced by the DSC-Q1000 (TA Instruments, US). The samples were tested right after preparation to prevent any possible loss of water through evaporation. For each measurement, ~10 mg of samples were sealed in a copper sample pan. In each DSC measurement, the following thermal history was programmed unless otherwise specified: (i) held at 10 °C for 10 min, (ii) cooled from +10 to –60 °C at a rate of 1 °C/min, (iii) held at –60 °C for 10 min, (iv) heated up to 10 °C at a rate of 1 °C/min. The program, (i) to (iv), was repeated twice or more to ensure the consistency of the results for each sample.

3.7 Summary

This chapter described the synthesis of polyampholyte hydrogel, reduced graphene oxide composite coating, zinc oxide nanowires, poly(glycerol sebacate) and its derivatives. Two key characterization techniques, SAXS and DSC, were also briefly reviewed from fundamental and instrumental aspects. Though further experimental details are given in each chapter, some underlying mechanisms of synthesis and characterization mentioned in the chapter may provide readers with some hints and inspiration for future experiment designs.

Chapter 4 Low-Temperature Ionic Conductivity Enhanced by Disrupted Ice Formation in Polyampholyte Hydrogels

4.1 Introduction

Tough hydrogels, mechanically soft but robust and tear-resistant materials in which hydrophilic polymer networks hold more water than the original polymer weight, are a promising class of material for bioimplantable electronics, sensors/actuators in soft machines, surgical glues, and gel electrolytes for energy storage devices.[221,61,9] As these materials are inherently rich in water content, understanding the phase behavior of water in the polymer network has important implications for low temperature applications where freezing of water can be detrimental. It is known that nanoscale confinement[222,185,223] and controlled hydrophilicity/phobicity[224] are effective strategies to control freezing behavior. Recently, Vogt and collaborators studied the dynamics of supercooled water molecules under nanoscale confinement within the cluster of hydrophobic domains and its impact on the anti-freezing behavior within hydrogels.[225]

Polyampholytes, a subclass of polyelectrolytes, are macromolecules that contain both acidic and basic groups that may produce positive and negative electrostatic charges, respectively, as a response to the surrounding environment.[36,131] The high density of the distributed opposite charges in polyampholyte chains introduces ionic cross-linking that can lead to well-defined three-dimensional structures in foldamers,[226] DNA condensation, and protein folding.[227] Recently, synthetic polyampholytes have shown promise in various potential applications such as mechanically tough and self-healing hydrogels,[17,18,137] anti-biofouling coating,[23] thermosensitive smart optical coating,[29] and self-adjustable adhesives.[25]

We have previously shown that polyampholyte hydrogels also have the potential to be used as an aqueous gel electrolyte in electrochemical storage devices.[154] In that work, a supercapacitor that employed a polyampholyte hydrogel electrolyte filled with 16.8 wt% potassium hydroxide rendered an enhanced specific capacitance of 75 F/g at −30 °C, whereas a control sample with the aqueous electrolyte without the polymer showed 24 F/g under identical conditions. As another example in this work, temperature-dependent ionic conductivities of a 10 wt% NaCl solution, a hydrogel precursor solution with 10 wt% NaCl (SOL-10-2.1; sample nomenclature in Table 4.1),

and polyampholyte hydrogel with 10 wt% NaCl (PA-10-2.1) are shown in Figure 4.1. With decreasing temperature, the ionic conductivity of the NaCl solution decreased gradually from 124.58 to 18.85 mS/cm (15 % of the +20 °C value) between +20 and −20 °C, respectively, then dropped dramatically to 0.055 mS/cm (0.045 %) at –30 °C. The eutectic temperature (–21 °C) in the water–NaCl phase equilibrium, where all remaining liquid transforms to solid, may explain the drastic ionic conductivity drop between –20 and –30 °C. On the other hand, PA-10-2.1 exhibited a gradual decrease in ionic conductivity from 28.78 to 7.07 (24.57 %), then to 2.62 mS/cm (9.10 %), at +20, –20 and –30 °C, respectively. The low-temperature conductivity enhancement is much more prominent than that of another control sample, SOL-10-2.1, where the non-polymerized precursor solution exhibited a limited effect with conductivity values of 89.62, 3.97 (4.43 %), and 0.87 (0.97 %) for +20, –20 and –30 °C, respectively.

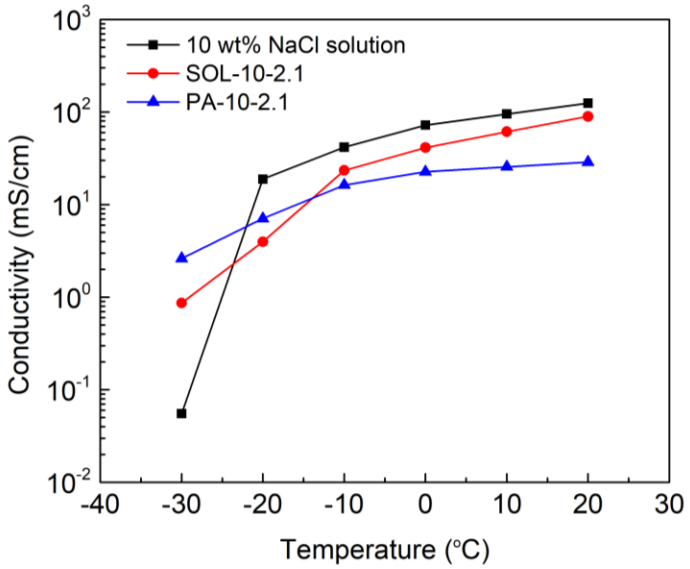

Figure 4.1 Ionic conductivities of an aqueous 10 wt% NaCl solution, the NaCl solution mixed with monomeric precursor molecules (SOL-10-2.1), and the NaCl solution in polymerized hydrogel (PA-10-2.1), plotted against temperature.

The results shown in Figure 4.1 suggest two possible reasons for the enhanced ionic conductivity in polyampholyte hydrogels. First, monomeric units in the polyampholyte play a role as additional salts, causing a depression of the eutectic temperature. If osmotic virial coefficients or Margules parameters are available for the monomers, such effects can be quantified by

thermodynamic models. [223,228] However, the solution thermodynamics argument cannot explain the further enhancement of the low-temperature ionic conductivity in the hydrogels. This effect can only be understood when the nanoscopic structure of polymer chains and the status of water molecules are elucidated as a function of temperature.

Experimental studies on the details of hierarchical structures of polyampholytes, have, in general, been relatively rare. Nisato *et al.* proposed a qualitative description of the globular structure of chains in polyampholyte hydrogels based on light scattering and swelling experiments.[30] However, the details of the globular structures, including size and chain density of each globule and the superstructure that the globules may produce, have not been explored. Within the polyampholyte family, the hierarchical structure of polyzwitterions, where both acidic and basic components reside in each repeating monomer unit, has been studied in detail. Polyzwitterions show a unique property called anti-polyelectrolyte behavior when the polyampholyte is in an isoelectric state (*i.e.,* the positive and negative charge densities are nearly equal).[31] Whereas ordinary polyelectrolytes undergo a collapse in their chain conformation when the salt concentration increases in the aqueous solution, polyzwitterions exhibit swelling behavior that leads to an increase of the solution viscosity and the solubility of the macromolecular component.[32,33,34,35] Moreover, the high polymer concentration in the polyzwitterion hydrogel leads to electrostatically induced hierarchical self-assembly that defines a multi-scale structural network in the hydrogel.[31] Safinya and coworkers recently investigated the effect of salt on the hierarchical structural formation of neurofilament hydrogel, whose structural assembly is dictated by ionic interactions between polyampholyte sidearm chains. The neurofilament hydrogel (~ 5 wt% neurofilament in salt water) undergoes transitions from liquid-crystalline hydrogel to isotropic gel, and to nematic hydrogel when the background salt concentration increases.[22]

In this work, we studied the structure of a polyampholyte random copolymer that consists of two oppositely-charged ionic monomers, sodium 4-vinylbenzenesulfonate (NaSS) and [3-(methacryloylamino) propyl] trimethylammonium chloride (MPTC), which is denoted as poly(NaSS-*co*-MPTC). Furthermore, we discuss the interactions with water molecules when the charge-balanced polyampholyte formed a hydrogel. Using small- and wide-angle X-ray scattering (SAXS and WAXS) as tools to study polymer network structures and their effects on the phase behavior of water in the hydrogels, we found that a networked globular structure effectively

prevented the freezing of water in the hydrogel. There is clear evidence of amorphous water molecules and slush-like, sub-micron-sized ice formation at low temperatures. Solid-state NMR assisted in identifying dynamic and frozen water within the hydrogels. All these findings are consistent with our observation of the increased ionic conductivity of the hydrogel at low temperatures. It is notable that multiple freeze–thaw cycles did not impact the phase behavior of water in the hydrogel soft materials.

4.2 Experimental Methods.

Polyampholyte Hydrogel Synthesis. The protocol as described by Gong *et al*.[17] was followed to copolymerize sodium 4-vinylbenzenesulfonate (cationic monomer; NaSS) and [3-(methacryloylamino)propyl] trimethylammonium chloride (anionic monomer; MPTC) with IRGACURE 2959 (photoinitiator) and NaCl. The chemicals were purchased from Sigma-Aldrich and used as received. The aqueous precursor solution with designed chemical concentrations (shown in Table 4.1) was injected into the gap between two glass plates separated by a 1 mm thick Teflon spacer. Hereafter, we denote the samples using the code PA-#-*c*, where the # is the NaCl concentration (wt%) in the polyampholyte hydrogel, and *c* is the total monomer concentration (M). The monomer polymerization was initiated by irradiating the sample with UV light with a lamp-to-sample distance of 5 mm (UV broadband lamp with a maximum peak at 365 nm with an intensity of 22 mW/cm^2; Jelight UVO-Cleaner Model-342, US). The weight% of NaCl in the as-prepared hydrogel is defined by Equation 4.1:

$$C_{\mathrm{NaCl}} = \frac{m_{\mathrm{NaCl}}}{m_{\mathrm{NaCl}} + m_{\mathrm{water}}} \times 100\% \qquad (4.1)$$

where m_{NaCl} is the total mass of NaCl, and m_{water} is the mass of water added in the precursor solution. It is noted that NaSS and MPTC contain sodium and chloride ions, respectively which were accounted for in the calculation for the m_{NaCl} value.

Table 4.1 The list of samples prepared.

Sample	NaSS conc.	MPTC conc.	NaCl conc.	UV time
PA-6-2.1	1.07 M	1.03 M	6 wt%	8 h
PA-8-2.1	1.07 M	1.03 M	8 wt%	8 h
PA-10-2.1	1.07 M	1.03 M	10 wt%	8 h
PA-10-1.05	0.536 M	0.515 M	10 wt%	8 h
SOL-10-2.1	1.07 M	1.03 M	10 wt%	0 h

a. In all cases, 0.25 mol% photoinitiator (compared to the total concentration of NaSS and MPTC) was added in the precursor solution.

Variable-Temperature Small/Wide Angle X-Ray Scattering Characterization. SAXS/WAXS samples were made by irradiating bees wax sealed glass capillaries (Charles Supper, US) containing a precursor solution with UV. The SAXS experiments were performed with the beamline 12-ID-B of the Advanced Photon Source at the Argonne National Laboratory in the US. The 14 keV X-ray beam was exposed to the 1.5 mm diameter capillary sample with an exposure time of typically 0.1 s. Scattered X-ray photons were measured with a Pilatus 2M (Dectris Ltd.) detector located about 2 m downstream of the sample. Ten images per sample were collected and averaged to confirm that no beam damage had occurred and to increase counting statistics. Background scattering from a capillary containing water was subtracted from sample data. In the temperature-dependent SAXS/WAXS measurements, the following thermal history was programmed: (i) held at 5 °C for 10 min, (ii) cooled from +5 to –40 °C at a rate of 5 °C/min, (iii) held at –40 °C for 10 min, (iv) heated up to 5 °C at a rate of 1 °C/min.

Ionic Conductivity Measurement. Ionic conductivity measurements of the NaCl and precursor solutions, as well as the polyampholyte hydrogel, were undertaken using screen-printed electrodes (DRP-150, DROPSENS, Spain) in a three-electrode configuration by electrochemical impedance spectroscopy (EIS, PGSTAT302N, Metrohm Autolab, Netherlands). The frequency range for EIS measurements was from 100 kilo-Hz to 10 milli-Hz, where an open circuit potential mode with an AC perturbation of 5 mV was used. The temperature was regulated using a temperature-controlled chamber (TS102G, Instec Inc., US). The sample temperature was decreased from 20 to −30 °C at a rate of 5 °C/min, and held at −30 °C for 10 min, followed by the EIS measurement. After each measurement, the sample was heated at a rate of 1 °C/min to the next desired temperature. The hydrogel samples were placed on top of the screen-printed electrode and compressed to ensure an

intimate contact between the electrode and the hydrogel. For solution measurements, a reservoir (depth 1 mm, area 10 × 10 mm^2) made by a spacer was used to contain the electrolyte solution. EIS results were fit with the Randles circuit model using software (Autolab NOVA) to determine the electrolyte resistance, which was converted into ionic conductivity based on the cell constant of the measurement setup. The EIS results for 10 wt% NaCl solution, SOL-10-2.1 and PA-10-2.1 are shown in Figure 4.2.

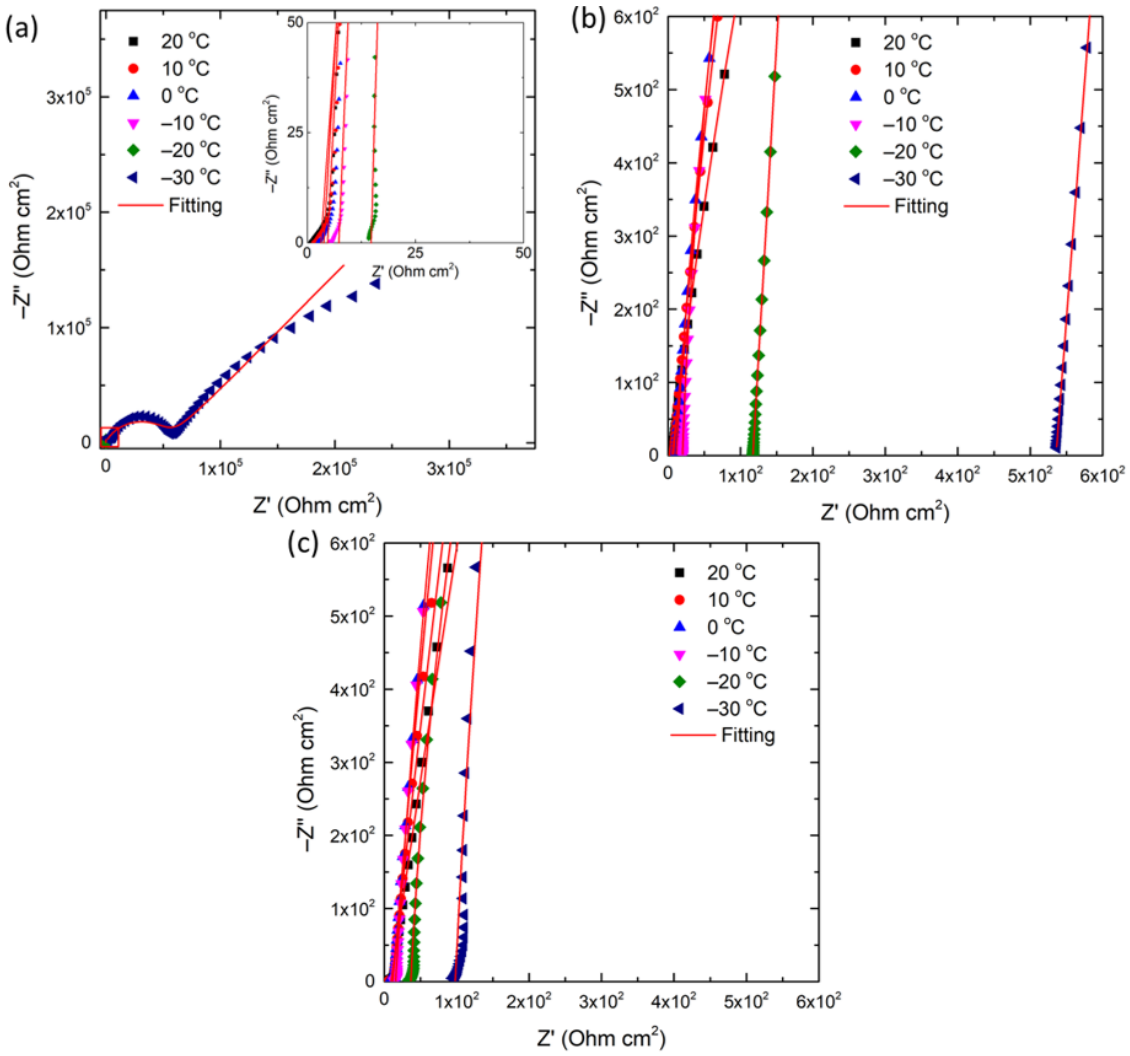

Figure 4.2 EIS results for (a) 10 wt% NaCl solution, (b) SOL-10-2.1 and (c) PA-10-2.1 at various temperatures. The inset in (a) is the magnified part of the region identified by the red box in the left-bottom corner of (a). Red solid lines were the fitting using the Randles circuit model.

We followed the general approach of determining the various parameters of an electrochemical system by fitting the impedance data to an equivalent electrical circuit. We used the Randles circuit model for data fitting as it physically interprets our electrochemical cell in the best possible manner.[229,156,230] Figure 4.3 represents a circuit model of a Randles cell which typically consists of four components: solution resistance (R_s), a constant phase element (*CPE*), charge transfer or polarization resistance (R_{CT}) and a Warburg diffusion element (Z_W). In physical terms: R_s corresponds to resistance against the migration of ions inside the electrolyte (solution or hydrogel); CPE corresponds to an imperfect double layer capacitor that forms at the interface between the electrode and surrounding electrolyte; R_{CT} is the charge transfer resistance for a kinetically controlled electrochemical reaction taking place at the interface between the electrode and electrolyte; *Zw* accounts for the diffusional impedance of the electrochemical system. The focus of our study is to extract the values of R_s at different temperatures, as shown in Table 4.2. In order to calculate the conductivity of the electrolyte, we used the following relation:

$$\kappa = \frac{c}{R_s} \qquad (4.2)$$

where c is the cell constant, which is a characteristic parameter of the experiment setups, and R_s is the solution resistance.

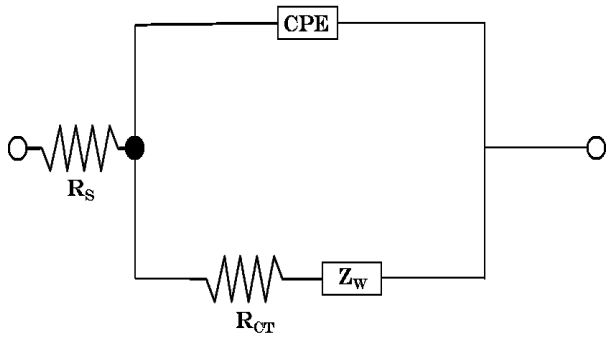

Figure 4.3 Equivalent Randles circuit for modelling of impedance data of the electrolyte system.

Table 4.2 Fitting parameters for EIS measurements

Temperature (°C)	10 wt% NaCl solution		SOL-10-2.1		PA-10-2.1	
	R_S(Ω cm^2)	% error	R_S(Ω cm^2)	% error	R_S(Ω cm^2)	% error
20	2.05	0.55	5.18	0.48	8.87	0.57
10	2.70	0.56	7.57	0.39	9.77	0.76
0	3.56	0.49	11.24	0.53	11.31	0.70
−10	6.17	0.33	19.79	0.51	15.68	1.08
−20	13.64	0.37	116.89	0.58	36.13	0.46
−30	4656.79	9.47	536.11	0.83	97.39	0.78

Field Emission Scanning Electron Microscope (FE-SEM) Characterization. For the FE-SEM sample preparation, two PA-10-2.1 samples were cooled from room temperature to 20 and −30 °C, at a rate of 1 °C/min using a temperature-controlled chamber, and held at the desired temperature for 30 min. After that, the samples were taken from the chamber, and immediately quenched in liquid nitrogen, followed by freeze-drying in a freeze-dryer (Super Modulyo, Savant). A ~5 nm thick Au layer was coated on the freeze-dried samples using a gold sputter unit (Denton; US). An FE-SEM (Zeiss, Sigma) was utilized for the morphological study.

Liquid NMR. The NMR spectra were acquired on a Varian 600 MHz NMR spectrometer (^{1}H, 599.7 MHz) at room temperature. The water peaks were suppressed using pre-saturation pulses. First, as-prepared PA-10-2.1 was weighed and dissolved in 4 M NaCl deuterium oxide solution overnight. The same mass of precursor solution for PA-10-2.1 was also diluted in the 4 M NaCl deuterium oxide solution. Weighed DSS (4,4-dimethyl-4-silapentane-1-sulfonic acid sodium salt) was added into both solutions as the internal standard substitute. The monomer conversion rate was determined by comparing the integrated peak area in the range of 7 to 5.5 ppm, which are proton signals from the alkene groups in the monomers (NaSS, and MPTC). The peak intensities were normalized to the most intense signal from the DSS, labeled 0 in both spectra.

Solid-State NMR. ^{1}H and ^{2}H NMR measurements were conducted at 11.75 T on a Bruker Avance spectrometer, operating at 500.3 and 76.8 MHz, respectively, for ^{1}H and ^{2}H. Samples were packed in 4 mm zirconia rotors and spectra were obtained with a Bruker 4 mm MAS probe operating in double resonance mode. ^{1}H NMR spectra were obtained with a Bloch pulse, using a 4.0 μs 90° degree pulse, a 2.0 s acquisition time, and a 1.0 s recycle delay. Room temperature ^{2}H NMR spectra were also obtained using a Bloch pulse, using a 2.5 μs pulse corresponding to a 45° flip angle, with

an acquisition time of 2.0 s and 1.0 s recycle delay. Non-ambient temperature ^{2}H NMR spectra were obtained with a solid-echo pulse sequence: $90° - \tau_1 - 90° - \tau_2 - AQ$, where τ_1 is the interpulse delay and τ_2, the refocusing delay, was set to a low value and data were left-shifted to ensure the FID began at its maximum. The 90° pulses were 5.0 μs, τ_1 was 20.0 μs, the acquisition time was 16 ms and the recycle delay was 1.0 s. Variable-temperature NMR data were obtained on the Avance 500 NMR spectrometer using the BVT 3000 VT unit provided by Bruker Biopsin. An ethanol/dry ice bath was used as the heat exchanger source, with dry air as the VT gas, whose flow rate was 1600 L/h. The temperature was calibrated based on the temperature dependence of the ^{207}Pb chemical shifts of methylammoniumlead chloride, following a protocol recently developed in this lab.[231]

4.3 Results and Discussion

4.3.1 Charge-Balanced Point Determination

All synthesized polyampholyte hydrogels in this dissertation were charge-balanced polyampholytes (*i.e.,* the amount of positively and negatively charged groups are the same in the hydrogel). It is important to experimentally determine the real feed monomer fraction to determine the exact charge-balance point. In a study on dilute aqueous solutions of polyampholytes, the coil size of the polyampholyte was shown to display a strong minimum at the charge-balance point.[36] Thus, the swelling ratio of the hydrogel will also show a minimum at the charge-balance point. We synthesized a series of polyampholyte hydrogels with various monomer fractions. The total monomer concentration was fixed at 1.2 M, the NaCl concentration in the precursor solution was fixed at 10 wt% and the UV curing time was fixed at 8 h. The as-prepared hydrogels were dialyzed in deionized water for one week to achieve equilibrated swelling. The swelling ratio, Q_{w}, is defined by Equation 4.3:

$$Q_{\mathrm{w}} = \frac{m_{\mathrm{equilibrium}}}{m_{\mathrm{as-prepared}}} \qquad (4.3)$$

where $m_{\mathrm{equilibrium}}$ and $m_{\mathrm{as-prepared}}$ are the masses of the equilibrated and the as-prepared hydrogels. The results of the swelling experiments are shown in Figure 4.4. Q_{w} decreased before the MPTC fraction (f_{MPTC}) reached 0.49 and sharply increased after this point, indicating that

Coulombic attraction prevails over the repulsion and the polymer chains collapse near the charge-balance point (f_{MPTC}= 0.49).

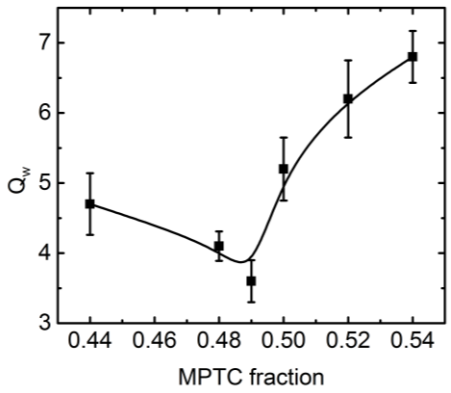

Figure 4.4 Swelling ratio as a function of MPTC fraction.

4.3.2 Total Monomer Conversion Rate

No obvious peak was observed in the PA-10-2.1 ^{1}H-NMR spectrum, indicating complete conversion after polymerization, as shown in Figure 4.5. A leaching test was also performed to measure the total monomer conversion rate by comparing the mass before and after dialysis. We assumed that the remaining unreacted monomers will leach out after one week dialysis in adequate deionized water. Based on the mass loss after considering the NaCl loss, the total monomer conversion rate was 98.1%.

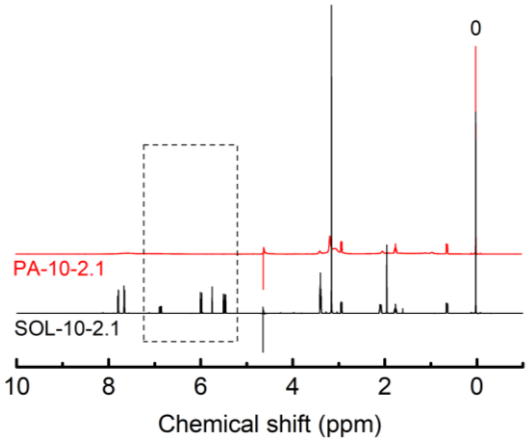

Figure 4.5 ^{1}H solution NMR spectra for PA-10-2.1 and the precursor solution SOL-10-2.1 (including the monomers NaSS, and MPTC) at room temperature.

4.3.3 Development of SAXS Theory for Clusters[2]

4.3.3.1 Model

Intensity from a model cluster containing N spheres (Figure 4.6) that are primary particles can be numerically calculated with the general theory below:

$$I(q) = \int \sum_{k=1}^{N} F(q, R_k) e^{-j\boldsymbol{q}\cdot\boldsymbol{r_k}} \, d\Omega \quad (4.4)$$

where R_k and $\boldsymbol{r_k}$ are the radius and position of kth sphere. The 1D scattering vector q is the magnitude of the 3D scattering vector $\boldsymbol{q}$. The integration over $d\Omega$ stands for orientational average. The form factor can be calculated as below:

$$P(q) = \sum_{k=1}^{N} |F(q, R_k)|^2 \quad (4.5)$$

where $F(q, R)$ is the spherical Bessel function for a sphere with radius R.

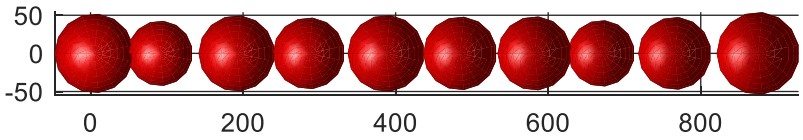

Figure 4.6 A model 1D array of spheres. Length L of the model is the center-to-center distance between first and last spheres. The model is composed of 10 spheres with mean radius 5 nm and 12% size variation. The gap between the particles is set to 0.5 nm.

Finally, simulated $I(q)$ and $P(q)$ are shown in Figure 4.7a. The calculated $I(q)$ shows clearly three regions separated by the positions denoted by closed and open arrows. The smallest q region is the Gunier region for the cluster, which is in this case the 1D array. The highest q region is the region where the primary particle scattering dominates. Between the two regions locates the Porod region of the cluster, exhibiting power-law slope of –1.

[2] Subsection 4.3.3 was written by Dr. Byeongdu Lee.

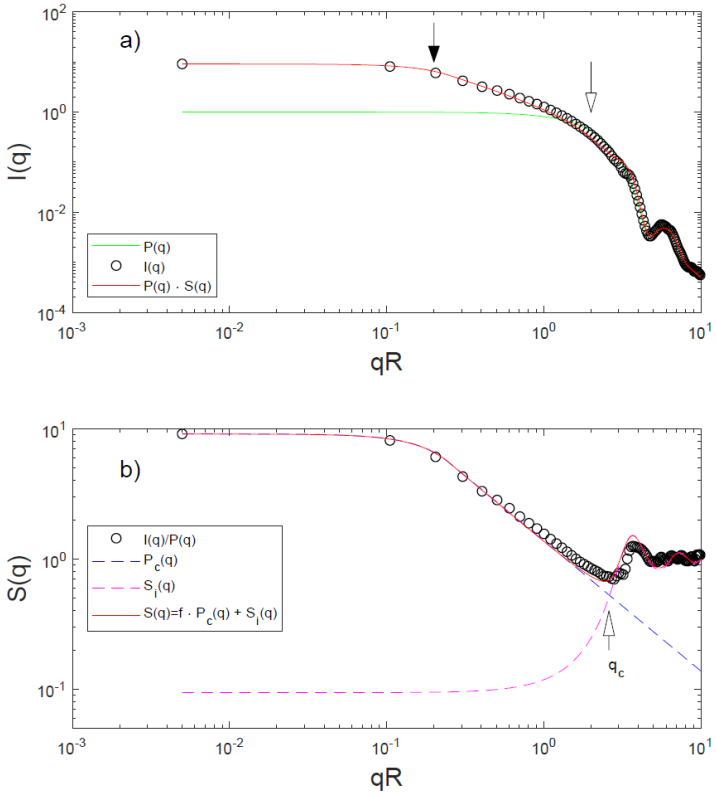

Figure 4.7 a) Simulated intensity $I(q)$ and form factor $P(q)$ from the model in Figure 4.6. b) $I(q)/P(q)$ is approximated with structure factor model shown in the equation above.

4.3.3.2 Structure Factor Derivation

The structure factor of the primary spheres forming the 1D array can be obtained by $I(q)/P(q)$, which is shown in Figure 4.7b. Analytically, the structure factor $S(q)$ can be calculated by orientational averaging:[232,233,234]

$$S(\boldsymbol{q}) = 1 + \int f(\boldsymbol{r}) n_{\infty}(\boldsymbol{r}) e^{-j\boldsymbol{q}\boldsymbol{r}} d\boldsymbol{r} \quad (4.6)$$

where $f(\boldsymbol{r})$ is the shape function of the cluster and $n_{\infty}(\boldsymbol{r})$ is the pair correlation function of the primary particles assuming that they fill infinite space keeping the same positional statistics or nature. The second terms can be written as below using the convolution theorem of Fourier transforms,[213]

$$\int f(\boldsymbol{r}) n_\infty(\boldsymbol{r}) e^{-j\boldsymbol{q}\boldsymbol{r}} d\boldsymbol{r} = \int f(\boldsymbol{r}) e^{-j\boldsymbol{q}\boldsymbol{r}} d\boldsymbol{r} \otimes \int n_\infty(\boldsymbol{r}) e^{-j\boldsymbol{q}\boldsymbol{r}} d\boldsymbol{r} \quad (4.7)$$

where the operator $\otimes$ stands for convolution. The first term on the right, the Fourier transform of $f(\boldsymbol{r})$, is the form factor of the cluster which we define as

$$\int f(\boldsymbol{r}) e^{-j\boldsymbol{q}\boldsymbol{r}} d\boldsymbol{r} \equiv P_c(\boldsymbol{q}) \qquad (4.8)$$

The second term on the right, the Fourier transform of $n_\infty(\boldsymbol{r})$, can be further broken down into two components, an interference function and null scattering terms, by employing the mean particle number density n_c,

$$\int n_\infty(\boldsymbol{r}) e^{-j\boldsymbol{q}\boldsymbol{r}} d\boldsymbol{r} = \int (n_\infty(\boldsymbol{r}) - n_c) e^{-j\boldsymbol{q}\boldsymbol{r}} d\boldsymbol{r} + N\delta(\boldsymbol{q}) \qquad (4.9)$$

We define the interference function as

$$\int (n_\infty(\boldsymbol{r}) - n_c) e^{-j\boldsymbol{q}\boldsymbol{r}} d\boldsymbol{r} \equiv i_i(\boldsymbol{q}) \qquad (4.10)$$

Since

$$P_c(\boldsymbol{q}) \otimes \big(N\delta(\boldsymbol{q})\big) = NP_c(\boldsymbol{q}) \quad (4.11)$$

the structure factor is finally written as below:[232,235]

$$S(\boldsymbol{q}) = 1 + P_c(\boldsymbol{q}) \otimes i_i(\boldsymbol{q}) + NP_c(\boldsymbol{q}) \quad (4.12)$$

The interference function is expressed as $i_i(\boldsymbol{q}) = S_i(\boldsymbol{q}) - 1$ and $S_i(\boldsymbol{q})$ is the structure factor of an infinite number of primary particles. So we consider $S_i(\boldsymbol{q})$ as the structure factor for internal arrangement of the primary particles in the cluster.

The role of the convolution in the second term is to broaden the peaks and valleys of the interference function. Considering that the structure factor of primary particles forming a non-regular cluster is already broad, we might simply neglect it. For the high q region, where $i_i(\boldsymbol{q}) > NP_c(\boldsymbol{q})$, $1 + P_c(\boldsymbol{q}) \otimes i_i(\boldsymbol{q})$ can be approximated as $S_i(\boldsymbol{q})$. For the small q region, where $i_i(\boldsymbol{q}) < NP_c(\boldsymbol{q})$, $1 + NP_c(\boldsymbol{q})$ can be approximated as $fP_c(\boldsymbol{q})$, where $f = N - 1$. Since the orientational average can be performed independently for each term, we can approximate $S(q)$ as

$$S'(q) = \begin{cases} fP_c(q) & q < q_c \\ S_i(q) & q > q_c \end{cases} \quad (4.13)$$

where q_c is a cross-over q that separates the high and small q regions. In this work, we smoothed the transition at q_c by adding a smoothing function, for example

$$S(q) = S'(q) + \left(|fP_c(q) - S_i(q)| + \frac{3}{2}\right)^{-4} - \left(\frac{5}{2}\right)^{-4} \quad (4.14)$$

When $fP_c(q)$ is not significant compared to $S_i(q)$ in the high q region, we may simplify $S(q)$ as

$$S(q) = fP_c(q) + S_i(q) \quad (4.15)$$

In order to simulate $S(q)$ for our 1D array cluster, we employed the Guinier–Porod equation for $P_c(q)$ (blue dashed curve in the bottom of Figure 4.7). The Guinier–Porod equation for a finite sized object requires 2 parameters: the radius of gyration $R_{g,c}$ and the Porod exponent P. In this work, the radius of gyration of the 1D array is calculated as $L/\sqrt{12}$. The Porod exponent is 1 since it is a 1D structure. f is about 9 because there are 10 particles (a bit larger than 9 due to polydispersity). The second term, $S_i(q)$, is to describe the structure factor of particles within the array. We employed the structure factor equation of the Percus–Yevick hard sphere potential (magenta dashed curve in the bottom of Figure 4.7). We define q_c for q where $fP_c(q) = S_i(q)$.

4.3.4 Structure of Polyampholyte Probed by SAXS

SAXS analyses were used to determine the structure of the as-prepared polyampholyte with different NaCl concentrations. The SAXS results shown in Figure 4.8a, measured on the as-prepared samples, reveal that the samples all contain molecular aggregates forming spherical objects consisting of Gaussian chains, as evidenced by the high q power-law slope of –2 (see fractal power-law exponent $D_f \sim 2$ in Table 4.3). In other words, the primary particles are in a well-solvated state (*i.e.,* polymer-rich water-containing domains). The shape of the primary particles is believed to be spherical since no power-law scattering was found in the very small q region; therefore we denote the primary particle as a globule. For some samples, the spherical form factor scattering alone did not fit the intensity profile in the small q regions, $q < 0.2$ Å^{-1}, indicating that the globular primary particles form a nanoscale cluster.

Table 4.3 Fitting parameters for SAXS results.

Sample	Cluster					Primary Particle (globule)				
	f	$R_{g,c}$(Å)	P	R_h(Å)	v(%)	f_p(a.u.)	$\bar{R}_p$(Å)	σ_p(Å)	D_f	$R_{g,p}$(Å)
PA-6-2.1	<<1	>>10	1.3	22.6	1.9	0.034	18.1	5.8	1.9	23.4
PA-8-2.1	<<1	>>10	1.3	15.0	1.8	0.035	18.2	6.0	1.5	24.0
PA-10-2.1	1.2	13.1	1.2	-	0	0.024	18.1	4.7	1.8	20.2
PA-10-1.05	9.0	31.1	1.0	-	0	0.012	17.8	5.2	1.8	21.4

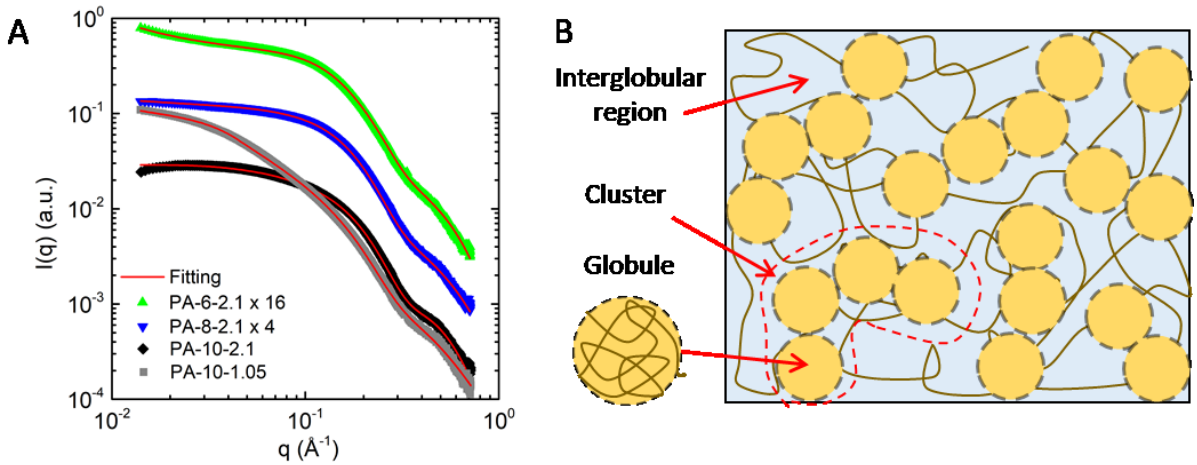

Figure 4.8 (a) SAXS data for PA-6-2.1, PA-8-2.1, PA-10-2.1, and PA-10-1.05. Here, the subtracted background is the capillary filled with 10 wt% NaCl solution. The red lines are the fits of the experimental data. (b) Schematic illustration of the polyampholyte hydrogel. The hydrogel consists of globules (*i.e.,* nanoscale hydrated particle-like structures with high polymer concentration) separated by water-rich domains (*i.e.*, inter-globular regions with low polymer concentration). The polymer globules aggregate to form clusters. See text for details.

To analyze the hierarchical structure, we developed the following SAXS model,

$$I(q) = (\Delta\rho)^2 f_p P\left(q; \bar{R}_p, \sigma_p, D_f\right) S(q) \qquad (4.16)$$

where $(\Delta\rho)^2$ and f_p are the X-ray scattering contrast and the number concentration (*e.g.,* molar concentration) of primary particles, respectively. When $I(q)$ for a sample is measured on an absolute scale, one can determine f_p if $(\Delta\rho)^2$ is known for the sample. In our experiment, $I(q)$ is measured in arbitrary units. Since we normalized $I(q)$ by the sample thickness, the *relative* values of f_p are meaningful assuming that $(\Delta\rho)^2$ does not vary from sample to sample. The form factor

of a primary particle $P(q)$ is modeled as that for polydisperse spheres with fractal internal structure.[236] The fractal power-law exponent $D_f \sim 2$ (*vide supra*) indicates that the internal structure of the primary particle is Gaussian chain-like.[237] The size distribution of the primary particles is modeled by the two parameters of the Schultz–Zimm size distribution; $\bar{R}_p$ and σ_p are the mean radius and variance of the external size of the primary particles, respectively. $R_{g,p}$ is the radius of gyration of the primary particle calculated from $\bar{R}_p$ and σ_p. Since the primary particles are aggregated to form clusters, the structure factor $S(q)$ is defined to include the hierarchical structure as,

$$S(q) = f \cdot P_c\left(q; R_{g,c}, P\right) + S_i(q; R_h, v) \qquad (4.17)$$

where P_c is the form factor of a cluster, which is calculated using the Guinier–Porod model.[237, 30, 238] It has two variables $R_{g,c}$ and P, which are radius of gyration and the Porod constant of the cluster, respectively. At q = 0, $P_c = 1$, and f is a scaling factor of the cluster form factor. In this definition, $f + 1$ denotes the mean number of primary particles forming a cluster. The Percus–Yevick (PY) hard sphere structure factor $S_i(q; R_h, v)$ is added to describe the internal arrangement of the primary particles in a cluster.[237] R_h and v are the hydrodynamic radius and volume fraction of the primary particles in a cluster, respectively.

Although the very low q scattering (q < 0.02 Å^{-1}) is not modeled due to the experimental resolution limit, it may provide a clue on structures larger than hundreds of nanometers. For instance, the low q upturn of the SAXS data for the PA-6-2.1 samples indicates macroscopic separation between water-rich and globule-rich domains. This can be understood considering that, in polyampholytes synthesized by random polymerization of positively and negatively charged groups, the net charge of each globule varies and is typically not zero.[10] At low salt concentration, the reduction of salt screening effects leads to a tendency for globules to form an aggregated superstructure, as observed in dilute polyampholyte solution.[144]

The effect of polymer concentration on the polyampholyte hydrogel structure was also studied by varying the monomer concentration in the precursor solutions. The fitting of SAXS profiles for PA-10-1.05 and PA-10-2.1 samples in Figure 4.8a indicates that both hydrogels form globules with a ~5 nm diameter primary unit. A slightly larger D_f for PA-10-1.05 than for PA-10-2.1

indicates that the monomer density in the globules is much lower for the former. Interestingly, those globules in PA-10-1.05 are aggregated into a 1D array as noticed from the Porod constant P ~ 1 for the cluster (Table 4.3), and the array consists of about 10 globules as seen from parameter f in Table 4.3. Assuming the shape of the cluster is a cylinder with its cross section identical to the cross section of the globules, its length can be calculated to be ~10 nm based on its radius of gyration using the relation, $R_{g,cylinder}^2 = \frac{R^2}{2} + \frac{L^2}{12}$, where R is the cylinder radius, and L is the length of a cylindrical rod. Since 10 nm is rather short for 10 globules in a row, the 1D array of globules is not likely rigid-rod-like but a more flexible necklace.

Based on these findings we can draw a schematic cartoon model of the polyampholyte chain networks, as seen in Figure 4.8b. Here, the charge-balanced polyampholyte chains form a networked structure of globules; the globules are spherical in shape, hydrated, on the nanoscale, contain polymer-rich domains and are interconnected to each other by polymer chains. The inter-globular regions are denoted as water-rich domains. The globule is similar to the case of a charge-balanced polyampholyte chain structure in the dilute solution.[36] It has been theoretically predicted that a charge-balanced polyampholyte chain forms a globular conformation because Debye–Huckel fluctuation induces attraction between charges. The size of the globule depends on ionic strength and on the number of repeating units of the polymer.[10,37] In our hydrogels, the concentrations of polyampholytes are much higher than concentrations of dilute solutions. Thus, a globule consists of several chains, while each chain may belong to a few neighboring globules simultaneously, resulting in a networked superstructure of globules. This feature is similar to the qualitative description suggested by Nisato *et al.*,[30] as well as to the ionic clusters in ionomers (*e.g.,* Nafion) due to the self-assembly of charged polymer chains.[239,240] Both size and the number of globules decrease with increasing NaCl concentration, as shown in Table 4.3. This implies that electrostatic interactions between oppositely charged chains become weaker because higher ionic strength would screen charges on the chains more efficiently. In other words, with increased salt ions, more polyampholyte chains tend to exist in the water-rich domain rather than to form globules.

4.3.5 Temperature-Dependent Structure Evolution

The structures of polymer and water molecules at low temperatures were surveyed simultaneously using SAXS and WAXS, respectively; these spectra were collected at various

temperatures from –40 to 5 °C with an interval of 1 °C at a ramping rate of +1 °C/min. In our work, we focused on melting behavior upon slow heating, as we attempted to extract the information under (nearly) equilibrium conditions; our study does not focus on ice crystallization or nucleation kinetics of confined water that occur in cooling processes. Figures 4.9a and 4.9b show examples of SAXS and WAXS spectra of PA-10-2.1, respectively. Figure 4.9c shows the size of globules in the polyampholyte hydrogel. The radius of gyration increased with increasing temperature, with the resolution limit of the smallest discernable globule size being ~10 Å. From the WAXS results, the relative amount of amorphous water was extracted by integrating the areas of the diffraction peaks for amorphous water (the hump located between 1.5 to 2.5 $Å^{-1}$), as shown in Figure 4.9d. These values were normalized by sample thickness, polymer concentration and minor beam intensity fluctuation. WAXS results indicate that a higher fraction of water molecules appear to be amorphous at a given low temperature when the hydrogel contains a higher NaCl concentration.

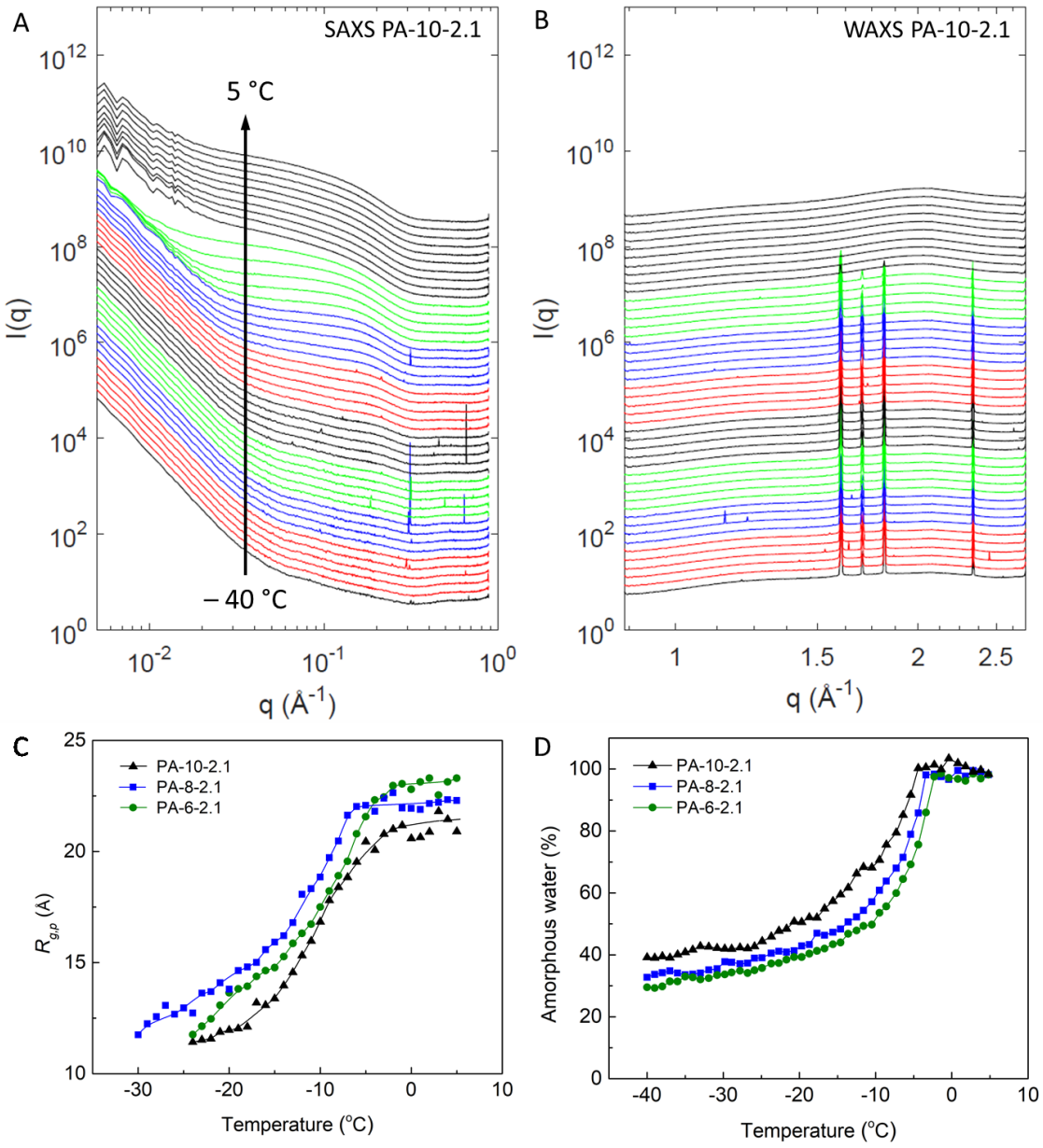

Figure 4.9 (a) and (b) Variable-temperature SAXS and WAXS results of PA-10-2.1, respectively. Here, the subtracted backgrounds for SAXS/WAXS were obtained from a blank capillary. These spectra were collected at various temperatures from –40 to 5 °C with an interval of 1 °C at a ramping rate of 1 °C/min. (c) The size of globules, and (d) normalized amounts of amorphous water in the polyampholyte hydrogel *versus* temperature. Solid lines are provided as guides to the eye.

Based on the variable temperature SAXS/WAXS results, we propose a qualitative description of the structural evolution of polymers and the behavior of water molecules in ice-forming polyampholyte hydrogels in Figures 4.10a and 4.10b. Upon cooling, the water molecules in interglobular regions (*i.e.*, water-rich domains) start to form ice. Water molecules trapped within the globules do not form ice because they cannot align themselves to form a periodic crystalline environment, due either to a strong confinement between the polymer chains or to a strong interaction with these chains. As ice crystals grow, the hydrated globules (*i.e.,* polymer-rich domains), which do not participate in the ice formation, come closer to each other. At the same time, the concentration of NaCl in the non-ice region becomes elevated, which increases electrostatic screening effects between the globules, leading to a better dispersion of the globules, and to a further reduction in globular size. Finally, ice crystals are inhibited from growing freely in size because of steric hindrance from the non-freezable globules and the polyampholyte networks between them that distribute across the entire hydrogel.

Direct visualization by microscopic techniques can be an effective method for confirming the morphological hypothesis based on spectroscopic methods. The SEM images in Figures 4.10c and 4.10d were obtained by liquid nitrogen quenching, followed by freeze-drying to visualize mesoscopic polymer structures after sublimating water molecules. Here, the sample in Figure 4.10c was quenched from room temperature; a homogenous distribution of fine nanostructures is found in the freeze-dried hydrogel. On the other hand, in Figure 4.10d, a SEM image of a sample that was pre-frozen at –30 °C before quenching with liquid nitrogen, stark differences in morphology are observed. Here, the darker trenches are attributed to evaporated, sub-micron-sized, slush-like ice domains between polymer-rich domains. The brighter regions correspond to the polymer-rich ice-free domain regions that are interconnected. Finally, it is notable that this temperature-dependent structure evolution of a salt-containing polyampholyte hydrogel is reversible (as evidence, see the DSC scanning of multiple freezing–thawing cycles shown in Figure 4.11).

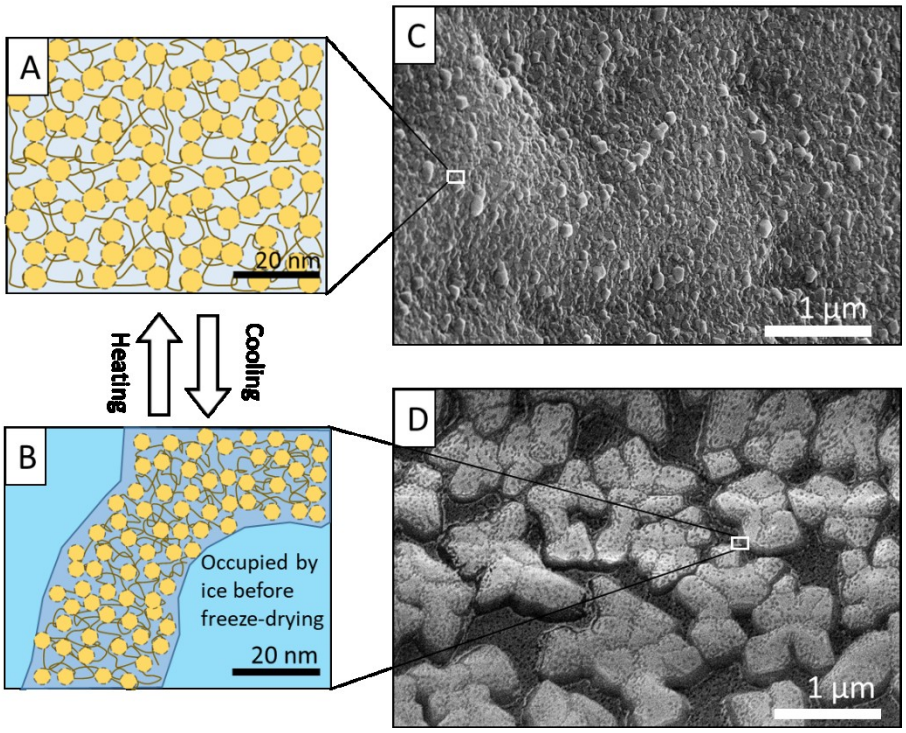

Figure 4.10 Temperature-dependent structural evolution of salt-containing polyampholyte hydrogel at (a) 20 °C and (b) –30 °C. Yellow circles in hatched outlines denote polymer-rich, but hydrated, globules. Cross-sectional FE-SEM images of PA-10-2.1 (c) at 20 °C, and (d) pre-frozen at –30 °C, followed by quenching in liquid nitrogen, and freeze-drying. (a) and (b) represent the hydrogel structures of regions identified by the with white boxes in (c) and (d), respectively.

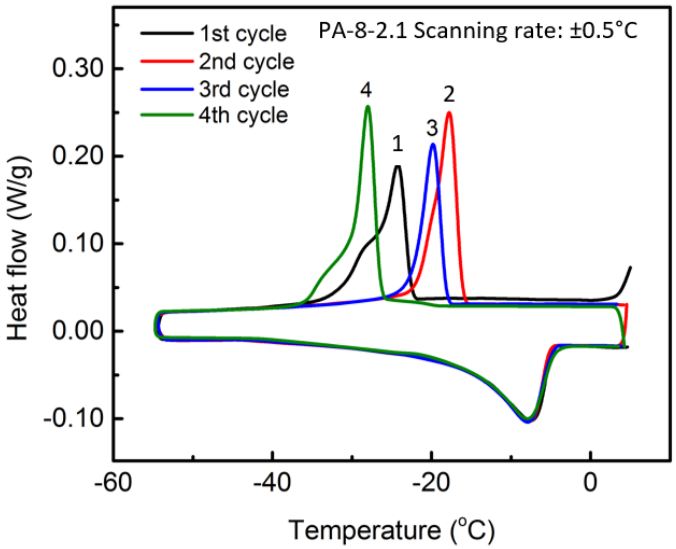

Figure 4.11 Raw DSC profiles (thawing) for PA-10-2.1 under multiple freeze–thaw cycles.

4.3.6 Variable-Temperature Solid-State NMR

To investigate the hypothesis that the interconnected polymer-rich domains play a role as channels for ionic conduction at low temperatures, non-spinning ^{1}H and ^{2}H solid-state NMR spectra of PA-10-2.1 and of its precursor solution were acquired at various temperatures (Figure 4.12). The ^{1}H solid-state NMR spectra obtained at 21 °C indicate relatively well resolved peaks, although in the case of PA-10-2.1, some broadening of all peaks is observed. The peak at 4.6 ppm is attributed to H_2O. In their investigation of poly(N-isopropylacrylamide) gel networks, Wang *et al.*[183] found that peaks attributed to free and bound water were separated by 0.09 ppm, as resolved by high-resolution measurements at 600 MHz. Unfortunately our ^{1}H resolution was insufficient to determine whether both types of water exist at room temperature. To investigate the status of water in these samples at lower temperatures, ^{2}H solid-state NMR spectra were obtained at –49 °C (Figure 4.12b). Spectra of both PA-10-2.1 and of its precursor consist of two distinct features: relatively sharp central peaks with underlying broad Pake patterns. The Pake pattern with a breadth between the extremities of > 150 kHz suggest a ^{2}H nuclear quadrupolar coupling, as the shape and the breadth of the pattern is comparable to those reported for hexagonal D_2O between –10 °C[241] and –196 °C.[242] Importantly, the relatively sharp central peaks with line widths at half maximum of 4.5 kHz suggest the existence of mobile water at –49 °C.

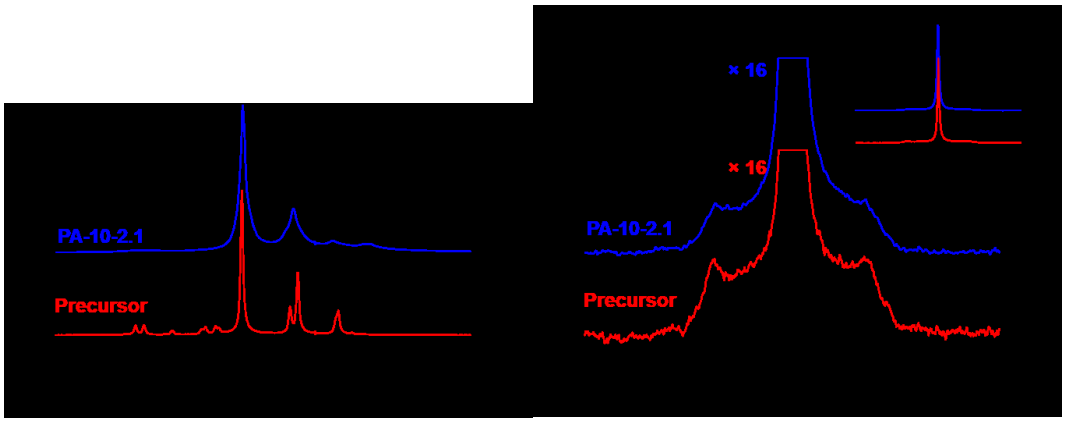

Figure 4.12 (a) ^{1}H solid-state NMR spectra of PA-10-2.1 (upper traces) and of the corresponding precursor solution (lower traces) acquired at 21 °C. (b) ^{2}H solid-state NMR spectra of the same samples acquired at –49 °C. The inset in the latter shows the complete spectra. All spectra were obtained from non-spinning operation of NMR.

The solid-state NMR observations are consistent with the SAXS/WAXS data discussed above. The ^{1}H solid-state NMR spectra obtained at room temperature suggest mobile water, with broadened peaks for the PA-10-2.1 sample a possible indication of a slight restriction in the motion (as shown in Figure 4.13). At lower temperature, the ^{2}H spectra indicate frozen water, consistent with the water-rich domains suggested from the SAXS/WAXS data. The hypothesis that a certain fraction of water molecules do not freeze due to confinement with the polymer chains or interactions with these chains is also verified by this data. The presence of two distinct feature types in the ^{2}H spectra rather than a continuum from a broad pattern to sharp peaks suggests two distinctive statuses for the water molecules.

The enhanced ionic conductivity in polyampholyte hydrogels at –30 °C in Figure 4.1 can be explained by our comprehensive experimental results from SAXS, WAXS, FE-SEM, and solid-state NMR. The SAXS results suggest that polyampholyte hydrogels at high salt concentration exhibit unique internal structure where even polymer-rich regions consist of a highly hydrated globular structure. At low temperatures, the polymer-rich regions keep a submicron-sized domain structure, which hinders the growth of ice crystals that are fragmented as slush-like structures, as shown by FE-SEM. Moreover, the existence of amorphous water molecules and the mobility of these molecules at temperatures as low as –49 °C are confirmed by WAXS and solid-state NMR. An ion's mobility (u) and its molar conductivity (λ) have the relationship $\lambda = zuF$, where z is the charge number, and F is Faraday's constant.[243] Due to the existence of mobile water in interconnected polymer-rich domains at low temperatures, the mobility of Na^{+} and Cl^{-} ions in PA-10-2.1 is elevated compared to the frozen control sample of 10 wt% NaCl solution in Figure 4.1, leading to a 48× increase in the ionic conductivity value.

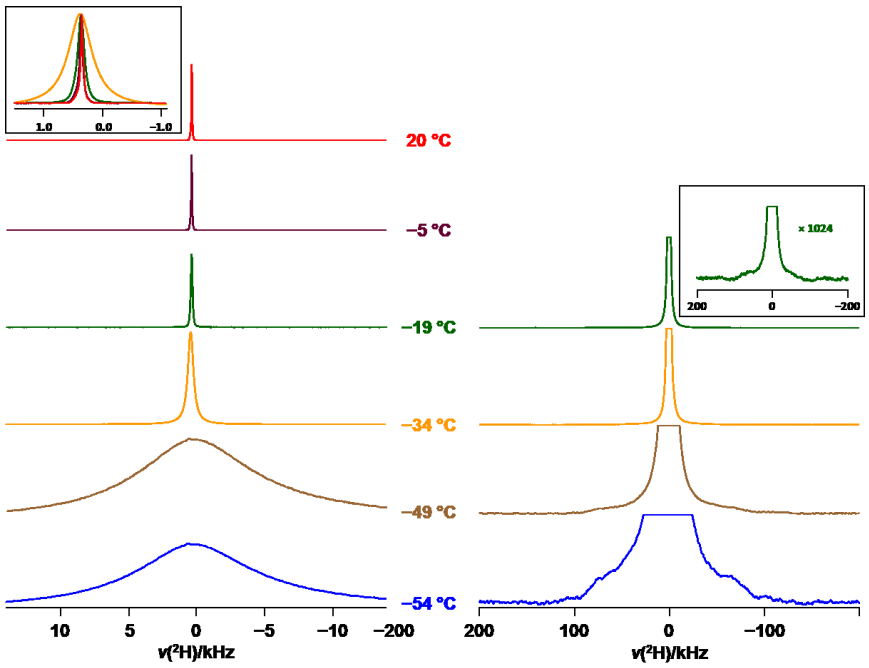

Figure 4.13 Variable temperature non-spinning ^{2}H NMR spectra of PA-10-2.1.Spectra on the left side were acquired with a single pulse with the inset displaying an overlay of the ^{2}H peaks for spectra acquired in the 20 to −38 °C range. To observe the broad non-mobile water resonance, a solid-echo pulse sequence was used. All spectra in the right side have been multiplied by a factor of 16 to illustrate the underlying Pake pattern. The inset shown on the right was multiplied by a factor of 1024 to illustrate the onset of the Pake pattern at this temperature; there was no detectable ^{2}H Pake pattern for spectra acquired at higher temperatures.

4.3.7 Visualizing the Globular Structure

Figure 4.14 shows the low-dose FE-SEM images of the freeze-dried as-prepared hydrogel (PA-10-2.1). There are two featured regions in Figure 4.14A. The darker trenches (labeled as "Trough") are attributed to sublimated ice domains between polymer-rich domains. The brighter regions (labeled as "Plateau") correspond to the polymer-rich ice-free domains. Figure 4.14B shows the spherical structures in the cracks of the Au-Pd coating in the "trough" regions. The diameters of the spherical particles range from 5 to 20 nm, which is consistent with the previous variable-temperature SAXS study, and is attributed to the self-assembly of charged polymer chains.[239,240] The spherical structures were also observed in the cracks of the Au-Pd coating in the "plateau" and the boundary of the "trough" and "plateau", as shown in Figure 4.14C and 4.14D,

which indicates that the globule structure is ubiquitous and is indeed the universal primary structure in the polyampholyte hydrogel.

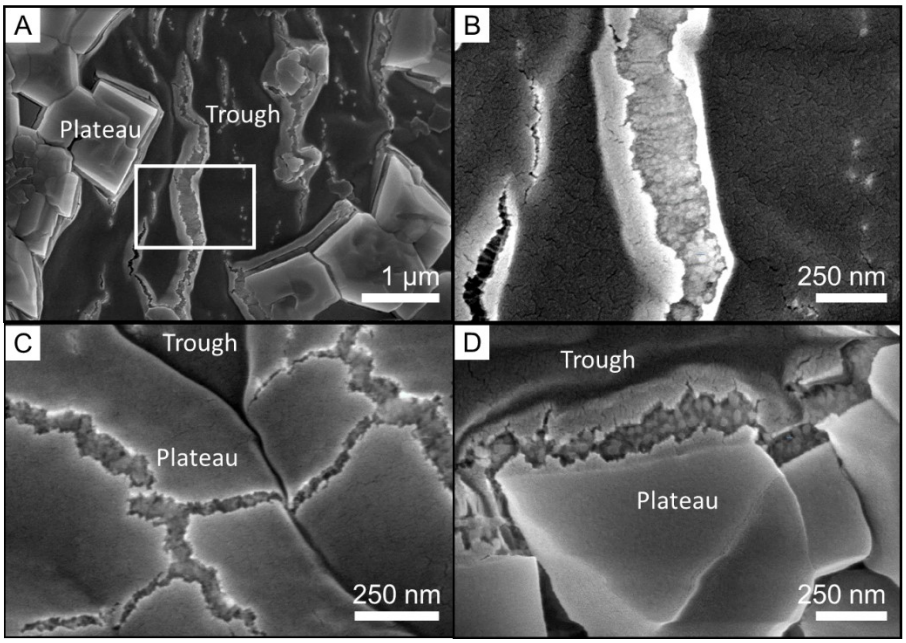

Figure 4.14 (A) The SEM image of freeze-dried polyampholyte hydrogel (PA-10-2.1). (B) Magnified images of the small regions identified in Figure 4.14A in the middle of the "trough". (C) Captured at the middle of the "plateau", and (D) at the boundary of the "trough" and "plateau".

To verify the FE-SEM result, we did STEM on the ground PA-10-2.1 sample, as shown in Figure 4.15. The image of black-field STEM is zoomed-in at the edge of hydrogel powder. The size of the spherical particles ranges from 5 to 10 nm. The result supported the existence of spherical structures observed in the FE-SEM images, which correspond to globule structures that we modelled from SAXS spectra in Figure 4.3.

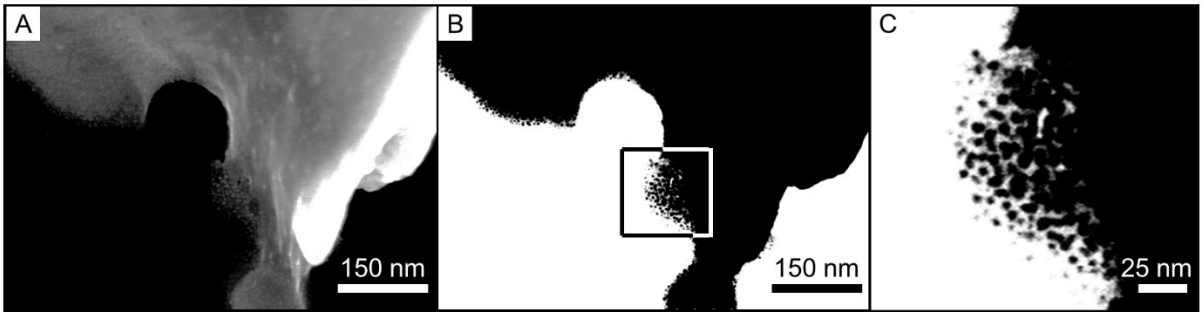

Figure 4.15 (A) Secondary electron image and (B) BF-STEM image of freeze-dried polyampholyte hydrogel powders. (C) A magnified image of the small region identified by the rectangular box in Figure 4.15B.

4.4 Conclusion

The SAXS results suggest a network of globule structures in the charge-balanced polyampholyte hydrogels with the hydrogel structure being dependent on the synthesis procedure. The globular network structure results in an increase in amorphous water at −30 °C, as supported by the WAXS results. Based on variable-temperature SAXS, WAXS, SEM and solid-state NMR data, the temperature evolution of polyampholyte hydrogel upon cooling–heating cycles was proposed. It is proposed that the interconnected polymer-rich domains result in a slush-like ice formation that allows enhanced ionic conductivity of the hydrogel in ice-forming conditions at low temperatures. Through FE-SEM and STEM, we observed globular structures in polyampholyte hydrogel. This observation sheds light on the development of high conductivity gel electrolytes for operation at low temperatures, as well as the development of anti-freezing surface coatings.

Chapter 5 Water States in Salt-Containing Polyampholyte Hydrogels

5.1 Introduction

The water state, which describes the fixation of water molecules due to their interaction with polymer chains, is a deterministic factor that governs the hydrogel's material properties, such as electrical conductivity,[19,20] anti-biofouling effects,[17,23] lubrication,[21,24] adhesion,[25] and water-retention ability.[22] Quantitative analysis on the endothermal peak from the heating scan of differential scanning calorimetry (DSC) can classify the water in the hydrogel into three distinctive categories.[176,179,180,181] Firstly, *non-freezable bound water* corresponds to the water molecules that are strongly bonded to polymer by hydrogen bonding or dipole–dipole interactions. These water molecules are found to be unfrozen even at –190 ºC. Secondly, *free water* represents the water molecules that are unaffected by the presence of polymer chains; in an absence of salt ions, these water molecules will freeze at or near 0 ºC. Thirdly, *freezable bound water* corresponds to the water molecules that have secondary interactions with the polymer chains. In other words, these water molecules are intensively interacting with the non-freezable bound water. Consequently, the activation energy required to rotate the freezable bound water molecules is larger than that required to rotate the free water molecules in the event of ice crystal formation, thus the freezing temperature is considerably lower than that of the free water. Likewise, the water–polymer interactions near molecular or atomic ions are described as bulk water, outer, and inner hydration shells, which have the same implications as free water, freezable, and non-freezable bound waters, respectively.[244]

In this chapter, we studied the water states of a polyampholyte random copolymer that consists of two oppositely charged ionic monomers, sodium 4-vinylbenzenesulfonate (NaSS) and [3-(methacryloylamino) propyl] trimethylammonium chloride (MPTC), which is denoted as poly(NaSS-*co*-MPTC). The phase behavior of water could be explained by water molecules in the hierarchical structure of the networked globules, which was consistent with our previous work as shown in Figure 5.1.[245]

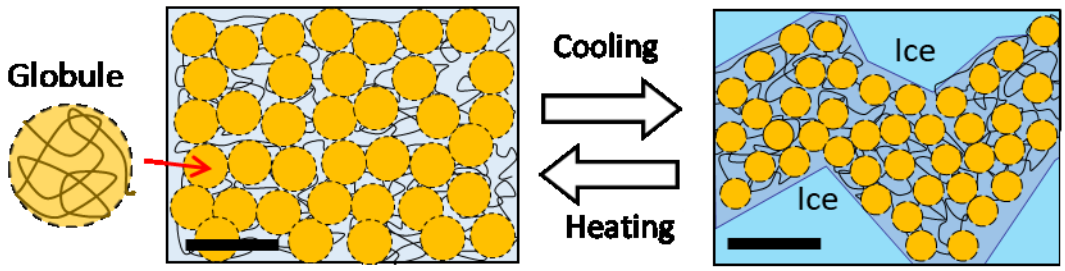

Figure 5.1 Illustration of temperature-dependent structural evolution of salt-containing polyampholyte hydrogel at 20 °C and –30 °C. Yellow circles denote polymer-rich, but hydrated, globules. The scale bars are 10 nm.

5.2 Experimental Methods

Polyampholyte hydrogel synthesis. We copolymerized sodium 4-vinylbenzenesulfonate (cationic monomer; NaSS) and [3-(methacryloylamino)propyl] trimethylammonium chloride (anionic monomer; MPTC) with IRGACURE 2959 (photoinitiator) and NaCl. The chemicals were purchased from Sigma-Aldrich and used as received. The aqueous precursor solution with designed chemical concentrations (shown in Table 5.1) was injected into the gap between two glass plates, where the gap was separated by a spacer (thickness 1 mm). The monomer polymerization was carried out by irradiation with a UV lamp (broadband light with a maximum peak at 365 nm with the intensity of 22 mW/cm^2; Jelight UVO-Cleaner Model-342) with a lamp-to-sample distance of 5 mm. In all cases, the total monomer conversion of NaSS and MPTC was measured to be ~98%, and the ratios of monomers between NaSS and MPTC were at the charge-balanced point, according to our previous work.[245] The samples prepared are listed in Table 5.1. Hereafter, we denote the samples using the code PA-#-$c(t)$, where the # is the NaCl concentration (wt%) in the polyampholyte hydrogel, c is the total monomer concentration (M), t is the UV curing time. The NaCl concentration in the hydrogel is defined by Equation 5.6:

$$C_{\mathrm{NaCl}} = \frac{m_{\mathrm{NaCl}}}{m_{\mathrm{NaCl}}+m_{\mathrm{water}}} \times 100\% \qquad (5.6)$$

where m_{NaCl} is the total mass of NaCl, and m_{water} is the mass of water added in the precursor solution. It is noted that NaSS and MPTC contain sodium and chloride ions, respectively which were accounted for in the calculation of the m_{NaCl} value.

Table 5.1 List of samples prepared.

Sample	NaSS conc.	MPTC conc.	NaCl conc.	UV time	Further treatment
PA-6-2.1(8)	1.07 M	1.03 M	6 wt%	8 h	-
PA-8-2.1(8)	1.07 M	1.03 M	8 wt%	8 h	-
PA-10-2.1(8)	1.07 M	1.03 M	10 wt%	8 h	-
PA-10-2.1(0)	1.07 M	1.03 M	10 wt%	0 h	-
PA-10-2.1(2)	1.07 M	1.03 M	10 wt%	2 h	-
PA-10-2.1(4)	1.07 M	1.03 M	10 wt%	4 h	-
PA-10-0.526(8)	0.268 M	0.258 M	10 wt%	8 h	-
PA-10-1.05(8)	0.536 M	0.515 M	10 wt%	8 h	-
D-PA-10-2.1(8)	1.07 M	1.03 M	10 wt%	8 h	Dialyzed in DIW

a. In all cases, 0.25 mol% photoinitiator (compared to the combined concentration of NaSS and MPTC) was added in the precursor solution.

DSC Characterizations. The water-polymer interactions in the polyampholyte hydrogel were quantified by differential scanning calorimetry (DSC, Q1000, TA Instruments, US). The samples were tested right after preparation to prevent any possible loss of water through evaporation. For each measurement, 10 mg of sample was sealed in a copper sample pan. For each DSC measurement, the following thermal history was programmed: (i) held at 10 °C for 10 min, (ii) cooled from +10 to –60 °C at a rate of 1 °C/min, (iii) held at –60 °C for 10 min, (iv) heated up to 10 °C at a rate of 1 °C/min. The program, (i) to (iv), was repeated twice or more to ensure the consistency of the results for each sample. We utilized the data from the heating cycle for further analysis. The DSC characterization was also carried out at rates of 0.5, 2, and 5 °C/min in the corresponding steps. The results show that consistent results could be obtained at rates of 1 °C/min or less. The details about the deconvolution of DSC profiles are shown in Figure 5.2. Raw DSC data were deconvoluted and interpreted using the Peak Analyzer function in the software (Origin). Initially, we defined the baseline of the DSC profiles as shown in Figure 5.2a. Points were placed at the linear parts of both ends, and then the baseline was defined using interpolation by the software (Figure 5.2b). Once the baseline was subtracted from the DSC data, the peaks were found by the analyzer automatically. Finally, the DSC profiles were deconvoluted into several bi-Guassian peaks (Figure 5.2c), and the peak centers (*i.e.,* the statistically defined gravity centers of the peaks), and peak areas were given by the software. The skewed peak can be fitted by bi-Gaussian fitting. The fitting equations are shown as,[246]

$$y = y_0 + He^{-0.5(\frac{x-x_c}{w_1})^2} \ (x < x_c) \ (5.7)$$

$$y = y_0 + He^{-0.5(\frac{x-x_c}{w_2})^2} \ (x > x_c) \ (5.8)$$

where y_0 is the baseline, H is the peak height, x_c is the peak position, w_1 and w_2 are the widths of the left and right side of the fitting peak.

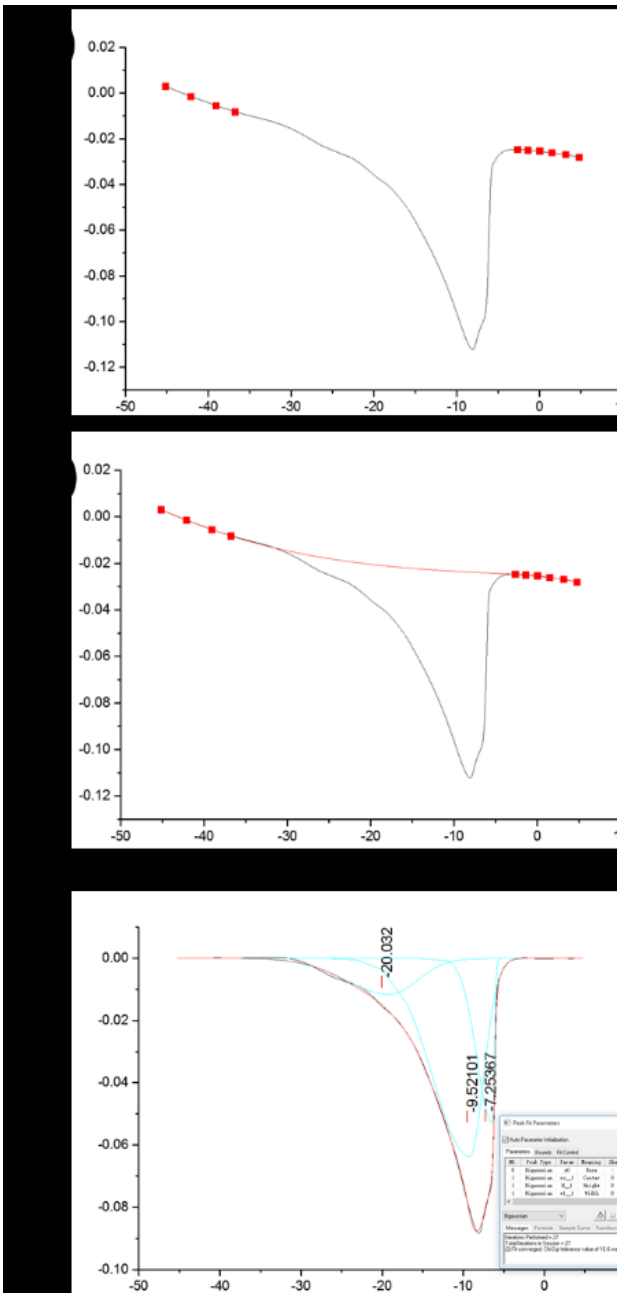

Figure 5.2 The deconvolution of raw DSC curves.

The fractions of different categories of water were calculated with,[179]

$$F_{\mathrm{i}} = \frac{\Delta H_{\mathrm{m,i}}}{\Delta H^{0}_{\mathrm{m,i}} F_{\mathrm{water}}} \qquad (5.9)$$

where F_{i} is the mass fraction of water in category i, $\Delta H^{0}_{\mathrm{m,i}}$ is the melting enthalpy of water in category i, $\Delta H^{0}_{\mathrm{m,FW}} = \Delta H^{0}_{\mathrm{m,FBW-P}} = 333.5$ J/g, $\Delta H^{0}_{\mathrm{m,FBW-S}} = 303$ J/g.[179,247,248] $\Delta H_{\mathrm{m,i}}$ is the melting enthalpy of water in state i, which is obtained from DSC deconvolution, and F_{water} is the total water mass fraction in the polyampholyte hydrogel.

5.3 Results and Discussion

The water states in the polyampholyte hydrogel were quantified by the deconvolution of the second heating cycle. As illustrated in Figure 5.3a, water molecules interact with five distinct species: sodium and chloride ions, non-polymerized (*i.e.,* monomeric) NaSS and MPTC, and poly(NaSS-*co*-MPTC). However, according to the total monomer conversion rate, the amount of monomeric NaSS and MPTC can be neglected for most of the samples (*i.e.,* samples after 8 h UV irradiation).[245] Based on the DSC results, we empirically classified the water states into the following four categories: (i) free water (FW), whose interactions with solutes or polymers are negligible; (ii) freezable bound water associated with polymer (FBW–P), which has secondary interactions with the polymers or the unreacted monomers; (iii) freezable bound water associated with salt (FBW–S), which has secondary interactions with the sodium chloride ions; and (iv) non-freezable bound water (NFBW), which forms a hydration layer on the polymeric, or the monomeric, or the ionic species.

Here, we identified the location of the three peaks from the first and the second order partial derivatives with respect to temperature of DSC scans, as described in Figure 5.3b. The peak at the highest temperature corresponds to FW, and its location is near the freezing temperature of salt water expected from the phase diagram of a H_2O and NaCl mixture at the corresponding salt concentration.[249] The peak that corresponds to FBW-P occurred at around –10 °C; here, both polymeric and monomeric samples exhibited a peak at the temperature. The peak for FBW–S occurred at around –21 °C, as expected from the eutectic freezing temperature of water and

hydrated NaCl [249]. The amounts of water in each water states (FW, FBW–P, and FBW–S) were quantified by the deconvolution of each DSC profile with bi-Gaussian fitting for each skewed peak.[176,179, 246] The amount of NFBW can be calculated by subtracting the total area of the peaks from the projected peak area by assuming the complete phase transition of water molecules (obtained by multiplying the water content by the latent heat of fusion). For each sample synthesis condition, we performed DSC for at least three different batches to confirm the reproducibility and to generate reliable error bars.

Finally, we note that the proposed classification between FW, FBW–P, and FBW–S is somewhat hypothetical because it is based solely on the deconvolution of DSC data. For example, a water molecular may have interaction with one or both polymer chains or salt, but from DSC we cannot say to which extent it belong to polymer chains or salt, the deconvolution process will assign it to a water category. The amount of NFBW, however, is undisputedly true, and it is more important for the low temperature conductivity since it may tell us the ice volume at a certain temperature.

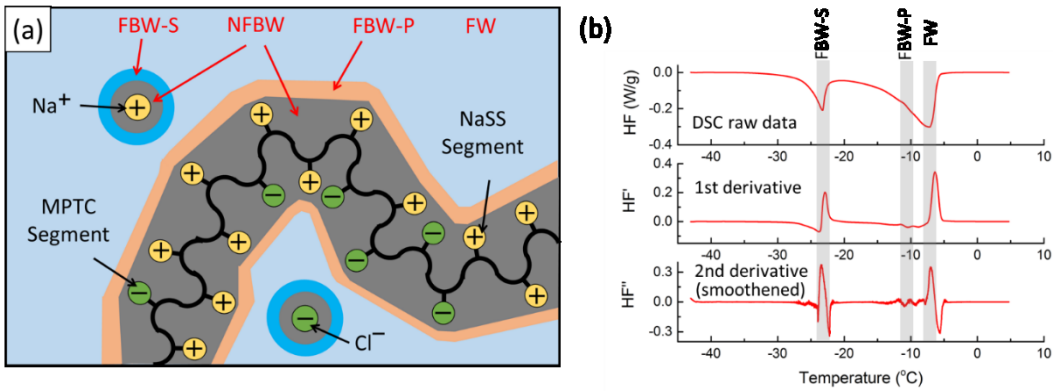

Figure 5.3 (a) Illustration of water-polymer interaction in salt-containing polyampholyte hydrogel system. See the main text for the definition of FW, FBW-P, FBW-S, and NFBW. (b) A typical DSC curve (top) of salt-containing polyampholyte hydrogel. The first (middle) and the second partial derivative (bottom) with respect to temperature of heat flow (HF) identify the location of the three peaks that corresponds to FW, FBW-P, and FBW-S from high to low temperatures. The grey bands show the approximate locations of the peaks. The exact location of the 'peak center' is defined as the statistical gravity center of each peak.

5.3.1 The Effect of Salt Concentration

Figure 5.4 summarizes the effect of salt concentration studied for as-prepared hydrogels. The selected three concentrations of NaCl in the water–NaCl mixture (*i.e.,* no monomeric or polymeric component in the wt% calculation) were 6 wt%, 8 wt% and 10 wt% (labeled as PA-6-2.1(8), PA-8-2.1(8), and PA-10-2.1(8) in Table 5.1, respectively). Figure 5.4a shows the DSC spectra with deconvolution fittings for the three hydrogels. Figure 5.4b shows that the peak temperatures of FW, FBW–P and FBW–S in hydrogel decrease as the salt concentration increases. A dramatic contrast could be seen between PA-6-2.1(8) and PA-10-2.1(8); the relative amount of FW and NFBW in PA-6-2.1(8) were 22.6 ± 1.7 % and 51.4 ± 2.6 %, whereas the PA-10-2.1(8) showed 4.6 ± 0.4 % and 78.6 ± 1.3 % for FW and NFBW, respectively. This result supports our earlier discussion that the polyampholyte chains swell with increasing concentration of salt in the solution, which is called anti-polyelectrolyte behavior.[32] Referring to the networked structure of globules illustrated in the Figure 5.1, the water molecules in the water-rich domains start to form ice upon cooling. However, water molecules which are trapped within the globules are not able to form ice because they cannot re-orient to form a periodic crystalline environment confined within relatively higher polymer chain density in the globules. When more salt exists in the polyampholyte hydrogel, the increased ionic strength causes the swelling of polymer chains. Therefore, more water molecules interact with polyampholyte chains; consequently, this leads to the increased amount of NFBW.

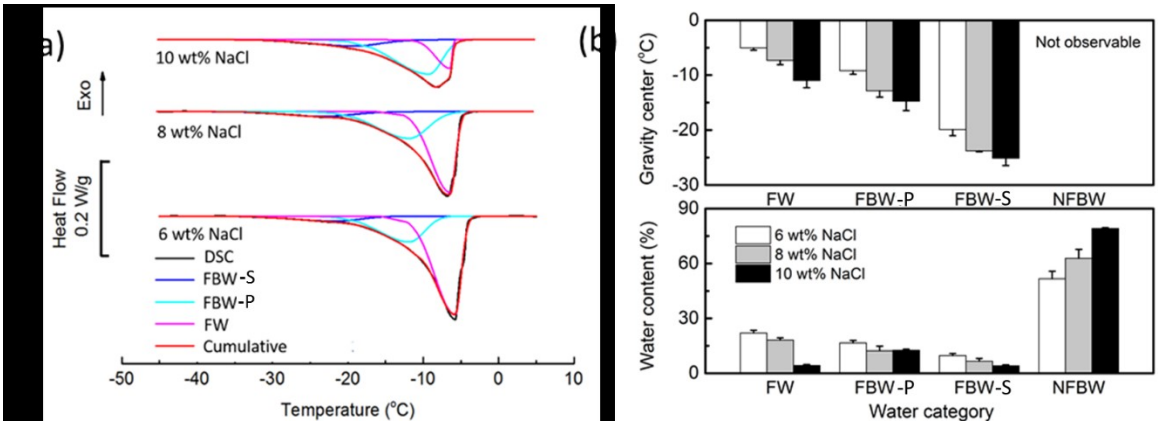

Figure 5.4 (a) DSC curves and their deconvolution fittings for polyampholyte hydrogel with the three different salt concentrations (PA-6-2.1(8), PA-8-2.1(8), and PA-10-2.1(8) in Table 5.1, respectively). (b) Top: peak centers of peaks for FW, FBW-P and FBW-S. Bottom: relative amounts of water in the different states.

One may wonder that the amorphous water amount probed by wide-angle X-ray scattering (WAXS) is ~40% at –40 °C for PA-10-2.1(8) in Chapter 4,[245] whereas the NFBW fraction of the same sample is 78.6%. The difference between the amorphous water amount from WAXS and the NFBW from DSC measurements can be attributed to the water molecules in the hydration shells of both polymer chains and mobile ions. Once temperature decreases, the free water molecules form ice whilst NaCl and polymer are concentrated in the non-frozen regions. Though the water molecules in these regions are non-frozen (*i.e.*, does not participate in the phase transition that is detected by DSC), the structure of the water molecules is ordered by cooperativity in ion hydration,[162,166,167,171] which implies that the ordered fraction may not contribute to the intensity of the amorphous water halo in the WAXS measurements (*i.e.*, local density fluctuation of water molecules). Moreover, $NaCl{\cdot}2H_2O$ forms at high NaCl concentration, but the melting of the dihydrate releases an untraceable amount of heat over a wide temperature range, which may not be identified by DSC because of an intrinsic limitation of the measurement.[248,250]

5.3.2 The Effect of Polymerization

The effect of polymerization on the water states was studied by irradiating the precursor solution at fixed monomer and salt concentrations with varying UV exposure times of 0, 2, 4, and 8 h (PA-10-2.1(0), PA-10-2.1(2), PA-10-2.1(4), and PA-10-2.1(8) respectively). Here, the average degree of polymerization increased with increasing UV exposure time, whereas zero UV exposure left the precursor solution in a completely non-polymerized state. The results in Figure 5.5 show that the peak centers are nearly independent of the UV exposure time. But the FW content decreased from 20.0 ± 2.1 % to 4.6 ± 0.4 % and the NFBW content increased from 58.3 ± 3.4 % to 78.6 ± 1.3 % when the monomers were polymerized with 8 h of UV exposure time. The results indicate that the higher degree of polymerization makes the polyampholyte more efficient in preventing ice formation. Prolonged UV exposure increases the degree of polymerization, this may impact the average globule size in the hydrogel, which is likely to be larger. It will then increase the amount of NFBW since a significant amount of water molecules confined in the globules are considered to be NFBW. In addition, polymer chains in the water-rich domains also contribute to the increase of NFBW. The decreased distance between globules may further reduce the content of FW.

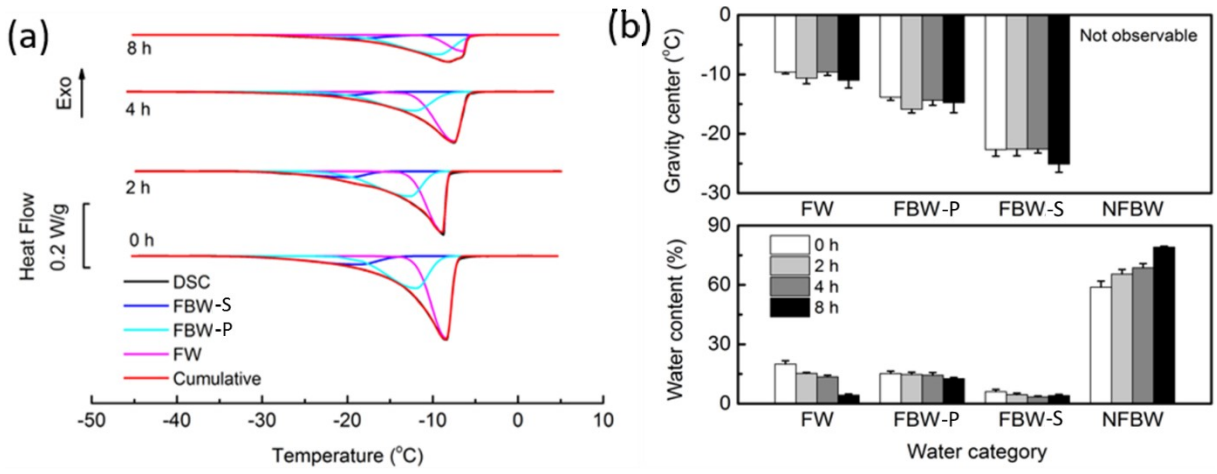

Figure 5.5 (a) DSC curves of samples with various UV curing time (PA-10-2.1(0), PA-10-2.1(2), PA-10-2.1(4), and PA-10-2.1(8) respectively). Here, 0 h curing time means that there was no polymerization (*i.e.,* only monomers and NaCl exist), whereas increasing curing time implies an increased degree of polymerization. (b) Top: peak centers for FW, FBW-P and FBW-S. Bottom: contents of water states obtained from deconvolution fittings.

5.3.3 The Effect of Polymer-to-Water Ratio

We also investigated the effect of polymer-to-water ratio on the water states in the polyampholyte hydrogel by varying monomer concentration in the precursor solutions (PA-10-0.526(8), PA-10-1.05(8), and PA-10-2.1(8), respectively). The DSC results, and the corresponding peak centers and the relative amounts of water in the different water states, are shown in Figure 5.6. Neat 10 wt% NaCl solution (*i.e.,* no NaSS, MPTC or Poly (NaSS-*co*-MPTC)) was used as a control sample. As the polymer-to-water ratio increased, the location of the peak centers of FW, FBW–P, and FBW–S decreased to lower temperatures. The FW content in the hydrogel decreased from 30.2 ± 2.5 % to 4.6 ± 0.4 % and the NFBW content increased from 45.8 ± 4.6 % to 78.6 ± 1.3 % for the 10 wt% NaCl solution and PA-10-2.1(8), respectively. The trend of increasing NFBW content can be attributed to the increased volume fraction of polymer in the system.

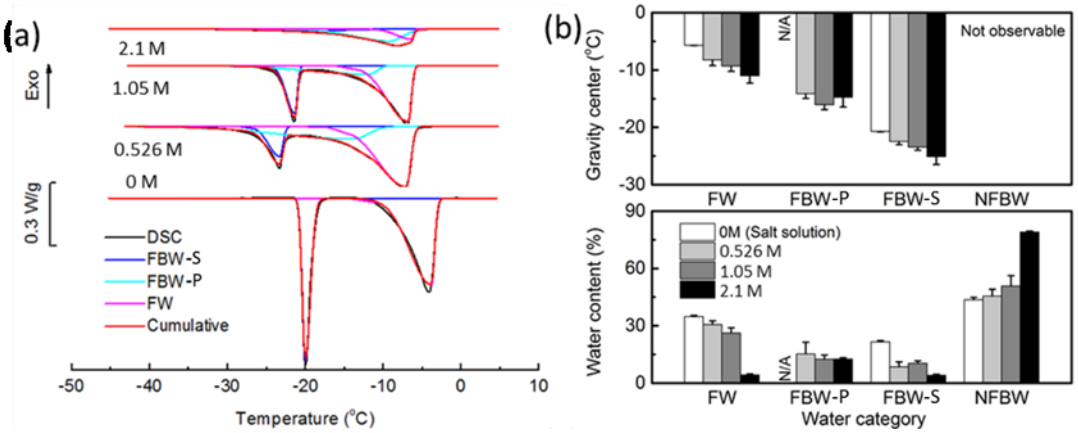

Figure 5.6 (a) DSC profile evolution with different monomer concentrations (i.e. different water-to-polymer ratio) at a fixed UV radiation time and salt concentration (10 wt% NaCl solution, PA-10-0.526(8), PA-10-1.05(8), and PA-10-2.1(8), respectively) and (b) Top: peak centers for FW, FBW-P and FBW-S. Bottom: relative contents of different water states.

5.3.4 The Effect of Dialysis in DIW

Finally, we studied the effect of dialysis in DIW that may be performed to remove excessive salt or unreacted monomers after the synthesis of polyampholyte hydrogels.[22] Here, we investigated the water state in as-prepared, and dialyzed hydrogels. PA-10-2.1(8) was labeled as as-prepared samples. Another batch of PA-10-2.1(8) was dialyzed for one week in DI water (D-PA-10-2.1(8)).

The DSC thermograms of these samples are shown in Figure 5.7a. Figure 5.7b presents the peak centers and amounts of water in the different states of PA-10-2.1(8) and D-PA-10-2.1(8). Comparison between the as-prepared and dialyzed samples shows a dramatic change in the peak centers of FW, which increases from –10.9 ± 1.4 to 1.2 ± 0.3 °C. The change of the peak centers and the absence of FBW–S can readily be understood by the presence and the absence of NaCl salt in the free water. Interestingly, FBW–P is also absent in the dialyzed polyampholyte. These results mean that the water in the water-rich domains of the dialyzed sample behaves like pure water. Notably, the content of NFBW also drops from 78.6 ± 1.3 % to 18.5 ± 4.9 % after the dialysis. The DSC results suggest that salt ions are essential to screen charges of the polymer chains and thereby prevent electrostatic attraction between the polymer chains. Dialysis leaches out the salt ions and as a result highly charged polymer chains with opposite charges collapse together in an

irreversible way.[251] In other words, the polyampholyte chains are 'zipped' and the water and the polyampholyte phase separate in the hydrogel.[22] Further discussion of the D-PA-10-2.1(8) and its SEM images is given in Appendix (Figure A1).

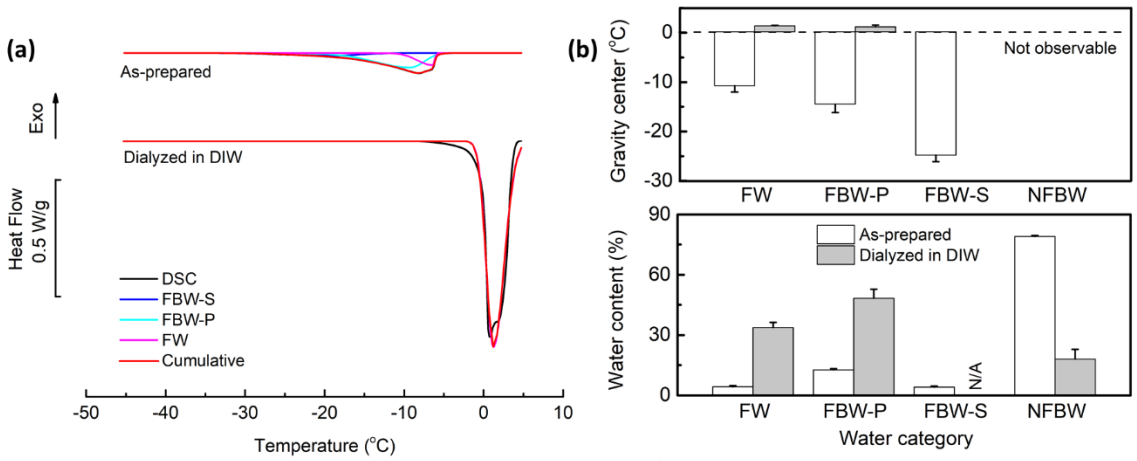

Figure 5.7 (a) DSC curves of polyampholyte hydrogels and their deconvolution fittings for PA-10-2.1(8), D-PA-10-2.1(8), and R-PA-10-2.1(8). (b) Top: peak centers for FW, FBW-P and FBW-S. Some peaks are not available due to lack of corresponding component. Bottom: relative contents of each water state.

5.4 Conclusion

In summary, through quantitative DSC analysis, we propose a differentiation of the water states in charge-balanced poly(NaSS-*co*-MPTC) polyampholyte hydrogel into the following four categories: FW, FBW–P, FBW–S, and NFBW. Different synthesis conditions may change the ice amount in the polyampholyte hydrogel, which is critical for the application as energy storage devices working at low temperature. Future studies on the relationship between the structure and the phase behavior of enclosed water can expand the horizon for low temperature applications of tough hydrogels. As one example of the applications, we harnessed the low temperature properties of polyampholyte hydrogel to develop an aqueous gel electrolyte material for a supercapacitor that performs excellently at low temperatures, such as –30 °C.[157]

Chapter 6 Highly Flexible, Multipixelated Thermosensitive Smart Windows Made of Tough Hydrogels

6.1 Introduction

Materials that can switch light absorption, scattering, and transmission properties in response to external stimuli offer new mechanisms to create smart windows for privacy, comfort, and energy efficiency.[38,39,40] The switching is typically triggered by electric field (*e.g.*, electrochromic control,[252] crystalline phase control,[253] *etc.*) or light intensity (photochromic).[252] For example, electrochromic materials, which often exist as a thin coating layer in smart windows, change their oxidation states as a function of externally applied electric field, whereas the oxidation state modulates the optical properties of the layer.[42,43] However, it requires continuous operation of such windows under the field, which is not energy efficient; in addition there are the issues of cost and long-term stability of the electrochromic materials. Therefore, a smart window that can passively modulate its transparency as a function of the environmental temperature (*i.e.*, thermochromic) is highly desired for energy-saving operation.[44] For example, one can design a smart window that can take advantage of the solar radiation (typically 0.3−2 μm in wavelength) into the building when the outside is cold, but block it when it is scorching hot. Metal oxide nanoparticles, such as vanadium oxide (VO_2) that have been utilized in electrochromic smart windows,[44] have been extensively explored as a potential candidate material for this purpose. In addition, the thermochromic VO_2-based thin films can block near-infrared light at temperatures > 40 °C, and thus can save energy for air conditioning in hot weather.[45,46] However, it remains challenging to balance the useful transition temperature and the degree of transparency change.[39,47] Another drawback of oxides is that they require a tightly sealing encapsulation layer to prevent oxidation from the environment,[48,49,50,51] which will change the optical properties, thus limiting the fitting and sizing of such smart windows for different built structures.

Recently, it has been shown that simply stretching and releasing a composite elastomer film offers a dramatic change in optical transmittance in the visible wavelength range.[254,255] It is also possible to achieve a fast response (~15 s/half of cycle) by stretching porous elastomers consisting of a surface-infused liquid.[256] Here, we exploit temperature induced phase separation in tough

hydrogels to create thermosensitive smart windows, whereas the elastomeric nature of the hydrogel films offers morphological flexibility in fitting variably sized windows.

Hydrogels or ionogels can contain a large amount of liquid in the polymer network while allowing for mechanical deformation without leakage. Recently, poly(N-isopropylacrylamide) (PNIPAAm) hydrogel has drawn much attention due to its unique combination of stretchability and thermochromism (*e.g.,* by forming VO_2 composite).[52,53,54,55,56] Specifically, it undergoes a transition from transparency to an opaque state upon heating above the lower critical solution temperature (LCST, ~32 °C), which is suitable for the smart window application.

Recently, researchers blended a small fraction of PNIPAAm as a nanoscopic aggregation in a self-healing gel matrix to achieve rapid switching from transparency to opalescent states within ~30 s.[56] Most synthetic hydrogels, including PNIPAAm, are intrinsically brittle and the mechanical integrity of such a layer over time is of concern. Therefore, development of a tough hydrogel that can overcome such limitations will allow us to achieve superb tear-resistance, stretchability, and self-healing ability.[12,8,60,61,17]

Polyampholyte hydrogels (PAHs), where the polymer networks are associated by ionic bonding between oppositely charged units in their backbone chains, are intrinsically tough, stretchable, and self-healing.[17] They have been used as absorbents in wastewater metal removal,[26] tissue adhesives,[27] and electrolyte for supercapacitors.[28] PAH exhibits a reversible optical transition from opaqueness to transparency upon heating above the upper critical solution temperature (UCST). This is because water and the polymer chains phase-separate at temperatures below the UCST to form macroscopic water-rich and polymer-rich domains. As Mie's theory states, the larger macroscopic water-rich domains scatter electromagnetic light to provide optical opaqueness; meanwhile, the smaller domains, or even a homogeneous medium, transmit most of the light transparently.

In this work, we introduce a new design of a thermosensitive smart window based on PAH. At a high temperature (*i.e.,* during the day), our PAH is transparent so that visible light can transmit. At a lower temperature (*i.e.,* at night), our PAH blocks the visible light, and the transmittance of mid-infrared (mid-IR) radiation (3−40 μm in wavelength, corresponding to the black body radiation at an ambient temperature) also decreases. Black body radiation through a window is a significant source of heat loss from a building.[257] Accordingly, our PAH-based smart windows

operate like regular windows during day time with high transparency, but become opaque at nighttime, allowing for privacy, and, more importantly, heat retention within the residence. By adjusting the monomer compositions in the PAHs (*i.e.,* molecular doping), we fine-tune the UCST to between ~25 and ~55 °C to reflect the typical daily temperature fluctuation within a building. Further, we fabricate a proof-of-concept, multipixel active smart window by integrating an array of stretchable heaters and with the PAH layer encapsulated by acrylic elastomers. The PAH conforms and adheres to the contour of various elastomer sheets when subjected to a large degree of stretching and twisting.

The fabrication of thermosensitive smart windows based on PAH can be described in two stages. In the first stage, PAHs with finely tuned cloud points were synthesized and characterized. They can be used alone as passive windows that change their transparency according to the surrounding temperature. In the second stage, a stretchable heater was integrated to the PAH to form an active device that is capable to adjust the transparency by tuning the temperature of the PAH layer.

6.2 Experimental Methods

PAH Synthesis. For polyampholyte hydrogel synthesis (PAH), we followed a protocol one-step random copolymerization developed by Gong *et al*.[17] sodium 4-vinylbenzenesulfonate (NaSS), (3-(methacryloylamino)propyl)trimethylammonium chloride (MPTC), [2-(acryloyloxy)ethyl]-Trimethylammonium chloride (DMAEA-Q), N,N'-methylenebis-(acrylamide) (cross-linker, MBAA) and 2-hydroxy-4'-(2-hydroxyethoxy)-2-methylpropiophenone (photoinitiator) were purchased from Sigma-Aldrich and used as received. The aqueous solution of 1 M NaSS, (1–*x*) M DMAEA-Q, *x* M MPTC, 2 mM MBAA and 1 mM photoinitiator was injected into the gap between two glass plates, where the gap was separated by a Teflon spacer (thickness 0.5 mm). For the characterizations of hydrogel optical properties, no polydimethylsiloxane (PDMS) film was attached to the glass plate as the substrate. However, for the smart window fabrication, a PDMS film was attached to one glass plate as the substrate for the PAH. A 4-hour irradiation with a UV lamp (22 mW/cm^2 broadband light with a maximum peak at 365 nm; Jelight, US) transforms the precursor solution into PAH. After the polymerization, PAH was peeled off from the glass plate, and then dialyzed in abundant deionized water (DI water) 12 h.

PAH Sample Characterization. A lab-made laser measurement system (as illustrated in Figure 6.1) was used to characterize PAH. A focus adjustable laser diode module (635nm, 4.5 mW, CPS635F, Thorlabs) was employed as the light sources in the system. Two photodiodes (PDB-C160SM, Luna Optoelectronics) connected to the data acquisition device (USB-6009, National Instruments) were installed at 0 and 75° to the laser beam axis to acquire the transmitted light, and scattered light, respectively. PAH samples (0.5 mm thickness) were kept in the temperature-control unit with 0.2 mm CaF_2 windows (TS102G, Instec Inc.) during the measurement. For the static temperature tests, samples were held at the desired temperature for 10 min before the measurement. For the dynamic temperature test, the signals were continuously acquired under programmed heating and cooling cycles between 15 °C and 65 °C at the ramping rates of ±5 °C/min, ± 10 °C/min, and ± 20 °C/min. The UV-vis transmittance spectra of PAH samples (0.5 mm thickness) were obtained on a NIR-UV spectrophotometer (Perkin-Elmer). The IR transmittance spectra were obtained on a Fourier transform infrared spectrophotometer (FTIR, Nicolet 8700, Thermo) with a temperature-control unit. In both UV-vis and FTIR measurements, samples were held at the desired temperature for 10 min before the measurement and the spectra upon heating were acquired. For the SEM sample preparation, two pieces of PAH-03 samples were kept at 20 °C and 55 °C on the hotplate for 5 min, and quenched in liquid nitrogen immediately, followed by freeze-drying in a freeze dryer (Super Modulyo, Savant). The water content of PAH was calculated based on the mass difference of pristine samples and freeze-dried samples. The morphologies of freeze-dried samples were investigated by field emission SEM (Sigma, Zeiss), after coating with a 10 nm gold layer by a gold sputter unit (Denton, US).

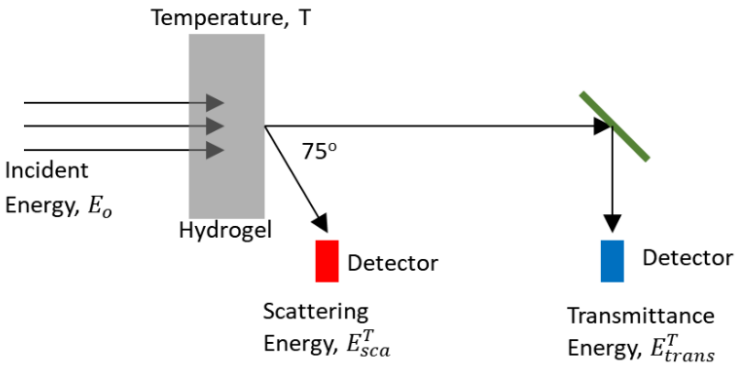

Figure 6.1 The setup of laser light scattering intensity measurement. The temperature of PAH with thickness of 0.5 mm was controlled from 10 to 70 °C in an interval of 5 °C.

Fabrication of a Temperature Responsive Smart Window. An array of heaters was directly printed by using our developed elastic conductive ink[258] and 3D-nScrypt printer. The printed heater trace had a thickness of 27–30 μm with a width of 250 μm. The diameter of the printer nozzle was 200 μm. After printing, the conductive traces were annealed at 110 °C for 2 hours, to vaporize all solvent left in the ink. To make the ink, we used methyl isobutyl ketone (MIBK) as the solvent. We designed several patterns of the array (as shown in Figure 6.2). The printed heaters were integrated beneath the PAH layer for active switching.

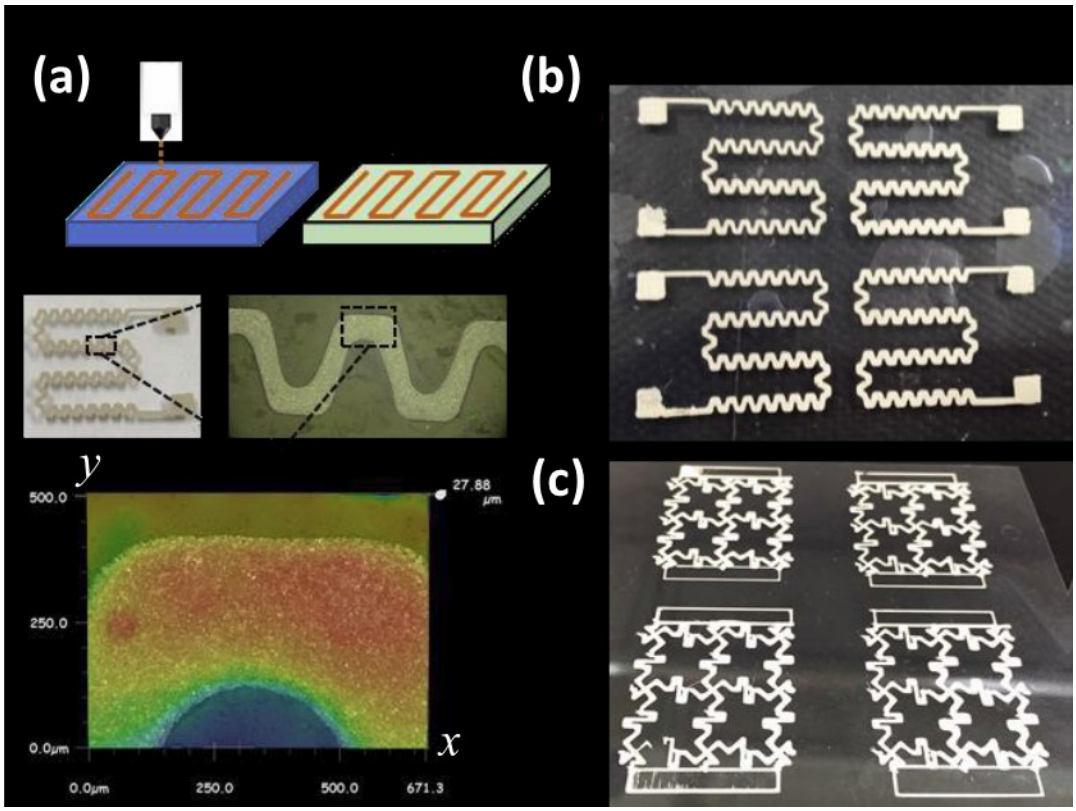

Figure 6.2 Design and fabrication of the stretchable heater array. (a) Schematic of jet-printing of the heater array on PET and transferring it to VHB substrate; and optical photographs and microscopy images. (b) and (c) Two different designs of the stretchable heater array.

In order to keep the merit of PAH as a flexible optical coating material, which will allow easy sizing and fitting into any existing windows, all components in the active device, including the heater and encapsulation layers, are made of elastomeric materials. Figure 6.3a illustrates different layers in the active smart window device. Fluoroelastomeric conducting ink developed

in our lab[258] was 3D printed (nozzle diameter of 200 μm) on an elastomeric polydimethylsiloxane (PDMS) film (0.1 mm thick), which served as the flexible and stretchable heater layer. In our study, the conductive ink showed a resistivity of 1.17×10^{-3} Ω cm at room temperature. The printed region with a cross-sectional area of 9×10^3 μm^2 functioned as a Joule heater when passing a large current. The PAH-03 layer was responsible for the optical switching.

An issue of hydrogel-based materials is the drying-out of water over prolonged operation time, leading to delamination and stability issues. This concern needs to be addressed especially for thermally activated devices. A previous study by Zhao's group addressed the issue by encapsulating hydrogels in elastomers.[259] In our work, the trilayer device (PAH-03/PDMS/ heater) was sandwiched between two layers of commercially available acrylic elastomer, VHB 4905 (3M). VHB is known for high deformability and can form strong adhesion with various electrode materials, including graphene[253] and hydrogel-based ionic conductors.[5,260] In our work, the VHB film offered a moderate adhesion to the hydrated PAH-03 and prevented the drying of water from the hydrogel. Overall, our device was inherently stretchable with each layer adhered to the other. Consequently, the fabricated device could operate under highly deformed conditions, as evidenced by Figure 6.3b (uniaxial strain up to 80%) and Figure 6.3c (twisting deformation). Figure 6.3d illustrates the operation of the active smart window, where the current input through the printed heater modulated the smart window's optical transparency. The adhesion between both elastomer layers (PDMS and VHB) and PAH-03, however, weakened after 3 days under the ambient condition, causing delamination at the interface. Long-term adhesion between the hydrogel and the elastomers will be essential to repeated device operations. It has been shown that tough hydrogels can be chemically anchored on the surface of PDMS,[259,253,260,261,262]

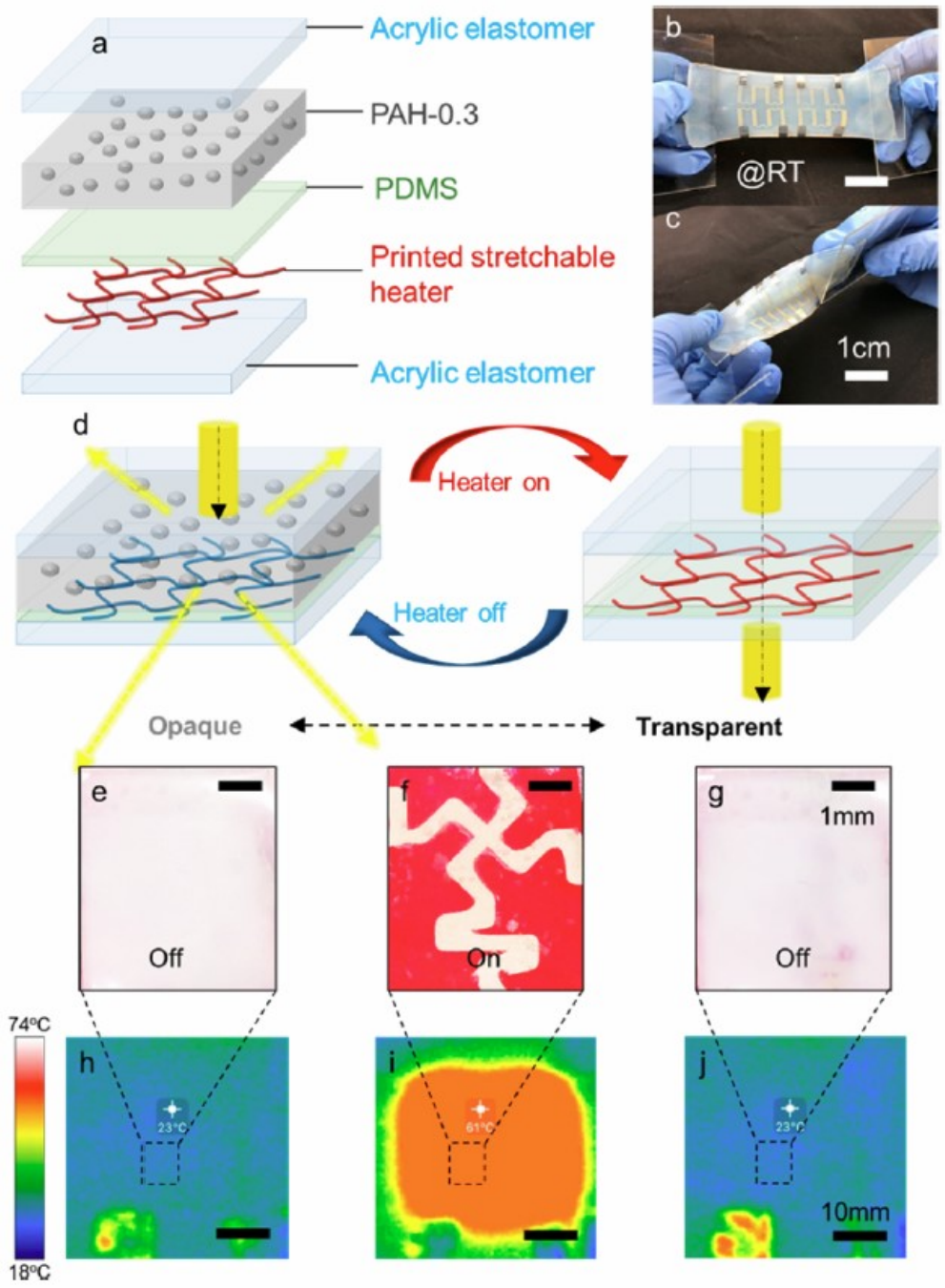

Figure 6.3 (a) Illustration of the individual layers in the active smart window using 0.5 mm thick PAH-03 as an optically functional medium. Top views of the smart window at (b) uniaxially stretched and (c) twisted modes of deformation. (d) Schematic of transparency control of the window by supplying direct current to the printed elastic heater. Simultaneously taken (e–g) optical and (h–j) thermogram images of the device under operation (25 and 45 s for heating and cooling, respectively).

Operation and Characterization of the Smart Window. The active window was activated by controlled direct current, which was supplied by a source meter Keithley-2400. Applied current and true resistance was synchronously measured during the activation. An infrared camera, SEEK Thermal Compact, was connected to a smart phone for thermal imaging of the device. A digital camera was used to capture optical media as the same time of thermal imaging.

Spherical Radius Determination of the Water-rich Domain. The spherical diameter of the water-rich domain was determined by the normalized scattering intensity, which was measured by our lab-made laser scattering measurement system for a wavelength λ = 635 nm at scattering angle θ = 75°. From Equation 6.1,[263]

$$I_{\text{sca}} = \frac{I_0 \lambda^2}{8\pi^2 r^2}[i_1(\theta) + i_2(\theta)] \quad (6.1)$$

where I_0 is the incident intensity, r is the spherical radius of the domains, λ is the light wavelength, θ is the scattering angle, and (i_1, i_2) are the intensity functions of Mie scattering. The formula for the normalized scattering intensity is obtained as $\overline{I_{sca}} = \overline{i_1} + \overline{i_2}$. The scattering intensity was known as $I_{\text{sca}} = I_0(1/r^2)\sigma'_{\text{sca}}$ where σ'_{sca} is the scattering cross section. Following Mie's theory,[263] the differential scattering cross section can be determined as $\sigma'_{\text{sca}} = \lambda^2(i_1 + i_2)/(8\pi^2)$, where:

$$i_1 = \left|\sum_{n=1}^{\infty} \frac{2n+1}{n(n+1)}[a_n \pi_n(\cos\theta) + b_n \tau_n(\sin\theta)]\right|^2 \quad (6.2)$$

$$i_2 = \left|\sum_{n=1}^{\infty} \frac{2n+1}{n(n+1)}[a_n \tau_n(\cos\theta) + b_n \pi_n(\sin\theta)]\right|^2 \quad (6.3)$$

with a_n and b_n as Ricatti–Bessel functions; and τ_n and π_n as the angular dependent functions. The infinite series i_1 and i_2 can be solved by Matlab programming numerically.

6.3 Results and Discussion

6.3.1 Controlling Cloud Points of the PAH

The PAH was synthesized from a precursor solution containing an anionic monomer, NaSS, two cationic monomers, DMAEA-Q and MPTC, with the cross-linker, MBAA, and the photoinitiator. After polymerization in a UV chamber, the resulting PAHs, Poly(DMAEA-Q-*co*-

NaSS-*co*-MPTC), were stretchable and tough in thick film form (0.5 mm). All PAH mentioned in this chapter are charge-balanced (*i.e.,* the same amount of anionic and cationic monomers). In addition, the monomer conversion rate of the resulting PAH was examined by ^{1}H NMR spectroscopy, as shown in Figure 6.4. The sample preparation is the following. As-prepared PAH was weighed and dissolved in 4 M NaCl deuterium oxide solution overnight. The same amount of precursor solution for PAH was also diluted in the NaCl deuterium oxide solution. Weighed DSS (4,4-dimethyl-4-silapentane-1-sulfonic acid sodium salt) was added into both solutions as the internal standard substitute. The monomer conversion rate was determined by comparing the integrated peak area in the range of 7 to 5.5 ppm, which are proton signals from the alkene groups in the monomers (NaSS, MPTC, DMAEA-Q, and MBAA). The intensity of peaks were normalized by the most intensive signal from DSS labelled as 1 in both spectra. No obvious peak was observed in PAH spectrum, indicating complete conversion after the polymerization.

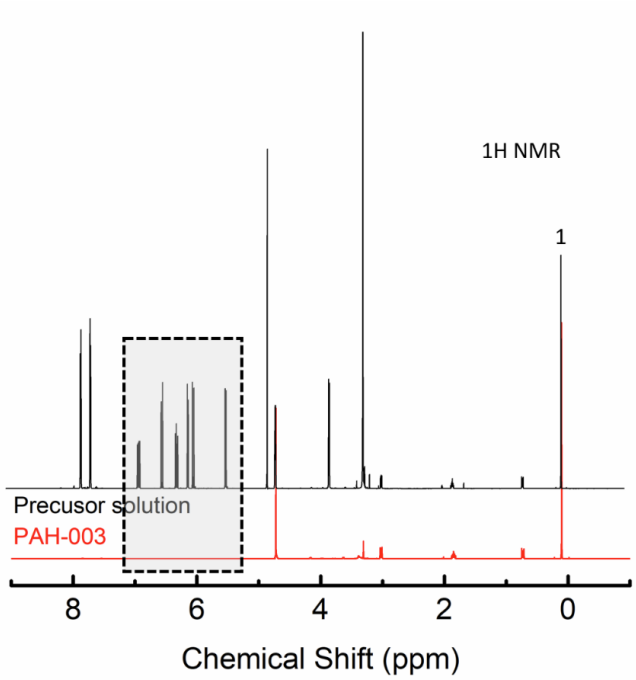

Figure 6.4 ^{1}H NMR spectra of the PAH-03 and the precursor solution (including the monomers NaSS, MPTC, DMAEA-Q, and MBAA) at room temperature.

The PAH with NASS and DMAEA-Q (*i.e.,* no MPTC) was previously shown to exhibit a cloud point of ~15 °C.[62] Here, we adjusted the cloud point of PAHs by tuning the hydrophobicity of the cationic monomers. A small quantity (≤ 0.5 wt%) of the cationic monomer DMAEA-Q was substituted with more hydrophobic MPTC. We refer to this procedure as molecular doping. Our nomenclature of PAH-0*x* indicates that 0.*x* % of DMAEA-Q is replaced with MPTC with respect to the molar concentration of total cationic species. Figure 6.5b shows a drastic transition of visible light transmittance for PAH-01, PAH-03, and PAH-05 with respect to temperature. The transition temperature increased with increasing MPTC content. Here, the driving force for phase separation is attributed to the hydrophobic effect, and thermal energy is needed for water molecules to break the hydrophobic interactions between the polymer chains to form a homogeneous, one-phase structure.[264,125,265] Hysteresis between heating and cooling curves was visible (~6 °C). The two panels in Figure 6.5c represent the transmittance of light (visible to near-IR; left panel) and thermal radiation (mid-IR; right panel) through PAH-03 (0.5 mm thick). Below the UCST, the transmittance values of the light range were < 1% at 20 °C and < 10% at 30 °C, respectively. Above the cloud point, homogenized PAH-03 transmitted a significant amount of the electromagnetic wave: from 60% (400 nm) to 82% (800 nm) at 50 °C and from 74% (400 nm) to 95% (800 nm) at 60 °C. Consequently, the PAH-03 switched from optically opalescent to transparent from 20 to 60 °C (see insets in Figure 6.5d and 6.5f). PAH-03 contained 72.1 ± 4.7 wt% water, which is known for a high level of absorption for mid-IR radiation. Hence, less than 2% mid-IR radiation (3−16 μm) was transmitted at 20 °C and less than 7% at 60 °C.

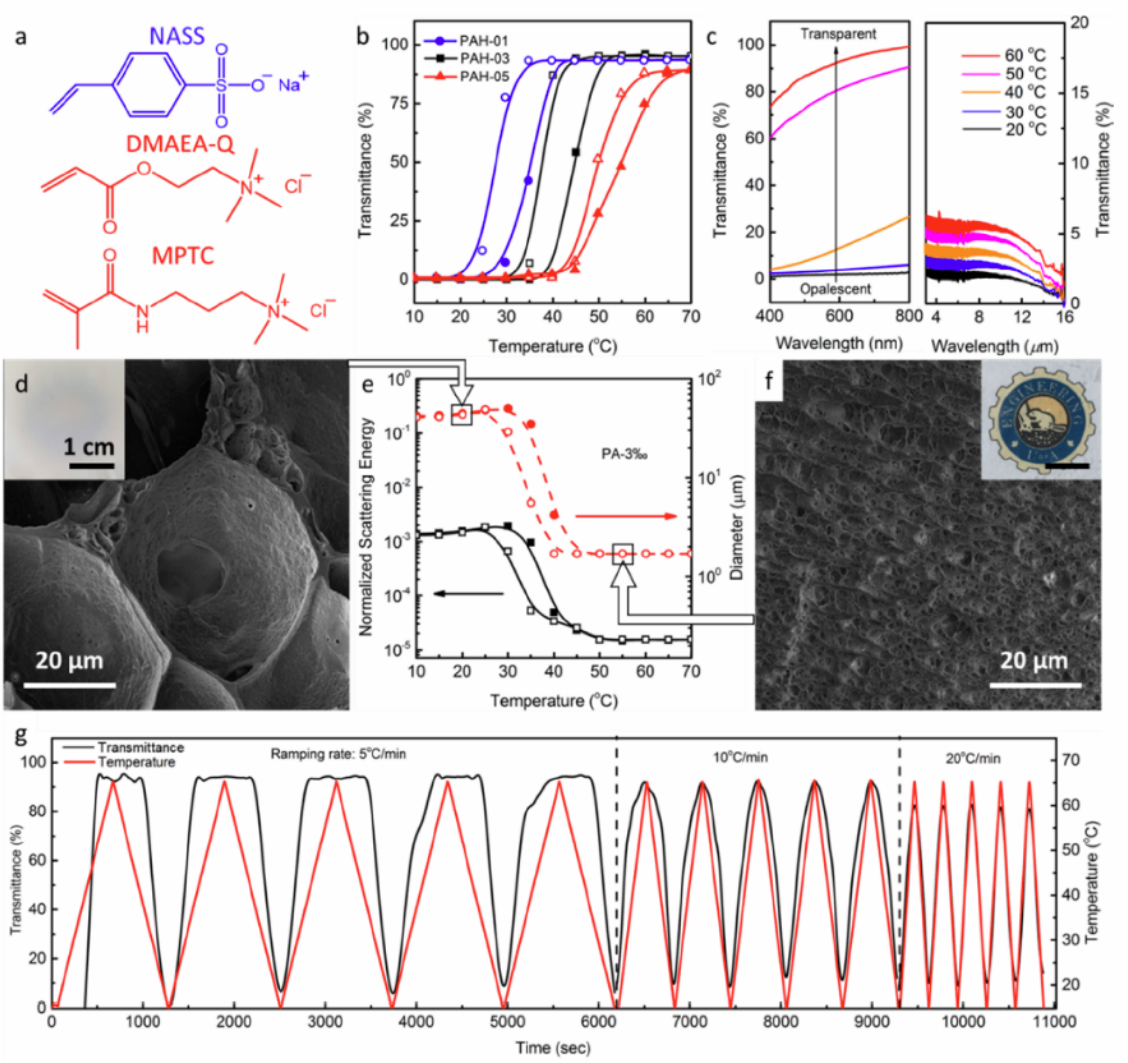

Figure 6.5 (a) Monomers used in the synthesis of polyampholyte hydrogels (PAHs). (b) Optical transmittance (635 nm incidence beam through 0.5 mm PAH films) as a function of temperature for PAH-01 (blue circle), PAH-03 (black square), and PAH-05 (red triangle). Open and closed symbols represent cooling and heating cycles, respectively. Transmittance of the PAH-03 film with respect to electromagnetic wavelength at different temperatures (c) in the optical range (left, visible to near-IR) and in the thermal radiation range (right, mid-IR). Cross-section SEM images of freeze-dried PAH-03 (d) at 20 °C and (f) at 55 °C quenched in liquid nitrogen. The insets are photographs of the U of A Engineering logo coated with the PAH-03 film at respective temperatures (opalescent at 20 °C and transparent at 55 °C). (e) Normalized scattering energies (635 nm laser beam through the PAH-03 film) and respective size of microstructure object (modelled as the diameters of spheres) as functions of temperature. (g) Dynamic optical response of PAH-03 to three temperature ramp rates of 5 °C/min, 10 °C/min, and 20 °C/min.

6.3.2 Phase Separation and Structure of PAH-03

We then investigated the light scattering of the phase-separated domains (wavelength, 635 nm; incidence angle, 75°). Figure 6.5e shows the normalized scattering intensity, which is the light intensity measured at the detector divided by the incident laser intensity measured at temperatures between 10 and 70 °C. As the temperature increased, the scattering intensity (black squares and solid lines) underwent a 2-orders-of-magnitude decrease from 2×10^{-3} (at 20 °C) to 1.2×10^{-5} (at 55 °C). The decrease in scattering intensity at the higher temperature is attributed to the reduced size of water-rich domains. Scanning electron microscope (SEM) images of freeze-dried PAH-03 captured the morphology of polymeric networks at 20 °C (Figure 6.5d) and at 55 °C (Figure 6.5f), respectively. A piece of PAH-03 sample was kept at 20 °C, and another was heated to be at 55 °C for 5 min; both were quenched in liquid nitrogen immediately to preserve the polymer structures in the hydrogel. At 20 °C, bubble-like porous structures (~40 μm in diameter) were observed, representing the macroscopic phase-separated water-rich domains. In contrast, the 55 °C sample appeared to have much smaller (~1 μm) and more homogeneously porous structures. In addition, a differential scanning calorimetry (DSC) measurement was acquired for the PAH-03 at temperatures between 15 and 65 °C (Figure 6.6a). A phase transition of PAH-03 indicated by DSC measurement was observed at 43.4 °C (heating) and 38.9 °C (cooling), values that were close to the apparent cloud point in Figure 6.5b, as determined by the first-order derivative of the transmittance of PAH-03 (Figure 6.6b and 6.6c). The size of the water-rich domains was further deduced from the scattering intensity values in Figure 6.5e. Following the Mie scattering theorem by approximating the water-rich domains as spherical objects, the calculated *r* values are shown in Figure 6.5e (red circles; dotted lines are a guide to the eye). The calculated domain size agrees well with the results from SEM (Figure 6.5d and 6.5f) and optical images (Figure 6.5b−6.5d (inset) and 6.5f (inset)), confirming the UCST between 30 and 40 °C for PAH-03.

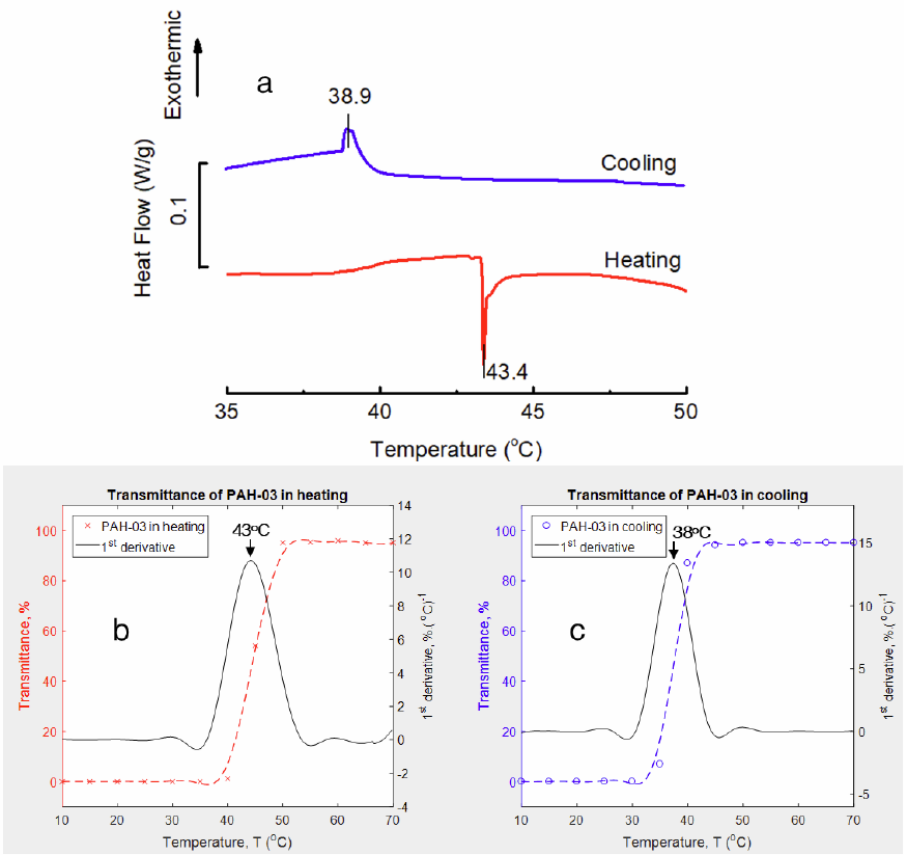

Figure 6.6 (a) Differential scanning calorimetry (DSC) for the PAH-03 in heating and cooling between 15 °C and 65 °C at the ramping rate of 5 °C/min. Transmittance vs. temperature curves and their 1st derivatives of the PAH-03 in (b) heating, and (c) cooling.

6.3.3 Dynamic Optical Response of PAH-03

The transmittance of PAH-03 at 635 nm was measured continuously under programmed heating and cooling cycles between 15 and 65 °C at ramping rates of ±5, ±10, and ±20 °C/min (Figure 6.5g). The triangular functions for temperature control have periods of 20, 10, and 5 min, respectively. The PAH-03 film demonstrated optical contrast values of 85%, 78%, and 67%, respectively. The transitions from opalescence to transparency and *vice versa* were reversible without any noticeable degradation throughout our measurement for more than 100 cycles, which is expected from the phase separation mechanism.

6.3.4 Operation of an Active Smart Window

Figure 6.3h–6.3j shows snap shots of measured hydrogel temperature evolution over a wide area. Figure 6.3e–6.3g shows optical images of a selected spot. At rest, the window as opalescent (Figure 6.3e), and the measured temperature was 23 °C (Figure 6.3h). Upon heating with 0.5A for 25 s, the whole pixel area became optically transparent (Figure 6.3f) while the temperature was equilibrated at 61 °C (Figure 6.3i). After removal of the current input for 45 s, the window went back to complete opalescence (Figure 6.3g), while most of the area was cooled down to 23 °C within the short period of time (Figure 6.3j). The complete switching cycle took 70 s, which is comparable with the fastest switching speed reported in the literature.[56]

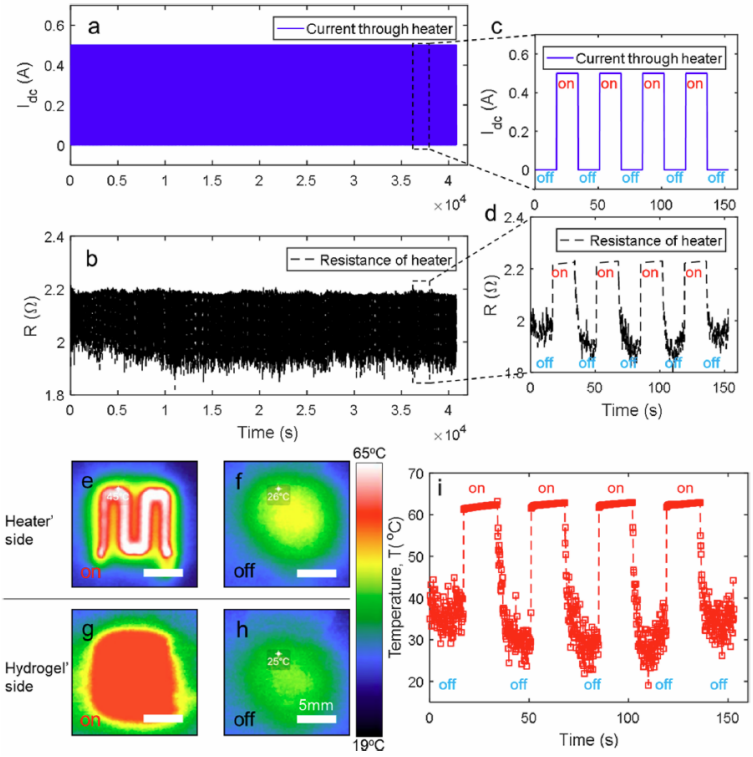

Figure 6.7 Time history of the applied current over (a) ~1000 cycles, (c) 4 cycles after 10 h. Measured resistance of (b) ~1000 cycles, (d) 4 cycles after 10 h of the heater in response to the cyclic current application. Thermograms recorded by a thermal infrared camera: on the heater's side activated by (e) 0.5 A (on) and (f) 0 A (off); on the hydrogel's side activated by (g) 0.5 A (on) and (h) 0 A (off). (i) Calculated temperature of the heater with a temperature coefficient of 4.8 × 10^{-3} /K (see Figure 6.8).

Figure 6.7 shows the electrothermal behavior of the elastic heater, operating under a uniaxial tensile strain of 50%. Here, the smart window was stretched to demonstrate its flexibility

of operation under deformation. We note that the switching mechanism is not related to the deformation. Figure 6.7a and 6.7b shows the thermal response of the heater under a pulse wave of alternating 0 to 0.5 A for > 1000 cycles over more than 10h. The period of the rectangular function was 36 s (18 s each for heating and cooling). Here, the resistance value can be directly converted to the temperature of the heater by using the measured temperature coefficient of our heater material, 4.8×10^{-3} /°C (Figure 6.7d was converted to Figure 6.7i). The resulting temperature distribution in the on and off states was measured by an IR camera from the heater's side and hydrogel's side, respectively (Figure 6.7e–h). The hydrogel side achieved a uniform temperature of ~60 °C by input of a current of 0.5 A for only18 s. After removal of the current for 18 s, the hydrogel film was cooled down to nearly ambient temperature. It should be noted that this time duration does not refer to the speed of optical switching to the level of ~100% transmittance contrast as indicated in Figure 6.5b.

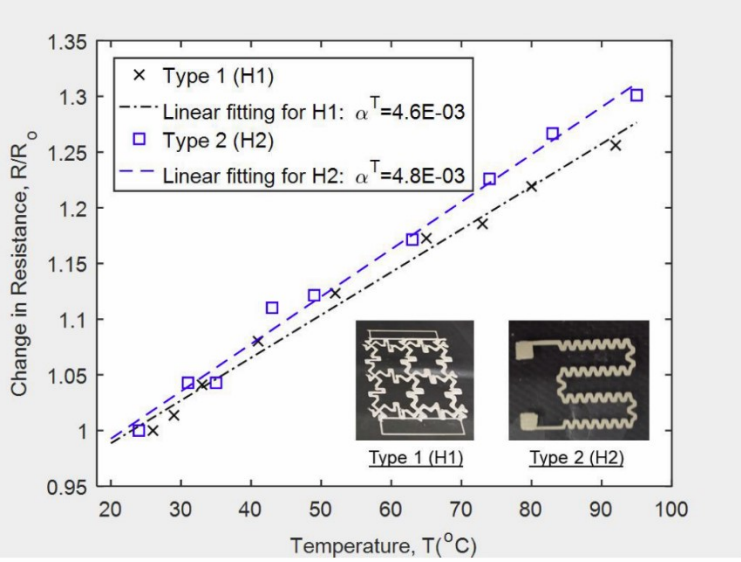

Figure 6.8 Temperature dependent resistance of stretchable heaters. Temperature coefficient of resistance α^T was determined by fitting the temperature-resistance curves linearly, with $\frac{R}{R_0} = 1 + \alpha^T(T - T_0)$ where R_0 is the initial resistance at room temperature T_0, and R is the resistance at elevated temperature T.

We further designed a 2 × 2 array pixelated active smart window. As seen in Figure 6.9a–d, optical and thermal transparency can be individually controlled by the geometry of the embedded

heaters. In future works, such a device can be further optimized by employing transparent heater materials.

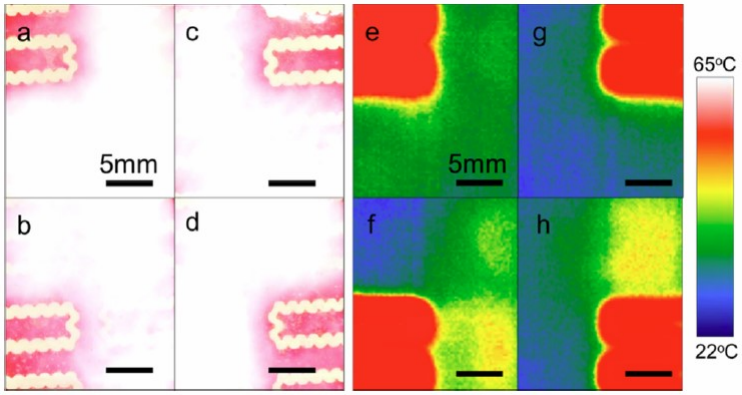

Figure 6.9 (a–d) Optical photographs of the device under pixelated control. (e–h) Thermograms of the heaters under pixelated activation.

6.4 Conclusion

In summary, we developed a flexible smart window from a polyampholyte hydrogel showing 80% in transmittance contrast from opalescence (at a low temperature) to transparency (at a high temperature), which could undergo a large deformation (up to 80% strain). The phase transition temperature of the polyampholyte hydrogels could be fine-tuned by molecular doping of a small amount of hydrophobic monomers into cationic monomers. By printing a stretchable elastic heater layer onto the hydrogel film, we demonstrated a pixelated array of actively tunable smart windows. The thermosensitive smart window we develop can be both passive and active, allowing for applications in different operation conditions. Our window is highly robust against large deformation, a characteristic not possible with a glass window and yet offering a fast switching speed. We believe the study presented here will offer new insights to design smart windows that cannot only change optical transparency but also retain indoor heat at night. Future work is needed to study the IR reflection of PAH, as well as tunability of mid-IR in response to temperature for the energy-saving aspect.

Chapter 7 Flexible and Self-Healing Aqueous Supercapacitors for Low Temperature Applications: Polyampholyte Gel Electrolytes with Biochar Electrodes

7.1 Introduction

Enhancing the low temperature performance of electrochemical storage devices is crucial in applications in automobiles, wearable devices, and energy grids in cold climates. At low temperatures (< −10 ºC) such devices suffer various issues, including reduced ion transport due to increased viscosity and embrittlement of polymeric binder components.[266] For electrochemical capacitors, *i.e.*, supercapacitors, low temperature operation is established down to −40 ºC, typically by using organic solvents or ionic liquids with low freezing points.[63,64,65] However, these liquids have other limitations, such as humidity dependent conductivity change, toxicity and environmental contamination when leaked, as well as high flammability and high vapor pressure, which may lead to hazardous explosions if local overheating occurs.[66,67,68,69,70] To mitigate potential hazards, active research is ongoing on aqueous electrolytes for energy storage devices, such as lithium ion[71] or sodium ion batteries,[72] as well as supercapacitors[73] in order to develop safe energy storage devices, but low temperature operation for aqueous electrolytes has not been established. There is a critical need to develop electrochemical energy storage devices that have desirable performance characteristics at low temperatures, with both suitable electrolyte and electrode.

Gel polymer electrolytes, swollen polymers containing electrolyte solutions with proper solvents or plasticizers, possess superior properties such as self-supporting shape and fast ionic transport, properties possessed by solid and liquid electrolytes, respectively. Compared to liquid electrolytes, gel polymer electrolytes are intrinsically free of leakage problems or the need for separators, reducing the requirement for costly special packaging.[74] Poly(vinyl alcohol) (PVA) is one of the widely used polymeric frameworks for aqueous gel polymer electrolytes with proton[75,76] or alkaline doping.[77,78] Potassium hydroxide (KOH) doped PVA hydrogels exhibit high ionic conductivities. However, the low temperature application of aqueous gel electrolytes is limited due to monolithic ice formation. Hydrogels from polyampholytes—polyelectrolytes containing

both anion and cation groups in a single chain—possess desirable structural properties found in gel polymer electrolytes such as rubber-like elasticity, extreme tear resistance against crack propagation, self-healing ability and self-adjusting adhesion.[17,18,25] In addition, our parallel research showed that polyampholyte hydrogel electrolyte maintains mechanical flexibility at very low temperature by slush-like ice formation; thus we envision making robust, flexible, and eco-friendly aqueous energy storage devices suitable for cold climates.

Carbon-based materials have been of intensive interest as electrodes for making energy storage devices. While activated carbon from coconut shell is the current gold standard in the supercapacitor industry,[267] carbon nanotubes and graphene have been extensively studied.[268,269] While most research focuses on nanostructure optimization for maximizing capacitance density by efficient ion transport and sieving, the key issue for industrial application lies in the optimal balance between material production cost and performance. In addition, low volumetric energy density caused by 'fluffiness' impedes the use of alternative carbon sources for making energy storage devices.[267]

Biochar (BC) produced from agriculture waste by slow pyrolysis at low temperature (400~700 °C) has attracted attention for soil fertility improvement, carbon sequestration and water purification.[84,85] Recent studies show possibilities of using biochar in energy storage devices.[86,87,88] Pure BC is not suitable as an electrode material for three reasons: low specific capacitance, the powdery nature of the material, and low electrical conductivity. Nitric acid treatment and thermal flashing can increase the specific capacitance of exfoliated biochar electrodes from 2.1 to 221.3 F/g.[87] Structural integrity and electrical conductivity are remedied by adding polymeric binders and conductive additives, respectively. These additional components make up a considerable fraction of the weight of electrodes, resulting in lower energy density and higher device cost.[89,90,91]

In this paper, we report the fabrication of a flexible and self-healing aqueous supercapacitor for low temperature applications using polyampholyte and biochar as base materials for gel electrolyte and electrode, respectively. Specifically, we employed a polyampholyte hydrogel as an electrolyte for electrochemical energy storage for the first time due to its preferable mechanical properties such as stretchability, tear-resistance, adjustable adhesion, and self-healing ability. More importantly, we found that polyampholyte hydrogels (PA) prohibited monolithic ice formation;

this leads to device flexibility in ice-forming temperatures, which will enable low temperature application of aqueous electrolytes as a cost-effective and eco-friendly solution for use in cold climates. For electrodes, we employed a soybean stover-based biochar with 7.5% (wt) reduced graphene oxide (BC-RGO) as a novel high-performance and cost-effective material. Using KOH to provide electrolytic ions, the polyampholyte-based supercapacitor (SC-PA) achieved specific capacitance of 193 F/g at 0.5 A/g with an energy density of 30 Wh/kg at room temperature. At −30 °C, its energy density was 10.5 Wh/kg, which is remarkably higher than that of a control sample (3.4 Wh/kg) consisting of BC-RGO electrodes with an unconfined KOH solution in a cellulose separator as the electrolyte.

7.2 Experimental Methods

***Biochar Preparation*.** Soybean stover was collected from agricultural fields in Korea as a model agricultural waste. The soybean stover was dried (at 60 °C), sieved (2 mm), and then pyrolyzed at 700 °C with a heating rate of 7 °C/min under anoxic conditions.

Fabrication of BC-Treated: BC-pristine was ground and sieved to obtain fine powder (325 mesh). The powder was treated with nitric acid (35% in water) at 75 °C for 4 h, filtered, and rinsed with deionized water and ethanol.[86,87] Drying in a convection oven at 120 °C overnight concluded the fabrication of BC-treated.

Fabrication of BC-RGO Electrodes. BC-treated was added into a graphene oxide (GO) solution (4 mg GO/mL, Graphenea, Spain). Here, 50 mg BC-treated was added to each milliliter of the GO solution. The mixture was cast on a glass plate at 80 °C for quick evaporation of the solvent. The dried BC-GO film was cut into platelet shapes 15 mm in diameter. As described in our previous paper,[270] the BC-GO platelet was reduced by an aqueous solution of L-ascorbic acid (Vitamin-C, 8mg/mL, Sigma-Aldrich, US). The reaction was done with a distillation apparatus in an oil bath at 95 °C. After 4 hours of reaction, the platelet was dialyzed in deionized water to remove remaining ascorbic acid. Then, the platelet was dried for an hour in a convection oven at 120 °C. The mass of each platelet was approximately 10 mg. The reduced platelet is denoted as BC-RGO. After that, the platelet was attached to a Kapton sheet (15 mm diameter, DuPont, US) to conclude the BC-RGO electrode fabrication.

Synthesis of Polyampholyte Hydrogel on a BC-RGO Electrode. For polyampholyte synthesis, we followed a protocol by Gong *et al.*,[17] who developed a one-step random copolymerization of sodium 4-vinylbenzenesulfonate (cationic monomer; NaSS) and [3-(methacryloylamino)propyl] trimethylammonium chloride (anionic monomer; MPTC) with 2-hydroxy-4'-(2-hydroxyethoxy) -2-methylpropiophenone (photoinitiator). The chemicals were purchased from Sigma-Aldrich and used as received. The aqueous solution of 1 M NaSS, 1 M MPTC and 0.001 M photoinitiator was injected into the gap between two glass plates, where the gap was separated by a Teflon spacer (thickness 250 μm). Here, one of the glass plates had an attached BC-RGO electrode. A 2 hour irradiation with a UV lamp (broadband light with a maximum peak at 365 nm; Jelight, US) transforms the precursor solution into polyampholyte hydrogel. The hydrogel is denoted as PA. After the gelation, the BC-RGO/PA pair was peeled off of the glass plate, and then dialyzed in a 3 M potassium hydroxide (KOH) solution for 12 h.

Assembly of Symmetric Supercapacitor. The symmetric supercapacitor was assembled by bonding the two BC-RGO/PA constructs by compression. The self-healing property of the PA facilitated the bonding process. The symmetric supercapacitor was dipped into a commercial room-temperature vulcanizing silicone (Shin-Etsu, Japan) for packaging. The silicone was cured for an hour to conclude the fabrication of the symmetric supercapacitor (SC-PA). A control sample of symmetric supercapacitor (SC-KOH), where the electrolyte is a 3 M aqueous solution of KOH, was also fabricated. In the control sample, the two BC-RGO electrodes are separated by a cellulose paper with macroscopic (~25 μm) open pores.

Characterization of BC-RGO Electrodes. A field emission scanning electron microscope (FE-SEM; Zeiss Sigma) was utilized for the morphological study along with a high-resolution transmission electron microscope (HR-TEM; JEOL 2200FS). X-ray diffraction (XRD) patterns were recorded on a Rigaku RU-200B X-ray diffractometer with a rotating anode X-ray generator using Cu Kα radiation (40 kV, 110 mA). X-ray photoelectron spectroscopy (XPS) was carried out on a Kratos Axis spectrometer with monochromatized Al Kα. The C1s peak at 284.6 eV was used to calibrate all XPS spectra. A Renishaw In Via microscope system was used to collect Raman spectra from samples. A 785 nm diode laser was used as an excitation source. Surface area and porosity were investigated using nitrogen adsorption at 77 K (Autosorb-iQ, Quantachrome Instruments, US). Specific surface area was calculated from the BET adsorption isotherm and pore

size distribution was calculated by Non-Linear Density Function Theory (NLDFT) based on a slit-pore model; the calculations were done with a built-in software (ASiQwin). The electrical conductivity was evaluated with a four-point probe station (Pro4-4400, Lucas Signatone Corporation, CA, US) connected to a Keithley 2400 source measure unit.

Electrochemical Measurements. The BC-RGO electrodes were tested in a three-electrode configuration in 3 M KOH electrolyte, where a platinum counter electrode and an Ag/AgCl reference electrode were used. Cyclic voltammetry (CV), galvanostatic charge–discharge (GCD) cycling and electrochemical impedance spectroscopy (EIS) were performed with an electrochemical station (1285A/1260A, Solartron, UK). The frequency range for EIS measurement was from 0.1 MHz to 10 mHz, where an open circuit potential mode with an AC perturbation of 5 mV was used. The durability of the BC-RGO electrodes was evaluated by applying 5000 successive GCD cycles at a current density of 2 A/g. The specific capacitance (C_s) of the BC-RGO electrode was calculated from the GCD curve using Equation 7.1:

$$C_s = \frac{I\Delta t}{m\Delta V} \qquad (7.1)$$

where I is the GCD current, Δt is the discharge time, m is the mass of the BC-RGO electrode (excluding mass of the Kapton substrate), and ΔV is the potential window after the correction for IR–drop.

The symmetric supercapacitors were tested in a two-electrode configuration. The BC-RGO electrode capacitance was evaluated from the GCD curve using Equation 7.2:

$$C_s = \frac{2I\Delta t}{m\Delta V} \qquad (7.2)$$

Here, the equivalent series resistance (ESR) of the supercapacitor was calculated by IR-drop in the galvanostatic charge–discharge curves as in Equation 7.3:

$$ESR = \frac{V_{\mathrm{IR-drop}}}{I} \qquad (7.3)$$

Two key factors of a supercapacitor, the gravimetric energy density (E) and the power density (P), are evaluated from the discharge curves of the GCD at different current densities using

Equation 7.4 and 7.5:[271]

$$E = I \int \frac{\Delta V dt}{2m} \quad (7.4)$$

$$P = \frac{E}{\Delta t} \quad (7.5)$$

Conductivity values of the electrolyte at temperatures ranging from +20 °C to −30 °C were measured in the cell placed in a Peltier stage (TS102G, Instec Inc.). Figure 7.1 shows photographs of the experimental setup. To ensure that equilibrium was reached at a specific temperature, data were collected after the output became stable. Likewise, supercapacitor performances (CV, GCD, and EIS) at a specific temperature were measured after 10 minutes of stabilization time.

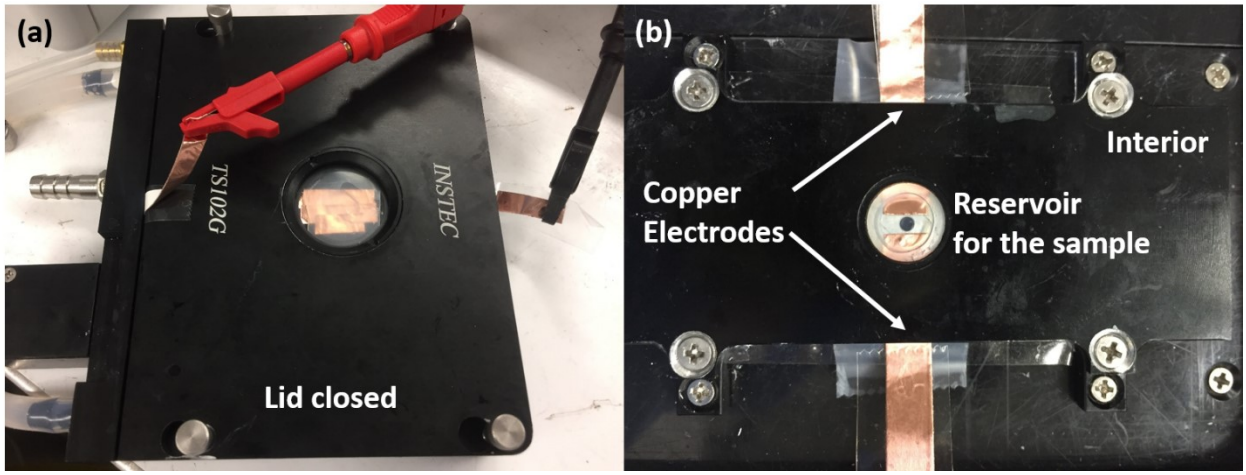

Figure 7.1 (a) Exterior and (b) interior pictures of our experimental setup for ionic conductivity measurement in the range of –30 to +20 °C.

Differential Scanning Calorimetry (DSC) Measurements. The relative amount of freezable and non-freezable water in neat 3 M KOH solution in water and in the solution in the polyampholyte hydrogel (*i.e.*, PA) were quantified by differential scanning calorimetry (DSC, Q1000, TA Instruments, US). The samples were tested immediately after preparation to prevent any possible loss of water through evaporation. For each measurement, 10 mg of sample was sealed in a copper sample pan. For each DSC measurement, the following thermal history was programmed: (i)

temperature held at 10 °C for 10 min, (ii) cooled from +10 to –60 °C at a rate of 1 °C/min, (iii) held at –60 °C for 10 min, (iv) heated to 10 °C at a rate of 1 °C/min. Here, we utilized the data from the heating cycle. The frozen water content can be calculated using Equation 7.6:[176]

$$F_{\text{frozen},T} = \frac{\Delta H_{\text{m},T}}{\Delta H_{\text{m}}^{0}(1-C)} \quad (7.6)$$

where $F_{\text{frozen,T}}$ is the fraction of frozen water at temperature T, ΔH_{m}^{0} is the melting enthalpy of pure water, ΔH_{m}^{0}= 333.5 J/g, and C is the polymer concentration in polyampholyte hydrogel, which is calculated by Equation 7.7:

$$C = \frac{m_{\text{dried}}}{m_{\text{pristine}}} \quad (7.7)$$

where m_{dried} is the mass of freeze-dried hydrogel, and m_{pristine} is the mass of as-prepared hydrogel that contained 3 M KOH solution.

7.3 Results and Discussion

7.3.1 Device Fabrication: an Overview

Figure 7.2 summarizes the procedure for SC-PA fabrication. Pristine biochar processed from soybean stover (BC-pristine) is ground, sieved and acid treated (Figure 7.2a). The treated biochar (BC-treated), however, is still in a powder form and is not electrically conductive. The addition of reduced graphene oxide (RGO) (7.5 wt%) provided a binder to maintain mechanical integrity and a conducting conduit. The composite is bendable and stretchable without powder disintegration, which is a suitable trait for making flexible devices. After bonding the composite electrode to a Kapton substrate (Figure 7.2b), copolymerization of sodium 4-vinylbenzenesulfonate (NaSS) and [3-(methacryloylamino)propyl]trimethyl-ammoniumchloride (MPTC) on the BC-RGO film in a UV chamber synthesizes the hydrogel of poly(NaSS-*co*-MPTC), denoted as PA (Figure 7.2c). Subsequently, the BC-RGO/PA pair is dialyzed in a 3 M KOH solution for 1 day (Figure 7.2d). A symmetric supercapacitor is assembled by pressing together two BC-RGO electrodes without the use of a separator (Figure 7.2e). Figure 7.2f describes the encapsulation process, which concludes the fabrication of the supercapacitor (SC-PA). A photograph of a SC-PA in operation is shown in Figure 7.2g.

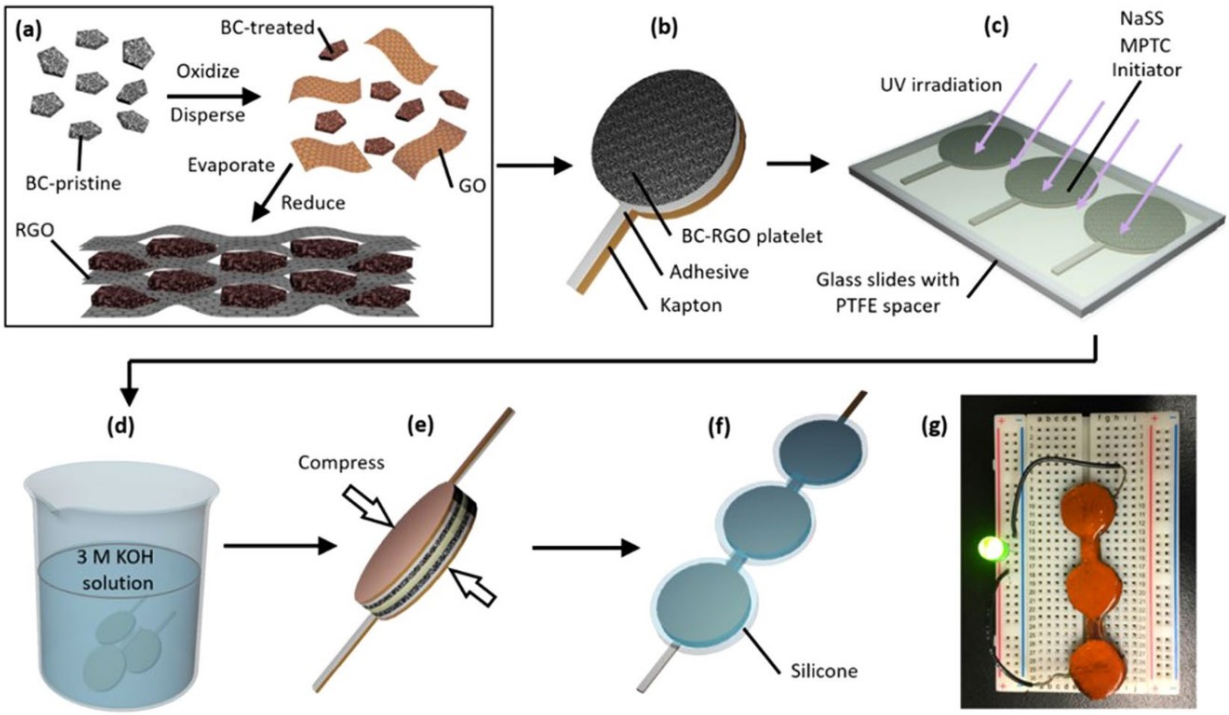

Figure 7.2 Schematic of supercapacitor (SC-PA) fabrication. (a) As-received biochar (BC-pristine) was oxidized (BC-treated) and dispersed in a graphene oxide solution. Subsequent solvent evaporation and graphene oxide reduction result in a consolidated electrode (BC-RGO) with high electrical conductivity. (b) The BC-RGO electrodes are supported on a Kapton substrate. (c) A polyampholyte hydrogel is synthesized on the BC-RGO electrodes by photo-initiated random copolymerization of NaSS and MPTC. (d) The electrolyte is dialyzed in 3 M KOH solution. (e) Compressing the dialyzed electrolyte/electrode pair with the top BC-RGO electrode will make a symmetric supercapacitor. (f) Three symmetric supercapacitors are encapsulated in silicone to light a green LED in (g).

7.3.2 Characterization of BC-RGO Composite Electrolyte

7.3.2.1 Electrode: Morphological Characterization

The morphological evolution of BC was examined by scanning electron microscopy (SEM) and transmission electron microscopy (TEM). The SEM images in Figure 7.3a–d show that the milling and the acid treatment reduced the average powder size of BC from ~100 μm to ~10 μm.

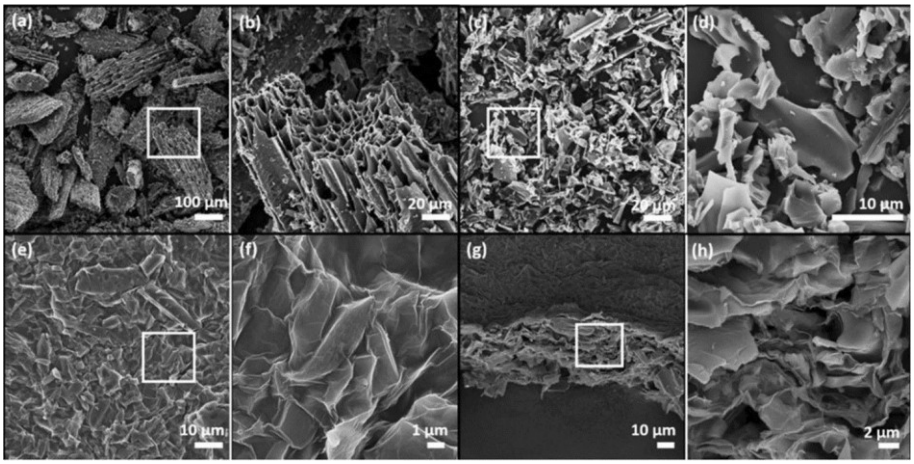

Figure 7.3 (a) The SEM image of as-received biochar (BC-pristine) and (b) a magnified image of the small region identified by the white rectangular box in Figure 7.3a. (c) The SEM image of oxidized biochar (BC-treated) and (d) a magnified image of the small region identified in Figure 7.3c. (e) The SEM image of the top of a BC-RGO electrode and (f) a magnified image of the small region identified in Figure 7.3e. (g) The SEM image of the BC-RGO cross section and (h) a magnified image of the small region identified in Figure 7.3g.

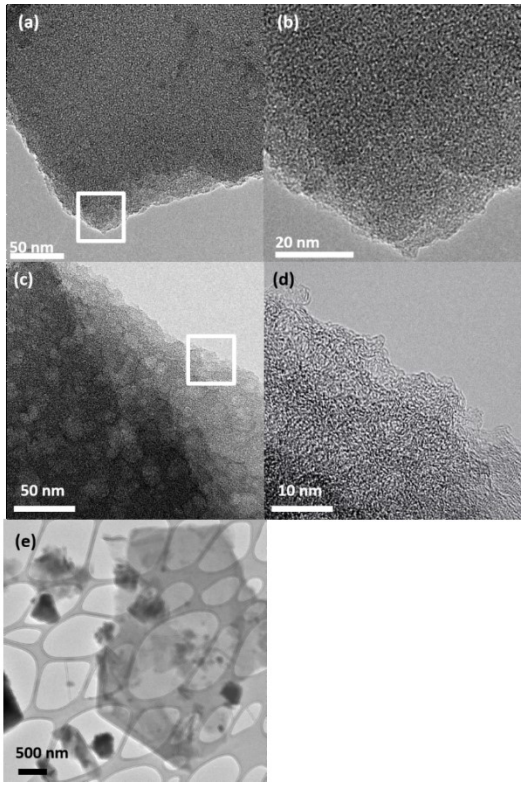

Figure 7.4 High resolution TEM images of BC-pristine ((a) and (b)), BC-treated ((c) and (d)), and low-resolution TEM image of BC-RGO (e). The white rectangles in the low magnification images, (a) and (c), indicate the regions of imaging in (b) and (d), respectively.

For TEM sample preparation, 10 mg of BC-pristine or BC-treated (biochar after the treatment described in the Experimental Section) was added to 20 mL ethanol and sonicated for 10 min. For the BC-RGO electrode (7.5 wt% RGO), the whole electrode was ground into powder before being dispersed in the ethanol. A droplet of the mixture was applied on TEM copper mesh, while any excess amount was removed with Kimwipes. The copper mesh was dried overnight in a convection oven at 120 °C. The TEM images show that the treatment generated an abundance of ~10 nm sized mesopores in BC-treated (Figure 7.4c), which is not found in BC-pristine (Figure 7.4a), with micropores and nanopores that are present all over the BC-treated (Figures 7.4d). The hierarchical porous structure is a clear indication of increased specific surface area. The top-view of the BC-RGO film (Figures 7.3e and 7.3f) highlights that the BC particles were well wrapped by RGO, resulting in structural integrity. The continuous RGO networks also provide electrical conductivity for the electrode. The cross-sectional views of BC-RGO (Figures 7.3g and 7.3h) indicate that the thickness of the electrode is ~40 μm. The BC-RGO contains macropores that can serve as ionic pathways for effective diffusion of electrolytes.[91,82]

The Braunauer–Emmett–Teller (BET) nitrogen adsorption method was used to determine the surface area of BC materials. The adsorption isotherms (volume of nitrogen per gram of BC material at standard temperature and pressure (STP); Figure 7.5a) reveal that the specific surface areas of BC-pristine and BC-treated were 187 and 414 m^2/g, respectively, which is consistent with TEM results (Figure 7.4) and earlier studies on acid treated BC.[272,87] The RGO wrapping further increased the specific surface area to 483 m^2/g. The pore size distribution of the micropores and mesopores were evaluated by Non-Local Density Functional Theory (NLDFT) (an indicator of pore size distribution; Figure 7.5b). For all three samples, there exists a sharp peak at 1.5 nm and a broad peak ranging from 2 to 4 nm, and the peak heights increase from BC-pristine to BC-treated, then to BC-RGO. It is notable that nanometer-scale mesopores (TEM image; Figure 7.4c) and macropores (Figure 7.3h) are also abundant in BC-RGO, indicating a hierarchical porous structure suitable for SC electrodes.[273]

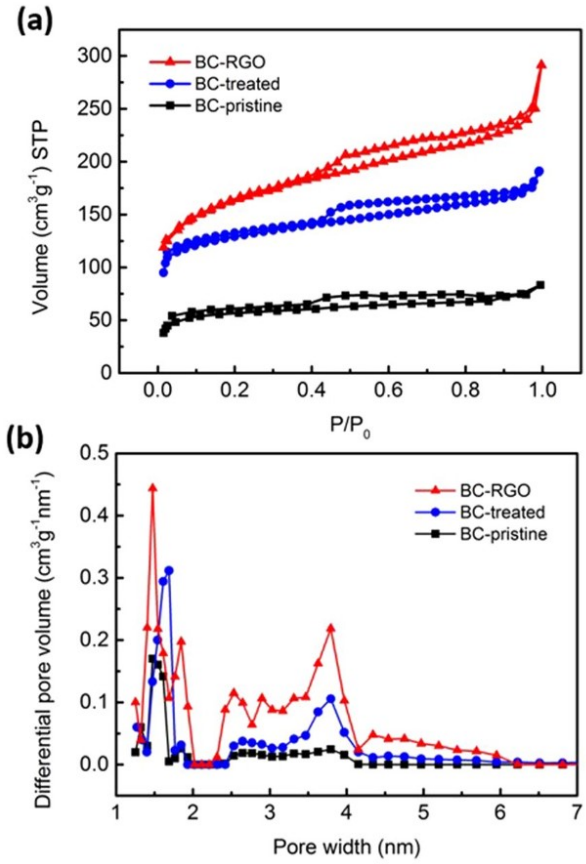

Figure 7.5 (a) Nitrogen adsorption isotherm according to the BET model and (b) Pore size distribution (represented as differential pore volume plotted against pore width) derived from (a), calculated with the NLDFT model.

7.3.2.2 Electrode: Chemical Analysis and Electrical Conductivity

The chemical compositions at the surfaces of samples were investigated by X-Ray Photoelectron Spectroscopy (XPS). As summarized in Table 7.1, the carbon content of BC-pristine was 75.9%, with 2.4% nitrogen and 21.7% oxygen atoms. After nitric acid treatment, the oxygen and nitrogen contents were both increased to 24.0% and 4.6%, respectively. High resolution spectra of N1s (Figure 7.6a) indicate the existence of three main surface nitrogen species, pyridinic nitrogen (~398.5 eV), pyridonic nitrogen (~ 400.2 eV) and nitrate (~407.3 eV).[274,275] The BC-treated samples exhibited dramatically increased nitrate signal compared to the BC-pristine, possibly indicating adsorbed nitric acid after the treatment. After the reduction process by L-ascorbic acid, the peak at ~406 eV disappeared, but a strong peak of surface nitrogen oxide group

was detected in the BC-RGO (the material for the supercapacitor electrode; a composite of BC-treated and reduced graphene oxide). The effect of the acid treatment was further studied by analyzing C1s spectra (Figure 7.6b). The spectral analysis suggests that the BC-treated samples have significant existence of C=O (~288.5 eV) and the amount of C–O bonding was noticeably increased as evidenced by the peak at 285.6 eV.[192] The existence of C–O bonding after the reduction by L-ascorbic acid (~285.8 eV) suggests that there are remaining hydroxyl groups on the surface of BC-RGO; we observed such a trend in our previous work.[270] It is notable that the hydroxyl groups on the surface can increase the apparent capacitance of the electrode by introducing the pseudo-capacitive effect of the quinone/hydroquinone redox pair.[86,81]

Table 7.1 Summary of physical and chemical properties of various biochar (BC) samples.

Samples	S_{BET} [a] [m^2/g]	V_{NLDFT} [a] [cm^3/g]	C% [b]	N% [b]	O% [b]	I_D/I_G [c]	σ [d] [S/m]
BC-pristine	187	0.076	75.9	2.4	21.7	1.7	1.5 ± 0.2
BC-treated	414	0.26	71.4	4.6	24.0	1.6	0.20 ± 0.03
BC-RGO	483	0.35	81.5	0.8	17.7	2.0	531 ± 27

[a] Specific surface area and pore size as deduced from the adsorption isotherms.
[b] Atomic percentage of C, O, and N as obtained from the sizes of XPS peaks.
[c] Intensity ratio between D and G bands as calculated from the Raman spectra.
[d] Electrical conductivity values as obtained from four-point probe measurements.

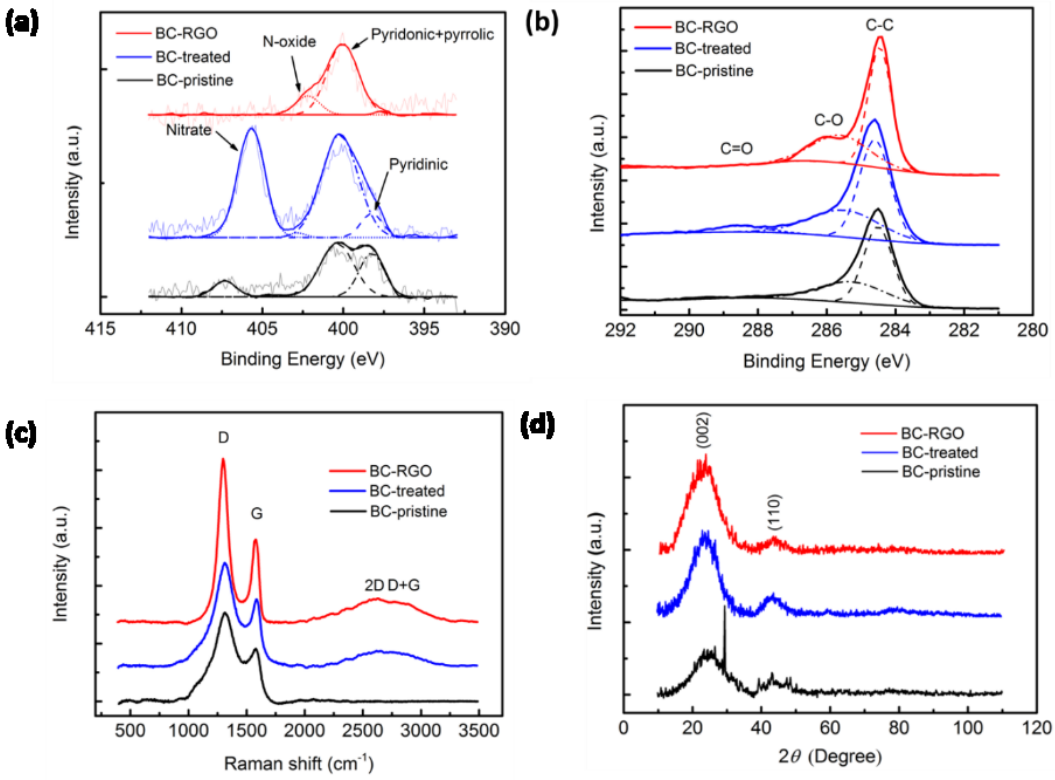

Figure 7.6 Chemical analysis of various biochar (BC) samples. X-ray photoelectron spectroscopy (XPS) profiles near (a) N1s and (b) C1s peaks. (c) Raman spectroscopy profiles. (d) X-ray diffraction (XRD) profiles.

Raman spectroscopy was used to probe the bonding structure of the carbonaceous materials. There are four distinguishable bands presented in Figure 7.6c. First, the D-mode (disordered band) is located between 1330 and 1360 cm^{-1}. Second, the G-mode (tangential mode), which corresponds to the stretching mode in the graphite plane, is located at 1580 cm^{-1}. As the third and fourth bands, the second-order modes, 2D and D+G, are located at 2680–2690 and 2910–3220 cm^{-1}, respectively.[276,277] The relative intensity of the D-mode and G-mode (I_D/I_G) depends strongly on the density of defects in the graphitic material. A larger I_D/I_G suggests a higher density of sp^3 carbon due to structural defects.[277] The values of I_D/I_G decreased from 1.66 to 1.57 after the acid treatment, indicating that the structure of carbon in BC-treated is more ordered compared to that of BC-pristine, probably due to the reduction of impurities that cause the formation of amorphous carbon.[87] The intensities of 2D and D+G are also increasing from BC-pristine, to BC-treated, then to BC-RGO, indicating that the structure became more ordered as the fabrication process proceeded.

XRD patterns of BC-pristine, BC-treated, and BC-RGO are displayed in Figure 7.6d. All three samples showed two broad peaks at around $2\theta = 24°$ and 43°, which are attributed to the (002) and (110) planes of graphitic carbon.[102] It is notable that BC-pristine exhibits a strong peak at $2\theta = 31°$, which belongs to a carbon allotrope with a six-fold helical chain structure whereas the bonding is entirely sp^2 hybridization.[278] Such a 6-fold peak was not observed in BC-treated and in BC-RGO, indicating a purification effect of the acid treatment.

A four-point probe measurement was used to evaluate the electrical conductivities of BC-pristine, BC-treated and BC-RGO. Here, 0.1 g of the powder of each BC was compressed into platelets at a pressure of 10 MPa. The thickness values of the platelets were obtained by cross-sectional SEM. The measured electrical conductivity values are shown in the last column of Table 7.1. The electrical conductivities of BC-pristine and BC-treated were 1.5 ± 0.2 S/m and 0.20 ± 0.03 S/m, respectively. After the introduction of the RGO, the conductivity value is dramatically increased to 531 ± 27 S/m. The moderately high conductivity of the powder material is very similar to the previously reported value for a KOH activated RGO electrode, which resulted in similar electrochemical performance as an electrode material for supercapacitors. The scanning rate could be further increased by decreasing the electrode mass during cyclic voltammetry.[279] This indicates that the RGO network provides an excellent conduit for electrons, and thus can serve as a charge collector in the electrochemical electrode.

7.3.2.3 Electrode: Electrochemical Properties

In order to evaluate the efficacy of BC-RGO as an electrode material for supercapacitors, the three-electrode configuration measurement was performed in a 3 M KOH aqueous solution as a model electrolyte. Here, the BC-RGO was the working electrode, whereas Ag/AgCl and Pt electrodes were serving as the reference and the counter electrodes, respectively. The cyclic voltammetry (CV) results are shown in Figure 7.7a**.** The potential window for each voltage cycle was from –0.9 V to +0.1 V (with respect to Ag/AgCl). Various scanning rates between 5 and 100 mV/s were evaluated. No obvious redox peaks were observed in the selected potential window. Figure 7.7b gives the GCD profile of the BC-RGO electrodes at varying current. The linearity in the output and charging and discharging cycle (the symmetric triangle shape of the output) implies the reversibility and stability of electrode materials during operation. The specific capacitance

versus current density values are shown as the inset in Figure 7.7b; specific capacitance values were calculated from the discharging time. At current density of 0.5 A/g, the specific capacitance of the BC-RGO reached 216 F/g. The specific capacitance decreased as the current increased. One explanation is that the drop in specific capacitance of BC-RGO electrode at high current density was due to the transport behavior of ions in electrolyte when confined in the hierarchical nanostructure of electrodes. At low current density, the ions can efficiently diffuse through the hierarchical porous structure of the BC-RGO electrodes. At high current density, the ionic transport into the nanostructures of the electrode may cause delay in redox interactions (*i.e.,* the charge transport to the electrolyte–electrode interface becomes the rate-determining process). The rather sudden drop of specific capacitance at high current density is an issue for future study; the performance can be further enhanced by finding the right feedstock for the biochar and/or by optimizing the processing conditions for electrode fabrication. The capacitance value normalized by specific surface area was 44.62 $\mu F/cm^2$ at 0.5 A/g. The high surface capacitance was contributed to the abundant surface functional groups, which can cause pseudo-capacitance effects. The hierarchical porous structure of BC-RGO, where macroscopic pores provide a high diffusion path for electrolytes and meso- and nanoscopic pores provide high specific surface area, is also beneficial to make the majority of pores accessible for electrochemical reactions. Moreover, the absence of binder and conductive additives enables the complete use of surface area on the surface of BC-RGO to store electrochemical energy. The Nyquist plot from an electrochemical impedance spectroscopy (EIS) measurement of BC-RGO (Figure 7.7c) comprised a semicircle in the high-frequency region and a linear plot in the low-frequency region. The equivalent series resistance (ESR) obtained by extrapolating the curve from the high-frequency region of the Nyquist plot to intersect the real-axis was only ~ 0.6 Ω. The approximately vertical line in the low-frequency region indicates fast ion transfer in aqueous electrolytes. The CV measurements of BC-RGO in various aqueous electrolyte systems were also performed (Figure 7.7d). The CV profiles show that the BC-RGO electrodes have the highest specific capacitance in 3 M KOH solution.

The results for BC-RGO electrodes with different loading amounts of RGO in the electrode were added as Figure 7.7e. Here, we observed that the BC-RGO provided larger specific capacitance when the electrode contained more BC-treated. The pure RGO electrodes show lower capacitance than those of BC-containing electrodes, and this can be attributed to self-aggregation or re-stacking of RGO sheets. Another point to consider is the mechanical integrity of the resulting

BC-RGO electrode. The electrodes with RGO equal to or less than this critical value were fragile and they were occasionally broken into pieces during the reduction in the ascorbic acid solution. Thus, even though BC-RGO electrodes with 5 wt% of RGO showed better electrochemical performance than those with 7.5 wt% RGO, the devices were fabricated with BC-RGO electrodes with 7.5 wt% RGO in the following parts of this paper.

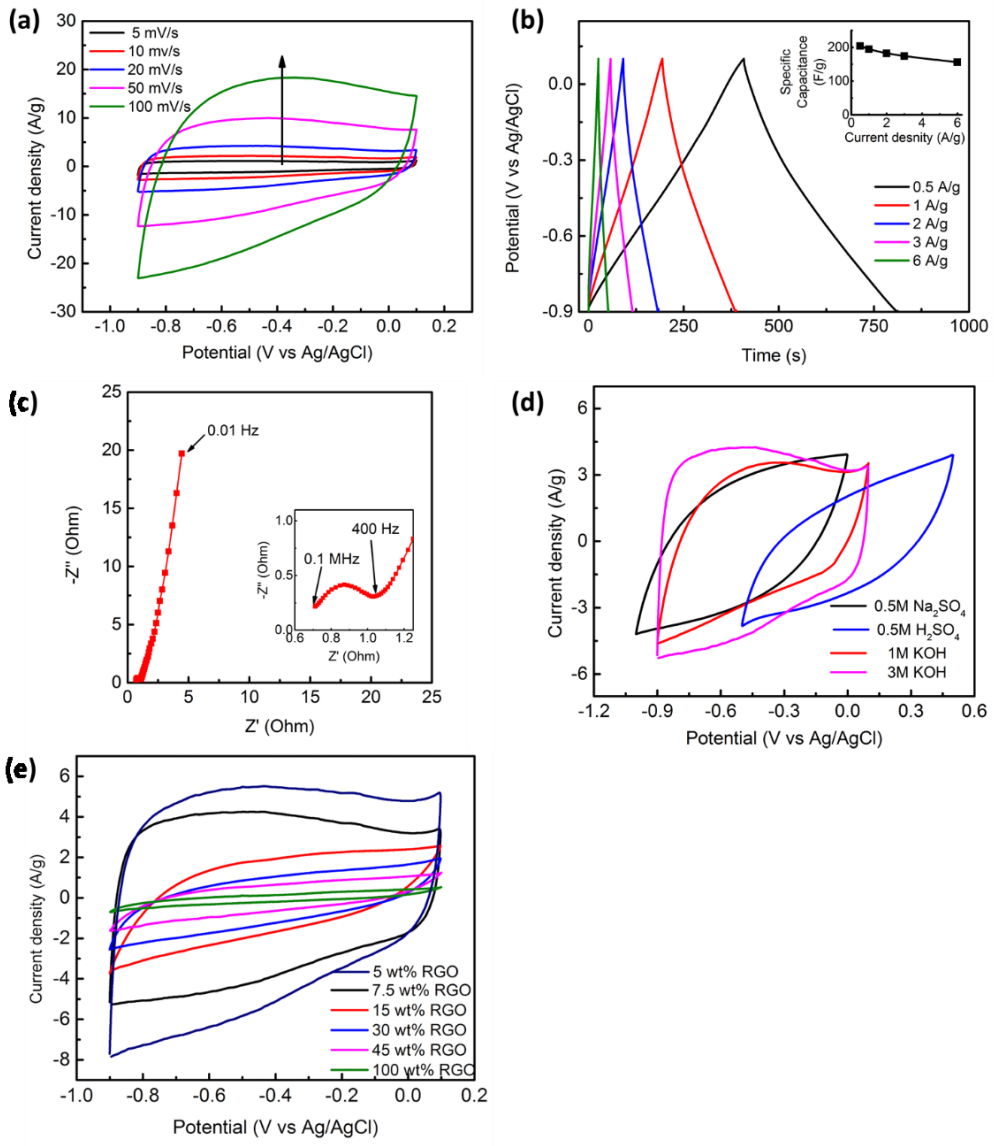

Figure 7.7 (a) Cyclic voltammetry (CV) profiles (b) Galvanostatic charging–discharging (GCD) profiles (inset: specific capacitance verses current density) and (c) the Nyquist plot of EIS measured in 3 M KOH aqueous electrolyte system. (d) CV of BC-RGO in different aqueous electrolytes at a scan rate of 20 mV/s. (e) CV of BC-RGO with different RGO weight percent in 3 M KOH solution at a scan rate of 20 mV/s.

7.3.3 Performance of Polyampholyte Supercapacitor at Room Temperature

In order to evaluate the efficacy of the polyampholyte hydrogel as a gel electrolyte material, we devised a control sample that employs a liquid aqueous KOH solution with a cellulose separator as an electrolyte (SC-KOH; configuration shown in Figure 7.8).

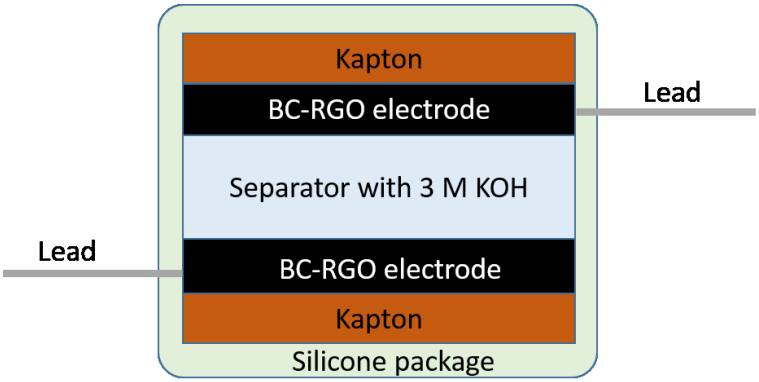

Figure 7.8 Device configuration of SC-KOH.

The polymer, water, and KOH concentrations of control samples were tuned to be same as the polyampholyte-KOH electrolyte, by precisely controlling the amount of KOH solution in the cellulose separator. Figure 7.9a shows the CV profiles of SC-PA with scan rates ranging from 5 to 100 mV/s. The curves display a quasi-rectangular and symmetric shape. Figure 7.9b presents the GCD curves of SC-PA at current densities ranging from 0.5 to 6 A/g. At 0.5 and 6 A/g, the specific capacitances of BC-RGO were 193 and 141 F/g, respectively. At a current density of 2 A/g, a capacitance retention of ~90% was obtained after 5000 successive GCD cycles (Figure 7.9c).

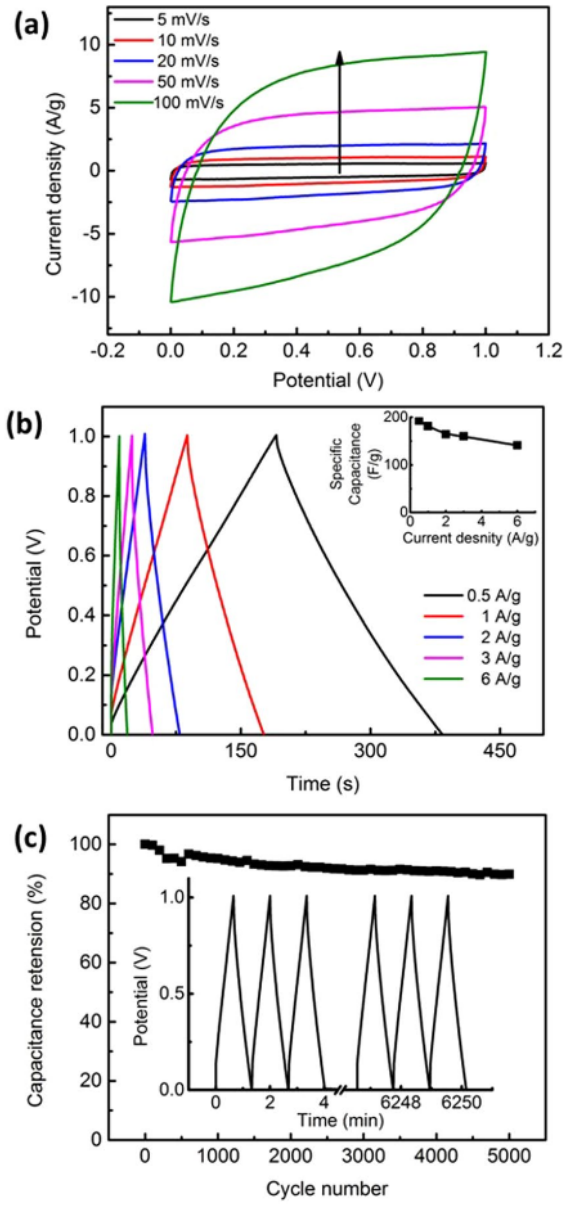

Figure 7.9 (a) Cyclic voltammetry (CV) and (b) galvanostatic charging–discharging (GCD) profiles of symmetric SC-PA KOH (inset: specific capacitance verses current density). The arrow in (a) indicates the direction of increasing scanning rate. (c) Cycle test of the fabricated supercapacitor (SC-PA). The inset presents first and last three galvanostatic charging–discharging (GCD) profiles.

Figures 7.10a and 7.10b show CV and GCD curves of SC-KOH, respectively. Figure 7.10c also compares the Nyquist plots of SC-PA and SC-KOH. ESR of SC-KOH was 0.86 Ω.

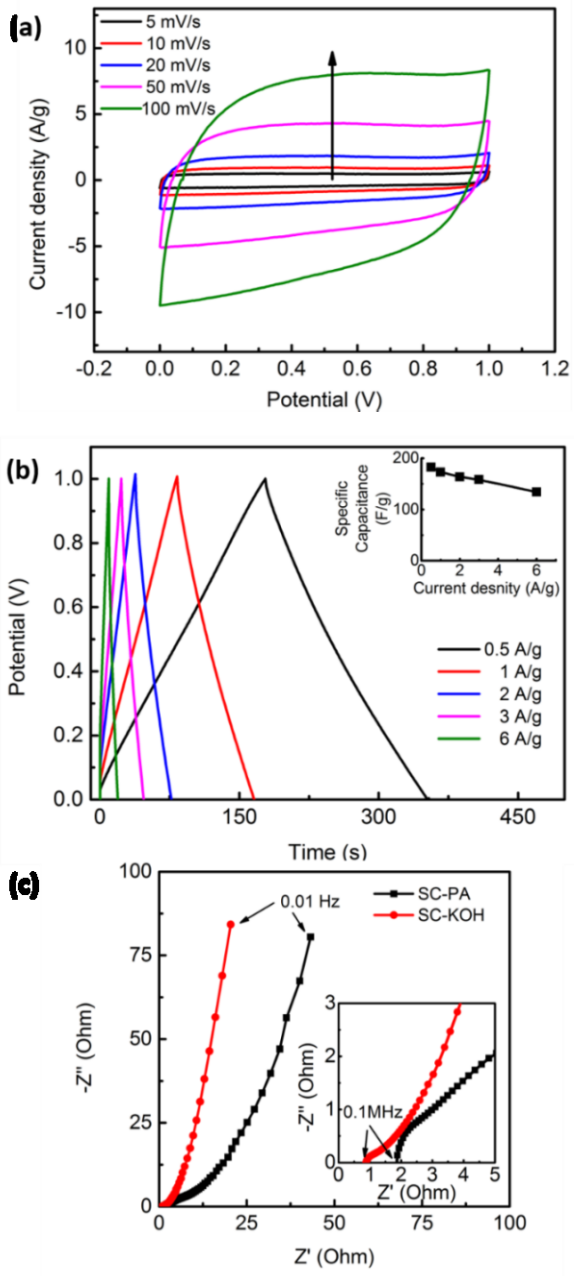

Figure 7.10 (a) Cyclic voltammetry (CV) profiles and (b) Galvanostatic charging–discharging (GCD) profile of SC-KOH (inset: specific capacitance verses current density). (c) Nyquist plot of EIS for SC-PA and SC-KOH.

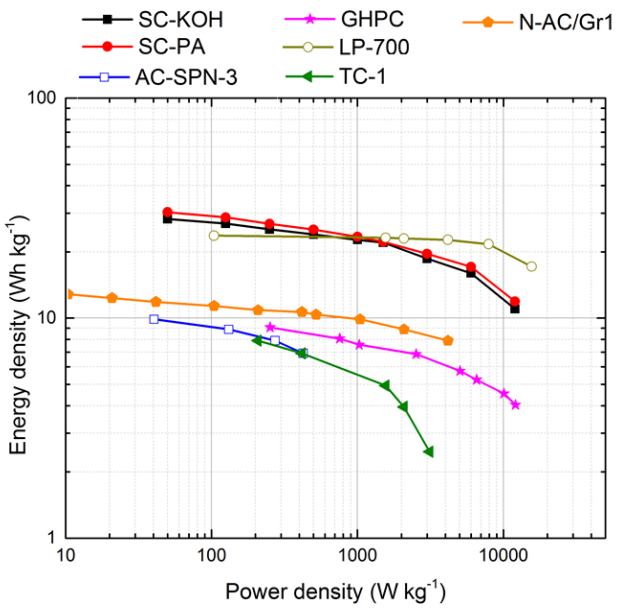

Figure 7.11 Performances of the SC-PA and SC-KOH devices were compared against previously published symmetric supercapacitors in references as AC-SPN-3,[102] GHPC,[280] LP-700,[281] TC-1,[282] and N-AC/Gr1.[283] Here, the references used biomass-derived carbonaceous materials as electrodes whereas the electrolytes were in aqueous solution form.

Energy density and power density are important properties of a supercapacitor. The Ragone plots of SC-PA and SC-KOH are compared with previous studies on biomass-based symmetric supercapacitors with aqueous electrolytes (Figure 7.11). The SC-PA has energy densities of 30.3, 23.4, and 11.9 Wh/kg at power densities of 50 W/kg, 1 kW/kg, and 12 kW/kg, respectively. The energy density of SC-PA is comparable to other published supercapacitors that employ coconut shell-based electrodes (state-of-the-art),[79] as well as other biomass-based electrodes.[102,284] It should be noted that the activated carbon materials mentioned were produced at 800 °C followed by chemical activation, and the values calculated were on the basis of active components in electrodes; typically, 5–20% of the total electrode mass is binders or conductive additives, which do not exist in our device.

7.3.4 Performance of Polyampholyte Supercapacitor at Low Temperature

The performance of the SC-PA was evaluated at temperatures ranging from 20 to −30 °C. Figure 7.12a shows the CV profiles of the SC-PA at different temperatures. The sweep rate was fixed at 20 mV/s. With a decreasing temperature, the area enveloped by the CV curve decreased,

while the increased resistance to ionic transport caused the shape of the cycle to deviate from a quasi-rectangle. Figure 7.12b shows the GCD curves of the SC-PA at a charging–discharging current of 1 A/g. Calculated specific capacitance verses temperature is given as an inset in the same figure. The values were 175, 163, 149, 132, 102, and 75 F/g at temperatures of 20, 10, 0, −10, −20, and −30 °C, respectively. The energy density of the SC-PA was 10.5 Wh/kg at a power density of 500 W/kg.

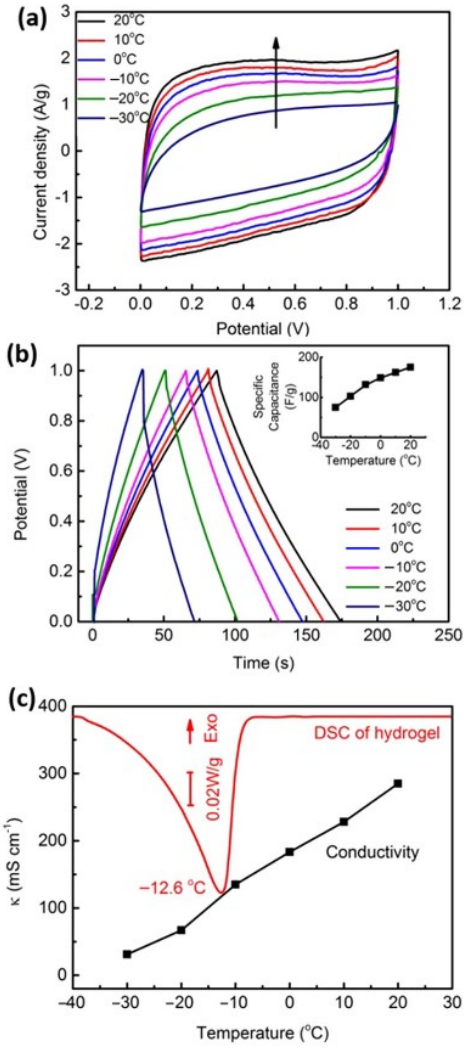

Figure 7.12 (a) Fabricated supercapacitor (SC-PA) temperature dependence of cyclic voltammetry (CV) profiles at a scan rate of 20 mV/s. The arrow indicates the direction of increasing temperatures. (b) Galvanostatic charging–discharging (GCD) profiles at a current density of 1 A/g. The inset indicates calculated specific capacitance with respect to temperature change. (c) A differential scanning calorimetry (DSC) result of 3 M KOH-containing polyampholyte hydrogel with increasing temperature compared with the change in conductivity as a function of temperature.

As indicated by the CV curves shown in Figure 7.13, the specific capacitance of the control SC-KOH was only 24 F/g at −30 °C, where the energy density was 3.4 Wh/kg at a power density of 500 W/kg, which is only 32% of the performance of the SC-PA at the same temperature.

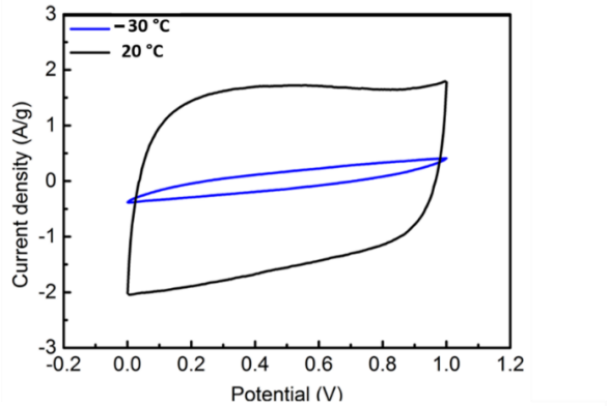

Figure 7.13 Cyclic voltammetry (CV) profiles of SC-KOH measured at 20 and –30 °C. The scanning rate was 20 mV/s.

It is notable that the only difference between the SC-PA and the SC-KOH is the medium that contains the aqueous solution of KOH; the polyampholyte network contains KOH in the SC-PA in a hydrogel form, whereas the separator that is used for the SC-KOH leaves the aqueous solution as a liquid. As mentioned in the previous discussion, the room temperature performance is shown to be comparable to the state-of-the-art values. And the electrochemical performance of the polyampholyte supercapacitor at low temperature was close to the values of other non-aqueous electrolyte supercapacitors reported at temperatures around –30°C, without worries about electrolyte leakage.[63,64,65] The specific capacitance of the activated graphene based supercapacitors in ionic liquid electrolyte was ~100 F/g at a scanning rate of 1 mV/s.[63] And specific capacitances of an ionogel-based solid-state supercapacitor were 68 and 34 F/g operating at –20 and –40°C, respectively, at a scanning rate of 5 mV/s.[285] To our knowledge, a specific capacitance comparable to that of our polyampholyte supercapacitor at subzero temperature has never been reported before in the literature for other aqueous-based electrolyte supercapacitor, or conventional solid-state supercapacitor using PVA-KOH gel or other gels.[269] Plus, due to the unique structure of polyampholyte networks in the hydrogel, the device is still flexible at subzero temperature, which will be discussed later in this chapter.

In order to understand the underlying mechanism of the improvement in supercapacitor performance at −30 °C, we performed a differential scanning calorimetry (DSC) measurement for a polyampholyte that contained the same concentration of KOH as in the SC-PA (Figure 7.12c). It is well known that water molecules strongly adsorbed on hydrophilic polymer chains cannot participate in ice formation, and thus are classified as 'non-freezable water' that can be found unfrozen down to −190 °C.[176,286] Likewise, strongly bound water on ionic species will form hydrated ions and will not freeze as ice, but the hydrated KOH will freeze at its eutectic temperature of −60.9 °C.[287] Based on these assumptions, we froze all 'freezable water' at −60.0 °C for 10 minutes, followed by bringing up the temperature to +10 °C at a slow rate of +1 °C per minute. An endothermal peak started to appear at −39.5 °C, reached a peak at −12.6 °C, and ended at −6.2 °C. The fraction of water molecules that participated in the freezing–thawing cycle was quantified by the area under the peak; here, 23.6% of water molecules were frozen at −60.0 °C. A control experiment with an aqueous solution of KOH held in place with a separator reveals that 30.4% of water molecules were frozen at the same temperature. It is unclear at the moment whether the 6.8% of the water molecules that could not be frozen due to polyampholyte chains accounted for the supercapacitor performance enhancement. The measured ionic conductivity in Figure 7.12c reveals that the conductivity is a strong function of temperature, but the formation of ice is not the only dominant factor determining the change in ionic conduction. One hypothesis for the improved supercapacitor performance, however, is that the morphology of ice is connected to the performance and that the crosslinked network structure of the polyampholyte chains disrupts the crystalline growth of ice. The 'slush ice model' is consistent with the fact that KOH containing polyampholyte hydrogel is still flexible whereas an aqueous KOH solution is a rigid monolithic ice at −30 °C. In our parallel study, we showed that the hierarchical nanostructure of polyampholyte hydrogel allows both polymer-rich (yet highly hydrated) and polymer-poor (yet populated with polymer strands) domains. Vogt *et al.* measured fast dynamics of local diffusivity of water molecules in hydrogel networks at extremely low temperatures (220 K), which shed light to the mechanism of our enhanced supercapacitor performance at low temperatures.[225] Future investigations that identify structure–property relations of polyampholyte hydrogels at low temperatures may shed light on the mechanism.

7.3.5 Mechanical Flexibility and Self-Healing Properties

The pristine SC-PA (Figure 7.14a) was bent to a radius of curvature of 5 mm (Figure 7.14b), showing nearly no degradation in supercapacitor performance (Figure 7.14a). The self-healing ability was tested by cutting the SC-PA into two pieces (perpendicular cut; Figure 7.14c), followed by a self-healing process (Figure 7.14d). Broken SC-PA was stored in KOH solution at 30 °C. The glass slides and PTFE spacer were utilized to align the two broken pieces of the SC-PA. The self-healed SC-PA (Figure 7.14d) showed ~80% of capacitance compared to the control (non-cut) device (Figure 7.14e). The 20% loss of capacitance of the self-healed SC-PA may be attributed to slight mismatch in overlapping of the broken BC-electrodes, resulting in an increase of ESR. As another example of self-healing, the SC-PA was sliced into two pieces by splitting the polyampholyte hydrogel electrolyte in the planar direction (planar cut; Figure 7.15b). After self-healing, the CV result almost exactly reproduced the control sample result, indicating a perfect self-healing (Figure 7.14e). The self-healing ability can be attributed to the reversible nature of ionic crosslinking in polyampholyte hydrogels,[17,18] as illustrated in Figure 7.14f. The bendable and self-healing nature of the SC-PA is promising for wearable and flexible electronics applications of the supercapacitor.

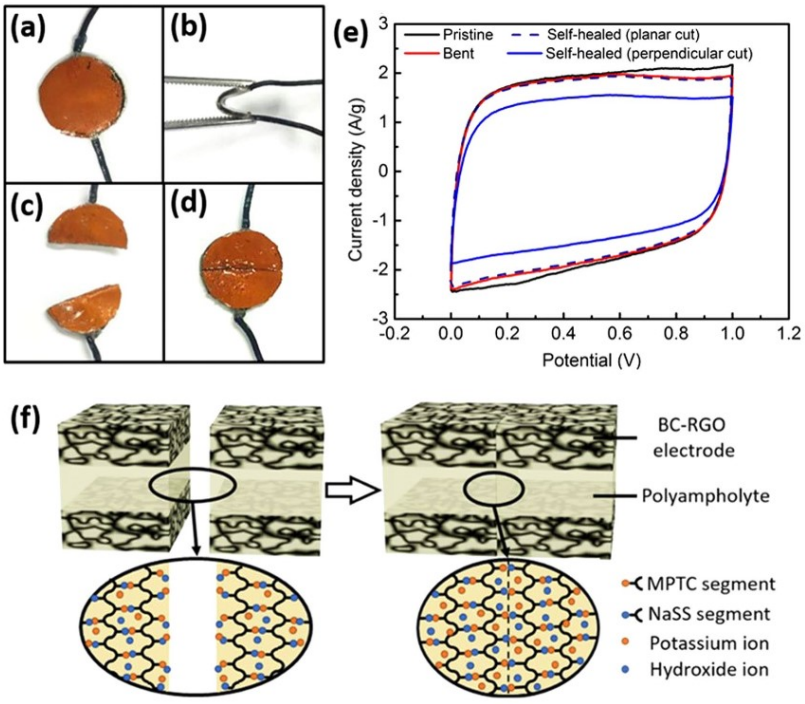

Figure 7.14 Photographs of (a) pristine, (b) bent, (c) broken, and (d) self-healed supercapacitor (SC-PA). (c) and (d) show the procedure for the perpendicular cut. The procedure for the planar cut is described in supporting information. (e) Cyclic voltammetry (CV) profile of pristine, bent and self-healed (perpendicular and planar cuts) SC-PAs at a scan rate of 20 mV/s. (f) Schematic illustration of polyampholyte hydrogel self-healing for the perpendicular cut.

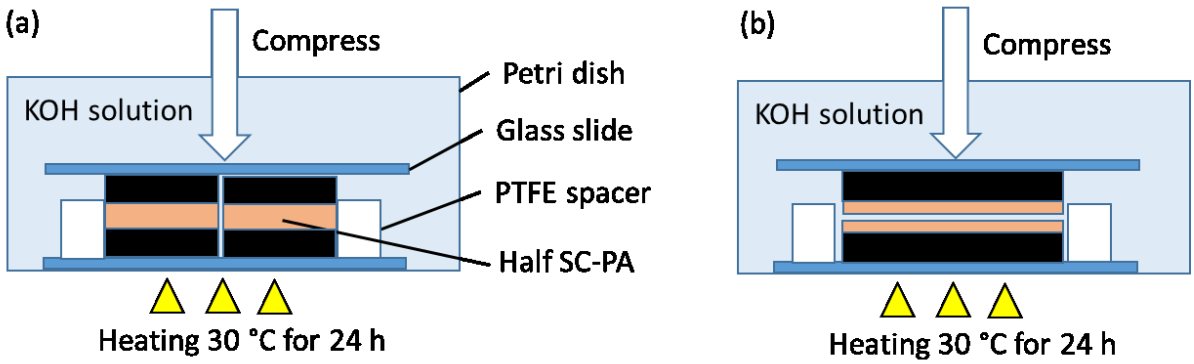

Figure 7.15 The setup for the self-healing of SC-PA. (a) SC-PA was cut into two pieces in the vertical direction (this describes the case for Figure 7.14c & d; perpendicular cut). (b) SC-PA was split into two pieces by slicing the polyampholyte hydrogel layer in the lateral direction (parallel cut).

7.4 Conclusion

A supercapacitor with a high energy density that operates at low temperature was fabricated with a combination of BC-RGO electrodes and a polyampholyte hydrogel. Reduced graphene oxide was incorporated with biochar to transform the pyrolyzed waste biomass into high performance binder-free electrodes for electrochemical energy storage devices. The specific capacitance of BC-RGO was 216 F/g at a current density of 0.5 A/g in the three-electrode configuration. The electrochemical performance can be further improved using biochar with higher specific surface area or by doping transition metal oxide.[288,289,290] A symmetric supercapacitor made with BC-RGO as the electrode and polyampholyte hydrogel as the electrolyte showed a high energy density of 30 Wh/kg, and a capacitance retention of ~90% after 5000 charge–discharge cycles. At low temperature (−30 °C), the SC-PA had an energy density of 10.5 Wh/kg at a power density of 500 W/kg, which is a clear improvement over the performance of SC-KOH at the same temperature owing to the use of polyampholyte as a hydrogel hosting material of the aqueous KOH electrolyte, showing a potential for energy storage, even for grid-scale solutions at low temperature.[291] The flexibility and self-healing properties indicate the possible application of SC-PA in flexible and wearable devices.

Chapter 8 Self-Reinforcing Graphene Coatings on 3D Printed Elastomers for Flexible Radio Frequency Antennas and Strain Sensors

8.1 Introduction

The emergence of the Internet of Things (IoT), in which many living and nonliving objects can access a network to share data, necessitates the development of antenna with various form factors enabled by novel materials.[102] While the antenna component for the IoT must be included without causing a significant increase to the price of the object, a printed radio frequency antenna provides the antenna functionality at an affordable price.[292] Whereas the objects for IoT typically have irregular topography, conventional antennas fabricated on rigid materials do not offer the required form factors and topological conformity to the object. In the wearable healthcare application, which is one of the promising fields for IoT, the objects include human skin, garments, and accessories, to name a few. They often are topographically corrugated and dimensionally stretchable/compressive. It is critical for the IoT, including the antenna component, to offer seamless integration to the objects to collect reliable physiological and kinematic data from human subjects.[293,294] Therefore, it is critical to develop an affordable processing route for the stretchable antenna component with various form factors; 3D printing of stretchable material can be a promising option.

3D printing is a versatile technique that can realize various form factors tailored to meet specific needs for applications.[295] Among various 3D printing techniques, Fused Deposition Modelling (FDM), through which an object with an arbitrary form factor is created within a layer-by-layer deposition by extruding thermoplastic materials, is the most popular option because the required 3D printer is highly affordable. A limitation of FDM is that it can print only thermoplastic polymers that can be extruded upon moderate heating. There are a few flexible or stretchable materials that have been commercialized specifically for FDM.[296] A recently commercialized FDM printable material, GEL-LAY™ filament, provides porous internal structure, which allows mechanical flexibility and significantly enhanced surface area. With a designed post-treatment chemistry, the foamy material can allow 3D printed structures with various functionalities by

coating the interior and exterior surfaces.

A wide range of materials have been employed as conductive inks for printed electronics.[92] Most of these materials require rather harsh post-printing treatment. Such processing caused compatibility problems for many substrates used for flexible electronics, such as paper, plastic sheet, or elastomer, which may denature upon heat and acid treatments. For example, conductive inks based on metal nanoparticles can achieve high conductivity, but require a sintering process at high temperature or other severe chemical or energetic post treatments to remove stabilizing agents or oxide layers. Noble metals allow rather mild post treatment conditions, but they are generally expensive.[94] Conductive polymer is another popular choice, but chemical stability has been a critical issue that prevents widespread use.[95] Carbon-based conductive inks, especially graphene-based inks, have been suggested as a balanced combination between high conductivity, mild processing, and chemical stability.[96]

The dispersion strategies of graphene inks are generally classified into two categories: (1) direct dispersion of graphene in a good solvent such as N-Methyl-2-pyrrolidone (NMP) or dimethylformamide (DMF) without additives[97,98] and (2) employment of binder materials, such as ethyl cellulose, as additives.[99,100] Using the former method, Hu *et al.* inkjet printed a binder-free graphene/NMP suspension on paper, followed by rolling compression to achieve a conductivity value of 4.3×10^4 S/m.[101] A drawback of the method is that NMP, a popular solvent that disperses graphene nanoflakes, typically causes swelling or dissolving of polymer substrates for the printing, leading to distortion or fracture of the printed graphene traces. In addition, the absence of active chemical binding between the graphene nanoflakes causes poor mechanical integrity that may induce the fracture of the printed graphene traces. The latter method that employs binder material can provide enhanced mechanical integrity by covalent bonding. However, the binder compromises the conductivity, thus a thermal post-treatment to decompose the material is needed, which is not ideal for flexible substrates. If the binder material itself is electrically conductive, on the other hand, both electrical conductivity and mechanical integrity can be achieved at the same time.

In this paper, we present a new processing method to fabricate conductive structures with an arbitrary shape factor via 3D printing followed by a carbonaceous conductive layer coating. FDM 3D printing of a commercial rubber/poly(vinyl alcohol) (rubber/PVA) blend filament provides a

facile pathway to generate arbitrary flexible and porous substrate. Then, we utilized reduced graphene oxide (RGO) as a binder material to wrap graphene nanoflakes (GNFs); we named the composite material as GNF-RGO. By the processing method, we fabricated flexible antennas and strain sensors.

8.2 Experimental Methods

Flexible Substrate Fabrication: A PORO-LAY GEL-LAY filament (MatterHackers Inc., USA) was purchased and used as such to print porous 3D structures as a substrate. The filament is composed of polymer blends of PVA and unspecified elastomeric component. After printing, selective dissolution of PVA component in water leaves the elastomeric component with microscopic porous structure. Ultrasonication for 3 days is required for complete dissolution of PVA. An overnight drying in a vacuum oven at 80 °C allows a thorough removal of water. The resulting structure is bendable, foldable, and slightly stretchable with a good shape resilience.

GNF-RGO Coating Fabrication: Graphene nanoflakes (N008-N, Angstron Materials Inc., USA) were used as received. Various amounts of GNFs were added into a graphene oxide (GO) solution (4 mg GO/mL in the water, Graphenea Inc., Spain) to form the GNF-GO suspension. The mixture was cast on a flexible 3D-printed substrate at 80 °C for quick evaporation of the solvent. The substrates with the GNF-GO coating were collected followed by a two-step reduction process. The first reduction step was done with a mild reducing agent, L-ascorbic acid (Vitamin-C, 8mg/mL in the water, Sigma-Aldrich, USA). The reaction was done with a distillation apparatus in an oil bath at 95 °C overnight.[270] The substrates with the GNF-RGO coating were dialyzed in deionized water. For selected samples, the second reduction step was done with a stronger reducing agent, 50 mM $NaBH_4$ in water (Sigma-Aldrich, USA) for 4 h to improve the electrical conductivity,[195] followed by dialysis in the deionized water. Then, the samples were dried for an hour in a convection oven at 120 °C.

Hereafter, we denote the samples using the code *ratio*-# after the names of GNF-GO or GNF-RGO, where the *ratio* is the mass ratio of GNF:GO in the suspension and # is the number of iterations of chemical reduction procedure. For example, GNF-GO-5 represents the GNF:GO mixture of 5:1 mass ratio that did not undergo any reduction procedure as a control sample. GNF-RGO-5-1 indicates that the composite underwent a reduction process using L-ascorbic acid. GNF-

RGO-5-2 implies that the reduced composite underwent *an additional* reduction step using a $NaBH_4$ solution.

Chemical Characterization: A field emission scanning electron microscope (FE-SEM; Sigma, Zeiss) was utilized for the morphological study. X-ray diffraction (XRD) patterns were recorded on a Rigaku RU-200B X-ray diffractometer with a rotating anode X-ray generator using Cu Kα radiation (40 kV, 110 mA). X-ray photoelectron spectroscopy (XPS) was carried out on a Kratos Axis spectrometer with monochromatized Al Kα. The C1s peak at 284.6 eV was used to calibrate all XPS spectra. A Renishaw In Via microscope system was used to collect Raman spectra from samples. A 785 nm diode laser was used as an excitation source.

Conductivity Measurement: The electrical conductivity was evaluated with a four-point probe station (Pro4-4400, Lucas Signatone, US) connected to a Keithley 2400 source measure unit. The thickness of the GNF-RGO coating on the substrate was obtained by cross-sectional SEM image. The cross-section of the sample was prepared by immersing a fabricated antenna in liquid nitrogen for several seconds and manually breaking it into two pieces. For each synthesis condition, we obtained statistical results from five samples of different batches. The durability of the sample was tested by repeated bending (radius of curvature of 1 cm) and releasing (unbending) cycles at 1 Hz frequency on a customized mechanical tester (UniVert, CellScale, Canada) equipped with a Keithley 2400.

Antenna Fabrication: Once the GNF-RGO coating was synthesized on a 3D printed flexible substrate, the samples were compressed at 10 MPa to get compact coating on the substrate (Figure 8.1a). A SubMiniature version A (SMA) connector was attached to the GNF-RGO coating by silver paste, and cured in a convection oven at 120 °C for 4 h. Then, the GNF-RGO antenna was dipped into a commercial room-temperature vulcanizing silicone (Shin-Etsu, Japan) for packaging. The silicone was cured for an hour to conclude the fabrication of the flexible GN-RGO antenna. A photograph of an as-prepared GNF-RGO antenna is shown in Figure 8.1c, which can be bent (Figure 8.1d) and twisted (Figure 8.1e).

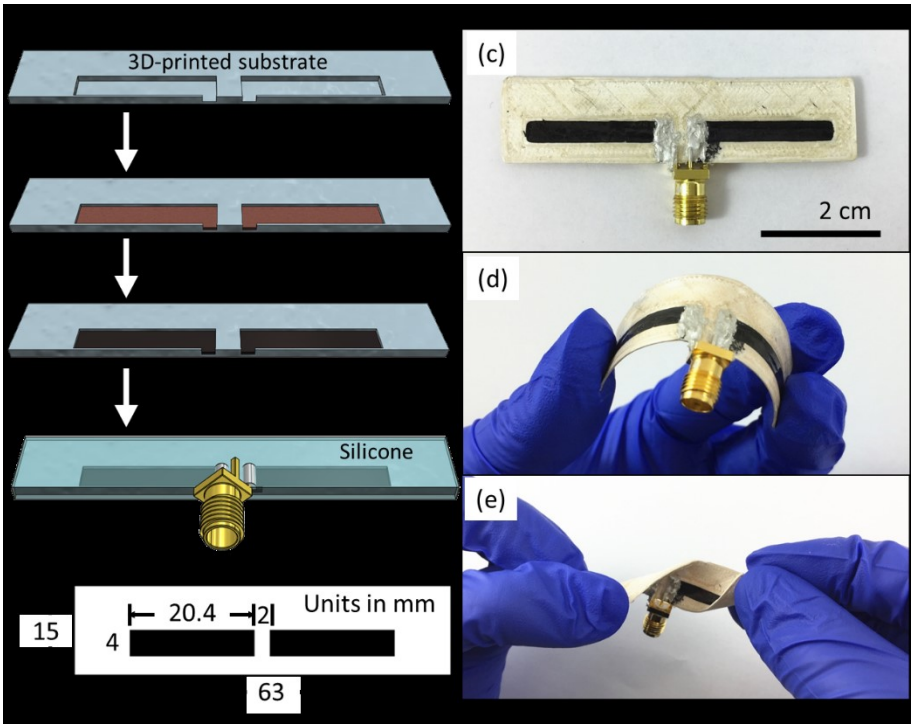

Figure 8.1 (a) Schematic illustration of antenna fabrication. (b) The layout of GNF-RGO-5-2 antenna. The photograph of (c) the as-prepared, (b) bent, and (c) twisted GNF-RGO antenna.

Antenna Performance Characterization: A simple vertical half-wave dipole antenna provides an omnidirectional donut-shaped radiation pattern which is adequate for applications that need a high coverage of radiation and data transfer.[297,298] This type of antenna radiates the power almost uniformly in all directions in a given plane. It consists of two identical conductors each with a size of a quarter of the resonating wavelength. Each conductor is connected to one side of the feed line to power up the antenna.

We measured the E-plane and the H-plane of the dipole antenna by the RFxpert measurement tool from EMSCAN, [299,300] which is capable of measuring the radiating-near-field region and then projects the results to the far-field region. The antenna efficiency was quantified by the reflection coefficient, which shows how much power fed to the antenna reflects as a function of frequency. For measuring the reflection coefficient, a vector network analyzer (VNA, E8362B) was used.

Strain Sensor Fabrication: The strain sensor was fabricated by coating GNF-RGO-5-2 on a 3D printed serpentine-shape substrate. Two copper sheets were attached to both ends of the serpentine-shape substrate as electrodes by silver paste, followed by curing in a convection oven at 120 °C

for 4 h. Then, the strain sensor was encapsulated by silicone, according to the protocol described in the antenna fabrication section.

Strain Sensor Performance Characterization: Tensile tests were conducted with a Keithley 2400. The samples underwent three loading-unloading cycles with 5 mm/min strain speed.

8.3 Results and Discussion

8.3.1 Morphology Before and After Compression

Figure 8.2a illustrates the morphological evolution during the processing. After the addition of GNF in the GO solution, a suspension of GNF-GO is formed. The GO in the suspension served as a dispersant to stabilize the GNF owing to its planar 2D structure and hydrophilicity.[192] During the evaporation of the water in the suspension, GO sheets were self-assembled into GO papers,[193] and GNFs intercalated between the GO sheets. After the reduction, the average distance between GO sheets was reduced because the chemical reduction caused the removal of labile oxygen-containing functional groups in the GO.[194] In the final GNF-RGO coating, the RGO plays a role as a binder to keep mechanical integrity while maintaining high electrical conductivity. As a result, we obtain a composite that is flexible without powder disintegration owing to the self-reinforcing nature of RGO that wraps GNF. This trait is suitable for application in flexible electronics.

The morphological evolution of GNF-RGO coating was examined by SEM. The SEM images in Figures 8.2b and 8.2c show the morphology of GNF-GO-5, which did not undergo reduction or compression steps. Here, it can be confirmed that GO forms a blanket-like network structure that wraps GNF particles everywhere. Each GNF particle, a stack of aggregated graphene platelets wrapped in the GO envelope, had an average thickness of ~50 nm (characterized by a separate SEM imaging; not shown) with a lateral dimension of ~1 μm. After repeating reduction and compression steps twice, Figure 2d and 2e show the top-view SEM images of the GNF-RGO-5-2. Here, the structure of the GNF-RGO became more compact.

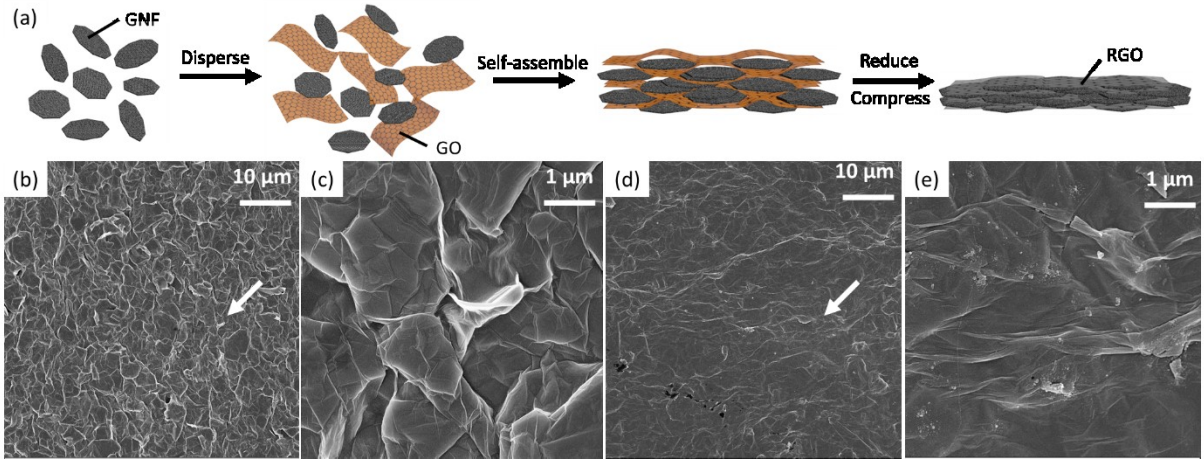

Figure 8.2 (a) Schematic illustrations that describe the processing of the GNF-RGO coating. (b) The SEM image of GNF-GO-5 and (c) a magnified image of the small region identified by the white arrow in Figure 8.2b. (d) The SEM image of compressed GNF-RGO-5-2 and (e) a magnified image of the white arrow region in Figure 8.2d.

8.3.2 Conductivity Optimization

A four-point probe measurement was used to evaluate the electrical conductivities of GNF-RGO coatings. As shown in Figure 8.3, GNF-GO coatings were not conductive before reduction because GO is an insulator. After the first reduction by L-ascorbic acid, the GNF-RGO composites were electrically conductive. The conductivity values increased with increasing GNF concentration in the precursor suspension. At low ratios of GNF:RGO (*i.e.*, low GNF content), the electrical conductivity was limited because of the abundance of the oxygen-containing functional groups in the RGO sheets that were left unreduced after the L-ascorbic acid treatment. The higher content of the GNF in the composite film increased the conductivity, as shown by the contrast between GNF-RGO-2-1 and GNF-RGO-5-1, which exhibited conductivity values of $0.72 \pm 0.22 \times 10^4$ and $2.49 \pm 0.28 \times 10^4$ S/m, respectively. The electrical conductivity of GNF-RGO-10-1, $2.61 \pm 0.30 \times 10^4$ S/m, was however not higher than that of GNF-RGO-5-1.

A subsequent treatment by a stronger reducing agent, $NaBH_4$, was shown to be efficient to remove the oxygen-containing functional groups in the RGO sheet.[195] Here, the electrical conductivity values were drastically improved, as presented in Figure 8.3a. The conductivity of GNF-RGO-5-2 reached the highest conductivity value of $4.47 \pm 0.61 \times 10^4$ S/m. Interestingly, the

conductivity of GNF-RGO-10-2, 4.16 ± 1.07 × 10^4 S/m, was not higher than that of GNF-RGO-5-2. Moreover, the GNF-RGO-10-2 coating was more brittle than that of GNF-RGO-5-2 due to the reduced amount of the RGO binder.

A drawback of using $NaBH_4$ was an intensive bubbling observed during the reduction. This occasionally caused the delamination of the composite coating, which was the reason that we did not perform $NaBH_4$ treatment as the first reduction step. The conductivity results of GNF-RGO-10-2 had a certain degree of inconsistency as indicated by a large standard deviation.

Therefore, we arrived at the conclusion that there is an optimum ratio of GNF:RGO to provide the best combination of electrical conductivity and mechanical integrity. A certain fraction of RGO in the composite coating is critical to maintain sufficient mechanical integrity whereas increasing the fraction of GNF increases the conductivity. Our results suggest that the mass ratio of GNF:GO = 5 in the suspension is the balanced point between the electrical conductivity and mechanical integrity. In addition, the two-step reduction protocol using a weaker reducing agent, followed by a stronger reducing agent turned out to be an effective combination. The first reduction step using the L-ascorbic acid provides mechanical integrity and moderate electrical conductivity to the composite coating. The second reduction step using $NaBH_4$ provides a further enhancement of the electrical conductivity.

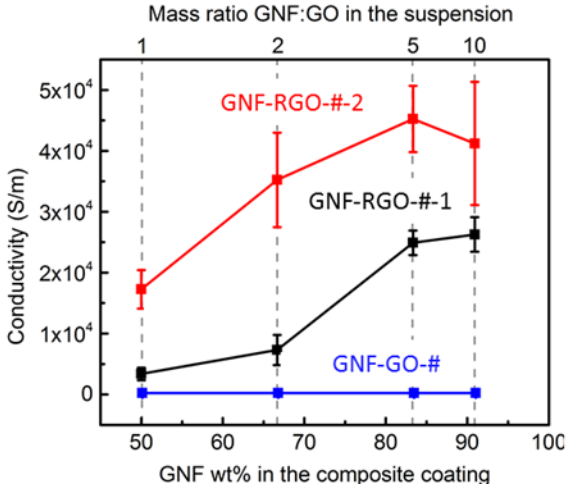

Figure 8.3 Electrical conductivity values of the composite coatings as a function of GNF:GO ratio and the composite's reduction steps. Here, GNF-RGO-#-1 denotes a reduction using L-ascorbic acid (step 1), whereas GNF-RGO-#-2 indicates a further reduction step using $NaBH_4$ (step 2).

8.3.3 Chemical Characterization

A field emission scanning electron microscope (FE-SEM; Sigma, Zeiss) was utilized for the morphological study. X-ray diffraction (XRD) patterns were recorded on a Rigaku RU-200B X-ray diffractometer with a rotating anode X-ray generator using Cu Kα radiation (40 kV, 110 mA). X-ray photoelectron spectroscopy (XPS) was carried out on a Kratos Axis spectrometer with monochromatized Al Kα. The C1s peak at 284.6 eV was used to calibrate all XPS spectra. A Renishaw In Via microscope system was used to collect Raman spectra from samples. A 785 nm diode laser was used as an excitation source.

Raman spectroscopy was used to probe the bonding structure of the carbonaceous materials. There are three distinguishable bands presented in Figure 8.4a. First, the D-mode (disordered band) was located between 1330 and 1360 cm^{-1}. Second, the G-mode (tangential mode), which corresponds to the stretching mode in the graphite plane, was located at 1580 cm^{-1}. Third, the second-order mode, conventionally denoted as 2D, was located at 2680–2690 cm^{-1}.[276] The relative intensity of the D-mode and G-mode (I_D/I_G) depends strongly on the density of defects in the graphitic material. A larger I_D/I_G value suggests a higher density of sp^3 carbon due to structural defects.[277] The values of I_D/I_G increase from 0.43 in GNF to 1.18 in GNF-GO-5, indicating that the structure of carbon in GNF-GO-5 is less ordered compared to that of pure GNFs because of the GO content. After the L-ascorbic acid reduction, the I_D/I_G value increases to 1.87, which indicates a further increase of sp^3 carbon (*i.e.*, decrease of the sp^2 carbons; an ideal graphene has 100% sp^2 bonding) upon GO reduction in the GNF-GO composite film.[301]

The chemical composition at the surfaces of samples was investigated by X-Ray photoelectron spectroscopy (XPS). As presented in Figure 8.4b, the carbon-to-oxygen atomic ratios (C:O) of the starting materials were 51.6 for the GNF and 1.7 for GO. After mixing the GNF and GO, the measured C:O values in GNF-GO-5 is 3.8. This value is significantly lower than the value calculated from the weight percent of each component, which is 11.7. The discrepancy can be explained by surface segregation of GO upon drying of the solvent. It is well known that XPS measures the chemical composition of the very top of the surface (~5 nm at the condition of operation).[302] The SEM image of GNF-GO-5 (Figure 8.2b) also did not show indicative features of flaky GNFs exposed at the surface; a layer of GO seemed to be on the top of the GNFs. Both features strongly indicate that the majority of the signals collected by XPS was generated from the

GO. After the L-ascorbic acid reduction, the C:O value of GNF-RGO-5-1 was increased to 7.8. The C:O value was further increased to 10.7 in the GNF-RGO-5-2, implying further reduction of the RGO. XRD patterns of GNF, GNF-GO-5, GNF-RGO-5-1 and GNF-RGO-5-2 are shown in Figure 8.4c. All four samples showed two peaks at $2\theta = 26.5°$ and 54.9°, which can be attributed to the (002) and (004) planes of graphitic carbon.[303] The inset shows a magnified view at 2θ values ranging from 10° to 15°, GNF-GO-5 exhibited a reflection with the peak at $2\theta = 11.6°$, attributed to GO (001),[304] which is the evidence of GO existence in the GNF-GO composite coating. This peak was not observed in GNF-RGO-5-1 and GNF-RGO-5-2, indicating that reduction by L-ascorbic acid destroyed periodic stacking between GO layers which existed in the as-prepared control sample (*i.e.*, GNF-GO).

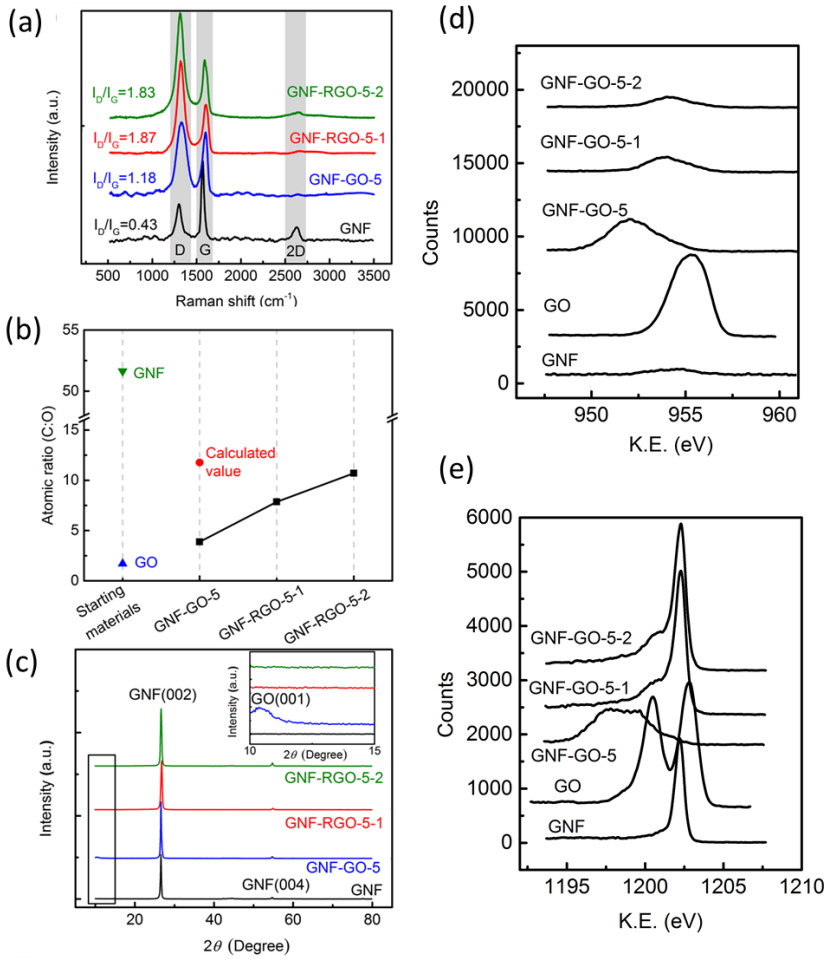

Figure 8.4 (a) Raman spectra of GNF, GNF-GO-5, GNF-RGO-5-1, and GNF-RGO-5-2. (b) Atomic ratio of carbon and oxygen obtained from XPS profiles. (c) XRD spectra of GNF, GNF-GO-5, GNF-RGO-5-1, and GNF-RGO-5-2. The inset is a magnified view at low 2θ region (between 10 and 15 degrees). X-ray photoelectron spectroscopy (XPS) profiles near (d) O1s and (e) C1s peaks.

8.3.4 Durability Test

The durability of the sample with GNF-RGO-5-2 coating without PDMS encapsulation was tested by repeated bending (radius of curvature of 1 cm) and releasing (unbending) cycles at 1 Hz frequency. We performed a comparative study between GNF-RGO-5-2 (test sample) and pressed GNF (control) on the 3D printed elastomer substrate. For GNF coating, a certain amount of GNF powder was spread on the substrate, and then compressed at 10 MPa to get a compact coating. The thickness of GNF coating was controlled to be the same as GNF-RGO-5-2 (~20 μm). The result of the cycle test is shown in the Figure 8.5a.

No obvious change in resistance was observed for GNF-RGO-5-2 coating up to 1000 cycles. In contrast, the normalized resistance (resistance normalized by the initial value) of the GNF coating was rapidly increased. The resistance of the GNF coating increased to 10 times its original resistance after ~400 cycles. The dramatic enhancement of durability in mechanical and electrical properties of the GNF-RGO-5-2 coatings is due to the covalent bonding between RGO 'envelopes' that wrap the GNF, whereas the covalent bonding was introduced from the chemical reduction process. Optical microscopy images in Figure 8.5b (pristine) and 8.5c (after 1000 cycles) show the durability of the coating. Here, only indistinctive buckling can be observed after 1000 cycles. However, the GNF control sample shows a severe loss of materials after undergoing bending stress cycles, as evidenced by comparing Figure 8.5d (pristine) and 8.5e (after 1000 cycles). Therefore, the RGO-wrapping process can be called "self-reinforcing" that can be useful for practical use of GNF particles.

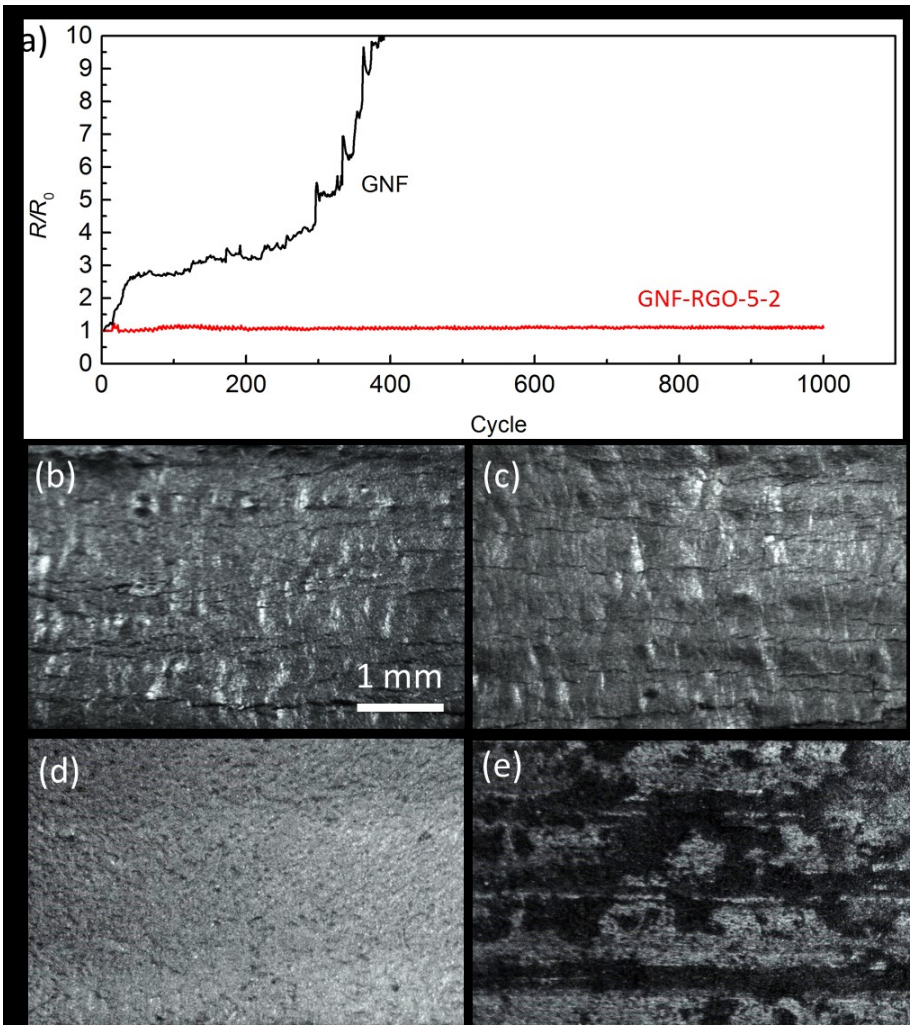

Figure 8.5 (a) Evolution of normalized resistance under bending stress cycles for GNF-RGO-5-2 and the control (GNF without RGO) coatings. The minimum radius of curvature for each cycle was 1 cm. Optical images of GNF-RGO-5-2 coating (b) before and (c) after 1000 cycles and of the control coating (d) before and (e) after 1000 cycles.

The resistance change of the GNF-RGO-5-2 coating (without PDMS encapsulation) versus bending radius of curvature was measured using a Keithley 2400 (Figure 8.6). No obvious resistance change in the samples was observed upon bending with the radius of curvature ranging from infinity to 0.5 cm. The result indicates that the GNF-RGO coating is suitable for flexible electronic applications.

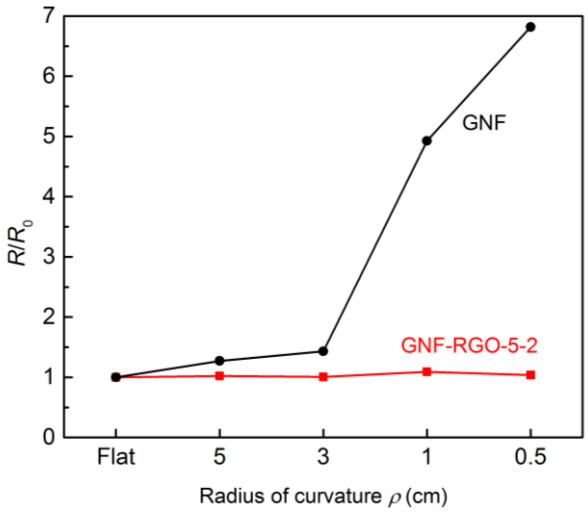

Figure 8.6 The resistance changes of GNF-RGO-5-2, and GNF coating versus the radius of curvature.

8.3.5 Flexible Radio Frequency Antennae

Before designing the antenna, we need to characterize the substrate (which the antenna is printed on) to extract its dielectric constant and loss tangent. Using a Keycom dielectric measurement open mode probe,[305] the dielectric constant and loss tangent of the substrate are obtained to be 3.6 and 0.06, respectively. Using the HFSS software, a prototype of the antenna was designed to align the center frequency at 2.45 GHz. The antenna was connected to a SMA connector by silver paste. Figure 8.7 shows the reflection coefficient and radiation pattern of the fabricated antenna. Figure 8.7a depicts the simulated and measured reflection coefficient of the fabricated dipole antenna. Here, the simulation and the measurement showed an acceptable agreement near the resonant frequency of 2.45 GHz. The discrepancy between simulation and measurement results at frequencies larger than 3 GHz is probably due to a non-ideal connection between the SMA connector and the two branches of the dipole antenna. The dielectric constant and loss tangent values of the substrate characterized and used in the simulation have a certain tolerance that may cause the discrepancy. We also used constant values for the parameters of the graphene in the whole frequency band in the simulations; however, they may vary as a function of frequency in the given range. To show that the antenna is flexible, the performance of the antenna was monitored under a range of bending radii (BR). Figure 8.7b shows the effect of BR of the

dipole antenna on the reflection coefficient. Here, a bandwidth (BW; the normalized range of frequencies with the reflection coefficient below –10 dB) of 35% was achieved at the frequencies between 2.1 and 3 GHz for BR values up to 2.5 cm.

The measured 3D radiation pattern depicted in Figure 8.7c shows a perfect donut-shaped pattern as expected. Figures 8.7d and 8.7e display the measured E-plane and H-plane of the antenna respectively for different bend radius. For different BRs, the H-plane remained omnidirectional and the E-plane kept the donut-shaped pattern. The measured peak gain at the center frequency is 0.3 dB which indicates the antenna has an acceptable performance.

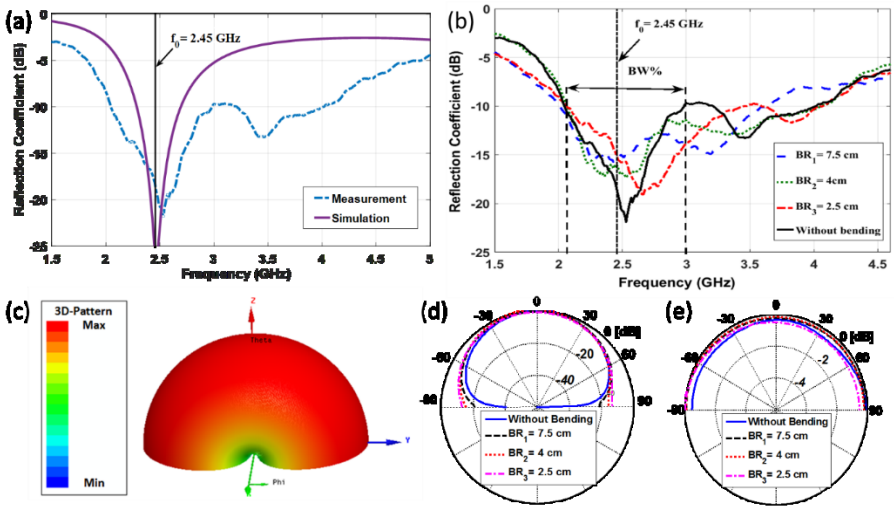

Figure 8.7 (a) The simulated and measured reflection coefficient of the dipole antenna, (b) the measurement results for different values of bend radii (BR), (c) the measured 3D radiation pattern, (d) the measured E-plane at 2.45 GHz for different BR, (e) the measured H-plane at 2.45 GHz for the different BR.

8.3.6 Strain Sensor

The GNF-RGO-5-2 composite was tested as a potential material for a strain sensor. Figure 8.8a shows a systematic increase of resistance of a serpentine-shaped GNF-RGO-5-2 coating up to 40% strain. When the sample was stretched more than 40%, the silicone encapsulation layer was delaminated from the coating due to the buckling effect. The 3D-printed serpentine shape allowed the device to measure strain values that exceed the 5% limit of conventional metal strain gauges,[306] as well as ~10% for some graphene-based strain-sensors.[307,308] The increased resistance

upon stretching can be explained by the model of overlapped graphene sheets, where the degree of overlapping between the graphene sheets dictates the overall resistance.[309] With increasing strain, the GNFs and RGO sheets tend to lose connectivity, resulting in an increase of the contact resistance between the GNFs and RGO sheets.

The resistance increased irreversibly after the first loading-unloading cycle. And then the output curve of the sensor became consistent between the second and third loading–unloading cycles. An earlier study pointed out the fact that some irreversible cracks are generated during the first loading cycle, which account for increased resistance. But, at the same time, they allowed structural relief for repeated loading–unloading cycles.[308] Such structural relief resembles the stretchability of a rigid object as a result of kirigami.[306] Here, we considered the first loading–unloading cycle as the initialization process for the strain sensor; in other words, we defined that the sample preparation of the strain sensor was concluded after the first loading–unloading cycle. Therefore, the performance of the strain sensor was evaluated based on the second and the third cycles.

The slope reflects the gauge factor, which is the sensitivity of the sensor to strain, given by,[310]

$$GF = (\Delta R/R_0)/\varepsilon \qquad (8.1)$$

where $\Delta R/R_0$ is the relative change in resistance and $\varepsilon = \Delta L/L_0$ is the mechanical strain. The gauge factors obtained from the loading and releasing steps in the second and third cycles were shown in Figure 8.8b. Here, we obtained the *GF* values of ~13 up to 40% strain. The gauge factor values were higher than those for the conventional metal strain sensor ($GF \approx 2$), and close to carbon nanotube–polymer composite strain sensors (*GF* between 5 and 22),[311] and sensor utilizing graphene–polymer composites ($GF \approx 12$).[312] The operating range (strain ~ 40%) of the fabricated strain sensor is also wider than that for the previously reported graphene based sensors (up to 20 %).[307,313,314,315,316]

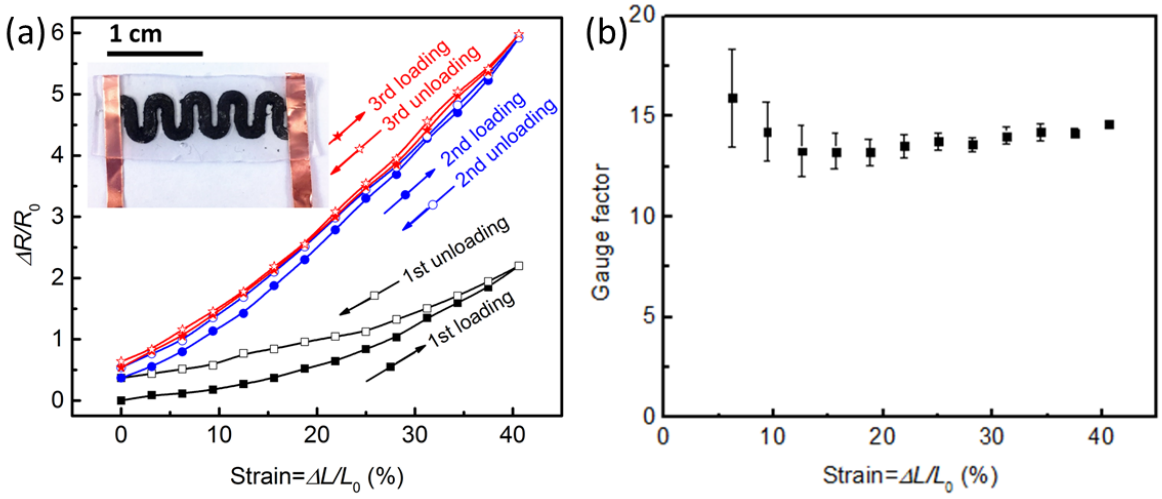

Figure 8.8 (a) The relative changes in resistance for the loading–unloading cycles versus strain. Inset: the optical image of the strain sensor. (b) The calculated gauge factor versus strain for the loading and releasing steps in the second and third cycles.

8.4 Conclusion

In summary, we developed a self-reinforcing nanocomposite of graphene nanoflakes that are enclosed by self-assembled GO particles. A two-step acid treatment protocol reduced GO into RGO, enhancing the electrical conductivity of the composite coating. The substrate material was 3D printed porous elastomer prepared by a commercial filament material. The whole process was conducted at a temperature lower than 120 °C without using any organic solvent. The GNF-RGO composite coatings were applied on 3D-printed objects to transform the non-functional elastomers into flexible radio frequency antennae and strain sensors. We foresee that the electrically conductive GNF-RGO composite coating can be utilized in various applications in flexible electronics and in wearable biomedical devices.

Chapter 9 Sponge-Templated Macroporous Graphene Network for Piezoelectric ZnO Nanogenerator

9.1 Introduction

Emerging technology of 'Internet of Things (IoT)', a proposed network evolution that many living and non-living objects have network connectivity to send and receive data, demands power sources be included in existing objects.[102] Batteries and solar cells are among possible solutions; however, presumably, consumers do not wish to see an increase in price for inexpensive commodity items. Printed radio-frequency identification (RFID) may provide wireless power transmission at the cost of cents per product.[292] When wireless transmission is unavailable to match the power consumption, an additional power device is required, preferably at the lowest production cost possible. Energy harvesting by utilizing piezoelectric materials that can convert mechanical motion to electrical energy is suitable for wearable products, where devices can be charged during daily activities.[103,104]

Originating from seminal contributions by Wang and co-workers,[105,106,107] arrays of zinc oxide (ZnO) nanowires have been utilized as promising electricity generators by the piezoelectric effect. The piezoelectricity stems from the crystalline structures of the nanowires and their self-rectifying nature at the electrical contact to substrate materials.[108,109,110] Recent studies suggest that ZnO arrays on graphene provide an attractive option for nanogenerators due to desirable Schottky barrier properties.[111,112,113,114] For IoT applications, remaining challenges include a simple and inexpensive synthesis of the nanomaterials and the maximization of the ZnO/graphene area per unit volume for high-density power generation. The former can be achieved by hydrothermal synthesis of ZnO nanowires, which allows a high density array of ZnO at the maximum processing temperature of ~90 °C.[115,116] The latter requires a 3D porous network of graphene with a low-cost fabrication method.[117,118,119]

Here we present a simple and inexpensive processing to produce a nanogenerator with 3D structure for enhanced performance and mechanical integrity. A commercially available polyurethane (PU) sponge was used as a substrate to provide a 3D macroporous network structure and ideal mechanical properties (structural integrity, modulus, and resilience) for the

nanogenerator. A graphene coating on the PU sponge was formed by reducing aqueous graphene oxide into a conductive 3D network. We developed a one-step hydrothermal method that grows ZnO nanowires on the graphene network. The whole process was performed in aqueous solution under 95°C with chemicals that are environmentally benign. The pores were then backfilled with another elastomeric soft material, poly(dimethyl siloxane) (PDMS). The backfilling provided protection for the nanowires from shedding off during operation. More importantly, the backfilling caused stress localization to the ZnO arrays under operational conditions, as supported by finite element analysis of stress distribution, thus it allowed an effective electricity generation.

9.2 Experimental Methods

9.2.1 Nanogenerator Fabrication

Graphene Oxide Dip-Coating. An as-received commercial polyurethane sponge (87035K41, McMaster-Carr, US) with dimension 3 × 3 × ~0.2 cm was immersed into graphene oxide (GO) solution (4 mg GO/mL, Graphenea, Spain). Typically, each sample could uptake 1.5 ml GO solution. Then the sponge was dried in a convection oven for six hours at 80 °C. The mass of sponge after the drying process was increased from 59.0 ± 3.4 mg to 64.3 ± 4.7 mg. The increased mass can be attributed to coated GO.

Graphene Oxide Reduction. We adopted an established protocol of a vitamin-C based reduction method.[83,317] The GO coated sponges were reduced using L-ascorbic acid aqueous solution (L-AA, 8 mg/mL, Sigma-Aldrich, US) in an oil bath with a distillation apparatus at 95 °C. After reaction for 4 h, the sponges were dialyzed in deionized water to remove remaining L-AA. Then the sponges were dried in a convection oven for six hours at 80 °C. After that, the sponges were attached to a copper/Kaptone sheet (DuPont, US) using silver paste and cured in a convection oven for six hours at 80 °C. The reduced GO on PU is denoted as RGO@PU.

ZnO Nanorod Synthesis. A ZnO precursor solution was first prepared by dissolving zinc nitrate hexahydrate (80 mM; Sigma-Aldrich, US), hexamethyleneteteramine (HMTA; 25 mM; Sigma-Aldrich, US), polyethylenimine (PEI; 5 mM; Sigma-Aldrich, US) and ammonia solution (30%, ACS reagent grade; 5 mL; Sigma-Aldrich, US) in 100 mL deionized (DI) water. The solution was stirred at room temperature for one hour until it became a clear solution.[196] The one-pot synthesis of ZnO nanowire was conducted in a 95 °C solution. The RGO@PU was placed on the liquid

surface and the container was closed for 10 minutes to allow the solution to permeate the entire sponge sample. Then, the cover was opened to facilitate precipitation of ZnO seeds due to a sudden vapor pressure drop. A slow agitation of RGO@PU allowed a uniform coating of the ZnO seed on the surface of the porous material. Subsequently, the sample was submerged in the solution and the cover was closed again for ZnO nanowire growth.[197] The as-grown sample was rinsed with DI water and ethanol and dried for further use. The mass of the sponge after the drying process increased from 64.3 ±4.7 mg to 117.2 ±16.1 mg. The increased mass can be attributed to ZnO nanowires.

Nanogenerator Integration. A 20 nm thick Au layer was coated on ZnO@RGO@PU with a gold sputter unit (Denton, US) for 180 s, followed by attaching another copper/Kaptone sheet. Two copper alligator clips were clamped to both electrodes to connect the circuit. Finally, a commercial polydimethylsiloxane-based (PDMS-based) material, Sylgard 184 (Corning, US) was infused into the sponge in a vacuum chamber at 9 torr and 60 °C for four hours. The final nanogenerator is shown in Figure 9.1a. The physical appearances after each process step are shown in Figure 9.2.

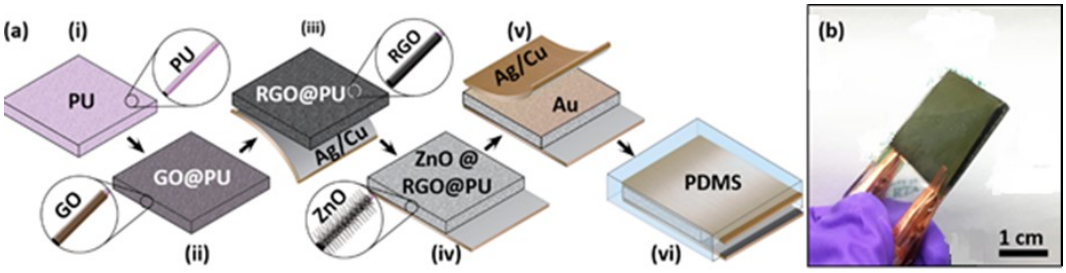

Figure 9.1 (a) Process of nanogenerator fabrication. (i) Pristine PU sponge. (ii) GO coated on the internal and external surfaces of the PU sponge. (iii) GO reduced by L-AA (RGO); bottom electrode attached. (iv) ZnO nanowires grown on the RGO. (v) A thin layer of sputtered Au on the top of the sample; top electrode attached. (vi) PDMS infused into the pores of the nanogenerator. The insets in (a) illustrate the microstructure of each step. (b) The photo of a fully assembled nanogenerator.

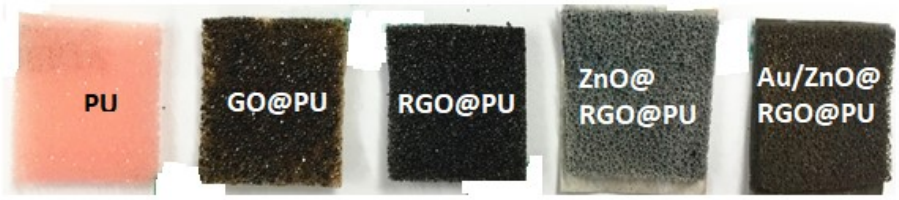

Figure 9.2 Physical appearance after each process step: (From left to right) (i) pristine polyurethane sponge (PU), (ii) PU coated by graphene oxide (GO@PU), (iii) GO@PU after chemical

reduction of the graphene oxide (RGO@PU), (iv) RGO@PU after zinc oxide (ZnO) growth (ZnO@RGO@PU), and (v) after coating 20nm think gold layer with a sputter (Au/ZnO@RGO@PU).

9.2.2 Nanogenerator Characterization

The surface morphologies of samples were investigated by field emission scanning electron microscopy (FE-SEM, Zeiss Sigma). X-ray diffraction (XRD) patterns were recorded on a Rigaku RU-200B X-ray diffractometer with a rotating anode X-ray generator using Cu Kα radiation (40 kV, 110 mA). The chemical bonding characteristics among samples were compared by a Fourier transform infrared (FTIR, Thermo Nicolet 8700) main bench with an attached Continuum FTIR microscope used in attenuated total reflection (ATR) mode with a Germanium Slide-On ATR microscope objective. X-ray photoelectron spectroscopy (XPS) was carried out on a Kratos Axis spectrometer with monochromatized Al Kα.The C1s peak at 284.6 eV was used to calibrate all XPS spectra. A Renishaw In Via microscope system was used to collect Raman spectra from samples. A 785 nm high performance diode laser (air cooled) was used as an excitation source. All Raman spectra were measured with a 20× objective with 60 s integration time. The laser power at the sample was 16 ± 0.5 mW. Ultraviolet photoelectron spectroscopy (UPS) spectra were obtained using a helium discharge source at 21.2 eV (He I) on the Kratos Axis Ultra spectrometer with a total instrumental broadening of 0.1 eV. Spectra were referenced to the Fermi level of a sputter-cleaned Au sample in contact with the sample, and set as 0 eV. The UV-vis absorption spectra of the ZnO nanowire suspension (0.1 g ZnO in 10 ml DI water) were obtained on a Perkin-Elmer NIR-UV spectrophotometer.

9.2.3 Piezoelectricity Measurements

Piezoelectricity (open circuit voltage and short circuit current density) was recorded under periodic flexural stress (0.2 Hz) using a digital source meter (Keithley-2400; background noise controlled at ± 0.5 nA) under ambient conditions. The radius of curvature was about 1 cm during bending. Sample durability was tested by a bicycle revolving at 30 rpm. Here, 20 spokes in the rear wheel bend the nanogenerator with a frequency of 10 Hz at a constant force; the output voltages were recorded.

9.3 Results and Discussions

9.3.1 Surface Characterization

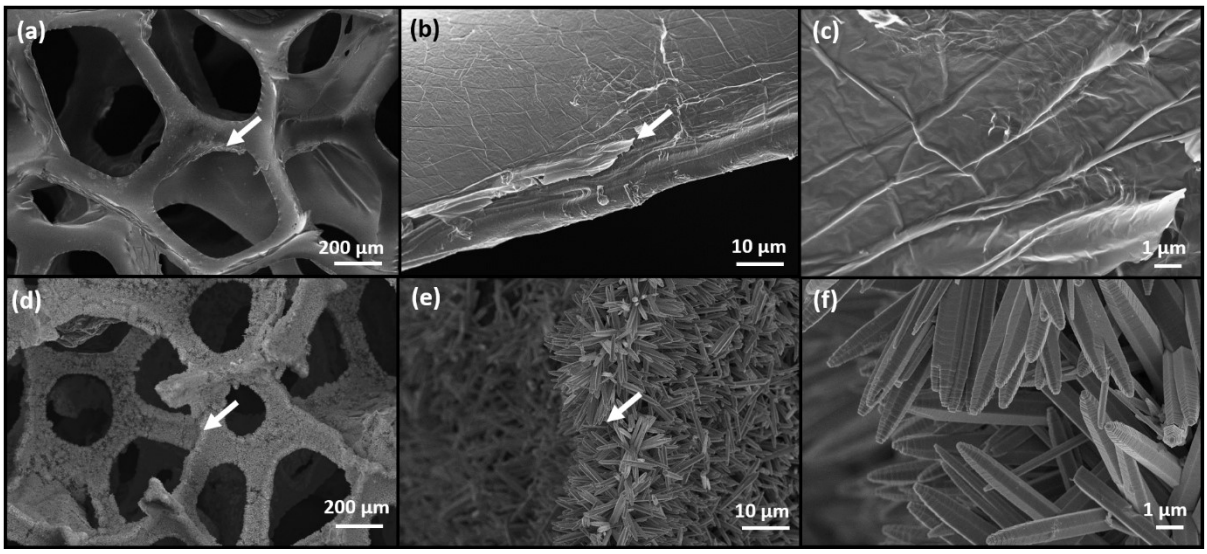

Figure 9.3 (a), (b) and (c) SEM images of RGO@PU with different magnification. (d), (e) and (f) SEM images of ZnO@RGO@PU with different magnification. The white arrows indicate the locations for the zoom-in.

The cross-sections of RGO@PU and ZnO@RGO@PU are given in Figure 9.3. The PU sponge has an open cell structure with ~500 µm pore size. The diameter of the PU fiber is ~150 µm. In Figure 9.3b, RGO@PU has a rougher surface compared to pristine PU (Figure 9.4), which indicates the presence of RGO. Upon immersion of the RGO coated sponge into a L-AA solution at 95 °C, the color of the sponge was changed from brown to black immediately. A decrease in the polar functionality on GO has been previously shown to increase the hydrophobicity of RGO.[277] In water-based solution, the altered wettability results in a high affinity of RGO to the hydrophobic PU template. The magnified images (Figure 9.3c) show a wrinkled surface morphology of the RGO coating on PU. Figure 9.3d and 9.3e show dense ZnO nanowires which were grown on the surface of RGO. The areal density of ZnO nanowires on RGO@PU surface is estimated to be 7.1 ± 0.8 × 10^7/cm^2 with 10.2 ± 1.4 µm length and 855 ± 192 nm in diameter, according to image analysis results (Figure 9.5).

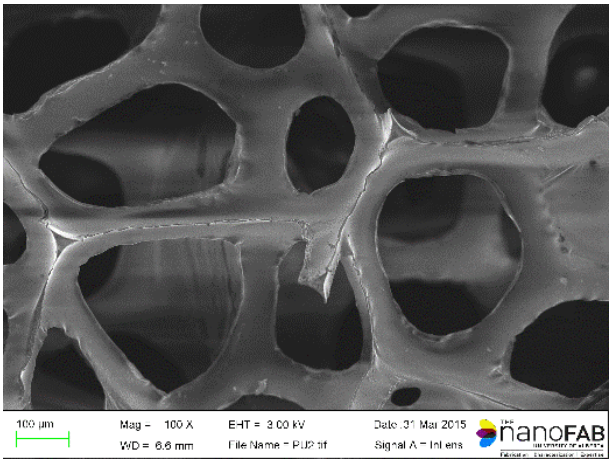

Figure 9.4 A SEM image of a pristine PU sponge. Initially, the surface appears smooth before coating with RGO.

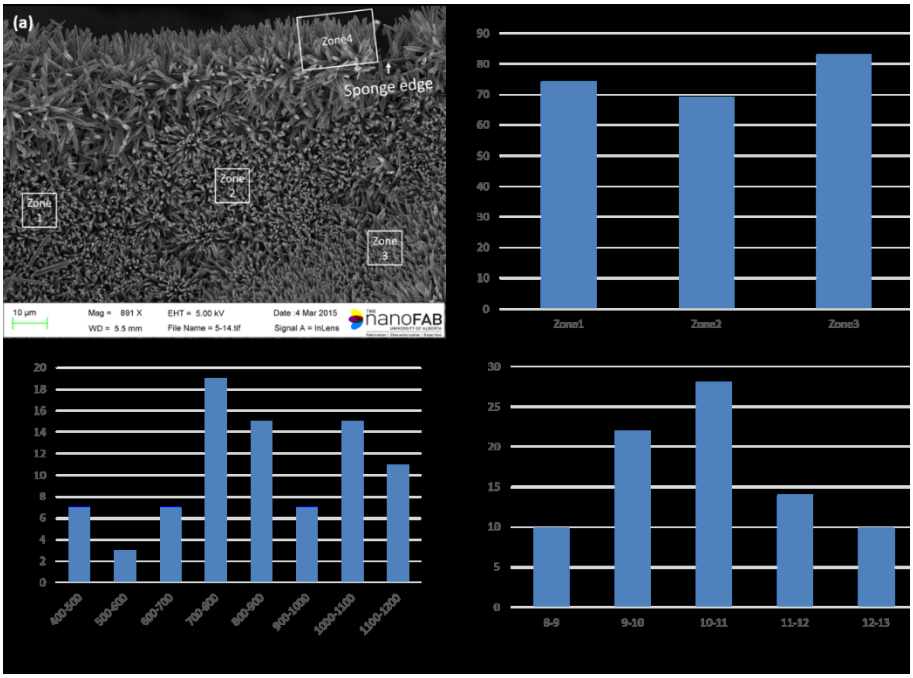

Figure 9.5 (a) A representative SEM image of the surface microstructure of ZnO@RGO@PU. The number density (b), diameter distribution (c), and length distribution (d) of the grown ZnO were obtained by analyzing the image in (a).

XRD patterns of PU, GO@PU and RGO@PU, ZnO@RGO@PU are displayed in Figure 9.6a. GO@PU (2) exhibits a reflection with a peak at $2\theta = 11.6$ degrees, which was not observed in PU

(1) and RGO@PU (3) patterns. This 13.1° peak is consistent with an interlayer spacing of 0.68 nm of GO sheets, implying that GO was reduced. Typical results from graphite, a peak at 2θ = 25 degrees (correlated to an interlayer spacing of 0.34 nm of graphite),[318] was not observed. The XRD pattern of ZnO@RGO@PU (4) confirmed that the as-grown ZnO nanowires were crystalline and all the diffraction peaks can be indexed to ZnO with the hexagonal wurtzite structure (JCPDS No. 75-0576). No typical XRD peaks for graphene were observed, which is due to the relatively low volumetric content of graphene compared to ZnO nanowires.

Raman spectroscopy was used to determine the structure of GO@PU and RGO@PU. There are two distinguishable bands in Figure 9.6b. The D-mode (disordered band) is located between 1330 and 1360 cm^{-1}. The G-mode (tangential mode), which corresponds to the stretching mode in the graphite plane, is located at 1580 cm^{-1}.[319,320] The relative intensity of the D-mode and G-mode depends strongly on the amount of disorder in the graphitic material.[321,322,323] The intensity ratio of D and G changed from 1.67 in GO to 1.91 in RGO@PU, which indicates a decrease in the average size of the sp^2 domains upon GO reduction.[277] This phenomenon was previously reported in GO reduction using a reducing agent.[317,83,277] It is notable that the peaks from PU did not appear in GO or RGO contained samples because of the screening effect of graphitic materials.[324]

The FTIR results (Figure 9.6c) are also in agreement with the conclusion that the GO was successfully reduced. The observation is supported by the following peaks: the broad IR adsorption from 3050 to 3800 cm^{-1} (hydroxyl groups with C–OH vibrations from carboxyl acid), about 1720 cm^{-1} (C=O stretching vibrations from carbonyl and carboxyl groups), 1400 cm^{-1} (O–H bending vibrations from hydroxyl groups), and between 1300 and 1350 cm^{-1} (C–OH stretching vibrations).[317,325] The absorption of the bands associated to oxygen functional groups is strongly decreased in the RGO@PU spectrum.

Reduction of GO was further confirmed by XPS. Figure 9.6d shows the C1s XPS spectra of GO and RGO. Before reduction, three peaks centered at 284.4, 286.7 and 288.1 eV were detected, where the peaks correspond to C=C/C–C (in aromatic rings), C–O and C=O, respectively.[192] After the reduction, the intensities of C–O and C=O peaks decreased dramatically. The areal ratio of the C1s peak to that of the O1s peak with a correction by atomic sensitivity factors (0.25 for C1s and 0.66 for O1s), allows an estimation of the atomic ratio in the material. In our experiment, the ratio of carbon to oxygen was 1.7 for GO and 6.2 for RGO (4 h reduction), which can be described as

evidence for highly reduced graphene oxide.[326]

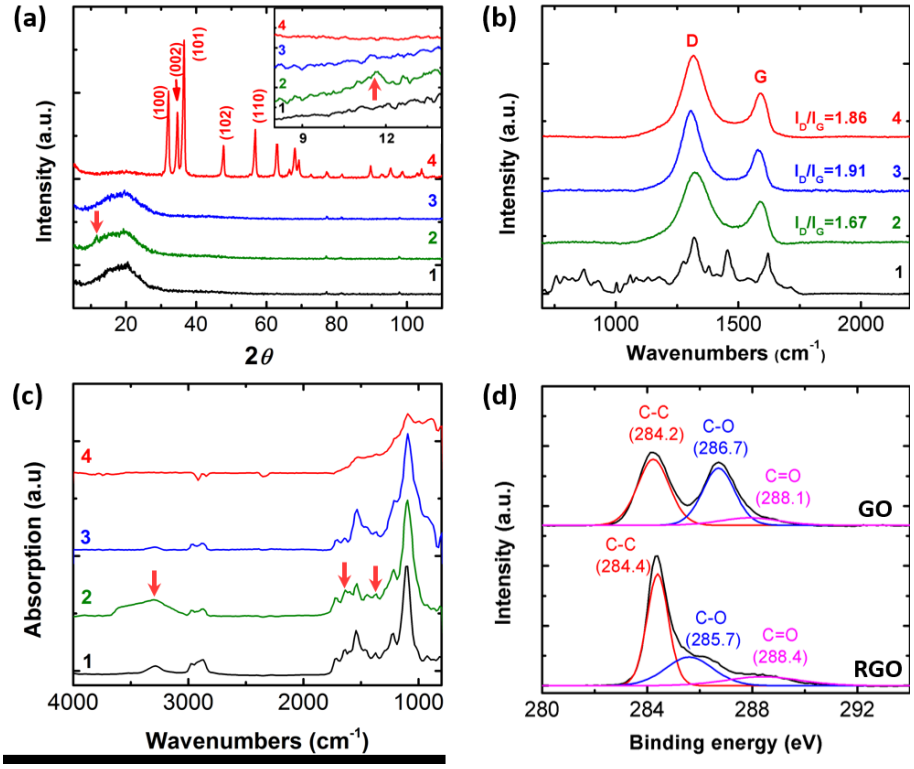

Figure 9.6 (a) XRD patterns (inset: close look at the low 2θ signals), (b) Raman spectra, (c) FTIR spectra of pristine PU (1), GO@PU (2), RGO@PU (3) and ZnO@RGO@PU (4). (d) XPS spectra of GO and RGO.

The resistances of GO@PU and RGO@PU were also measured. Samples with dimension 3 × 3 × ~0.2 cm were sandwiched between two copper electrodes. The resistances of GO@PU and RGO@PU are 674 ± 69 kΩ and 26.7 ± 3.9 Ω, respectively. The notable improvement in conductivity indicates GO was reduced to RGO and can serve as the carrier collector in the nanogenerator.

9.3.2 Piezoelectricity Measurements

Figure 9.7a shows the current–voltage (*I–V*) behavior of the nanogenerator at zero strain. The asymmetric *I–V* curve implies rectifying behavior, which stems from the differences in electrical contact at the ZnO/RGO and the ZnO/Au interfaces. The UPS spectra in Figure 9.7b reveals valence energy levels of GO, RGO and ZnO nanowires with respect to the source emission line

(He 1α; 21.2 eV). The valence band maximum and work function of ZnO nanowires were 7.1 eV and 4.8 eV, respectively. The optical band gap of ZnO nanowires was determined from the UV-vis spectrum in Figure 9.7c, which the peak was located at 3.2 eV. Then, the conduction band minimum of ZnO was calculated using the valence band maximum and the band gap, which the peak was located 3.9 eV. The obtained values for ZnO nanowires are similar to those reported in literature.[327,328] The work function of RGO is 4.5 eV probed by UPS, which is larger than the reported work function of graphene prepared by the chemical vapor deposition method.[329] Kumar *et al.* reported that the oxygen-containing functionalities have a decisive influence on the RGO work function.[330] Incorporation of electron withdrawing groups such as hydroxyl, carboxyl and epoxy in graphene increases the work function and the increment is proportional to the final oxygen concentration in RGO. In our case, experimental results show that the oxygen concentration of GO dropped from 37% to 14%, and the work function decreased from 5.9 eV to 4.5 eV. An energy band diagram of the nanogenerator is illustrated in Figure 9.7d. The mismatch between the work functions of ZnO and Au causes a band bending, which results in an energy barrier for electrons from Au to ZnO of 1.2 eV (Figure 9.7e). On the other side of the contact, ZnO nanowires have an ohmic contact with RGO. When the forward bias is applied, the Fermi level of Au is lower than that of ZnO. The energy barrier is decreased for electrons to transport from ZnO nanowires to Au, leading to a forward bias current in the nanogenerator. When the reverse bias is applied, the Fermi level of Au is raised above that of the ZnO nanowires. The Schottky barrier blocks the flow of electrons from Au to ZnO causing the observed rectifying behavior.

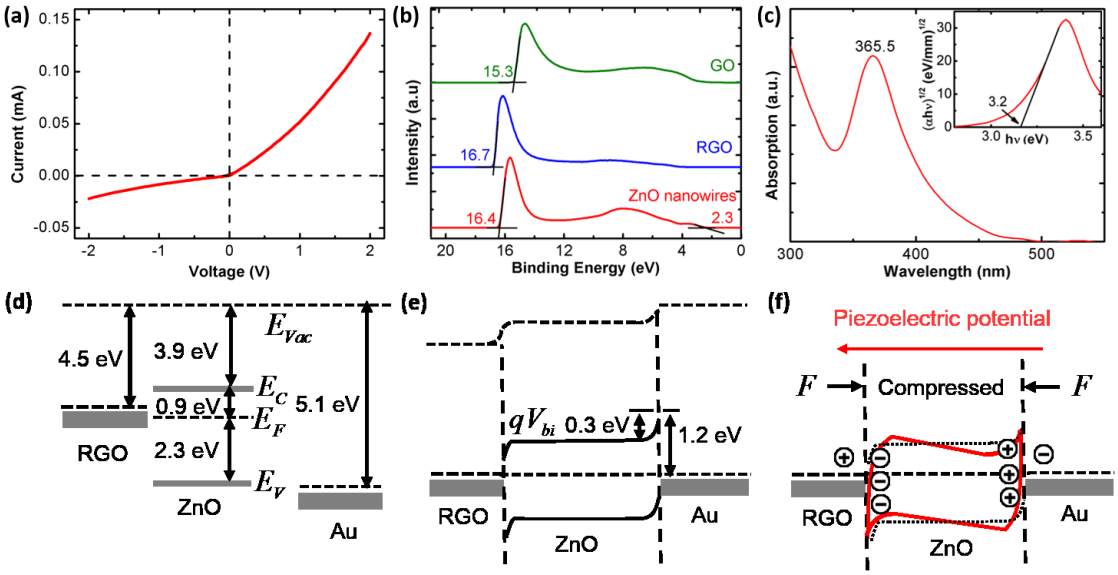

Figure 9.7 (a) *I–V* characteristics of nanogenerator. (b) UPS of GO, RGO and ZnO nanowires. The onset points of the UPS spectra were extracted using the linear extrapolation method shown in the figure, which are 15.3 16.7 and 16.4 eV for GO, RGO and ZnO nanowires, respectively. Spectra were referenced to the Fermi level of a sputter-cleaned Au sample in contact with the samples, and set as 0 eV. The data indicated that the work functions of GO, RGO and ZnO nanowires are 5.9, 4.5 and 4.8 eV respectively. The valence band edge energy of ZnO nanowires is 2.3 eV and the valence band maximum can be calculated to be 7.1 eV.[328] (c) UV-vis spectra of ZnO nanowires. The optical band gap is determined by the inset of the Tauc plot, which is 3.2 eV. Band diagrams of Au/ZnO/RGO junction (d) before and (e) after contact formation. The direction of forward bias is defined as from Au to ZnO nanowires. (f) The band diagram of Au/ZnO/RGO junction with stress. The ionic charges in ZnO are due to piezoelectric polarization and the charges in RGO and Au are due to Coulombic interaction.

Figure 9.8a and 9.8c show the open circuit voltage and short circuit current density measured from the nanogenerator. Upon bending with the frequency of 0.2 Hz, the nanogenerator yielded an open circuit voltage ranging between 0.25 and 0.41 V and a short circuit current density ranging between 1.18 and 1.70 μA/cm^2. The asymmetricities between bending and releasing in voltage and current outputs are because releasing happens quicker than bending in our experiment.[331] A switching polarity test (Figure 9.8b and 9.8d) of the nanogenerator was conducted for forward and reverse connections to confirm that the measured signals originated from the piezoelectric effect, not as an artifact from the measurement system. The nanogenerator yielded open circuit voltage ranging between –0.23 and –0.45 V and short circuit current density ranging between –1.20 and –2.05 μA/cm^2. When the nanogenerator was bent, immobile ionic charges were

created in the ZnO nanowires (Figure 9.8f). The piezoelectric potential will attract and accumulate countercharges in the Au and RGO adjacent to the ZnO.[105, 332,333] These charges generate the induced potential in the Au and RGO, resulting in negative peaks in Figure 9.8a and 9.8c. When the ZnO nanowires are released, the piezoelectric potential will disappear, and accumulated electrons in Au will flow to RGO through an external circuit because electrons are not able to surmount the Schottky barrier at the interface of the ZnO nanowires. It is known that the output behavior of the nanogenerator also depends on the bending and releasing rates because the amount of accumulated electrons can be related to the lifetime of the piezoelectric potential. However, in our case, the dielectric relaxation time (3.5 ms for an Au nanoparticle with 50 nm in diameter[334]) is three orders of magnitude smaller than the manual bending rate (5 s/cycle), thus accumulated electrons will screen the piezoelectric potential before the external force is released.

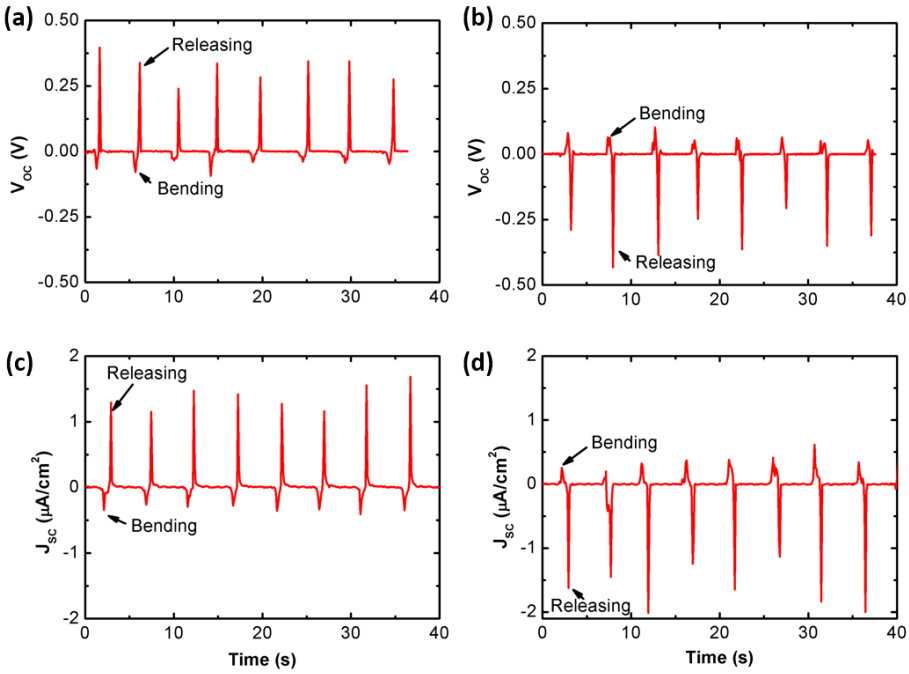

Figure 9.8 Open circuit voltage measured from the nanogenerator by (a) forward and (b) reverse connections. Short circuit current density measured from the nanogenerator by (c) forward and (d) reverse connections

The performance of the nanogenerator described in the current chapter can be further improved by resolving the following challenges. First, the conductivity of RGO is not high, which reduces the efficiency of charge transport to the current collector. It is notable that, in the case that

the RGO's conductivity is not high enough, a similar pattern of output voltage and current with that of a rectifying device without relation to rectifying effect is possible. In our study, however, the rectification effect seems to be a real result, as evidenced in Figure 9.7. Second, the protocol for Au layer coating must be improved to achieve a complete coverage on the other side (*i.e.*, the opposite side from RGO). Third, the synthesis of ZnO nanowires can further be improved to achieve ultrahigh-density nanowires with orientation exactly perpendicular to the local sponge surface. Fourth, a poling process may further improve the performance. Fifth, the sponge we used had a large fraction of porosities; an optimal pore size and porosity needs to be explored in future studies.

9.3.3 Durability Test

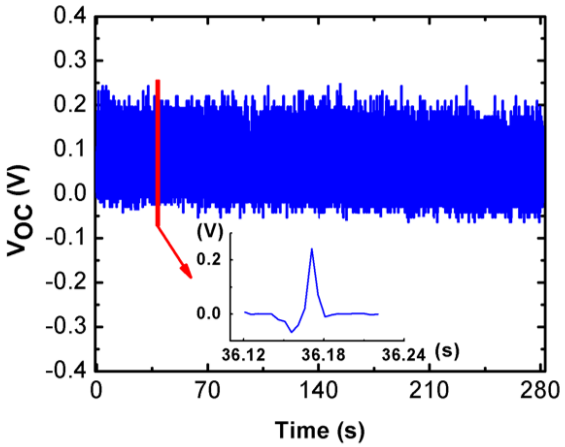

Figure 9.9 The output voltages recorded when the rear wheel was revolving at 30 rpm.

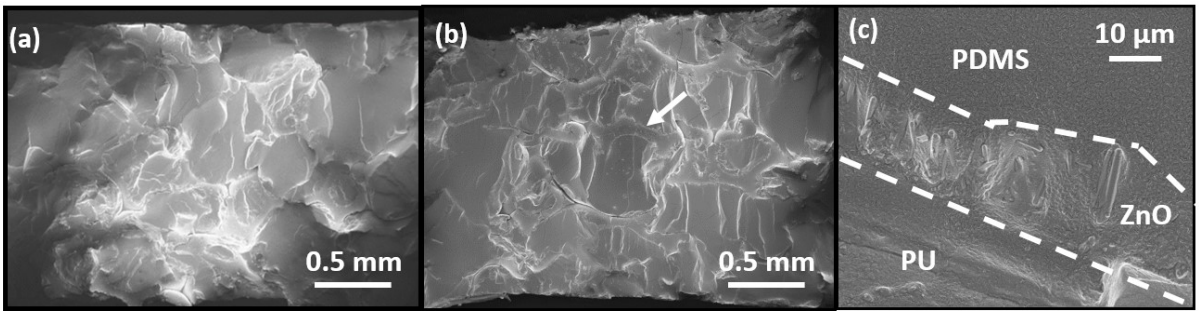

Figure 9.10 (a) Cross section of the nanogenerator before the durability test. (b) Cross section of the nanogenerator after ~3000 cycles. White arrows indicate the locations for the zoom-in. (c) Zoomed-in image at the PDMS/ZnO nanowires/PU interfaces. White dotted lines show the boundaries of PDMS/ZnO and PU/ZnO.

The durability of the nanogenerator was tested. The output voltages were recorded in Figure 9.9 when the rear wheel was revolving at a speed of 30 rpm. The nanogenerator yielded a minimum voltage of about –0.06 V and a maximum voltage of about 0.25 V due to bending and releasing, respectively. The inset in Figure 9.9 shows a single cycle which was about 0.1 s. Because the radius of curvature produced by bending by the spokes is larger than that of manually produced by manual bending, the maximum output voltage of the bicycle test was smaller compared to that in Figure 9.8. After 2800 bending and releasing cycles there was no distinguishable decay in open circuit voltage. Figure 9.10a and 9.10b show the cross-sections of the nanogenerator before and after ~3000 cycles of the bicycle test. The SEM images further confirm that the device was not degraded during operation. Delamination at the interface between hard (ZnO and graphene) and soft (PU and PDMS) materials was not found (Figure 9.10c), suggesting that PDMS prevents the spallation of ZnO nanorods during repeated reversed bending in the durability test.

9.3.4 Finite Element Analysis of Macroporous Structure

Since the output voltage is closely related to how the ZnO nanowires are deformed with external force, a finite element method (FEM) simulation was used to estimate how the stress is distributed in the nanogenerator. We designed a 2D plate model with dimensions of 1.6 mm by 2 mm. The geometry of the nanogenerator cross-section is illustrated in Figure 9.11a. In our devices, the volume fraction of RGO is relative low, thus we included ZnO nanowires, PU and PDMS in consideration. The material parameters are given in Table 9.1. To simplify the model, all materials were considered to be isotropic and uniform. The boundary condition during the bending process is described in Figure 9.12. In our FEM simulation, we considered the geometry of the nanogenerator under bending to be that shown in Figure 9.12. The displacement of the plate boundary was calculated and assigned to boundary elements.

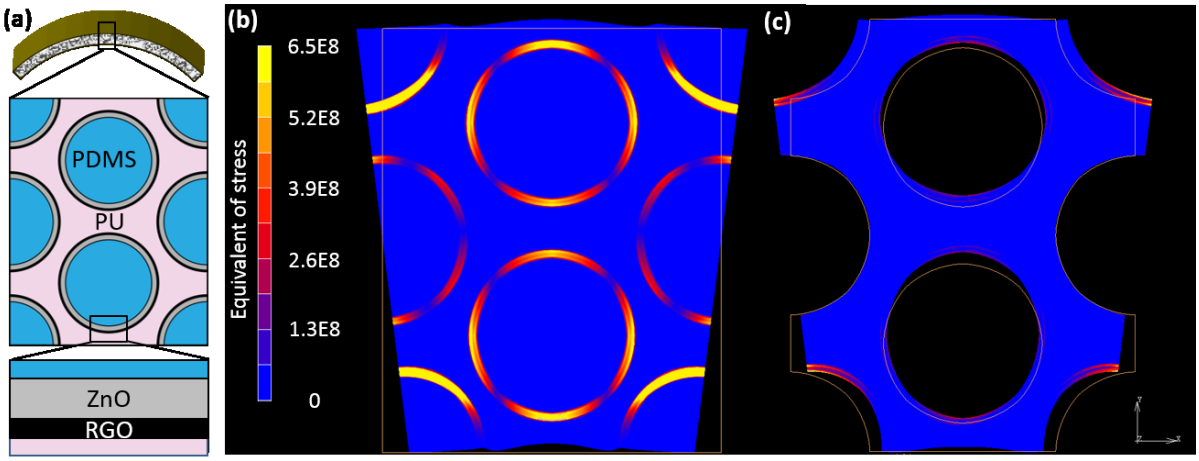

Figure 9.11 (a) Illustration of the structure of the nanogenerator. The RGO layer is not included in the FEM model due to its small thickness. (b) FEM simulation for the stress distribution in the nanogenerator with PDMS and (c) without PDMS.

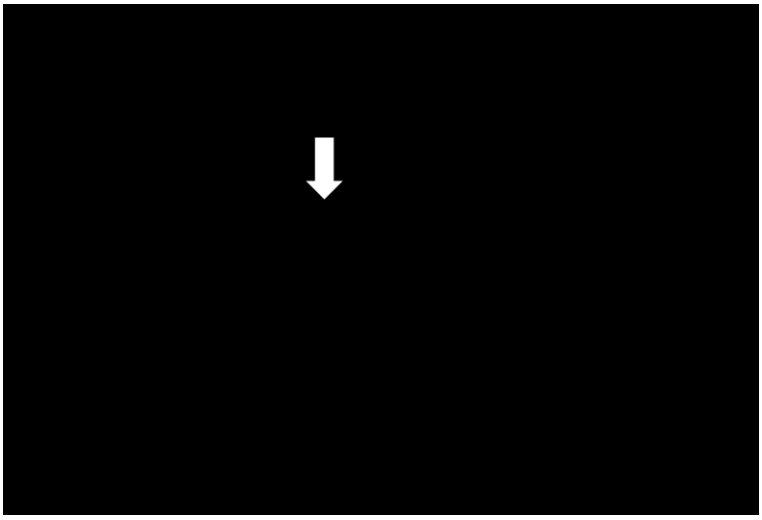

Figure 9.12 The geometry of nanogenerator under bending for FEM simulation.

Table 9.1 Material parameters used in the FEM simulation.

Materials[a,b]	Young's modulus	Poisson's ratio	Thickness
PU[335]	10 MPa	0.50	-
PDMS[336]	3 MPa	0.50	-
ZnO[337]	30 GPa	0.35	10 μm[b,c]

[a] All materials are considered isotropic to simplify the model.
[b] The RGO layer is not included because of its relatively low content and small thickness.
[c] The layer of ZnO nanowires is considered to be a uniform layer. The thicknesses were obtained by SEM imaging.

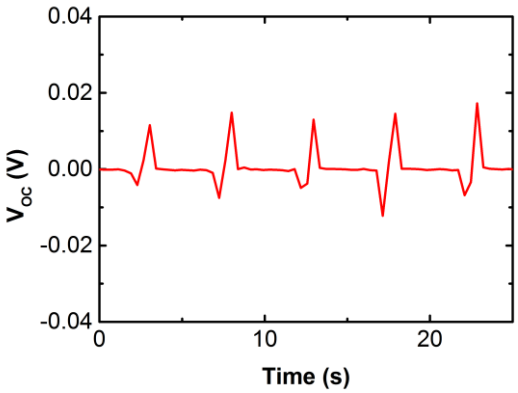

Figure 9.13 The open circuit voltage of the nanogenerator without PDMS.

Briefly, the displacement of the plate boundary was calculated and assigned to boundary elements by the bending curvature with the assumption of a pure bending mode. Figure 9.11b and 9.11c shows the simulation results of the nanogenerator with and without PDMS, respectively. With the presence of PDMS backfilling, Figure 9.11b shows that the equivalent stress of the ZnO nanowire layer is four orders of magnitude larger than that in PU and PDMS. However, the stress is not concentrated on ZnO nanowires (Figure 9.11c), as supported by the measured open circuit voltage from the nanogenerator without backfilled PDMS shown in Figure 9.13. Here, the open circuit voltages (upon release) yielded values ranging from +0.012 to +0.017 V, which are about 20 times smaller than those with backfilled PDMS (cf., Figure 9.8a). The difference indicates that

the role of PDMS is not only protection for the ZnO nanowires, but also an effective stress concentrator for the nanogenerator.

9.4 Conclusion

We demonstrated a low temperature processing method to fabricate a ZnO nanowire based electricity generator with a 3D structure templated on a commodity sponge material. GO was dip-coated from aqueous solution on the commodity sponge and reduced by L-AA, resulting in the transformation of a PU sponge into a conductive 3D network. Then, ZnO nanowires were grown by a one-step hydrothermal method in an aqueous solution below 95 °C. The mechanism of piezoelectricity and the band structure of our device were discussed over a band diagram that shows a Schottky contact at the ZnO/Au interface and ohmic contact at the ZnO/RGO interface. The diagram explained the self-rectification and the output mechanism of the piezoelectric nanogenerator. The nanogenerator yielded open circuit voltage ranging up to ~0.5 V and short circuit current density ranging up to ~2 $\mu A/cm^2$, upon bending every 5 s. In an improvised durability test, degradation in output voltage was not found after ~3000 bending and releasing cycles. Finally, finite element analysis of stress distribution showed that the stress is localized to the ZnO arrays under operating conditions with the presence of PDMS, thus allowing effective electricity generation. The novel and environmentally benign processing route that produced this high-performance nanogenerator opens up the possibility for industrial scale production.

Chapter 10 Criteria for Quick and Consistent Synthesis of Poly(glycerol sebacate) for Tailored Mechanical Properties

10.1 Introduction

Poly(glycerol sebacate) (PGS) and its derivatives make up an attractive class of biomaterials for cell scaffolding owing to their tunable mechanical properties with programmable biodegradability.[338,339,340] Furthermore, their soft and stretchable mechanical properties can be matched with those of the target organs. This can prevent inflammation caused by mechanical abrasion between implants and tissues, rendering the materials promising candidates for drug delivery patches and substrates for implantable biosensors. Although PGS is a thermoset polymer, its prepolymer can be melted at low temperature and dissolved into organic solutions; thus, various applications including micropatterned structure by lithography,[341,342] macroporous scaffolds by salt leaching,[343] and fibrous structures by electrospinning[344,345] are possible. Another emerging area of potential application is a substrate for stretchable electronics with programmed *in vivo* dissolution.[346,347]

In practice, the application of PGS is often hampered by frequent inconsistency in reproducing process conditions. Li *et al*.[348] pointed out that reported properties of PGS synthesized under similar conditions have significantly distinctive properties among different research groups. The major issue that contributes to the inconsistency in PGS synthesis is the volatile nature of glycerol in a low-pressure and high-temperature environment. A possible cause of the inconsistency can be subtle variations in synthesis conditions. Glycerol loss alters the chemical constitution of the final product; thus, it has a pronounced effect on PGS properties as well as the kinetics of PGS synthesis.[349] The subtlety of the synthesis chemistry causes a failure in expecting the property of PGS by thermal history; therefore, defining a new process parameter that incorporates the glycerol loss is necessary to achieve consistency. The new indicator can also be applicable to materials that undergo esterification, which involves mass loss from water condensation and volatile reactants.[350,351]

PGS synthesis has conventionally been a time- and energy-intensive procedure. A conventional two-step procedure incorporates a prepolymerization step that usually takes 24 h in

an inert gas atmosphere, followed by a curing procedure.[338] To reduce the synthesis time, Aydin *et al.* suggested that the prepolymerization step can be replaced by cooking for 3 min at 650 W in a household microwave oven.[352] The simple and inexpensive method by microwave oven has the potential to simplify the synthesis of PGS; thus, a rigorous comparison to the conventional prepolymerization can be beneficial.

PGS's stretchable mechanical properties render it a suitable candidate for cell scaffolds used in dynamic environments such as cartilage, heart, and lungs.[353,354,355] For neat PGS materials, however, the tunable range of Young's modulus by varying thermal history is limited to between 0.25 and 1.45 MPa with elongations at break above 100%.[356,357,358] These Young's moduli match with those of vascular wall (0.3–0.6 MPa), smooth muscle (0.01–1.27 MPa), and knee articular cartilage (2.1–11.8 MPa);[359] thus, applicability is limited to the soft tissues. For example, Young's modulus of PGS scaffold is two orders of magnitude lower than that of polycaprolactone scaffold, which is suitable for bone tissue engineering.[360,361] To further strengthen the mechanical properties of PGS, additives such as cross-linkers and nanoparticles can be blended into PGS. For example, Pereira *et al.* added hexamethylene diisocyanate into PGS to increase the Young's modulus from 0.38 to 19.7 MPa.[357] The authors speculated that the increased stiffness stems from the rigidity of the added cross-linker. Adding nanoparticles into the PGS matrix has also been effective in tailoring the mechanical properties.[362,363] Wu *et al.* mixed amine-terminated fumed silica into neat poly(glycerol-sebacate-citrate) to increase the tensile strength from 0.9 to 5.3 MPa at 17 wt %.[364] Furthermore, the introduction of fumed silica also weakened the cytotoxicity.[364]

In this study, we propose that a chemical indicator, the degree of esterification (DE) of the synthesized PGS (the extent of reaction between carboxyl groups in sebacic acid and hydroxyl groups in glycerol), can be used to determine the physical status and mechanical properties in a precise and reproducible way. Additionally, we show that the degree of glycerol loss must also be quantified to calibrate the prediction on the basis of DE. From samples with a wide range of prepolymerization methods (thermal vs microwave) and curing thermal history (temperature and time), we demonstrated a linear relation between the Young's modulus of cured PGS and the DE, whereas deviations from the linearity can be predicted by the degree of glycerol loss. For further enhancement of mechanical properties, we studied the effect of adding cross-linking agent, 4,4′-

methylene diphenyl diisocyanate (MDI), and a commodity class of nanoparticles, fumed silica. Finally, we studied the effect of DE and the additives on degradation behavior in PBS solution.

10.2 Experimental Methods

Neat PGS by Conventional Method. PGS was synthesized in two steps. First, a 1:1 molar ratio of glycerol (99%, Sigma-Aldrich) and sebacic acid (SA; 99%, Sigma-Aldrich) were mixed together at room temperature, and the mixture was placed in a convection oven under nitrogen atmosphere at 120, 130, or 140 °C for 24 h. The prepolymerization process resulted in waxy or liquid-like materials when cooled to room temperature. Then, the prepolymers were dissolved in tetrahydrofuran (THF) to form prepolymer/THF solution (0.5 g/mL in THF), and then it was cast into the molds made of aluminum foil (length × width = 10 × 10 cm^2). The prepolymers were placed in a vacuum oven, which was then slowly evacuated to ∼1 mTorr. The specimens were cured for 6–66 h at the same temperature as the prepolymerization process.

Neat PGS by Microwave-Assisted Processing. As a time- and energy-efficient alternative, prepolymerization was performed by using a microwave oven (Panasonic NN-ST642W) in a chemical hood. The microwave oven was set to provide an output of 600 W to the mixture of glycerol and SA. Although the time for the prepolymerization process summed up to 30 min, the microwave oven was vented by opening the door, and the temperature of the mixture was measured by thermometer every 1 min to prevent overheating of samples and buildup of produced gas. After completing the microwave step, prepolymers were allowed to cool and dissolved in THF at room temperature. The solutions were cast into the molds. The specimens were then cured at 130 °C in a vacuum oven for periods of 6–66 h.

Cross-Linking Agent and Nanoparticle Addition. MDI (Sigma-Aldrich) and AEROSIL 380 hydrophilic fumed silica (FS, EVONIK, Parsippany, NJ) were used as additives to modify the mechanical property of neat PGS, denoted as PGS-MDI and PGS-FS, respectively. After prepolymerizing in nitrogen atmosphere at 130 °C for 24 h, the prepolymers were allowed to cool and dissolved with the additives in a cosolvent, THF. For PGS-FS, FS was added into THF solution, which was bath sonicated for 2 h to achieve a good dispersion. Then, specimens were cured at 130 °C in vacuum for 24 h. The maximum loading of the additives, MDI (7.8 wt %) and FS (10 wt %), was limited by experimental difficulties during the preparation. Namely, both MDI and FS

significantly increased the viscosity of the PGS prepolymer solutions. The increased viscosity caused the generation of trapped bubbles in the prepolymer that could not be effectively removed in subsequent processes. After curing, the resulting samples had rough surfaces and trapped bubbles, thus were not suitable for tensile testing.

Molecularly Rigid Cross-Linking Agent. MDI was used as a cross-linking agent that reinforces Young's modulus by adding molecules to the PGS matrix at the molecular level due to rigid phenyl groups. MDI links between hydroxyl groups of a PGS chain using the isocyanate groups. In the current study, the molar mixing ratios between glycerol/SA/MDI in THF solution are 1:1:0.05 and 1:1:0.1, denoted as MDI 4.1 wt % and MDI 7.8 wt %, respectively.

Lacey Structured Inorganic Nanoparticles. FS was added to the PGS to form a nanocomposite. FS has a lacey structure with bead-shaped silica nanoparticles, where the diameter of each particle is about 20 nm. In the current study, 1, 3, 5, and 10 wt % PGS-FS nanocomposites were prepared.

Degree of Esterification in PGS. After the polymerization process is completed, the degree of esterification (DE) was determined by two methods: (i) by quantifying the remaining carboxyl groups and (ii) by measuring mass reduction because of water evaporation.[348] The remaining carboxyl groups were quantified by titration. Here, 0.5 g of specimen was immersed in an ethanol (25 wt %)/toluene (75 wt %) solution in a 250 mL Erlenmeyer flask. A total of 10 drops of bromothymol blue solution were added as a pH indicator. The Erlenmeyer flasks were kept sealed with Parafilm during the titration to prevent the interaction between the specimens and atmospheric CO_2 to form K_2CO_3. In case of high cross-linking density (>76%), complete solvent dissolution was not possible. In such cases, the specimens were ground to form fine powders to allow a full swelling for accurate titration. For each sample, complete dissolution or swelling typically took 2 h. A standardized 0.1 mol/L ethanol solution of potassium hydroxide was used to quantify the remaining carboxyl groups by titration. A color change from yellow to bluish-green indicated the completion of the titration process. For the insoluble powders, 1 h of stabilization time was allowed to accurately define the end point. For each sample, at least three titrations were performed. The degree of the esterification was then calculated by Equation 10.1:[348]

$$\mathrm{DE} = \frac{(V_1 - V_0)C_{\mathrm{KOH}}/(m_{\mathrm{SA}} + m_{\mathrm{G}})}{2/(M_{\mathrm{SA}} + M_{\mathrm{G}} n_{\mathrm{G}}/n_{\mathrm{SA}})} \quad (10.1)$$

where V_1 is the volume of KOH solution used for the specimen titration; V_0 is the volume of KOH solution used for the blank test; C_{KOH} is the concentration of KOH solution; subscripts SA and G denote SA and glycerol, respectively; and *m*, *M*, and n denote the masses, the molecular weights, and the molarities, respectively.

The glycerol loss was quantified as follows. The mixture of glycerol and SA was weighed before and during PGS synthesis. If all molecules in the esterification reaction are non-volatile, then the weight difference can be used to determine the DE. However, glycerol is volatile in the current experimental system; thus, attempts to determine DE without considering weight loss renders nonphysical values >100% DE. Instead, mass loss can be used to calculate the glycerol loss using the following Equation 10.2:[348]

$$\text{Glycerol loss} = \frac{2M_{\mathrm{H2O}}}{M_{\mathrm{G}}}\left(\mathrm{DE} - \frac{\Delta m/M_{\mathrm{H2O}}}{(2m_{\mathrm{SA}}/M_{\mathrm{SA}})}\right) \quad (10.2)$$

where Δm is the total weight loss of the mixture during the synthesis and M_{H2O} is the molecular weight of water.

Fourier Transform Infrared Spectroscopy. Fourier transform infrared (FTIR) spectroscopy was used to compare the chemical bonding characteristics among pre- and cured polymers. A Thermo Nicolet (Madison, WI) 8700 main bench with an attached Continuum FTIR microscope was used in attenuated total reflection (ATR) mode with a Germanium Slide-On ATR microscope objective.

Tensile Tests. Tensile tests were conducted on an Instron 5943 mechanical tester equipped with a 10 kN load cell. Sample preparation and measurement were performed according to ASTM standard D 412-98a.[93] For each sample, three or more polymer strips (25 × 5 mm^2, length × width; 0.8–1.2 mm thickness) were prepared. The Young's modulus of each specimen was calculated by the linear fitting of stress–strain curves at low strain (<10%). The ultimate tensile strength (UTS) was the highest stress that each specimen could reach and elongation at break was the strain when the specimen was completely torn apart.

Degradation Study. For each sample, five polymer strips (5 × 5 mm^2, length × width; 0.8–1.2 mm thickness) were stored in standard phosphate buffer saline (PBS; 1×) at 37 °C for 7, 14, 21, and 28 days. The PBS solutions were refreshed daily. To obtain the exact mass, the degraded polymer strips were dried in a convection oven at 60 °C overnight, then weighed.

10.3 Results and Discussions

10.3.1 PGS Prepolymerization in Nitrogen at Different Temperatures

The characteristics of PGS prepolymerized and cured at different times and temperatures in a nitrogen atmosphere during prepolymerization and curing were compared. The prepolymerization step was fixed to 24 h, whereas the curing step ranged between 6 and 66 h for each sample. The prepolymerization and the curing were done at the same temperature for each sample. The DE and the total mass loss of synthesized PGS are shown in Figure 10.1a and 10.1b. Initially, an intensive esterification was observed between SA and glycerol, as reflected in the DE, followed by an apparent slowing down. The drop in reaction rate was caused by the difference in reactivity of hydroxyl groups in glycerol. The primary hydroxyl groups were more likely prone to react with carboxyl groups in SA. The primary hydroxyl groups were mostly consumed during the first 24 h (*i.e.,* prepolymerization step); then, the reaction between carboxyl groups and secondary hydroxyl groups to cross-link the PGS chains took place. A notable mass loss at the beginning of the curing step can be observed in Figure 10.1b. This is due to the difference in vapor pressure between the prepolymerization and the curing steps. The prepolymerization step took place in a nitrogen atmosphere at 1 atm, whereas curing is done under vacuum at ~1 mTorr. Naturally, unreacted glycerol molecules are evaporated quickly from the specimens upon the beginning of the curing step. The calculated glycerol loss in Figure 10.1c increases from 21.86 to 23.26 and 24.32% as prepolymerization and curing temperature increases from 120 to 130 and 140 °C, respectively, for the total 90 h of the high temperature processes. As a consequence of glycerol evaporation, the molar ratios of glycerol to SA were changing during the whole PGS synthesis process. The actual molar ratios of glycerol to SA decreased from 0.80 to 0.75 when curing temperatures increased from 120 to 140 °C, respectively.

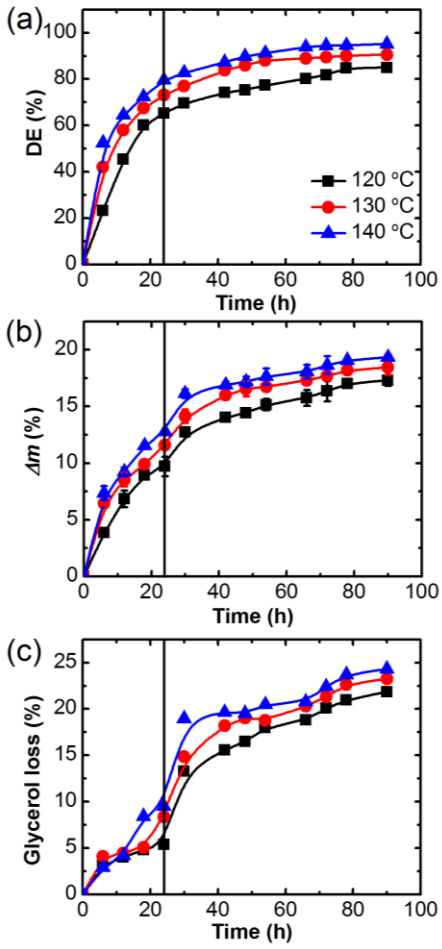

Figure 10.1 Time-dependent evolution of (a) DE, (b) mass loss (Δm), and (c) glycerol loss of PGS specimens during thermal treatment. The solid line at 24 h denotes the sample transfer from prepolymerization in the nitrogen atmosphere to curing in vacuum. For each sample, the same temperature was used for the prepolymerization and the curing steps.

Establishing relations between esterification, thermal history, and physical status of specimens can provide a comprehensive insight about how polymerization and cross-linking impact the physical properties of PGS. At a DE of up to 76%, the specimens can be completely dissolved in the ethanol/toluene solution, whereas the physical appearance may vary as waxy or fluidlike states. As shown in Figure 10.2, the specimens were opaque white wax when the DE was lower than 46%. They were hard, crisp, and not sticky at room temperature. When the DE was between 46 and 65%, the specimens were still waxy but soft because they could be deformed by finger compression; at the same time, they are optically translucent. Between 65 and 76% DE, the

specimens appear as a translucent liquid with high viscosity at room temperature. Between 76 and 84% DE, the specimens were sticky elastomers: stretchable and adhesive. The specimens can only partly dissolve in the ethanol/toluene solution. The adhesiveness was caused by the remaining hydroxyl groups in the PGS. At 84% DE, the specimens were elastomeric but not sticky. They can easily be removed from the aluminum mold without leaving residues. During titration, the ground powder swelled in the ethanol/toluene solution without observable dissolution. The observations were in accordance with the prior study[365] in which the physical status of polymer experiences a step-by-step change by increasing the chain length and cross-link density.

The transition of PGS solubility in ethanol/toluene solution at 76% DE indicates the change in PGS structure. At a DE of under 76%, the complete solubility of PGS suggests that the cross-link density is so low that the level of cross-linking between polymer chains is not reaching a continuum that spans a large volume of the sample. Above 76% DE, however, there is a rather abrupt transition that triggers a heavy level of cross-linking between chains. This phenomenon can be explained as follows: At the beginning of the PGS synthesis process, the primary hydroxyl groups (*i.e.,* at the two ends of the carbon backbone) in the glycerol molecules are predominantly reacting with carboxyl groups. Thus, the formation of linear chains is preferred over branching or cross-linking in the early stage of esterification. This is due to the fact that the activation energy for reaction is lower for the primary hydroxyl groups than for the secondary hydroxyl groups in glycerol.[358]

In summary, the physical status map in Figure 10.2 suggests a comprehensive guideline for thermal treatment for producing the desirable physical status of PGS. For example, when one aims to produce a robust, non-sticky elastomer, > 84% DE needs to be achieved. Likewise, one can target 76% < DE < 84% when aiming to produce an elastomeric adhesive based on PGS.

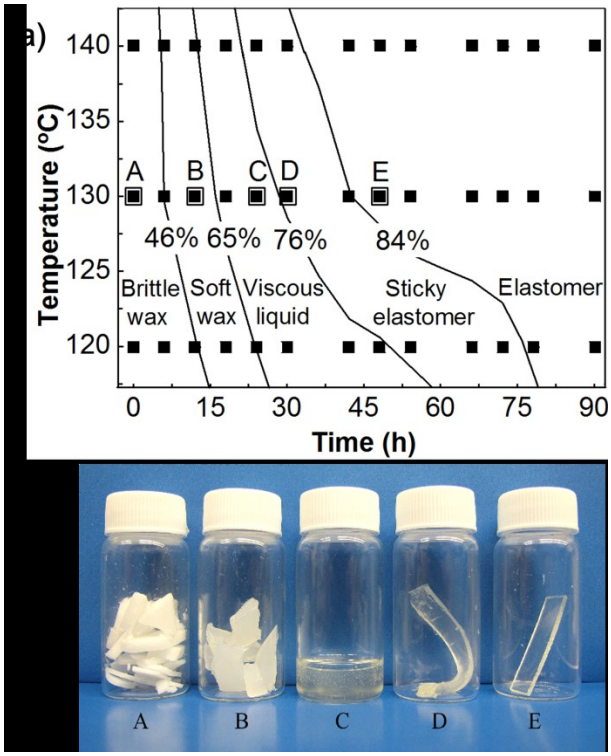

Figure 10.2 (a) Map that describes the relationship between DE and specimen statuses. Filled squares in the figure denote the time and temperature values for thermal treatment (prepolymerization and curing; see Figure 10.1 for explanations) where the measurement of DE and the observation of physical status were made for each specimen. (b) Representative pictures of the five physical statuses at room temperature: A, brittle opaque wax; B, soft translucent wax; C, viscous translucent liquid, D, soft sticky elastomers; E, nonsticky elastomers. The five large squares with letters on top in (a) represent the thermal treatment conditions for the samples shown in (b).

10.3.2 PGS Prepolymerization Using Microwave

A quantitative study on the effect of a microwave-induced prepolymerization step was performed as a function of elapsed time up to 30 min. At every minute, specimens were taken from the microwave to detect the mass loss and temperature. The frequent intervention also prevented overheating and reaction gas buildup. The DE values were obtained with a 3 min interval between data points. At earlier times, up to 6 min, DE values were also obtained every minute. As shown in Figure 10.3, the microwave can steadily increase the DE with a significantly more rapid pace than can prepolymerization in a nitrogen atmosphere between 120 and 140 °C. Only 30 min of

microwave time was required to achieve 52% DE, whereas prepolymerization in nitrogen for 12 h was required to reach 56% DE.

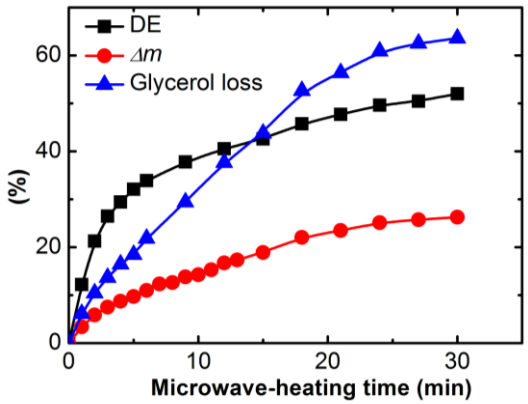

Figure 10.3 Evolution of DE, mass loss (Δ*m*), and glycerol loss values as prepolymerization time increases during microwave heating.

Figure 10.3 shows the DE, the mass loss (Δ*m*), and the glycerol loss evolutions with microwave time. In addition to the quick and efficient esterification, the graph reveals extensive glycerol evaporation. This is due to an intensive energy transfer of the microwaving process. Spatial inhomogeneity of the energy transfer is another well-known problem of using a microwave oven. When overheated, boiling was predominantly observed at the center of the oven. The transient temperature of the mixture measured immediately after the microwave heating process was up to 170 °C. The calculated value of glycerol loss after 30 min of microwave time was 63%, which was much higher than the 5–10% value for the samples prepolymerized for 24 h in nitrogen atmosphere at 1 atm between 120 and 140 °C. In fact, it is even higher than ~20%, which is the typical value from samples that are thermally prepolymerized and then cured under vacuum for 66 h. The observation of the slope change of the curves in Figure 10.3 indicates that the rate of esterification decreases far faster than that of the glycerol loss up to 24 min. From 0 to 3 min, the DE value rapidly increases from 0 to ~30%, whereas the increase slows down significantly from 3 to 30 min, where only 22% increase was obtained over 27 min. The glycerol loss, however, was nearly a linear function up to ~55% loss at 18 min. Therefore, we chose 3 min as a trade-off between efficient prepolymerization and violent glycerol loss.

To investigate whether there is a noticeable difference in chemical bonding between thermal and microwave-assisted prepolymerization methods, we performed FTIR for a number of samples with comparable DE values. The results are shown in Figure 10.4. Absorption peaks at specific wavenumbers represent the relative number of chemical bonds. For example, the stretching mode of the O–H bond produces a characteristic peak at 3300 cm^{-1}, and peaks at 2930 and 2850 cm^{-1} can be attributed to alkene groups. Absorptions at 1730 and 1707 cm^{-1} are caused by a C═O stretching mode. As the DE increases, the intensities of the C═O-bond-induced peaks increases, whereas the intensities of peaks from O–H bonds decrease, indicating an increased density of cross-links. By comparing (4) to (5) and (6) to (7), it can be seem that the specimens prepared by the two different prepolymerization methods do not show any noticeable difference in FTIR peak shapes when the values of DE are identical. This observation indicates that the two distinct prepolymerization methods do not induce a difference in molecular bonding.

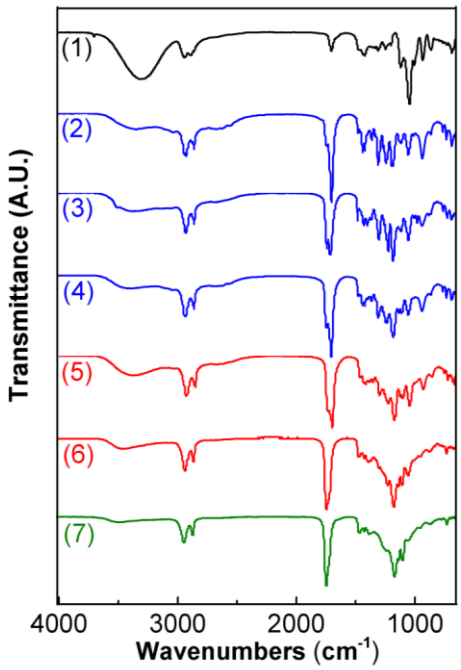

Figure 10.4 FTIR spectra of specimens prepared by different methods: (1) pristine mixture of SA and glycerol, DE = 0; (2) prepolymerized by 3 min of microwave heating, DE = 27%; (3) prepolymerized by 6 min of microwave heating, DE = 34%; (4) prepolymerized by 15 min of microwave heating, DE = 43%; (5) prepolymerized in nitrogen atmosphere for 6 h at 130 °C, DE = 42%; (6) prepolymerized in nitrogen atmosphere for 24 h at 130 °C, DE = 73%; (7) prepolymerized by 3 min of microwave heating, followed by curing under vacuum for 48 h at 130 °C, DE = 74%.

Figure 10.5 shows the effect of vacuum curing on the samples prepolymerized by 3 min of microwave heating. After prepolymerization, the DE was only about 27%, much lower than that of specimens prepolymerized in a nitrogen atmosphere for 24 h (72% at 130 °C). After curing in the vacuum oven for 66, the glycerol loss was about 67%, much higher than that for the nitrogen-prepolymerization counterpart (23% at 130 °C). The glycerol loss also caused a significant alteration in the chemical constitution of the PGS materials. In other words, the molar ratio of glycerol to SA was 0.33 after 66 h of curing at 130 °C; this value is even more severely distorted compared to that of the nitrogen prepolymerization counterpart (0.77, starting molar ratio was 1 in all cases). The extremely high glycerol loss is caused by the low DE in the prepolymerization process. The lower DE indicated that a significant amount of glycerol remained unreacted after microwave prepolymerization, causing severe glycerol evaporation at the beginning of the curing step under vacuum. Possibly, spatial inhomogeneity of the microwave heating process may have worsened this problem. A future study at a similar DE value can provide a rigorous comparison between the two prepolymerization methods.

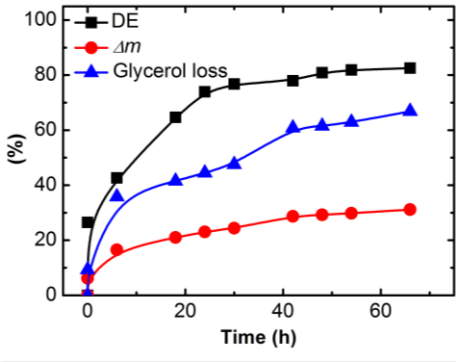

Figure 10.5 Evolution of DE, mass loss (Δ*m*), and glycerol loss values as curing time increases at 130 °C under vacuum. All specimens were prepolymerized by microwave heating for 3 min. The values for the as-prepolymerized specimen are plotted at 0 h. The sudden changes in DE, Δ*m* and glycerol loss are due to microwave heating.

10.3.3 Mechanical Properties of PGS and Its Derivatives

The tensile properties of PGS specimens were tested. Figure 10.6a is the typical tensile test curve of PGS prepared at 130 °C. The Young's modulus increased as the total thermal treatment time increased from 42 to 78 h (from 0.13 ± 0.03 to 1.33 ± 0.05 MPa), whereas the elongations at

break decreased (from 5.53 ± 0.18 to 0.76 ± 0.13). The same trends were also observed for the specimens prepared at 120 and 140 °C in Figure 10.7. The obtained values of Young's moduli, ultimate tensile strength (UTS), and elongation at break are in quantitative agreement with the values from other research groups[348,366] on the basis of thermal history.

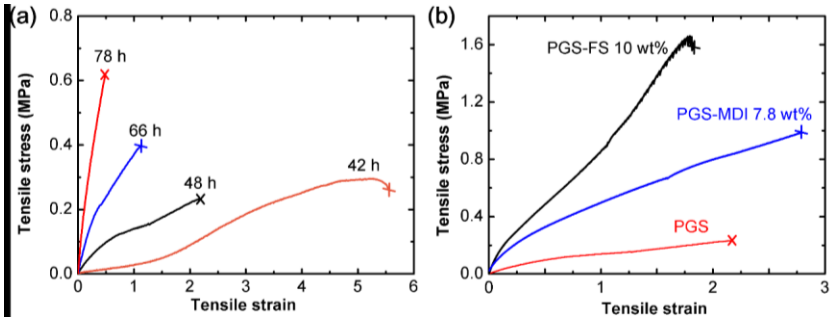

Figure 10.6 (a) Stress–strain curves of PGS specimens prepared with 42, 48, 66, and 78 h total thermal treatment at 130 °C (prepolymerized for 24 h and then cured for 18, 24, 42, and 54 h, respectively). (b) Stress–strain curves of PGS, PGS-MDI 7.8 wt %, and PGS-FS 10 wt %. Specimens were prepolymerized for 24 h and then cured for 24 h at 130 °C

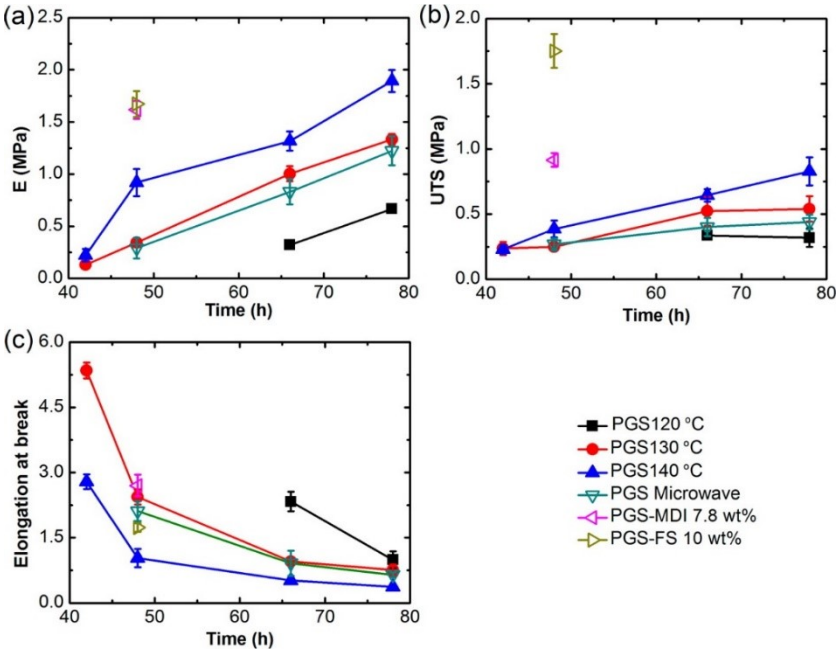

Figure 10.7 (a) Young's modulus, (b) UTS, and (c) elongation at break values as plotted against the total thermal treatment time.

Young's moduli for various processing conditions, including data points from the reference,[348] are plotted against the DE values in Figure 10.8a. Here, we assume that the onset of cross-linking between chains corresponds to the transition of physical statuses from viscous liquid to sticky elastomer. This is based on an assumption that the transition happens when the primary hydroxyl groups of glycerol molecules are depleted and the carboxyl groups in SA start to react with secondary hydroxyl groups in glycerol to form cross-linking. Therefore, we estimated zero Young's modulus at the DE of the transition point. In addition, the ester groups are the only source of cross-linking bonds in neat PGS; thus, we assumed that the cross-link density is proportional to the DE. From an entropic spring model for rubbers, the relationship between Young's modulus and cross-link density is represented by Equation 10.3:[367]

$$n = E/3RT \quad (10.3)$$

where n is the mole of active network chains per unit volume, E is the Young's modulus, R is the universal gas constant, and T is the absolute temperature. Because two active network chains are produced by a cross-link, which is proportional to the DE, the Young's modulus is proportional to the DE. The fitting line (dash red) in Figure 10.8a is the linear regression of the data points, excluding the specimens prepared by microwave heating. The intersection of the fitting line and the zero Young's modulus line is 79%, which means that the Young's modulus converges to 0 when the DE is 79%. The value is in a convincing agreement with the critical DE value of 76% for physical state transition between viscous liquid and soft elastomer as well as the limit for the complete solubility in the ethanol/toluene solution for titration.

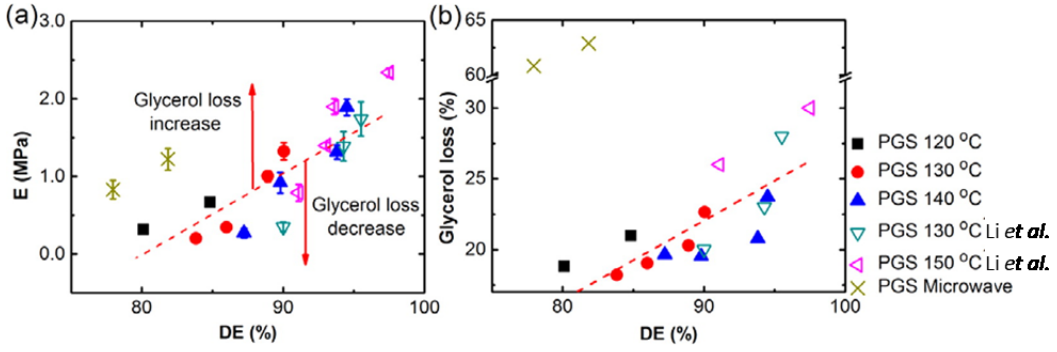

Figure 10.8 (a) Young's moduli and (b) glycerol loss values plotted against the DE values. Data are obtained from the current study and Li *et al.*[348] The dash red fitting lines are the linear regression, excluding specimens prepolymerized by microwave heating.

In addition, the glycerol loss has a pronounced effect on the PGS properties by changing the molar ratio between glycerol and SA in the polymer chains. In Figure 10.8b, the glycerol losses from all specimens are in the range of 15–30% when we exclude the specimens prepared by microwave heating. Glycerol loss increases with increasing DE; consequently, the molar ratio of glycerol to SA decreases. Because the molecular rigidity of the two molecules are different, the lower molar ratio of glycerol to SA results in a more rigid PGS.[368,369] Therefore, the Young's modulus will appear higher than the model prediction if the glycerol loss is more severe. If we consider that the higher DE usually accompanies a higher level of glycerol loss then one can confirm that the slope in the linear regression is inevitably overestimated. In other words, the intercept at the zero Young's modulus of the fitting line would be less than 79% if the line was not distorted by the additional glycerol loss.

The large deviation of the Young's moduli values of microwave-assisted prepolymerization specimens can also be understood on the basis of the same logic. The molar ratios of glycerol to SA are very different between specimens prepolymerized in a nitrogen oven (Figure 10.1) and by microwave heating (Figure 10.5), roughly around 0.8 and 0.4, respectively. This explains the large deviation of Young's modulus for microwaved specimens to higher values. In addition, it also can explain the left shift of the physical state transition boundary between viscous liquid and the soft elastomers. For example, the DE value of the PGS specimen with 3 min prepolymerization in microwave followed by curing at 130 °C for 24h was 74%, and the Young's modulus was 0.29 ± 0.10 MPa. According to Figure 10.2, viscous liquid is expected instead of the observed soft elastomer. Therefore, the effect of glycerol loss in determining the boundaries between the physical states needs to be considered. To minimize the effect of the glycerol loss, polyol with a higher molecular weight may be considered for the synthesis of poly(polyol sebacate) polymers.[369,370]

The effects of molecularly rigid cross-linking agents on the Young's moduli are shown in Figures 10.6b and Figure 10.9. The graphs clearly show that the Young's modulus increases with the addition of MDI (from 0.34 ± 0.04 to 1.62 ± 0.09 MPa with increasing MDI content from 0 to 7.8 wt %). The elongation at break also slightly improves (from 2.44 ± 0.17 to 2.70 ± 0.25). The improvement is in agreement with earlier studies of PGS derivatives with additional cross-linking agents with molecular rigidity.[371,372] It must be noted that the amount of MDI must be moderate

because an excessive amount of MDI makes the material nonelastomeric. In addition, some of the earlier studies report the cytotoxicity of MDI molecules.[373]

The addition of FS also significantly improves the ultimate tensile strength and the Young's modulus of PGS-FS nanocomposite compared to those of neat PGS with the same synthesis conditions. (Young's moduli and UTS values increase from 0.34 ± 0.04 to 1.67 ± 0.12 MPa and from 0.25 ± 0.03 to 1.75 ± 0.13 MPa, respectively, as the FS content increases from 0 to 10 wt %.) However, the elongation at break was slightly compromised (from 2.44 ± 0.17 to 1.73 ± 0.13). A possible explanation of the reduced elongation at the break is that the hard FS particles act as crack initiators and concentrators in the soft PGS matrix. It can also be hypothesized that improved adhesion between FS and PGS may alleviate the problem. Further studies, including the compatibility between FS and PGS and the network/aggregation structures of FS, can lead to further optimization of the mechanical properties of the PGS-FS composites.

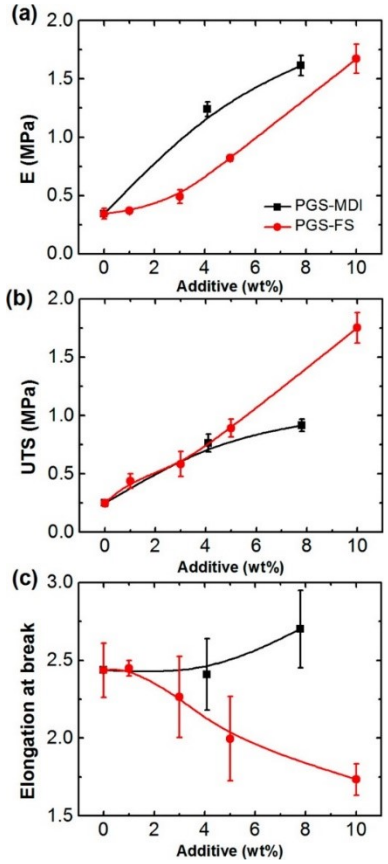

Figure 10.9 (a) Young's moduli, (b) UTS, and (c) elongation at break plotted against weight percents of MDI and FS loaded in the PGS matrix.

10.3.4 Degradation Study of PGS and Its Derivatives

The degradation of PGS and its derivatives in PBS solution was studied. Figure 10.10a shows the mass evolution of PGS samples stored in PBS at 37 °C. The dotted line in Figure 10.10 means the samples were degraded into viscous liquid; thus, we were unable to collect and weigh them. For neat PGS (48 h, 130 °C; DE = 86%), the mass loss after 14 days was 18.76 ± 1.72%, and the sample became viscous liquid after 17 days. As the curing time increased to 66, 78, and 90 h (*i.e.,* DE increases to 89, 90, and 92%, respectively), the mass loss after 28 days decreased to 16.93 ± 1.48, 14.67 ± 2.90, and 13.21 ± 1.93%, respectively. With the increase of the DE, the degradation rate decreased because a greater number of ester bonds needed to be broken during degradation via a surface erosion mechanism.[356] Figure 10.10b describes the mass loss of PGS derivatives during the degradation process. All samples in Figure 10.10b were cured for 48 h at 130 °C. The graph shows that the degradation rate decreases with the addition of MDI. For PGS-MDI 4.1 wt %, the mass loss after 21 days was 23.34 ± 4.12%, and the sample became totally viscous liquid after 24 days. For PGS-MDI 7.8 wt %, the mass loss after 28 days was 18.96 ± 2.48%. Note that the degradation rate is much slower than that of neat PGS at the same curing time (viscous liquid after 17 days). This can be attributed to increased cross-linking density because of the cross-linking agent, MDI. The addition of FS nanopaticles is also effective in decreasing the degradation rate (27.68 ± 2.08% for PGS-FS 5 wt % and 10.23 ± 1.67% for PGS-FS 10 wt %). This may be due to the increased strand density caused by the esterification of FS nanoparticles within the PGS networks.[363]

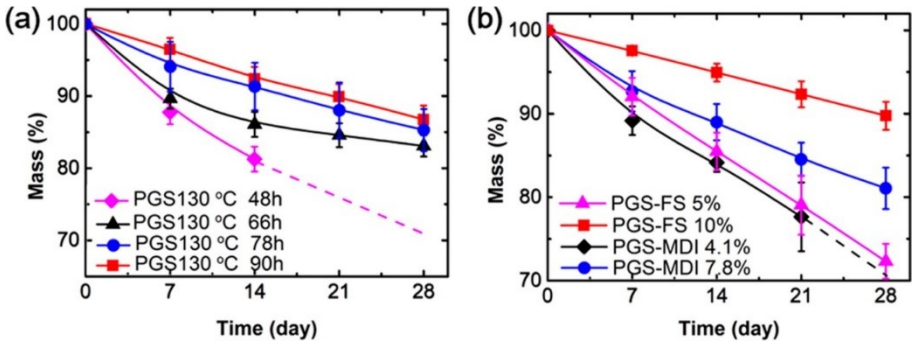

Figure 10.10 Degradation of PGS and its derivatives as quantified by mass loss vs storing time in 1× PBS. (a) Neat PGS samples prepared with 48, 66, 78, and 90 h of total thermal treatment times at 130 °C (prepolymerized for 24 h and then cured for 24, 42, 54, and 66 h, respectively; compare with Figure 10.1 to facilitate understanding). (b) The derivatives of PGS, namely PGS-FS 5 wt %, PGS-FS 10 wt %, PGS-MDI 4.1 wt %, and PGS-MDI 7.8 wt %. Specimens were prepolymerized for 24 h and then cured for 24 h at 130 °C.

10.4 Conclusion

The degree of esterification (DE) is shown to be effective in quantitatively predicting the physical state and Young's moduli and degradation of PGS. Loss of volatile monomers during esterification, glycerol in PGS's case, is shown to cause a deviation from the prediction based on the DE. In short, one can precisely tailor the mechanical properties and degradation of PGS by an experimentally obtainable chemical property, the DE, whereas a more precise prediction can be achieved by a further deconvolution of quantifying the glycerol/SA ratio. This strategy can also be applied to different categories of polymers that involve condensation polymerization with the volatility of the reactants.

To achieve consistency in properties for the quick synthesis method of microwave-assisted prepolymerization, the effect of microwave time was also studied in terms of the DE. The microwave method is shown to be effective to achieve a high degree of DE in a short time (for less than 30 min), suggesting that it can provide a time- and energy-conserving synthesis pathway compared to a conventional prepolymerization method in a nitrogen oven (for hours to days). For example, 15 min of microwave treatment provided the same value of DE as 6 h in a nitrogen atmosphere at 130 °C. The FTIR study showed that there is no noticeable difference between the methods in terms of chemical bonds. However, intensive glycerol evaporation caused a severe distortion in the ratio of glycerol to SA, which results in a stiffer PGS when cured.

The addition of cross-linking agents with rigid molecular structure, such as MDI, can result in a significant increase in the Young's modulus without compromising the stretchability. This indicates that cross-linking agents with various molecular structures can provide an efficient pathway to tailor the properties of PGS derivatives for various applications to which neat PGS cannot be applied. Nanoparticles, fumed silica in this study, were also shown to be effective in enhancing the Young's modulus and UTS. Further studies on optimizing the additives may open up the possibility of PGS-derived materials to wide applications. Both cross-linking agents and nanoparticles can significant decrease the degradation rate by increasing strand density in PGS networks.

Chapter 11 Summary and Future Work

11.1 Summary

In Chapter 4, a network of globule structures in the charge-balanced poly(NaSS-*co*-MPTC) polyampholyte hydrogels is discovered by SAXS and visualized by SEM techniques. Highly hydrated globules with a radius of gyration of 2 ~ 2.5 nm formed a networked structure in the charge-balanced polyampholyte hydrogels, whereas the size and the clustering are dependent on synthesis parameters. The globular network structure results in an increase in amorphous water at −30 °C, as supported by WAXS results. Based on variable-temperature SAXS, WAXS, SEM, STEM and solid-state NMR results, it was proposed that these highly hydrated networked globules formed percolated polymer-rich domains while sub-micron, slush-like ice crystals formed from water-rich domains, resulting in ion-conducting channels that are rich in amorphous water molecules at low temperatures. In Chapter 5, through quantitative DSC analysis, we propose a differentiation of the water states in the polyampholyte hydrogel into four categories and quantify the ice formation in polyampholyte hydrogel at sub-zero temperature. Different synthesis conditions may change the ice amount in the polyampholyte hydrogel. Finally, in Chapter 6, based on the qualitative understanding of enhanced ionic conductivity of polyampholyte hydrogel, a supercapacitor made of polyampholyte was fabricated.

In Chapters 6 to 9, we developed several devices which can be utilized in various applications in flexible electronics and in wearable biomedical devices. In Chapter 6, a flexible smart window is made by a polyampholyte hydrogel showing 80% in transmittance contrast from opalescence (at a low temperature) to transparency (at a high temperature), which could undergo a large deformation (up to 80% strain). By printing a stretchable elastic heater layer onto the hydrogel film, we demonstrated a pixelated array of actively tunable smart windows. In Chapter 7, a supercapacitor with flexibility, self-healing properties and a high energy density that works at low temperature was fabricated with a combination of BC-RGO electrodes and a polyampholyte hydrogel showing a high energy density of 30 Wh/kg, and a capacitance retention of ~90% after 5000 charge–discharge cycles. At low temperature (−30 °C), the SC-PA had an energy density of 10.5 Wh/kg at a power density of 500 W/kg. In Chapter 8, we suggested a self-reinforcing nanocomposite of graphene nanoflakes that are enclosed by self-assembled GO particles. A two-

step acid treatment protocol reduced GO into RGO, enhancing the electrical conductivity of the composite coating. The substrate material was 3D printed porous elastomers prepared by a commercial filament material. The GNF-RGO composite coatings were applied on 3D-printed objects to transform the non-functional elastomers into flexible radio frequency antennae and strain sensors. In Chapter 9, the fabricated nanogenerator yielded open circuit voltage ranging up to ~0.5 V and short circuit current density ranging up to ~2 μA/cm^2, upon bending every 5 s. In an improvised durability test, degradation in output voltage was not found after ~3000 bending and releasing cycles. Moreover, in Chapter 10, a promising biocompatible elastomer for biomedical applications, PGS, was investigated. The mechanical properties and degradation of PGS can be precisely tailored by an experimentally obtainable chemical property, the DE, whereas a more precise prediction can be achieved by a further deconvolution of quantifying the glycerol/SA ratio. To achieve consistency in properties for the quick synthesis method of microwave-assisted prepolymerization, the effect of microwave time was also studied in terms of the DE. The microwave method is shown to be effective to achieve a high degree of DE in a short time (for less than 30 min), suggesting that it can provide a time- and energy-conserving synthesis pathway compared to a conventional prepolymerization method in a nitrogen oven (for hours to days). However, intensive glycerol evaporation caused a severe distortion in the ratio of glycerol to SA, which results in a stiffer PGS when cured. The addition of cross-linking agents with rigid molecular structure, such as MDI, can result in a significant increase in the Young's modulus without compromising the stretchability. Nanoparticles, fumed silica, were also shown to be effective in enhancing the Young's modulus and UTS.

11.2 Future Work

The findings of Chapters 4 and 5 shed light on the development of high conductivity gel electrolytes for application as energy storage devices operating at low temperature, because the ionic conductivity of the hydrogel electrolyte layer dominates the series resistance of the electrochemical storage device, and further affects the power density of the device, following the relationship:[374] $P_{\max} = \frac{U^2}{4RM}$, where $P_{\max}$ is the maximum power density, M is the total mass of active materials in the device, U is the cell voltage, and R is the equivalent series resistance of the device. At low temperature, the resistance increases sharply when the electrolyte freezes, leading

to a compromised electrolytic performance. However, in polyampholyte hydrogel based electrolytes, the water states and ice morphology are changed due to the existence of globular structure self-assembled by polyampholyte chains, leading to an increased ionic conductivity.[154] When temperature decreases, the frozen hydrogel has two bi-continues domains, *i.e.,* an ice-domain and a polymer-rich domain, as evidenced by SEM image. Thus, the ionic conductivity of the frozen hydrogel is contributed to by Na^+ and Cl^- in the three well-defined regions, which are the ice domain, the polymer-rich domain, and the interface between the ice and polymer-rich domains. It is reasonable to speculate that those Na^+ and Cl^- have different mobilities in the three regions. Our previous solid-state NMR results (Figure 4.12 and 4.13) showed the presence of two distinct feature types in the ^2H spectra with both the Pake pattern and the sharp peak at –49 °C suggesting at least two distinctive statuses for the water molecules with different mobilities in the frozen hydrogel. More variable-temperature solid-state ^{23}Na NMR results have to be acquired to get the relationship between the mobility of ^{23}Na ions and temperature in the polyampholyte hydrogel. The information will be further used to connect the concepts of the ice amount, water states, and ionic conductivity in a quantitative manner. This future work will provide guidance for designing the ionic conductive hydrogel as the gel electrolyte in energy storage devices.

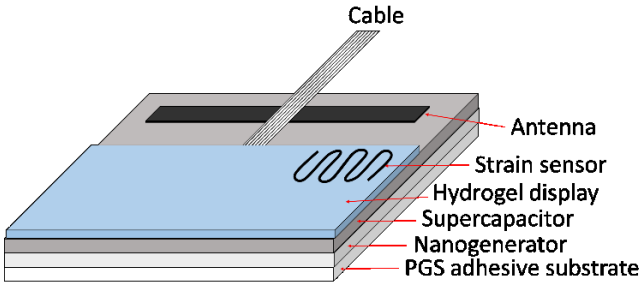

Figure 11.1 Illustration of a conceptual device using the materials and devices developed in this dissertation.

The similarity among devices and materials developed in Chapters 6 to 10 is that all of them are intrinsically flexible, which shows the possibility of integrating them into one device. For example, as shown in Figure 11.1, we propose a conceptual device with a multilayer architecture. Since the conceived device is for wearable application, a biocompatible adhesive layer made of PGS elastomer can be applied. The second layer is a nanogenerator, which can harvest energy by converting mechanical motion to electrical energy. Then the electrical energy generated will be

stored in the third layer, which is a solid-state supercapacitor. The excessive energy can also be output to the external device via a cable. On the top of the device, a multi-pixelated smart window is employed as a simple controlled display. The antenna fabricated by inject-printing techniques provides wireless data transmission, while the stain sensor can monitor the strain level of the device to prevent mechanical failure caused by excessive deformation. We foresee that such a device configuration can be utilized in various applications in flexible electronics and in wearable biomedical devices.

References

1. Wichterle, O.; Lim, D., Hydrophilic Gels for Biological Use. *Nature* **1960,** *185*, 117.
2. Buwalda, S. J.; Boere, K. W. M.; Dijkstra, P. J.; Feijen, J.; Vermonden, T.; Hennink, W. E., Hydrogels in a Historical Perspective: From Simple Networks to Smart Materials. *Journal of Controlled Release* **2014,** *190*, 254-273.
3. Kopecek, J., Hydrogels: From Soft Contact Lenses and Implants to Self-Assembled Nanomaterials. *Journal of Polymer Science Part A: Polymer Chemistry* **2009,** *47*, 5929-5946.
4. Yahia, L.; Chirani, N.; Gritsch, L.; Motta, F. L.; Fare, S., History and Applications of Hydrogels. *Journal of biomedical sciences* **2015,** *4*, 100013.
5. Keplinger, C.; Sun, J.-Y.; Foo, C. C.; Rothemund, P.; Whitesides, G. M.; Suo, Z., Stretchable, Transparent, Ionic Conductors. *Science* **2013,** *341*, 984-987.
6. Kim, S.; Laschi, C.; Trimmer, B., Soft Robotics: A Bioinspired Evolution in Robotics. *Trends in biotechnology* **2013,** *31*, 287-294.
7. Calvert, P., Hydrogels for Soft Machines. *Advanced Materials* **2009,** *21*, 743-756.
8. Sun, J.-Y.; Zhao, X.; Illeperuma, W. R.; Chaudhuri, O.; Oh, K. H.; Mooney, D. J.; Vlassak, J. J.; Suo, Z., Highly Stretchable and Tough Hydrogels. *Nature* **2012,** *489*, 133.
9. Gong, J. P., Why Are Double Network Hydrogels So Tough? *Soft Matter* **2010,** *6*, 2583-2590.
10. Gong, J. P.; Katsuyama, Y.; Kurokawa, T.; Osada, Y., Double-Network Hydrogels with Extremely High Mechanical Strength. *Advanced Materials* **2003,** *15*, 1155-1158.
11. Tsukeshiba, H.; Huang, M.; Na, Y.-H.; Kurokawa, T.; Kuwabara, R.; Tanaka, Y.; Furukawa, H.; Osada, Y.; Gong, J. P., Effect of Polymer Entanglement on the Toughening of Double Network Hydrogels. *The Journal of Physical Chemistry B* **2005,** *109*, 16304-16309.
12. Haraguchi, K., Nanocomposite Hydrogels. *Current Opinion in Solid State and Materials Science* **2007,** *11*, 47-54.
13. Haraguchi, K.; Takehisa, T., Nanocomposite Hydrogels: A Unique Organic–Inorganic Network Structure with Extraordinary Mechanical, Optical, and Swelling/De-Swelling Properties. *Advanced Materials* **2002,** *14*, 1120-1124.
14. Haraguchi, K.; Takehisa, T.; Fan, S., Effects of Clay Content on the Properties of Nanocomposite Hydrogels Composed of Poly (N-Isopropylacrylamide) and Clay. *Macromolecules* **2002,** *35*, 10162-10171.
15. Zhao, C.; Domon, Y.; Okumura, Y.; Okabe, S.; Shibayama, M.; Ito, K., Sliding Mode of Cyclodextrin in Polyrotaxane and Slide-Ring Gel. *Journal of Physics: Condensed Matter* **2005,** *17*, S2841.
16. Karino, T.; Okumura, Y.; Ito, K.; Shibayama, M., Sans Studies on Spatial Inhomogeneities of Slide-Ring Gels. *Macromolecules* **2004,** *37*, 6177-6182.
17. Sun, T. L.; Kurokawa, T.; Kuroda, S.; Ihsan, A. B.; Akasaki, T.; Sato, K.; Haque, M. A.; Nakajima, T.; Gong, J. P., Physical Hydrogels Composed of Polyampholytes Demonstrate High Toughness and Viscoelasticity. *Nature Materials* **2013,** *12*, 932-937.
18. Ihsan, A. B.; Sun, T. L.; Kurokawa, T.; Karobi, S. N.; Nakajima, T.; Nonoyama, T.; Roy, C. K.; Luo, F.; Gong, J. P., Self-Healing Behaviors of Tough Polyampholyte Hydrogels. *Macromolecules* **2016**, *49*, 4245-4252.

19. Asaka, K.; Fujiwara, N.; Oguro, K.; Onishi, K.; Sewa, S., State of Water and Ionic Conductivity of Solid Polymer Electrolyte Membranes in Relation to Polymer Actuators. *Journal of Electroanalytical Chemistry* **2001,** *505*, 24-32.
20. Hickner, M. A., Water-Mediated Transport in Ion-Containing Polymers. *Journal of Polymer Science Part B: Polymer Physics* **2012,** *50*, 9-20.
21. Briscoe, W. H.; Titmuss, S.; Tiberg, F.; Thomas, R. K.; McGillivray, D. J.; Klein, J., Boundary Lubrication under Water. *Nature* **2006,** *444*, 191-194.
22. Deek, J.; Chung, P. J.; Kayser, J.; Bausch, A. R.; Safinya, C. R., Neurofilament Sidearms Modulate Parallel and Crossed-Filament Orientations Inducing Nematic to Isotropic and Re-Entrant Birefringent Hydrogels. *Nature communications* **2013,** *4*, 2224.
23. Chen, S.; Li, L.; Zhao, C.; Zheng, J., Surface Hydration: Principles and Applications toward Low-Fouling/Nonfouling Biomaterials. *Polymer* **2010,** *51*, 5283-5293.
24. Chen, M.; Briscoe, W. H.; Armes, S. P.; Klein, J., Lubrication at Physiological Pressures by Polyzwitterionic Brushes. *Science* **2009,** *323*, 1698-1701.
25. Roy, C. K.; Guo, H. L.; Sun, T. L.; Bin Ihsan, A.; Kurokawa, T.; Takahata, M.; Nonoyama, T.; Nakajima, T.; Gong, J. P., Self-Adjustable Adhesion of Polyampholyte Hydrogels. *Advanced Materials* **2015,** *27*, 7344.
26. Zhou, G.; Luo, J.; Liu, C.; Chu, L.; Ma, J.; Tang, Y.; Zeng, Z.; Luo, S., A Highly Efficient Polyampholyte Hydrogel Sorbent Based Fixed-Bed Process for Heavy Metal Removal in Actual Industrial Effluent. *Water Research* **2016,** *89*, 151-160.
27. Wei, Z.; Yang, J. H.; Zhou, J.; Xu, F.; Zrinyi, M.; Dussault, P. H.; Osada, Y.; Chen, Y. M., Self-Healing Gels Based on Constitutional Dynamic Chemistry and Their Potential Applications. *Chemical Society Reviews* **2014,** *43*, 8114-8131.
28. Li, X.; Liu, L.; Wang, X.; Ok, Y. S.; Elliott, J. A. W.; Chang, S. X.; Chung, H.-J., Flexible and Self-Healing Aqueous Supercapacitors for Low Temperature Applications: Polyampholyte Gel Electrolytes with Biochar Electrodes. *Scientific Reports* **2017,** *7*, 1685.
29. La, T.-G.; Li, X.; Kumar, A.; Fu, Y.; Yang, S.; Chung, H.-J., Highly Flexible, Multipixelated Thermosensitive Smart Windows Made of Tough Hydrogels. *ACS Applied Materials & Interfaces* **2017,** *9*, 33100-33106.
30. Nisato, G.; Munch, J.; Candau, S., Swelling, Structure, and Elasticity of Polyampholyte Hydrogels. *Langmuir* **1999,** *15*, 4236-4244.
31. Georgiev, G. S.; Kamenska, E. B.; Vassileva, E. D.; Kamenova, I. P.; Georgieva, V. T.; Iliev, S. B.; Ivanov, I. A., Self-Assembly, Antipolyelectrolyte Effect, and Nonbiofouling Properties of Polyzwitterions. *Biomacromolecules* **2006,** *7*, 1329-1334.
32. Wang, F.; Yang, J.; Zhao, J., Understanding Anti-Polyelectrolyte Behavior of a Well-Defined Polyzwitterion at the Single-Chain Level. *Polymer international* **2015,** *64*, 999-1005.
33. Schulz, D. N.; Peiffer, D. G.; Agarwal, P. K.; Larabee, J.; Kaladas, J. J.; Soni, L.; Handwerker, B.; Garner, R. T., Phase Behaviour and Solution Properties of Sulphobetaine Polymers. *Polymer* **1986,** *27*, 1734-1742.
34. Huglin, M. B.; Radwan, M. A., Unperturbed Dimensions of a Zwitterionic Polymethacrylate. *Polymer international* **1991,** *26*, 97-104.
35. Ye, T.; Song, Y.; Zheng, Q., Salt Response and Rheological Behavior of Acrylamide-Sulfobetaine Copolymer. *Colloid and Polymer Science* **2016,** *294*, 389-397.
36. Dobrynin, A. V.; Colby, R. H.; Rubinstein, M., Polyampholytes. *Journal of Polymer Science Part B: Polymer Physics* **2004,** *42*, 3513-3538.

37. Edwards, S.; King, P.; Pincus, P., Phase Changes in Polyampholytes. *Ferroelectrics* **1980,** *30*, 3-6.
38. Bechinger, C.; Ferrere, S.; Zaban, A.; Sprague, J.; Gregg, B. A., Photoelectrochromic Windows and Displays. *Nature* **1996,** *383*, 608.
39. Granqvist, C. G., Electrochromics for Smart Windows: Oxide-Based Thin Films and Devices. *Thin Solid Films* **2014,** *564*, 1-38.
40. Wang, Y.; Runnerstrom, E. L.; Milliron, D. J., Switchable Materials for Smart Windows. *Annual review of chemical and biomolecular engineering* **2016,** *7*, 283-304.
41. Gomez-Romero, P., Hybrid Organic-Inorganic Materials - in Search of Synergic Activity. *Advanced Materials* **2001,** *13*, 163-174.
42. Granqvist, C.; Azens, A.; Hjelm, A.; Kullman, L.; Niklasson, G. A.; Rönnow, D.; Mattsson, M. S.; Veszelei, M.; Vaivars, G., Recent Advances in Electrochromics for Smart Windows Applications. *Solar energy* **1998,** *63*, 199-216.
43. Jensen, J.; Krebs, F. C., From the Bottom up–Flexible Solid State Electrochromic Devices. *Advanced Materials* **2014,** *26*, 7231-7234.
44. Babulanam, S. M.; Eriksson, T. S.; Niklasson, G. A.; Granqvist, C. G., Thermochromic Vo2 Films for Energy-Efficient Windows. *Solar Energy Materials* **1987,** *16*, 347-363.
45. Lu, N.; Zhang, P.; Zhang, Q.; Qiao, R.; He, Q.; Li, H.-B.; Wang, Y.; Guo, J.; Zhang, D.; Duan, Z., Electric-Field Control of Tri-State Phase Transformation with a Selective Dual-Ion Switch. *Nature* **2017,** *546*, 124.
46. Wang, N.; Duchamp, M.; Dunin-Borkowski, R. E.; Liu, S.; Zeng, X.; Cao, X.; Long, Y., Terbium-Doped Vo2 Thin Films: Reduced Phase Transition Temperature and Largely Enhanced Luminous Transmittance. *Langmuir* **2016,** *32*, 759-764.
47. Chen, Z.; Gao, Y.; Kang, L.; Cao, C.; Chen, S.; Luo, H., Fine Crystalline Vo 2 Nanoparticles: Synthesis, Abnormal Phase Transition Temperatures and Excellent Optical Properties of a Derived Vo 2 Nanocomposite Foil. *Journal of Materials Chemistry A* **2014,** *2*, 2718-2727.
48. Kim, H.; Kim, Y.; Kim, K. S.; Jeong, H. Y.; Jang, A.-R.; Han, S. H.; Yoon, D. H.; Suh, K. S.; Shin, H. S.; Kim, T., Flexible Thermochromic Window Based on Hybridized Vo2/Graphene. *ACS nano* **2013,** *7*, 5769-5776.
49. Patil, R. A.; Devan, R. S.; Liou, Y.; Ma, Y.-R., Efficient Electrochromic Smart Windows of One-Dimensional Pure Brookite Tio2 Nanoneedles. *Solar Energy Materials and Solar Cells* **2016,** *147*, 240-245.
50. Laurenti, M.; Bianco, S.; Castellino, M.; Garino, N.; Virga, A.; Pirri, C. F.; Mandracci, P., Toward Plastic Smart Windows: Optimization of Indium Tin Oxide Electrodes for the Synthesis of Electrochromic Devices on Polycarbonate Substrates. *ACS applied materials & interfaces* **2016,** *8*, 8032-8042.
51. Bella, F.; Leftheriotis, G.; Griffini, G.; Syrrokostas, G.; Turri, S.; Grätzel, M.; Gerbaldi, C., A New Design Paradigm for Smart Windows: Photocurable Polymers for Quasi-Solid Photoelectrochromic Devices with Excellent Long-Term Stability under Real Outdoor Operating Conditions. *Advanced Functional Materials* **2016,** *26*, 1127-1137.
52. Zhou, Y.; Cai, Y.; Hu, X.; Long, Y., Temperature-Responsive Hydrogel with Ultra-Large Solar Modulation and High Luminous Transmission for "Smart Window" Applications. *Journal of Materials Chemistry A* **2014,** *2*, 13550-13555.

53. Yang, Y.-S.; Zhou, Y.; Chiang, F. B. Y.; Long, Y., Temperature-Responsive Hydroxypropylcellulose Based Thermochromic Material and Its Smart Window Application. *RSC Advances* **2016,** *6*, 61449-61453.
54. Liu, J.; An, T.; Chen, Z.; Wang, Z.; Zhou, H.; Fan, T.; Zhang, D.; Antonietti, M., Carbon Nitride Nanosheets as Visible Light Photocatalytic Initiators and Crosslinkers for Hydrogels with Thermoresponsive Turbidity. *Journal of Materials Chemistry A* **2017,** *5*, 8933-8938.
55. Zhou, Y.; Layani, M.; Boey, F. Y. C.; Sokolov, I.; Magdassi, S.; Long, Y., Electro-Thermochromic Devices Composed of Self-Assembled Transparent Electrodes and Hydrogels. *Advanced Materials Technologies* **2016,** *1*, 1600069.
56. Owusu-Nkwantabisah, S.; Gillmor, J.; Switalski, S.; Mis, M. R.; Bennett, G.; Moody, R.; Antalek, B.; Gutierrez, R.; Slater, G., Synergistic Thermoresponsive Optical Properties of a Composite Self-Healing Hydrogel. *Macromolecules* **2017,** *50*, 3671-3679.
57. Blake, P.; Brimicombe, P. D.; Nair, R. R.; Booth, T. J.; Jiang, D.; Schedin, F.; Ponomarenko, L. A.; Morozov, S. V.; Gleeson, H. F.; Hill, E. W.; Geim, A. K.; Novoselov, K. S., Graphene-Based Liquid Crystal Device. *Nano Letters* **2008,** *8*, 1704-1708.
58. Khandelwal, H.; Loonen, R. C. G. M.; Hensen, J. L. M.; Debije, M. G.; Schenning, A. P. H. J., Electrically Switchable Polymer Stabilised Broadband Infrared Reflectors and Their Potential as Smart Windows for Energy Saving in Buildings. *Scientific Reports* **2015,** *5*, 11773.
59. Gong, X. Q.; Li, J. X.; Chen, S. Y.; Wen, W. J., Copolymer Solution-Based "Smart Window". *Applied Physics Letters* **2009,** *95,* 251907.
60. Haque, M. A.; Kurokawa, T.; Gong, J. P., Super Tough Double Network Hydrogels and Their Application as Biomaterials. *Polymer* **2012,** *53*, 1805-1822.
61. Zhao, X., Multi-Scale Multi-Mechanism Design of Tough Hydrogels: Building Dissipation into Stretchy Networks. *Soft Matter* **2014,** *10*, 672-687.
62. Ihsan, A. B.; Sun, T. L.; Kurokawa, T.; Karobi, S. N.; Nakajima, T.; Nonoyama, T.; Roy, C. K.; Luo, F.; Gong, J. P., Self-Healing Behaviors of Tough Polyampholyte Hydrogels. *Macromolecules* **2016,** *49*, 4245-4252.
63. Tsai, W.-Y.; Lin, R.; Murali, S.; Li Zhang, L.; McDonough, J. K.; Ruoff, R. S.; Taberna, P.-L.; Gogotsi, Y.; Simon, P., Outstanding Performance of Activated Graphene Based Supercapacitors in Ionic Liquid Electrolyte from −50 to 80 °C. *Nano Energy* **2013,** *2*, 403-411.
64. Lin, R.; Taberna, P.-L.; Fantini, S.; Presser, V.; Pérez, C. R.; Malbosc, F.; Rupesinghe, N. L.; Teo, K. B. K.; Gogotsi, Y.; Simon, P., Capacitive Energy Storage from −50 to 100 °C Using an Ionic Liquid Electrolyte. *The Journal of Physical Chemistry Letters* **2011,** *2*, 2396-2401.
65. Brandon, E. J.; West, W. C.; Smart, M. C.; Whitcanack, L. D.; Plett, G. A., Extending the Low Temperature Operational Limit of Double-Layer Capacitors. *Journal of Power Sources* **2007,** *170*, 225-232.
66. Armand, M.; Endres, F.; MacFarlane, D. R.; Ohno, H.; Scrosati, B., Ionic-Liquid Materials for the Electrochemical Challenges of the Future. *Nature materials* **2009,** *8*, 621-629.
67. Ranke, J.; Müller, A.; Bottin-Weber, U.; Stock, F.; Stolte, S.; Arning, J.; Störmann, R.; Jastorff, B., Lipophilicity Parameters for Ionic Liquid Cations and Their Correlation to in Vitro Cytotoxicity. *Ecotoxicology and environmental safety* **2007,** *67*, 430-438.
68. Tang, S.; Baker, G. A.; Zhao, H., Ether- and Alcohol-Functionalized Task-Specific Ionic Liquids: Attractive Properties and Applications. *Chemical Society Reviews* **2012,** *41*, 4030-4066.
69. Zhao, D. B.; Liao, Y. C.; Zhang, Z. D., Toxicity of Ionic Liquids. *Clean-Soil Air Water* **2007,** *35*, 42-48.

70. Quartarone, E.; Mustarelli, P., Electrolytes for Solid-State Lithium Rechargeable Batteries: Recent Advances and Perspectives. *Chemical Society Reviews* **2011,** *40*, 2525-2540.
71. Luo, J.-Y.; Cui, W.-J.; He, P.; Xia, Y.-Y., Raising the Cycling Stability of Aqueous Lithium-Ion Batteries by Eliminating Oxygen in the Electrolyte. *Nature chemistry* **2010,** *2*, 760-765.
72. Pan, H.; Hu, Y.-S.; Chen, L., Room-Temperature Stationary Sodium-Ion Batteries for Large-Scale Electric Energy Storage. *Energy & Environmental Science* **2013,** *6*, 2338-2360.
73. Wang, F.; Xiao, S.; Hou, Y.; Hu, C.; Liu, L.; Wu, Y., Electrode Materials for Aqueous Asymmetric Supercapacitors. *RSC Advances* **2013,** *3*, 13059-13084.
74. Yang, P.; Mai, W., Flexible Solid-State Electrochemical Supercapacitors. *Nano Energy* **2014,** *8*, 274-290.
75. Meng, C.; Liu, C.; Chen, L.; Hu, C.; Fan, S., Highly Flexible and All-Solid-State Paperlike Polymer Supercapacitors. *Nano letters* **2010,** *10*, 4025-4031.
76. Yu, H.; Wu, J.; Fan, L.; Lin, Y.; Xu, K.; Tang, Z.; Cheng, C.; Tang, S.; Lin, J.; Huang, M.; Lan, Z., A Novel Redox-Mediated Gel Polymer Electrolyte for High-Performance Supercapacitor. *Journal of Power Sources* **2012,** *198*, 402-407.
77. Yang, C.-C.; Hsu, S.-T.; Chien, W.-C., All Solid-State Electric Double-Layer Capacitors Based on Alkaline Polyvinyl Alcohol Polymer Electrolytes. *Journal of Power Sources* **2005,** *152*, 303-310.
78. Yang, C.-C.; Lin, S., Preparation of Alkaline Pva-Based Polymer Electrolytes for Ni–Mh and Zn–Air Batteries. *Journal of applied electrochemistry* **2003,** *33*, 777-784.
79. Mi, J.; Wang, X.-R.; Fan, R.-J.; Qu, W.-H.; Li, W.-C., Coconut-Shell-Based Porous Carbons with a Tunable Micro/Mesopore Ratio for High-Performance Supercapacitors. *Energy & Fuels* **2012,** *26*, 5321-5329.
80. Weinstein, L.; Dash, R., Have Exotic Carbons Failed? *Materials Today* **2013,** *16,* 356-357.
81. Yu, G.; Hu, L.; Liu, N.; Wang, H.; Vosgueritchian, M.; Yang, Y.; Cui, Y.; Bao, Z., Enhancing the Supercapacitor Performance of Graphene/Mno2 Nanostructured Electrodes by Conductive Wrapping. *Nano Lett* **2011,** *11*, 4438-4442.
82. Gao, Y.; Zhou, Y.; Xiong, W.; Jiang, L.; Mahjouri-samani, M.; Thirugnanam, P.; Huang, X.; Wang, M.; Jiang, L.; Lu, Y., Transparent, Flexible, and Solid-State Supercapacitors Based on Graphene Electrodes. *APL Materials* **2013,** *1*, 012101.
83. Zhang, J.; Yang, H.; Shen, G.; Cheng, P.; Zhang, J.; Guo, S., Reduction of Graphene Oxide Via L-Ascorbic Acid. *Chemical Communications* **2010,** *46*, 1112-1114.
84. Lehmann, J., A Handful of Carbon. *Nature* **2007,** *447*, 143-144.
85. Ok, Y. S.; Chang, S. X.; Gao, B.; Chung, H.-J., Smart Biochar Technology—a Shifting Paradigm Towards Advanced Materials and Healthcare Research. *Environmental Technology & Innovation* **2015,** *4*, 206-209.
86. Guo, W.; Cheng, C.; Wu, Y. Z.; Jiang, Y. A.; Gao, J.; Li, D.; Jiang, L., Bio-Inspired Two-Dimensional Nanofluidic Generators Based on a Layered Graphene Hydrogel Membrane. *Advanced Materials* **2013,** *25*, 6064-6068.
87. Genovese, M.; Jiang, J.; Lian, K.; Holm, N., High Capacitive Performance of Exfoliated Biochar Nanosheets from Biomass Waste Corn Cob. *Journal of Materials Chemistry A* **2015,** *3*, 2903-2913.
88. Wang, H.; Xu, Z. W.; Kohandehghan, A.; Li, Z.; Cui, K.; Tan, X. H.; Stephenson, T. J.; King'ondu, C. K.; Holt, C. M. B.; Olsen, B. C.; Tak, J. K.; Harfield, D.; Anyia, A. O.; Mitlin, D.,

Interconnected Carbon Nanosheets Derived from Hemp for Ultrafast Supercapacitors with High Energy. *Acs Nano* **2013,** *7*, 5131-5141.
89. Sumboja, A.; Foo, C. Y.; Wang, X.; Lee, P. S., Large Areal Mass, Flexible and Free-Standing Reduced Graphene Oxide/Manganese Dioxide Paper for Asymmetric Supercapacitor Device. *Advanced Materials* **2013,** *25*, 2809-2815.
90. Xiong, Z.; Liao, C.; Han, W.; Wang, X., Mechanically Tough Large-Area Hierarchical Porous Graphene Films for High-Performance Flexible Supercapacitor Applications. *Advanced Materials* **2015,** *27*, 4469-4475.
91. Xu, Y.; Tao, Y.; Zheng, X.; Ma, H.; Luo, J.; Kang, F.; Yang, Q.-H., A Metal-Free Supercapacitor Electrode Material with a Record High Volumetric Capacitance over 800 F Cm−3. *Advanced Materials* **2015,** *27*, 8082-8087.
92. Tekin, E.; Smith, P. J.; Schubert, U. S., Inkjet Printing as a Deposition and Patterning Tool for Polymers and Inorganic Particles. *Soft Matter* **2008,** *4*, 703-713.
93. Whittow, W. G.; Chauraya, A.; Vardaxoglou, J.; Li, Y.; Torah, R.; Yang, K.; Beeby, S.; Tudor, J., Inkjet-Printed Microstrip Patch Antennas Realized on Textile for Wearable Applications. *Antennas and Wireless Propagation Letters, IEEE* **2014,** *13*, 71-74.
94. Kamyshny, A.; Magdassi, S., Conductive Nanomaterials for Printed Electronics. *small* **2014,** *10*, 3515-3535.
95. Mengistie, D. A.; Ibrahem, M. A.; Wang, P.-C.; Chu, C.-W., Highly Conductive Pedot:Pss Treated with Formic Acid for Ito-Free Polymer Solar Cells. *ACS applied materials & interfaces* **2014,** *6*, 2292-2299.
96. Secor, E. B.; Hersam, M. C., Emerging Carbon and Post-Carbon Nanomaterial Inks for Printed Electronics. *The Journal of Physical Chemistry Letters* **2015,** *6*, 620-626.
97. Huang, X.; Leng, T.; Zhang, X.; Chen, J. C.; Chang, K. H.; Geim, A. K.; Novoselov, K. S.; Hu, Z., Binder-Free Highly Conductive Graphene Laminate for Low Cost Printed Radio Frequency Applications. *Applied Physics Letters* **2015,** *106*, 203105.
98. Huang, X.; Leng, T.; Zhu, M.; Zhang, X.; Chen, J.; Chang, K.; Aqeeli, M.; Geim, A. K.; Novoselov, K. S.; Hu, Z., Highly Flexible and Conductive Printed Graphene for Wireless Wearable Communications Applications. *Scientific Reports* **2015,** *5*, 18298.
99. Secor, E. B.; Prabhumirashi, P. L.; Puntambekar, K.; Geier, M. L.; Hersam, M. C., Inkjet Printing of High Conductivity, Flexible Graphene Patterns. *The Journal of Physical Chemistry Letters* **2013,** *4*, 1347-1351.
100. Li, J.; Ye, F.; Vaziri, S.; Muhammed, M.; Lemme, M. C.; Östling, M., Efficient Inkjet Printing of Graphene. *Advanced Materials* **2013,** *25*, 3985-3992.
101. Shin, K.-Y.; Lee, J. S.; Hong, J.-Y.; Jang, J., One-Step Fabrication of a Highly Conductive and Durable Copper Paste and Its Flexible Dipole Tag-Antenna Application. *Chem. Commun.* **2014,** *50*, 3093-3096.
102. Xu, J.; Gao, Q.; Zhang, Y.; Tan, Y.; Tian, W.; Zhu, L.; Jiang, L., Preparing Two-Dimensional Microporous Carbon from Pistachio Nutshell with High Areal Capacitance as Supercapacitor Materials. *Scientific Reports* **2014,** *4*, 5545.
103. Talemi, P.; Delaigue, M.; Murphy, P.; Fabretto, M., Flexible Polymer-on-Polymer Architecture for Piezo/Pyroelectric Energy Harvesting. *ACS applied materials & interfaces* **2015,** *7*, 8465-8471.
104. Saravanakumar, B.; Thiyagarajan, K.; Alluri, N. R.; SoYoon, S.; Taehyun, K.; Lin, Z.-H.; Kim, S.-J., Fabrication of an Eco-Friendly Composite Nanogenerator for Self-Powered Photosensor Applications. *Carbon* **2015,** *84*, 56-65.

105. Wang, Z. L., Towards Self-Powered Nanosystems: From Nanogenerators to Nanopiezotronics. *Advanced Functional Materials* **2008,** *18*, 3553-3567.
106. Song, J.; Zhou, J.; Wang, Z. L., Piezoelectric and Semiconducting Coupled Power Generating Process of a Single Zno Belt/Wire. A Technology for Harvesting Electricity from the Environment. *Nano letters* **2006,** *6*, 1656-1662.
107. Wang, Z. L.; Song, J., Piezoelectric Nanogenerators Based on Zinc Oxide Nanowire Arrays. *Science* **2006,** *312*, 242-246.
108. Shin, S.-H.; Kim, Y.-H.; Lee, M. H.; Jung, J.-Y.; Seol, J. H.; Nah, J., Lithium-Doped Zinc Oxide Nanowires–Polymer Composite for High Performance Flexible Piezoelectric Nanogenerator. *ACS nano* **2014,** *8*, 10844-10850.
109. Hasan, M. R.; Baek, S.-H.; Seong, K. S.; Kim, J. H.; Park, I.-K., Hierarchical Zno Nanorods on Si Micropillar Arrays for Performance Enhancement of Piezoelectric Nanogenerators. *ACS applied materials & interfaces* **2015**.
110. Hu, C. J.; Lin, Y. H.; Tang, C. W.; Tsai, M. Y.; Hsu, W. K.; Kuo, H. F., Zno-Coated Carbon Nanotubes: Flexible Piezoelectric Generators. *Advanced Materials* **2011,** *23*, 2941-2945.
111. Kumar, B.; Lee, K. Y.; Park, H.-K.; Chae, S. J.; Lee, Y. H.; Kim, S.-W., Controlled Growth of Semiconducting Nanowire, Nanowall, and Hybrid Nanostructures on Graphene for Piezoelectric Nanogenerators. *ACS nano* **2011,** *5*, 4197-4204.
112. Choi, D.; Choi, M. Y.; Choi, W. M.; Shin, H. J.; Park, H. K.; Seo, J. S.; Park, J.; Yoon, S. M.; Chae, S. J.; Lee, Y. H., Fully Rollable Transparent Nanogenerators Based on Graphene Electrodes. *Advanced Materials* **2010,** *22*, 2187-2192.
113. Shin, D.-M.; Tsege, E. L.; Kang, S. H.; Seung, W.; Kim, S.-W.; Kim, H. K.; Hong, S. W.; Hwang, Y.-H., Freestanding Zno Nanorod/Graphene/Zno Nanorod Epitaxial Double Heterostructure for Improved Piezoelectric Nanogenerators. *Nano Energy* **2015**, 268-277.
114. Nam, G.-H.; Baek, S.-H.; Cho, C.-H.; Park, I.-K., A Flexible and Transparent Graphene/Zno Nanorod Hybrid Structure Fabricated by Exfoliating a Graphite Substrate. *Nanoscale* **2014,** *6*, 11653-11658.
115. Chevalier-César, C.; Capochichi-Gnambodoe, M.; Leprince-Wang, Y., Growth Mechanism Studies of Zno Nanowire Arrays Via Hydrothermal Method. *Applied Physics A* **2014,** *115*, 953-960.
116. Chang, H.; Sun, Z.; Ho, K. Y.-F.; Tao, X.; Yan, F.; Kwok, W.-M.; Zheng, Z., A Highly Sensitive Ultraviolet Sensor Based on a Facile in Situ Solution-Grown Zno Nanorod/Graphene Heterostructure. *Nanoscale* **2011,** *3*, 258-264.
117. Lee, S. H.; Kim, H. W.; Hwang, J. O.; Lee, W. J.; Kwon, J.; Bielawski, C. W.; Ruoff, R. S.; Kim, S. O., Three-Dimensional Self-Assembly of Graphene Oxide Platelets into Mechanically Flexible Macroporous Carbon Films. *Angewandte Chemie International Edition* **2010,** *49*, 10084-10088.
118. Maiti, U. N.; Lim, J.; Lee, K. E.; Lee, W. J.; Kim, S. O., Three-Dimensional Shape Engineered, Interfacial Gelation of Reduced Graphene Oxide for High Rate, Large Capacity Supercapacitors. *Advanced Materials* **2014,** *26*, 615-619.
119. Lee, W. J.; Maiti, U. N.; Lee, J. M.; Lim, J.; Han, T. H.; Kim, S. O., Nitrogen-Doped Carbon Nanotubes and Graphene Composite Structures for Energy and Catalytic Applications. *Chemical Communications* **2014,** *50*, 6818-6830.
120. Rubinstein, M.; Colby, R. H., *Polymer Physics*. OUP Oxford: 2003.
121. Künzler, J. F., Hydrogels. In *Encyclopedia of Polymer Science and Technology*, John Wiley & Sons, Inc.: 2002.

122. Ohlemacher, A.; Candau, F.; Munch, J.; Candau, S., Aqueous Solution Properties of Polyampholytes: Effect of the Net Charge Distribution. *Journal of Polymer Science Part B: Polymer Physics* **1996,** *34*, 2747-2757.
123. Candau, F.; Ohlemacher, A.; Munch, J.; Candau, S., Effect of the Net Charge Distribution on the Aqueous Solution Properties of Polyampholytes. *Revue de l'Institut Français du Pétrole* **1997,** *52*, 133-137.
124. Skouri, M.; Munch, J.; Candau, S.; Neyret, S.; Candau, F., Conformation of Neutral Polyampholyte Chains in Salt Solutions: A Light Scattering Study. *Macromolecules* **1994,** *27*, 69-76.
125. Seuring, J.; Agarwal, S., Polymers with Upper Critical Solution Temperature in Aqueous Solution. *Macromolecular rapid communications* **2012,** *33*, 1898-1920.
126. Silverstein, T. P., Hydrophobic Solvation Not Via Clathrate Water Cages. *Journal of Chemical Education* **2008,** *85*, 917.
127. Burgess, J., *Metal Ions in Solution*, Ellis Horwood, Chichester, Sussex, England, 1978.
128. Hunter, C. A., Quantifying Intermolecular Interactions: Guidelines for the Molecular Recognition Toolbox. *Angewandte Chemie International Edition* **2004,** *43*, 5310-5324.
129. Terentjev, E. M.; Weitz, D. A., *The Oxford Handbook of Soft Condensed Matter*. Oxford Handbooks: 2015.
130. Osada, Y.; Khokhlov, A., *Polymer Gels and Networks*. CRC Press: 2001.
131. Kudaibergenov, S. E., Recent Advances in the Study of Synthetic Polyampholytes in Solutions. In *Polymer Latexes-Epoxide Resins-Polyampholytes*, Springer: 1999; pp 115-197.
132. Ali, S. A.; Rasheed, A., Synthesis and Solution Properties of a Betaine-Sulfur Dioxide Polyampholyte. *Polymer* **1999,** *40*, 6849-6857.
133. Zheng, G. Z.; Meshitsuka, G.; Ishizu, A., Properties of an Amphoteric Cellulose Derivative Containing Anionic Carboxymethyl and Cationic 2-Hydroxy-3-(Trimethylammonio) Propyl Substituents. *Journal of Polymer Science Part B: Polymer Physics* **1995,** *33*, 867-877.
134. Salamone, J.; Ahmed, I.; Rodriguez, E.; Quach, L.; Watterson, A., Synthesis and Solution Properties of Ampholytic Acrylamide Ionomers. *Journal of Macromolecular Science—Chemistry* **1988,** *25*, 811-837.
135. Victor, J.; Imbert, J., Collapse of an Alternating Polyampholyte: Evidence for Tricriticality in 2 and 3 Dimensions. *EPL (Europhysics Letters)* **1993,** *24*, 189.
136. Wittmer, J.; Johner, A.; Joanny, J., Random and Alternating Polyampholytes. *EPL (Europhysics Letters)* **1993,** *24*, 263.
137. Sun, T. L.; Luo, F.; Kurokawa, T.; Karobi, S. N.; Nakajima, T.; Gong, J. P., Molecular Structure of Self-Healing Polyampholyte Hydrogels Analyzed from Tensile Behaviors. *Soft Matter* **2015,** *11*, 9355-9366.
138. Aguilar, M. R.; Gallardo, A.; Fernández, M. d. M.; Román, J. S., In Situ Quantitative 1h Nmr Monitoring of Monomer Consumption: A Simple and Fast Way of Estimating Reactivity Ratios. *Macromolecules* **2002,** *35*, 2036-2041.
139. Kantor, Y.; Kardar, M., Instabilities of Charged Polyampholytes. *Physical Review E* **1995**, *51*, 1299.
140. Dobrynin, A. V.; Rubinstein, M.; Joanny, J.-F., Adsorption of a Polyampholyte Chain on a Charged Surface. *Macromolecules* **1997,** *30*, 4332-4341.
141. Dobrynin, A. V.; Rubinstein, M., Flory Theory of a Polyampholyte Chain. *Journal de Physique II* **1995,** *5*, 677-695.

142. Higgs, P. G.; Joanny, J. F., Theory of Polyampholyte Solutions. *The Journal of Chemical Physics* **1991,** *94*, 1543-1554.
143. Everaers, R.; Johner, A.; Joanny, J.-F., Polyampholytes: From Single Chains to Solutions. *Macromolecules* **1997,** *30*, 8478-8498.
144. Everaers, R.; Johner, A.; Joanny, J.-F., Complexation and Precipitation in Polyampholyte Solutions. *EPL (Europhysics Letters)* **1997,** *37*, 275.
145. Tanaka, M.; Tanaka, T., Clumps of Randomly Charged Polymers: Molecular Dynamics Simulation of Condensation, Crystallization, and Swelling. *Physical Review E* **2000,** *62*, 3803.
146. Dobrynin, A. V., Fluctuation Theory of Charged Ab-Random Copolymers. *Journal de Physique II* **1995,** *5*, 1241-1253.
147. Kudaibergenov, S. E.; Sigitov, V. B., Swelling, Shrinking, Deformation, and Oscillation of Polyampholyte Gels Based on Vinyl 2-Aminoethyl Ether and Sodium Acrylate. *Langmuir* **1999,** *15*, 4230-4235.
148. Ihsan, A. B.; Sun, T. L.; Kuroda, S.; Haque, M. A.; Kurokawa, T.; Nakajima, T.; Gong, J. P., A Phase Diagram of Neutral Polyampholyte - from Solution to Tough Hydrogel. *Journal of Materials Chemistry B* **2013,** *1*, 4555-4562.
149. Luo, F.; Sun, T. L.; Nakajima, T.; King, D. R.; Kurokawa, T.; Zhao, Y.; Ihsan, A. B.; Li, X.; Guo, H.; Gong, J. P., Strong and Tough Polyion-Complex Hydrogels from Oppositely Charged Polyelectrolytes: A Comparative Study with Polyampholyte Hydrogels. *Macromolecules* **2016,** *49*, 2750-2760.
150. Chrambach, A.; Rodbard, D., Polyacrylamide Gel Electrophoresis. *Science* **1971,** *172*, 440-451.
151. Stammen, J. A.; Williams, S.; Ku, D. N.; Guldberg, R. E., Mechanical Properties of a Novel Pva Hydrogel in Shear and Unconfined Compression. *Biomaterials* **2001,** *22*, 799-806.
152. He, C.; Kim, S. W.; Lee, D. S., In Situ Gelling Stimuli-Sensitive Block Copolymer Hydrogels for Drug Delivery. *Journal of controlled release* **2008,** *127*, 189-207.
153. Sun, T. L.; Kurokawa, T.; Kuroda, S.; Bin Ihsan, A.; Akasaki, T.; Sato, K.; Haque, M. A.; Nakajima, T.; Gong, J. P., Physical Hydrogels Composed of Polyampholytes Demonstrate High Toughness and Viscoelasticity. *Nature Materials* **2013,** *12*, 932-937.
154. Li, X.; Liu, L.; Wang, X.; Ok, Y. S.; Elliott, J. A. W.; Chang, S. X.; Chung, H.-J., Flexible and Self-Healing Aqueous Supercapacitors for Low Temperature Applications: Polyampholyte Gel Electrolytes with Biochar Electrodes. *Scientific Reports* **2017,** *7*, 1685.
155. Niskanen, J.; Tenhu, H., How to Manipulate the Upper Critical Solution Temperature (Ucst)? *Polymer Chemistry* **2017,** *8*, 220-232.
156. Nohara, S.; Wada, H.; Furukawa, N.; Inoue, H.; Morita, M.; Iwakura, C., Electrochemical Characterization of New Electric Double Layer Capacitor with Polymer Hydrogel Electrolyte. *Electrochimica acta* **2003,** *48*, 749-753.
157. Li, X.; Liu, L.; Wang, X.; Ok, Y. S.; Elliott, J. A. W.; Chang, S. X.; Chung, H.-J., Flexible and Self-Healing Aqueous Supercapacitors for Low Temperature Applications: Polyampholyte Gel Electrolytes with Biochar Electrodes. *Scientific Reports* **2017,** *7*, 1685.
158. Wright, M. R., *An Introduction to Aqueous Electrolyte Solutions*. John Wiley & Sons: 2007.
159. Bockris, J. O. M.; Conway, B. E.; White, R. E., *Modern Aspects of Electrochemistry*. Springer Science & Business Media: 2012; Vol. 22.
160. Shimizu, S.; Matubayasi, N., Ion Hydration: Linking Self-Diffusion and Reorientational Motion to Water Structure. *Physical Chemistry Chemical Physics* **2018**, 5909-5917.

161. Gavish, N.; Promislow, K., Dependence of the Dielectric Constant of Electrolyte Solutions on Ionic Concentration: A Microfield Approach. *Physical Review E* **2016,** *94*, 012611.
162. Li, R.; Jiang, Z.; Chen, F.; Yang, H.; Guan, Y., Hydrogen Bonded Structure of Water and Aqueous Solutions of Sodium Halides: A Raman Spectroscopic Study. *Journal of molecular structure* **2004,** *707*, 83-88.
163. Jalilehvand, F.; Spångberg, D.; Lindqvist-Reis, P.; Hermansson, K.; Persson, I.; Sandström, M., Hydration of the Calcium Ion. An Exafs, Large-Angle X-Ray Scattering, and Molecular Dynamics Simulation Study. *Journal of the American Chemical Society* **2001,** *123*, 431-441.
164. Ohtaki, H.; Radnai, T., Structure and Dynamics of Hydrated Ions. *Chemical reviews* **1993,** *93*, 1157-1204.
165. Cooper, R. J.; Chang, T. M.; Williams, E. R., Hydrated Alkali Metal Ions: Spectroscopic Evidence for Clathrates. *The Journal of Physical Chemistry A* **2013,** *117*, 6571-6579.
166. Peslherbe, G. H.; Ladanyi, B. M.; Hynes, J. T., Structure of Nai Ion Pairs in Water Clusters. *Chemical Physics* **2000,** *258*, 201-224.
167. Marcus, Y., Effect of Ions on the Structure of Water: Structure Making and Breaking. *Chemical reviews* **2009,** *109*, 1346-1370.
168. Kondoh, M.; Ohshima, Y.; Tsubouchi, M., Ion Effects on the Structure of Water Studied by Terahertz Time-Domain Spectroscopy. *Chemical Physics Letters* **2014,** *591*, 317-322.
169. Tobias, D. J.; Hemminger, J. C., Getting Specific About Specific Ion Effects. *Science* **2008,** *319*, 1197-1198.
170. Zangi, R., Can Salting-in/Salting-out Ions Be Classified as Chaotropes/Kosmotropes? *The Journal of Physical Chemistry B* **2009,** *114*, 643-650.
171. Tielrooij, K.; Garcia-Araez, N.; Bonn, M.; Bakker, H., Cooperativity in Ion Hydration. *Science* **2010,** *328*, 1006-1009.
172. Hodge, R.; Edward, G. H.; Simon, G. P., Water Absorption and States of Water in Semicrystalline Poly (Vinyl Alcohol) Films. *Polymer* **1996,** *37*, 1371-1376.
173. Higuchi, A.; Iijima, T., Dsc Investigation of the States of Water in Poly (Vinyl Alcohol) Membranes. *Polymer* **1985,** *26*, 1207-1211.
174. Li, W. B.; Xue, F.; Cheng, R. S., States of Water in Partially Swollen Poly(Vinyl Alcohol) Hydrogels. *Polymer* **2005,** *46*, 12026-12031.
175. Baba, T.; Sakamoto, R.; Shibukawa, M.; Oguma, K., Solute Retention and the States of Water in Polyethylene Glycol and Poly (Vinyl Alcohol) Gels. *Journal of Chromatography A* **2004,** *1040*, 45-51.
176. Takeshita, Y.; Becker, E.; Sakata, S.; Miwa, T.; Sawada, T., States of Water Absorbed in Water-Borne Urethane/Epoxy Coatings. *Polymer* **2014,** *55*, 2505-2513.
177. Nakamura, K.; Hatakeyama, T.; Hatakeyama, H., Relationship between Hydrogen Bonding and Bound Water in Polyhydroxystyrene Derivatives. *Polymer* **1983,** *24*, 871-876.
178. Liu, W. G.; De Yao, K., What Causes the Unfrozen Water in Polymers: Hydrogen Bonds between Water and Polymer Chains? *Polymer* **2001,** *42*, 3943-3947.
179. Li, W.; Zheng, Y.; Cheng, R., Transition of Hydration States of Poly (Vinyl Alcohol) in Aqueous Solution. *Polymer* **2008,** *49*, 4740-4744.
180. Li, L. F.; Ren, L.; Wang, L.; Liu, S.; Zhang, Y. R.; Tang, L. Q.; Wang, Y. J., Effect of Water State and Polymer Chain Motion on the Mechanical Properties of a Bacterial Cellulose and Polyvinyl Alcohol (Bc/Pva) Hydrogel. *Rsc Advances* **2015,** *5*, 25525-25531.

181. Lin, H.; Dan, W. H.; Dan, N. H., The Water State in Crosslinked Poly(Vinyl Alcohol)-Collagen Hydrogel and Its Swelling Behavior. *Journal of applied polymer science* **2012,** *123*, 2753-2761.
182. Shapiro, Y. E., Structure and Dynamics of Hydrogels and Organogels: An Nmr Spectroscopy Approach. *Progress in Polymer Science* **2011,** *36*, 1184-1253.
183. Wang, N.; Ru, G.; Wang, L.; Feng, J., 1h Mas Nmr Studies of the Phase Separation of Poly (N-Isopropylacrylamide) Gel in Binary Solvents. *Langmuir* **2009,** *25*, 5898-5902.
184. Díez-Peña, E.; Quijada-Garrido, I.; Barrales-Rienda, J. M.; Wilhelm, M.; Spiess, H. W., Nmr Studies of the Structure and Dynamics of Polymer Gels Based on N-Isopropylacrylamide (Nipaam) and Methacrylic Acid (Maa). *Macromolecular Chemistry and Physics* **2002,** *203*, 491-502.
185. Suzuki, Y.; Steinhart, M.; Graf, R.; Butt, H.-J. r.; Floudas, G., Dynamics of Ice/Water Confined in Nanoporous Alumina. *The Journal of Physical Chemistry B* **2015,** *119*, 14814-14820.
186. Suzuki, Y.; Steinhart, M.; Butt, H.-J. r.; Floudas, G., Kinetics of Ice Nucleation Confined in Nanoporous Alumina. *The Journal of Physical Chemistry B* **2015,** *119*, 11960-11966.
187. Fairbanks, B. D.; Schwartz, M. P.; Bowman, C. N.; Anseth, K. S., Photoinitiated Polymerization of Peg-Diacrylate with Lithium Phenyl-2,4,6-Trimethylbenzoylphosphinate: Polymerization Rate and Cytocompatibility. *Biomaterials* **2009,** *30*, 6702-6707.
188. Nicodemus, G. D.; Bryant, S. J., Cell Encapsulation in Biodegradable Hydrogels for Tissue Engineering Applications. *Tissue Engineering Part B: Reviews* **2008,** *14*, 149-165.
189. Phelps, E. A.; Landázuri, N.; Thulé, P. M.; Taylor, W. R.; García, A. J., Bioartificial Matrices for Therapeutic Vascularization. *Proceedings of the National Academy of Sciences* **2010,** *107*, 3323-3328.
190. McGilvray, K. L.; Decan, M. R.; Wang, D.; Scaiano, J. C., Facile Photochemical Synthesis of Unprotected Aqueous Gold Nanoparticles. *Journal of the American Chemical Society* **2006,** *128*, 15980-15981.
191. Flory, P. J., *Principles of Polymer Chemistry*. Cornell University Press: 1953.
192. Dreyer, D. R.; Park, S.; Bielawski, C. W.; Ruoff, R. S., The Chemistry of Graphene Oxide. *Chemical Society Reviews* **2010,** *39*, 228-240.
193. Dikin, D. A.; Stankovich, S.; Zimney, E. J.; Piner, R. D.; Dommett, G. H.; Evmenenko, G.; Nguyen, S. T.; Ruoff, R. S., Preparation and Characterization of Graphene Oxide Paper. *Nature* **2007,** *448*, 457-460.
194. Park, S.; An, J.; Potts, J. R.; Velamakanni, A.; Murali, S.; Ruoff, R. S., Hydrazine-Reduction of Graphite-and Graphene Oxide. *Carbon* **2011,** *49*, 3019-3023.
195. Shin, H. J.; Kim, K. K.; Benayad, A.; Yoon, S. M.; Park, H. K.; Jung, I. S.; Jin, M. H.; Jeong, H. K.; Kim, J. M.; Choi, J. Y., Efficient Reduction of Graphite Oxide by Sodium Borohydride and Its Effect on Electrical Conductance. *Advanced Functional Materials* **2009,** *19*, 1987-1992.
196. Liu, K.; Wu, W.; Chen, B.; Chen, X.; Zhang, N., Continuous Growth and Improved Pl Property of Zno Nanoarrays with Assistance of Polyethylenimine. *Nanoscale* **2013,** *5*, 5986-5993.
197. Baxter, J. B.; Aydil, E. S., Nanowire-Based Dye-Sensitized Solar Cells. *Applied Physics Letters* **2005,** *86*, 053114.
198. Chu, B.; Hsiao, B. S., Small-Angle X-Ray Scattering of Polymers. *Chemical Reviews* **2001,** *101*, 1727-1762.
199. Shibayama, M., Spatial Inhomogeneity and Dynamic Fluctuations of Polymer Gels. *Macromolecular Chemistry and Physics* **1998,** *199*, 1-30.

200. Shibayama, M., Structure-Mechanical Property Relationship of Tough Hydrogels. *Soft Matter* **2012,** *8*, 8030-8038.
201. Shibayama, M., Small-Angle Neutron Scattering on Polymer Gels: Phase Behavior, Inhomogeneities and Deformation Mechanisms. *Polymer journal* **2011,** *43*, 18.
202. Mansur, H. S.; Oréfice, R. L.; Mansur, A. A., Characterization of Poly (Vinyl Alcohol)/Poly (Ethylene Glycol) Hydrogels and Pva-Derived Hybrids by Small-Angle X-Ray Scattering and Ftir Spectroscopy. *Polymer* **2004,** *45*, 7193-7202.
203. Hunt, J. N.; Feldman, K. E.; Lynd, N. A.; Deek, J.; Campos, L. M.; Spruell, J. M.; Hernandez, B. M.; Kramer, E. J.; Hawker, C. J., Tunable, High Modulus Hydrogels Driven by Ionic Coacervation. *Advanced Materials* **2011,** *23*, 2327-2331.
204. Chiu, Y.-L.; Chen, M.-C.; Chen, C.-Y.; Lee, P.-W.; Mi, F.-L.; Jeng, U.-S.; Chen, H.-L.; Sung, H.-W., Rapidly in Situ Forming Hydrophobically-Modified Chitosan Hydrogels Via Ph-Responsive Nanostructure Transformation. *Soft Matter* **2009,** *5*, 962-965.
205. Glatter, O.; Kratky, O., *Small Angle X-Ray Scattering*. Academic Press: 1982.
206. Bras, W.; Ryan, A. J., Sample Environments and Techniques Combined with Small Angle X-Ray Scattering. *Advances in colloid and interface science* **1998,** *75*, 1-43.
207. Chu, B.; Harney, P. J.; Li, Y.; Linliu, K.; Yeh, F.; Hsiao, B. S., A Laser-Aided Prealigned Pinhole Collimator for Synchrotron X Rays. *Review of scientific instruments* **1994,** *65*, 597-602.
208. Hughes, D.; Mahendrasingam, A.; Martin, C.; Oatway, W.; Heeley, E.; Bingham, S.; Fuller, W., An Instrument for the Collection of Simultaneous Small and Wide Angle X-Ray Scattering and Stress–Strain Data During Deformation of Polymers at High Strain Rates Using Synchrotron Radiation Sources. *Review of scientific instruments* **1999,** *70*, 4051-4054.
209. Hongladarom, K.; Ugaz, V.; Cinader, D.; Burghardt, W.; Quintana, J.; Hsiao, B.; Dadmun, M.; Hamilton, W.; Butler, P., Birefringence, X-Ray Scattering, and Neutron Scattering Measurements of Molecular Orientation in Sheared Liquid Crystal Polymer Solutions. *Macromolecules* **1996,** *29*, 5346-5355.
210. Ran, S.; Zong, X.; Fang, D.; Hsiao, B. S.; Chu, B.; Ross, R., Novel Image Analysis of Two-Dimensional X-Ray Fiber Diffraction Patterns: Example of a Polypropylene Fiber Drawing Study. *Journal of applied crystallography* **2000,** *33*, 1031-1036.
211. Saw, C. K., *X-Ray Scattering Techniques for Characterization of Nanosystems in Lifesciences*. Wiley Online Library: 2005.
212. Schnablegger, H.; Singh, Y., *The Saxs Guide*. 3rd edition ed.; 2013.
213. Roe, R. J., *Methods of X-Ray and Neutron Scattering in Polymer Science*. Oxford University Press: 2000.
214. Menczel, J. D.; Judovits, L.; Prime, R. B.; Bair, H. E.; Reading, M.; Swier, S., Differential Scanning Calorimetry (Dsc). *Thermal analysis of polymers: Fundamentals and applications* **2009**, 7-239.
215. Standard Terminology Relating to Thermal Analysis and Rheology. ASTM International: West Conshohocken, PA, 2016; Vol. ASTM E473
216. Sarı, A.; Karaipekli, A., Thermal Conductivity and Latent Heat Thermal Energy Storage Characteristics of Paraffin/Expanded Graphite Composite as Phase Change Material. *Applied Thermal Engineering* **2007,** *27*, 1271-1277.
217. Clark Jr, M. B.; Burkhardt, C. A.; Gardella Jr, J. A., Surface Studies of Polymer Blends. 3. An Esca, Ir and Dsc Study of Poly (. Epsilon.-Caprolactone)/Poly (Vinyl Chloride) Homopolymer Blends. *Macromolecules* **1989,** *22*, 4495-4501.

218. Giron, D., Applications of Thermal Analysis and Coupled Techniques in Pharmaceutical Industry. *Journal of thermal analysis and Calorimetry* **2002,** *68*, 335-357.
219. Rieger, J., The Glass Transition Temperature Tg of Polymers—Comparison of the Values from Differential Thermal Analysis (Dta, Dsc) and Dynamic Mechanical Measurements (Torsion Pendulum). *Polymer testing* **2001,** *20*, 199-204.
220. Sen, A.; Weiss, R.; Garton, A., Grafted-Block Copolymer Networks Formed by Transition Metal Coordination of Styrene-and Butadiene-Based Polymers. ACS Publications: 1989.
221. Peak, C. W.; Wilker, J. J.; Schmidt, G., A Review on Tough and Sticky Hydrogels. *Colloid and Polymer Science* **2013,** *291*, 2031-2047.
222. Alabarse, F.; Haines, J.; Cambon, O.; Levelut, C.; Bourgogne, D.; Haidoux, A.; Granier, D.; Coasne, B., Freezing of Water Confined at the Nanoscale. *Physical review letters* **2012,** *109*, 035701.
223. Liu, F.; Zargarzadeh, L.; Chung, H.-J.; Elliott, J. A. W., Thermodynamic Investigation of the Effect of Interface Curvature on the Solid–Liquid Equilibrium and Eutectic Point of Binary Mixtures. *The Journal of Physical Chemistry B* **2017,** *121*, 9452-9462.
224. Lv, J.; Song, Y.; Jiang, L.; Wang, J., Bio-Inspired Strategies for Anti-Icing. *ACS nano* **2014,** *8*, 3152-3169.
225. Wiener, C. G.; Tyagi, M.; Liu, Y.; Weiss, R. A.; Vogt, B. D., Supramolecular Hydrophobic Aggregates in Hydrogels Partially Inhibit Ice Formation. *The Journal of Physical Chemistry B* **2016**.
226. Goodman, C. M.; Choi, S.; Shandler, S.; DeGrado, W. F., Foldamers as Versatile Frameworks for the Design and Evolution of Function. *Nature Chemical Biology* **2007,** *3*, 252-262.
227. Dill, K. A.; Ozkan, S. B.; Shell, M. S.; Weikl, T. R., The Protein Folding Problem. In *Annual Review of Biophysics*, Annual Reviews: Palo Alto, 2008; Vol. 37, pp 289-316.
228. Zielinski, M. W.; McGann, L. E.; Nychka, J. A.; Elliott, J. A. W., Comparison of Non-Ideal Solution Theories for Multi-Solute Solutions in Cryobiology and Tabulation of Required Coefficients. *Cryobiology* **2014,** *69*, 305-317.
229. Yu, H.; Wu, J.; Fan, L.; Xu, K.; Zhong, X.; Lin, Y.; Lin, J., Improvement of the Performance for Quasi-Solid-State Supercapacitor by Using Pva–Koh–Ki Polymer Gel Electrolyte. *Electrochimica acta* **2011,** *56*, 6881-6886.
230. Sun, K. C.; Arbab, A. A.; Sahito, I. A.; Qadir, M. B.; Choi, B. J.; Kwon, S. C.; Yeo, S. Y.; Yi, S. C.; Jeong, S. H., A Pvdf-Based Electrolyte Membrane for a Carbon Counter Electrode in Dye-Sensitized Solar Cells. *Rsc Advances* **2017,** *7*, 20908-20918.
231. Bernard, G. M.; Goyal, A.; Miskolzie, M.; McKay, R.; Wu, Q.; Wasylishen, R. E.; Michaelis, V. K., Methylammonium Lead Chloride: A Sensitive Sample for an Accurate Nmr Thermometer. *Journal of Magnetic Resonance* **2017,** *283*, 14-21.
232. Farrow, C. L.; Billinge, S. J., Relationship between the Atomic Pair Distribution Function and Small-Angle Scattering: Implications for Modeling of Nanoparticles. *Acta Crystallographica Section A: Foundations of Crystallography* **2009,** *65*, 232-239.
233. Gilbert, B., Finite Size Effects on the Real-Space Pair Distribution Function of Nanoparticles. *Journal of applied crystallography* **2008,** *41*, 554-562.
234. Kodama, K.; Iikubo, S.; Taguchi, T.; Shamoto, S. i., Finite Size Effects of Nanoparticles on the Atomic Pair Distribution Functions. *Acta Crystallographica Section A: Foundations of Crystallography* **2006,** *62*, 444-453.

235. Senesi, A. J.; Lee, B., Small-Angle Scattering of Particle Assemblies. *Journal of applied crystallography* **2015,** *48*, 1172-1182.
236. Besselink, R.; ten Elshof, J. E., Mass-Fractal Growth in Niobia/Silsesquioxane Mixtures: A Small-Angle X-Ray Scattering Study. *Journal of applied crystallography* **2014,** *47*, 1606-1613.
237. Li, T.; Senesi, A. J.; Lee, B., Small Angle X-Ray Scattering for Nanoparticle Research. *Chemical reviews* **2016,** *116*, 11128-11180.
238. Hammouda, B., A New Guinier–Porod Model. *Journal of applied crystallography* **2010,** *43*, 716-719.
239. MacKnight, W.; Taggart, W.; Stein, R. In *A Model for the Structure of Ionomers*, Journal of Polymer Science: Polymer Symposia, Wiley Online Library: 1974; pp 113-128.
240. Gierke, T.; Munn, G.; Wilson, F., The Morphology in Nafion Perfluorinated Membrane Products, as Determined by Wide-and Small-Angle X-Ray Studies. *Journal of Polymer Science: Polymer Physics Edition* **1981,** *19*, 1687-1704.
241. Jackson, J. A.; Rabideau, S. W., Deuteron Magnetic Resonance in Polycrystalline Heavy Ice (D2o). *The Journal of Chemical Physics* **1964,** *41*, 4008-4008.
242. Edmonds, D.; Mackay, A., The Pure Quadrupole Resonance of the Deuteron in Ice. *Journal of Magnetic Resonance (1969)* **1975,** *20*, 515-519.
243. Atkins, P.; De Paula, J., *Elements of Physical Chemistry*. Oxford University Press, USA: 2013.
244. Habib, M. A., Solvent Dipoles at the Electrode-Solution Interface. In *Modern Aspects of Electrochemistry*, Springer: 1977; pp 131-182.
245. Li, X.; Charaya, H.; Bernard, G.; Michaelis, V.; Elliott, J.; Lee, B.; Chung, H.-J., Low-Temperature Ionic Conductivity Enhanced by Disrupted Ice Formation in Polyampholyte Hydrogels. *Macromolecules* **2018**, in press.
246. Pogatscher, S.; Leutenegger, D.; Schawe, J. E. K.; Uggowitzer, P. J.; Löffler, J. F., Solid–Solid Phase Transitions Via Melting in Metals. *Nature communications* **2016,** *7*, 11113.
247. Han, B.; Bischof, J. C., Thermodynamic Nonequilibrium Phase Change Behavior and Thermal Properties of Biological Solutions for Cryobiology Applications. *Journal of biomechanical engineering* **2004,** *126*, 196-203.
248. Leys, J.; Losada-Pérez, P.; Glorieux, C.; Thoen, J., The Melting Behaviour of Water and Water–Sodium Chloride Solutions Studied by High-Resolution Peltier-Element-Based Adiabatic Scanning Calorimetry. *Journal of thermal analysis and Calorimetry* **2017,** *129*, 1727-1739.
249. Haynes, W. M., *Crc Handbook of Chemistry and Physics*. CRC press: 2014.
250. Han, B.; Choi, J. H.; Dantzig, J. A.; Bischof, J. C., A Quantitative Analysis on Latent Heat of an Aqueous Binary Mixture. *Cryobiology* **2006,** *52*, 146-151.
251. Kumar, R.; Fredrickson, G. H., Theory of Polyzwitterion Conformations. *The Journal of Chemical Physics* **2009,** *131*, 104901.
252. Gomez-Romero, P., Hybrid Organic–Inorganic Materials—in Search of Synergic Activity. *Advanced Materials* **2001,** *13*, 163-174.
253. Zang, J.; Ryu, S.; Pugno, N.; Wang, Q.; Tu, Q.; Buehler, M. J.; Zhao, X., Multifunctionality and Control of the Crumpling and Unfolding of Large-Area Graphene. *Nature materials* **2013,** *12*, 321.
254. Ge, D.; Lee, E.; Yang, L.; Cho, Y.; Li, M.; Gianola, D. S.; Yang, S., A Robust Smart Window: Reversibly Switching from High Transparency to Angle-Independent Structural Color Display. *Advanced Materials* **2015,** *27*, 2489-2495.

255. López Jiménez, F.; Kumar, S.; Reis, P. M., Soft Color Composites with Tunable Optical Transmittance. *Advanced Optical Materials* **2016,** *4*, 620-626.
256. Yao, X.; Hu, Y.; Grinthal, A.; Wong, T.-S.; Mahadevan, L.; Aizenberg, J., Adaptive Fluid-Infused Porous Films with Tunable Transparency and Wettability. *Nature materials* **2013,** *12*, 529.
257. Givoni, B., *Passive Low Energy Cooling of Buildings*. John Wiley & Sons: 1994.
258. Kumar, A.; Saghlatoon, H.; La, T.-G.; Honari, M. M.; Charaya, H.; Damis, H. A.; Mirzavand, R.; Mousavi, P.; Chung, H.-J., A Highly Deformable Conducting Traces for Printed Antennas and Interconnects: Silver/Fluoropolymer Composite Amalgamated by Triethanolamine. *Flexible and Printed Electronics* **2017,** *2*, 045001.
259. Yuk, H.; Zhang, T.; Parada, G. A.; Liu, X.; Zhao, X., Skin-Inspired Hydrogel-Elastomer Hybrids with Robust Interfaces and Functional Microstructures. *Nat Commun* **2016,** *7*.
260. Sun, J. Y.; Keplinger, C.; Whitesides, G. M.; Suo, Z., Ionic Skin. *Advanced Materials* **2014,** *26*, 7608-7614.
261. Cha, C.; Antoniadou, E.; Lee, M.; Jeong, J. H.; Ahmed, W. W.; Saif, T. A.; Boppart, S. A.; Kong, H., Tailoring Hydrogel Adhesion to Polydimethylsiloxane Substrates Using Polysaccharide Glue. *Angewandte Chemie International Edition* **2013,** *52*, 6949-6952.
262. Yuk, H.; Zhang, T.; Lin, S.; Parada, G. A.; Zhao, X., Tough Bonding of Hydrogels to Diverse Non-Porous Surfaces. *Nature materials* **2016,** *15*, 190.
263. Wiscombe, W. J., *Mie Scattering Calculations: Advances in Technique and Fast, Vector-Speed Computer Codes*. National Technical Information Service, US Department of Commerce: 1979.
264. Seuring, J.; Bayer, F. M.; Huber, K.; Agarwal, S., Upper Critical Solution Temperature of Poly (N-Acryloyl Glycinamide) in Water: A Concealed Property. *Macromolecules* **2011,** *45*, 374-384.
265. Woodfield, P. A.; Zhu, Y.; Pei, Y.; Roth, P. J., Hydrophobically Modified Sulfobetaine Copolymers with Tunable Aqueous Ucst through Postpolymerization Modification of Poly (Pentafluorophenyl Acrylate). *Macromolecules* **2014,** *47*, 750-762.
266. Tarascon, J.-M.; Armand, M., Issues and Challenges Facing Rechargeable Lithium Batteries. *Nature* **2001,** *414*, 359-367.
267. Weinstein, L.; Dash, R., Supercapacitor Carbons. *Materials Today* **2013,** *16*, 356-357.
268. Béguin, F.; Presser, V.; Balducci, A.; Frackowiak, E., Carbons and Electrolytes for Advanced Supercapacitors. *Advanced Materials* **2014,** *26*, 2219-2251.
269. Lu, X.; Yu, M.; Wang, G.; Tong, Y.; Li, Y., Flexible Solid-State Supercapacitors: Design, Fabrication and Applications. *Energy & Environmental Science* **2014,** *7*, 2160-2181.
270. Li, X.; Chen, Y.; Kumar, A.; Mahmoud, A.; Nychka, J. A.; Chung, H.-J., Sponge-Templated Macroporous Graphene Network for Piezoelectric Zno Nanogenerator. *ACS applied materials & interfaces* **2015,** *7*, 20753-20760.
271. Arbizzani, C.; Mastragostino, M.; Soavi, F., New Trends in Electrochemical Supercapacitors. *Journal of Power Sources* **2001,** *100*, 164-170.
272. Yin, C. Y.; Aroua, M. K.; Daud, W. M. A. W., Review of Modifications of Activated Carbon for Enhancing Contaminant Uptakes from Aqueous Solutions. *Separation and Purification Technology* **2007,** *52*, 403-415.
273. Xia, K.; Gao, Q.; Jiang, J.; Hu, J., Hierarchical Porous Carbons with Controlled Micropores and Mesopores for Supercapacitor Electrode Materials. *Carbon* **2008,** *46*, 1718-1726.

274. Kumar, B.; Asadi, M.; Pisasale, D.; Sinha-Ray, S.; Rosen, B. A.; Haasch, R.; Abiade, J.; Yarin, A. L.; Salehi-Khojin, A., Renewable and Metal-Free Carbon Nanofibre Catalysts for Carbon Dioxide Reduction. *Nature Communications* **2013,** *4*, 2819.
275. Zhang, J.; Xia, Z.; Dai, L., Carbon-Based Electrocatalysts for Advanced Energy Conversion and Storage. *Science Advances* **2015,** *1*, e1500564
276. Casiraghi, C.; Hartschuh, A.; Qian, H.; Piscanec, S.; Georgi, C.; Fasoli, A.; Novoselov, K.; Basko, D.; Ferrari, A., Raman Spectroscopy of Graphene Edges. *Nano letters* **2009,** *9*, 1433-1441.
277. Stankovich, S.; Dikin, D. A.; Piner, R. D.; Kohlhaas, K. A.; Kleinhammes, A.; Jia, Y.; Wu, Y.; Nguyen, S. T.; Ruoff, R. S., Synthesis of Graphene-Based Nanosheets Via Chemical Reduction of Exfoliated Graphite Oxide. *Carbon* **2007,** *45*, 1558-1565.
278. Wang, J.-T.; Chen, C.; Wang, E.; Kawazoe, Y., A New Carbon Allotrope with Six-Fold Helical Chains in All-Sp2 Bonding Networks. *Scientific Reports* **2014,** *4*, 4339.
279. Stoller, M. D.; Ruoff, R. S., Best Practice Methods for Determining an Electrode Material's Performance for Ultracapacitors. *Energy & Environmental Science* **2010,** *3*, 1294-1301.
280. Zhu, Z.; Jiang, H.; Guo, S.; Cheng, Q.; Hu, Y.; Li, C., Dual Tuning of Biomass-Derived Hierarchical Carbon Nanostructures for Supercapacitors: The Role of Balanced Meso/Microporosity and Graphene. *Scientific Reports* **2015,** *5*, 15936.
281. Wang, K. L.; Cao, Y. H.; Wang, X. M.; Castro, M. A.; Luo, B.; Gu, Z. R.; Liu, J.; Hoefelmeyer, J. D.; Fan, Q. H., Rod-Shape Porous Carbon Derived from Aniline Modified Lignin for Symmetric Supercapacitors. *Journal of Power Sources* **2016,** *307*, 462-467.
282. Zhao, Y. Q.; Lu, M.; Tao, P. Y.; Zhang, Y. J.; Gong, X. T.; Yang, Z.; Zhang, G. Q.; Li, H. L., Hierarchically Porous and Heteroatom Doped Carbon Derived from Tobacco Rods for Supercapacitors. *Journal of Power Sources* **2016,** *307*, 391-400.
283. Xie, Q. X.; Bao, R. R.; Zheng, A. R.; Zhang, Y. F.; Wu, S. H.; Xie, C.; Zhao, P., Sustainable Low-Cost Green Electrodes with High Volumetric Capacitance for Aqueous Symmetric Supercapacitors with High Energy Density. *Acs Sustainable Chemistry & Engineering* **2016,** *4*, 1422-1430.
284. Liu, B.; Zhang, L.; Qi, P.; Zhu, M.; Wang, G.; Ma, Y.; Guo, X.; Chen, H.; Zhang, B.; Zhao, Z., Nitrogen-Doped Banana Peel–Derived Porous Carbon Foam as Binder-Free Electrode for Supercapacitors. *Nanomaterials* **2016,** *6*, 18.
285. Nègre, L.; Daffos, B.; Turq, V.; Taberna, P.-L.; Simon, P., Ionogel-Based Solid-State Supercapacitor Operating over a Wide Range of Temperature. *Electrochimica Acta* **2016,** *206*, 490-495.
286. Ping, Z.; Nguyen, Q.; Chen, S.; Zhou, J.; Ding, Y., States of Water in Different Hydrophilic Polymers—Dsc and Ftir Studies. *Polymer* **2001,** *42*, 8461-8467.
287. Khodakovsky, I.; Mironenko, M.; Chernysheva, I.; Pokrovsky, O., Solutes in Liquid Radioactive Waste Solutions. *Contaminant Hydrology: Cold Regions Modeling* **2000**, 75.
288. Jian, Z.; Raju, V.; Li, Z.; Xing, Z.; Hu, Y. S.; Ji, X., A High-Power Symmetric Na-Ion Pseudocapacitor. *Advanced Functional Materials* **2015,** *25*, 5778-5785.
289. Zhu, Y.; Wu, Z.; Jing, M.; Hou, H.; Yang, Y.; Zhang, Y.; Yang, X.; Song, W.; Jia, X.; Ji, X., Porous Nico 2 O 4 Spheres Tuned through Carbon Quantum Dots Utilised as Advanced Materials for an Asymmetric Supercapacitor. *Journal of Materials Chemistry A* **2015,** *3*, 866-877.
290. Zhu, Y.; Ji, X.; Pan, C.; Sun, Q.; Song, W.; Fang, L.; Chen, Q.; Banks, C. E., A Carbon Quantum Dot Decorated Ruo 2 Network: Outstanding Supercapacitances under Ultrafast Charge and Discharge. *Energy & Environmental Science* **2013,** *6*, 3665-3675.

291. Pasta, M.; Wessells, C. D.; Huggins, R. A.; Cui, Y., A High-Rate and Long Cycle Life Aqueous Electrolyte Battery for Grid-Scale Energy Storage. *Nature communications* **2012,** *3*, 1149.
292. Zhan, Y.; Mei, Y.; Zheng, L., Materials Capability and Device Performance in Flexible Electronics for the Internet of Things. *Journal of Materials Chemistry C* **2014,** *2*, 1220-1232.
293. Andreu-Perez, J.; Leff, D. R.; Ip, H.; Yang, G.-Z., From Wearable Sensors to Smart Implants-–toward Pervasive and Personalized Healthcare. *IEEE Transactions on Biomedical Engineering* **2015,** *62*, 2750-2762.
294. Constantinescu, G.; Jeong, J.-W.; Li, X.; Scott, D. K.; Jang, K.-I.; Chung, H.-J.; Rogers, J. A.; Rieger, J., Epidermal Electronics for Electromyography: An Application to Swallowing Therapy. *Medical Engineering & Physics* **2016,** *38*, 807-812.
295. Mohamed, O. A.; Masood, S. H.; Bhowmik, J. L., Optimization of Fused Deposition Modeling Process Parameters: A Review of Current Research and Future Prospects. *Advances in Manufacturing* **2015,** *3*, 42-53.
296. Bikas, H.; Stavropoulos, P.; Chryssolouris, G., Additive Manufacturing Methods and Modelling Approaches: A Critical Review. *The International Journal of Advanced Manufacturing Technology* **2016,** *83*, 389-405.
297. Li, Y.; Luk, K.-M., A Multi-Beam End-Fire Magneto-Electric Dipole Antenna Array for Millimeter-Wave Applications. *IEEE Transactions on Antennas and Propagation* **2016**, *64*, 2894-2904.
298. Kajfez, D.; Elsherbeni, A. Z.; Demir, V.; Hasse, R., Omnidirectional Square Loop Segmented Antenna. *IEEE Antennas and Wireless Propagation Letters* **2016,** *15*, 846-849.
299. Zandvakili, M.; Honari, M. M.; Sameoto, D.; Mousavi, P. In *Microfluidic Liquid Metal Based Mechanically Reconfigurable Antenna Using Reversible Gecko Adhesive Based Bonding*, Microwave Symposium (IMS), 2016 IEEE MTT-S International, IEEE: 2016; pp 1-4.
300. Liu, X.; Wu, D.; Wang, H.; Wang, Q., Self-Recovering Tough Gel Electrolyte with Adjustable Supercapacitor Performance. *Advanced Materials* **2014,** *26*, 4370-4375.
301. Fernández-Merino, M. J.; Guardia, L.; Paredes, J. I.; Villar-Rodil, S.; Solís-Fernández, P.; Martínez-Alonso, A.; Tascón, J. M. D., Vitamin C Is an Ideal Substitute for Hydrazine in the Reduction of Graphene Oxide Suspensions. *The Journal of Physical Chemistry C* **2010,** *114*, 6426-6432.
302. Van der Heide, P., *X-Ray Photoelectron Spectroscopy: An Introduction to Principles and Practices*. John Wiley & Sons: 2011.
303. Raghavan, N.; Thangavel, S.; Venugopal, G., Enhanced Photocatalytic Degradation of Methylene Blue by Reduced Graphene-Oxide/Titanium Dioxide/Zinc Oxide Ternary Nanocomposites. *Materials Science in Semiconductor Processing* **2015,** *30*, 321-329.
304. Wu, Y.; Huang, M.; Song, N.; Hu, W., Electrochemical Detection of Guaiacol in Bamboo Juice Based on the Enhancement Effect of Rgo Nanosheets. *Analytical Methods* **2014,** *6*, 2729-2735.
305. Wang, H.; Zhu, B.; Jiang, W.; Yang, Y.; Leow, W. R.; Wang, H.; Chen, X., A Mechanically and Electrically Self-Healing Supercapacitor. *Advanced Materials* **2014,** *26*, 3638-3643.
306. Yamada, T.; Hayamizu, Y.; Yamamoto, Y.; Yomogida, Y.; Izadi-Najafabadi, A.; Futaba, D. N.; Hata, K., A Stretchable Carbon Nanotube Strain Sensor for Human-Motion Detection. *Nature nanotechnology* **2011,** *6*, 296-301.
307. Li, X.; Zhang, R.; Yu, W.; Wang, K.; Wei, J.; Wu, D.; Cao, A.; Li, Z.; Cheng, Y.; Zheng, Q.; Ruoff, R. S.; Zhu, H., Stretchable and Highly Sensitive Graphene-on-Polymer Strain Sensors. *Scientific Reports* **2012,** *2*, 870.

308. Tian, H.; Shu, Y.; Cui, Y.-L.; Mi, W.-T.; Yang, Y.; Xie, D.; Ren, T.-L., Scalable Fabrication of High-Performance and Flexible Graphene Strain Sensors. *Nanoscale* **2014,** *6*, 699-705.
309. Hempel, M.; Nezich, D.; Kong, J.; Hofmann, M., A Novel Class of Strain Gauges Based on Layered Percolative Films of 2d Materials. *Nano letters* **2012,** *12*, 5714-5718.
310. Yang, S.; Lu, N., Gauge Factor and Stretchability of Silicon-on-Polymer Strain Gauges. *Sensors* **2013,** *13*, 8577.
311. Hu, N.; Karube, Y.; Arai, M.; Watanabe, T.; Yan, C.; Li, Y.; Liu, Y.; Fukunaga, H., Investigation on Sensitivity of a Polymer/Carbon Nanotube Composite Strain Sensor. *Carbon* **2010,** *48*, 680-687.
312. Eswaraiah, V.; Balasubramaniam, K.; Ramaprabhu, S., One-Pot Synthesis of Conducting Graphene–Polymer Composites and Their Strain Sensing Application. *Nanoscale* **2012,** *4*, 1258-1262.
313. Zhao, J.; He, C.; Yang, R.; Shi, Z.; Cheng, M.; Yang, W.; Xie, G.; Wang, D.; Shi, D.; Zhang, G., Ultra-Sensitive Strain Sensors Based on Piezoresistive Nanographene Films. *Applied Physics Letters* **2012,** *101*, 063112.
314. Bae, S.-H.; Lee, Y.; Sharma, B. K.; Lee, H.-J.; Kim, J.-H.; Ahn, J.-H., Graphene-Based Transparent Strain Sensor. *Carbon* **2013,** *51*, 236-242.
315. Li, J.; Zhao, S.; Zeng, X.; Huang, W.; Gong, Z.; Zhang, G.; Sun, R.; Wong, C.-P., Highly Stretchable and Sensitive Strain Sensor Based on Facilely Prepared Three-Dimensional Graphene Foam Composite. *ACS applied materials & interfaces* **2016,** *8*, 18954-18961.
316. Wang, Y.; Wang, L.; Yang, T. T.; Li, X.; Zang, X. B.; Zhu, M.; Wang, K. L.; Wu, D. H.; Zhu, H. W., Wearable and Highly Sensitive Graphene Strain Sensors for Human Motion Monitoring. *Advanced Functional Materials* **2014,** *24*, 4666-4670.
317. Fernandez-Merino, M.; Guardia, L.; Paredes, J.; Villar-Rodil, S.; Solis-Fernandez, P.; Martinez-Alonso, A.; Tascon, J., Vitamin C Is an Ideal Substitute for Hydrazine in the Reduction of Graphene Oxide Suspensions. *The Journal of Physical Chemistry C* **2010,** *114*, 6426-6432.
318. Zhang, K.; Zhang, L. L.; Zhao, X. S.; Wu, J., Graphene/Polyaniline Nanofiber Composites as Supercapacitor Electrodes. *Chemistry of Materials* **2010,** *22*, 1392-1401.
319. Casiraghi, C.; Hartschuh, A.; Qian, H.; Piscanec, S.; Georgi, C.; Fasoli, A.; Novoselov, K. S.; Basko, D. M.; Ferrari, A. C., Raman Spectroscopy of Graphene Edges. *Nano letters* **2009,** *9*, 1433-1441.
320. Kudin, K. N.; Ozbas, B.; Schniepp, H. C.; Prud'homme, R. K.; Aksay, I. A.; Car, R., Raman Spectra of Graphite Oxide and Functionalized Graphene Sheets. *Nano letters* **2008,** *8*, 36-41.
321. Ferrari, A. C.; Robertson, J., Interpretation of Raman Spectra of Disordered and Amorphous Carbon. *Physical Review B* **2000,** *61*, 14095-14107.
322. Ferrari, A. C.; Robertson, J., Resonant Raman Spectroscopy of Disordered, Amorphous, and Diamondlike Carbon. *Physical Review B* **2001,** *64*, 13.
323. Graf, D.; Molitor, F.; Ensslin, K.; Stampfer, C.; Jungen, A.; Hierold, C.; Wirtz, L., Spatially Resolved Raman Spectroscopy of Single- and Few-Layer Graphene. *Nano letters* **2007,** *7*, 238-242.
324. Xia, H.; Song, M., Preparation and Characterization of Polyurethane–Carbon Nanotube Composites. *Soft Matter* **2005,** *1*, 386-394.
325. Acik, M.; Lee, G.; Mattevi, C.; Chhowalla, M.; Cho, K.; Chabal, Y., Unusual Infrared-Absorption Mechanism in Thermally Reduced Graphene Oxide. *Nature materials* **2010,** *9*, 840-845.

326. Compton, O. C.; Nguyen, S. T., Graphene Oxide, Highly Reduced Graphene Oxide, and Graphene: Versatile Building Blocks for Carbon-Based Materials. *Small* **2010,** *6*, 711-723.
327. Hwang, J. O.; Lee, D. H.; Kim, J. Y.; Han, T. H.; Kim, B. H.; Park, M.; No, K.; Kim, S. O., Vertical Zno Nanowires/Graphene Hybrids for Transparent and Flexible Field Emission. *Journal of Materials Chemistry* **2011,** *21*, 3432-3437.
328. Feng, W.; Rangan, S.; Cao, Y.; Galoppini, E.; Bartynski, R. A.; Garfunkel, E., Energy Level Alignment of Polythiophene/Zno Hybrid Solar Cells. *Journal of Materials Chemistry A* **2014,** *2*, 7034-7044.
329. Kwon, K. C.; Choi, K. S.; Kim, S. Y., Increased Work Function in Few-Layer Graphene Sheets Via Metal Chloride Doping. *Advanced Functional Materials* **2012,** *22*, 4724-4731.
330. Kumar, P. V.; Bernardi, M.; Grossman, J. C., The Impact of Functionalization on the Stability, Work Function, and Photoluminescence of Reduced Graphene Oxide. *ACS nano* **2013,** *7*, 1638-1645.
331. Park, K. I.; Lee, M.; Liu, Y.; Moon, S.; Hwang, G. T.; Zhu, G.; Kim, J. E.; Kim, S. O.; Kim, D. K.; Wang, Z. L., Flexible Nanocomposite Generator Made of Batio3 Nanoparticles and Graphitic Carbons. *Advanced Materials* **2012,** *24*, 2999-3004.
332. Yang, S.; Wang, L.; Tian, X.; Xu, Z.; Wang, W.; Bai, X.; Wang, E., The Piezotronic Effect of Zinc Oxide Nanowires Studied by in Situ Tem. *Advanced Materials* **2012,** *24*, 4676-4682.
333. Wang, Z. L., *Piezotronics and Piezo-Phototronics*. Springer Berlin Heidelberg: 2013.
334. Abdelhalim, M. A. K.; Mady, M. M.; Ghannam, M. M., Dielectric Constant, Electrical Conductivity and Relaxation Time Measurements of Different Gold Nanoparticle Sizes. *International Journal of the Physical Sciences in Publication* **2011**.
335. Chizhik, S. A.; Huang, Z.; Gorbunov, V. V.; Myshkin, N. K.; Tsukruk, V. V., Micromechanical Properties of Elastic Polymeric Materials as Probed by Scanning Force Microscopy. *Langmuir* **1998,** *14*, 2606-2609.
336. Johnston, I.; McCluskey, D.; Tan, C.; Tracey, M., Mechanical Characterization of Bulk Sylgard 184 for Microfluidics and Microengineering. *Journal of Micromechanics and Microengineering* **2014,** *24*, 035017.
337. Ni, H.; Li, X. D., Young's Modulus of Zno Nanobelts Measured Using Atomic Force Microscopy and Nanoindentation Techniques. *Nanotechnology* **2006,** *17*, 3591-3597.
338. Wang, Y.; Ameer, G. A.; Sheppard, B. J.; Langer, R., A Tough Biodegradable Elastomer. *Nat Biotech* **2002,** *20*, 602-606.
339. Chen, Q.-Z.; Harding, S. E.; Ali, N. N.; Lyon, A. R.; Boccaccini, A. R., Biomaterials in Cardiac Tissue Engineering: Ten Years of Research Survey. *Materials Science and Engineering: R: Reports* **2008,** *59*, 1-37.
340. Bettinger, C. J.; Weinberg, E. J.; Kulig, K. M.; Vacanti, J. P.; Wang, Y.; Borenstein, J. T.; Langer, R., Three-Dimensional Microfluidic Tissue-Engineering Scaffolds Using a Flexible Biodegradable Polymer. *Advanced Materials* **2006,** *18*, 165-169.
341. Freed, L. E.; Engelmayr, G. C.; Borenstein, J. T.; Moutos, F. T.; Guilak, F., Advanced Material Strategies for Tissue Engineering Scaffolds. *Advanced Materials* **2009,** *21*, 3410-3418.
342. Engelmayr, G. C.; Cheng, M.; Bettinger, C. J.; Borenstein, J. T.; Langer, R.; Freed, L. E., Accordion-Like Honeycombs for Tissue Engineering of Cardiac Anisotropy. *Nat Mater* **2008,** *7*, 1003-1010.
343. Gao, J.; Crapo, P. M.; Wang, Y., Macroporous Elastomeric Scaffolds with Extensive Micropores for Soft Tissue Engineering. *Tissue engineering* **2006,** *12*, 917-925.

344. Yi, F.; LaVan, D. A., Poly (Glycerol Sebacate) Nanofiber Scaffolds by Core/Shell Electrospinning. *Macromolecular bioscience* **2008,** *8*, 803-806.
345. Kharaziha, M.; Nikkhah, M.; Shin, S.-R.; Annabi, N.; Masoumi, N.; Gaharwar, A. K.; Camci-Unal, G.; Khademhosseini, A., Pgs:Gelatin Nanofibrous Scaffolds with Tunable Mechanical And structural Properties for Engineering Cardiac Tissues. *Biomaterials* **2013,** *34*, 6355-6366.
346. Hwang, S.-W.; Huang, X.; Seo, J.-H.; Song, J.-K.; Kim, S.; Hage-Ali, S.; Chung, H.-J.; Tao, H.; Omenetto, F. G.; Ma, Z.; Rogers, J. A., Materials for Bioresorbable Radio Frequency Electronics. *Advanced Materials* **2013,** *25*, 3526-3531.
347. Xu, L.; Gutbrod, S. R.; Bonifas, A. P.; Su, Y.; Sulkin, M. S.; Lu, N.; Chung, H.-J.; Jang, K.-I.; Liu, Z.; Ying, M., 3d Multifunctional Integumentary Membranes for Spatiotemporal Cardiac Measurements and Stimulation across the Entire Epicardium. *Nature communications* **2014,** *5*.
348. Li, Y.; Cook, W. D.; Moorhoff, C.; Huang, W. C.; Chen, Q. Z., Synthesis, Characterization and Properties of Biocompatible Poly (Glycerol Sebacate) Pre-Polymer and Gel. *Polymer International* **2013,** *62*, 534-547.
349. Maliger, R.; Halley, P. J.; Cooper-White, J. J., Poly (Glycerol–Sebacate) Bioelastomers—Kinetics of Step-Growth Reactions Using Fourier Transform (Ft)-Raman Spectroscopy. *Journal of Applied Polymer Science* **2013,** *127*, 3980-3986.
350. Zhang, H.; Grinstaff, M. W., Recent Advances in Glycerol Polymers: Chemistry and Biomedical Applications. *Macromolecular Rapid Communications* **2014**, *35*, 1906-1924.
351. Bettinger, C. J., Biodegradable Elastomers for Tissue Engineering and Cell–Biomaterial Interactions. *Macromolecular Bioscience* **2011,** *11*, 467-482.
352. Aydin, H.; Salimi, K.; Rzayev, Z.; Pişkin, E., Microwave-Assisted Rapid Synthesis of Poly (Glycerol-Sebacate) Elastomers. *Biomaterials Science* **2013,** *1*, 503-509.
353. Makris, E. A.; Hadidi, P.; Athanasiou, K. A., The Knee Meniscus: Structure–Function, Pathophysiology, Current Repair Techniques, and Prospects for Regeneration. *Biomaterials* **2011,** *32*, 7411-7431.
354. Chen, Q.-Z.; Bismarck, A.; Hansen, U.; Junaid, S.; Tran, M. Q.; Harding, S. E.; Ali, N. N.; Boccaccini, A. R., Characterisation of a Soft Elastomer Poly(Glycerol Sebacate) Designed to Match the Mechanical Properties of Myocardial Tissue. *Biomaterials* **2008,** *29*, 47-57.
355. Jeong, C. G.; Hollister, S. J., A Comparison of the Influence of Material on in Vitro Cartilage Tissue Engineering with Pcl, Pgs, and Poc 3d Scaffold Architecture Seeded with Chondrocytes. *Biomaterials* **2010,** *31*, 4304-4312.
356. Pomerantseva, I.; Krebs, N.; Hart, A.; Neville, C. M.; Huang, A. Y.; Sundback, C. A., Degradation Behavior of Poly (Glycerol Sebacate). *Journal of biomedical materials research Part A* **2009,** *91*, 1038-1047.
357. Pereira, M. J. N.; Ouyang, B.; Sundback, C. A.; Lang, N.; Friehs, I.; Mureli, S.; Pomerantseva, I.; McFadden, J.; Mochel, M. C.; Mwizerwa, O., A Highly Tunable Biocompatible and Multifunctional Biodegradable Elastomer. *Advanced Materials* **2013,** *25*, 1209-1215.
358. Chen, Q.; Liang, S.; Thouas, G. A., Elastomeric Biomaterials for Tissue Engineering. *Progress in Polymer Science* **2013,** *38*, 584-671.
359. Liu, Q.; Jiang, L.; Shi, R.; Zhang, L., Synthesis, Preparation, in Vitro Degradation, and Application of Novel Degradable Bioelastomers—a Review. *Progress in Polymer Science* **2012,** *37*, 715-765.

360. Williams, J. M.; Adewunmi, A.; Schek, R. M.; Flanagan, C. L.; Krebsbach, P. H.; Feinberg, S. E.; Hollister, S. J.; Das, S., Bone Tissue Engineering Using Polycaprolactone Scaffolds Fabricated Via Selective Laser Sintering. *Biomaterials* **2005,** *26*, 4817-4827.
361. Hutmacher, D. W.; Schantz, T.; Zein, I.; Ng, K. W.; Teoh, S. H.; Tan, K. C., Mechanical Properties and Cell Cultural Response of Polycaprolactone Scaffolds Designed and Fabricated Via Fused Deposition Modeling. *Journal of biomedical materials research* **2001,** *55*, 203-216.
362. Walls, H.; Zhou, J.; Yerian, J. A.; Fedkiw, P. S.; Khan, S. A.; Stowe, M. K.; Baker, G. L., Fumed Silica-Based Composite Polymer Electrolytes: Synthesis, Rheology, and Electrochemistry. *Journal of Power Sources* **2000,** *89*, 156-162.
363. Liang, S.; Cook, W. D.; Chen, Q., Physical Characterization of Poly (Glycerol Sebacate)/Bioglass® Composites. *Polymer International* **2012,** *61*, 17-22.
364. Wu, Y.; Shi, R.; Chen, D.; Zhang, L.; Tian, W., Nanosilica Filled Poly (Glycerol-Sebacate-Citrate) Elastomers with Improved Mechanical Properties, Adjustable Degradability, and Better Biocompatibility. *Journal of Applied Polymer Science* **2012,** *123*, 1612-1620.
365. Richards, R., Polyethylene-Structure, Crystallinity and Properties. *Journal of Applied Chemistry* **1951,** *1*, 370-376.
366. Jaafar, I. H.; Ammar, M. M.; Jedlicka, S. S.; Pearson, R. A.; Coulter, J. P., Spectroscopic Evaluation, Thermal, and Thermomechanical Characterization of Poly (Glycerol-Sebacate) with Variations in Curing Temperatures and Durations. *Journal of materials science* **2010,** *45*, 2525-2529.
367. Dunn, A. S., Introduction to Physical Polymer Science (2nd Edition). By L. H. Sperling, New York, 1992 John Wiley & Sons Inc. John Wiley & Sons Inc., New York, 1992.
368. Kemppainen, J. M.; Hollister, S. J., Tailoring the Mechanical Properties of 3d-Designed Poly (Glycerol Sebacate) Scaffolds for Cartilage Applications. *Journal of Biomedical Materials Research Part A* **2010,** *94*, 9-18.
369. Bruggeman, J. P.; de Bruin, B.-J.; Bettinger, C. J.; Langer, R., Biodegradable Poly (Polyol Sebacate) Polymers. *Biomaterials* **2008,** *29*, 4726-4735.
370. Yuan, L.; Wenchao, H.; Wayne, D. C.; Qizhi, C., A Comparative Study on Poly(Xylitol Sebacate) and Poly(Glycerol Sebacate): Mechanical Properties, Biodegradation and Cytocompatibility. *Biomedical Materials* **2013,** *8*, 035006.
371. Cheng, H.; Hill, P. S.; Siegwart, D. J.; Vacanti, N.; Lytton-Jean, A. K.; Cho, S. W.; Ye, A.; Langer, R.; Anderson, D. G., A Novel Family of Biodegradable Poly (Ester Amide) Elastomers. *Advanced Materials* **2011,** *23*, H95-H100.
372. Dey, J.; Xu, H.; Shen, J.; Thevenot, P.; Gondi, S. R.; Nguyen, K. T.; Sumerlin, B. S.; Tang, L.; Yang, J., Development of Biodegradable Crosslinked Urethane-Doped Polyester Elastomers. *Biomaterials* **2008,** *29*, 4637-4649.
373. Petsonk, E. L.; Wang, M. L.; Lewis, D. M.; Siegel, P. D.; Husberg, B. J., Asthma-Like Symptoms in Wood Product Plant Workers Exposed to Methylene Diphenyl Diisocyanate. *CHEST Journal* **2000,** *118*, 1183-1193.
374. Wang, G.; Zhang, L.; Zhang, J., A Review of Electrode Materials for Electrochemical Supercapacitors. *Chemical Society Reviews* **2012,** *41*, 797-828.

Appendices

A1. Hydrogel Structures of Sample Dialyzed in DIW and KOH

Polyampholyte Hydrogel Synthesis. The protocol of polyampholyte synthesis was described in Chapter 4. Briefly, 1 M sodium 4-vinylbenzenesulfonate (NaSS) and 1 M [3-(methacryloylamino)propyl] trimethylammonium chloride (MPTC) with IRGACURE 2959 (photoinitiator, 0.25 mol%, compared to the total concentration of NaSS and MPTC) and NaCl were dissolved in deionized water to form the precursor solution. In the precursor solution, NaCl is 10 wt% (sodium and chloride ions contained in NaSS and MPTC were accounted for). The aqueous precursor solution was injected into the gap between two glass plates separated by a 1 mm thick Teflon spacer, followed by polymerization initiated by irradiating the sample with UV light with a lamp-to-sample distance of 5 mm (broadband light with a maximum peak at 365 nm with the intensity of 22 mW/cm^2, Jelight UVO-Cleaner Model-342, US). The samples prepared are listed in Table 6.1. Hereafter, we denote the samples using the code PA-#-*c*, where the # is the NaCl concentration (wt%) in the polyampholyte hydrogel and *c* is the total monomer concentration (M).

Table A1 List of samples

Sample	NaSS conc.	MPTC conc.	NaCl conc.	UV time	Further treatment
PA-10-2.1	1.07 M	1.03 M	10 wt%	8 h	-
D-PA-10-2.1	1.07 M	1.03 M	10 wt%	8 h	Dialyzed in DIW
K-PA-10-2.1	1.07 M	1.03 M	10 wt%	8 h	Dialyzed in 6 M KOH

a. In all cases, 0.25 mol% photoinitiator (compared to the combined concentration of NaSS and MPTC) was added in the precursor solution.
b. PA-10-2.1 samples were dialyzed in DIW and 6 M KOH for one week to prepare D-PA-10-2.1 and K-PA-10-2.1, respectively.

Freeze-Died Hydrogel Characterizations. Polyampholyte hydrogel sample was freeze-dried before SEM characterization. For D-PA-10-2.1 and K-PA-10-2.1, the samples were only quenched in liquid nitrogen, followed by freeze-drying. A ~10 nm thick Au–Pd layer was coated on the freeze-dried samples using a gold sputter unit (Denton; US). An FE-SEM (Zeiss, Sigma) was utilized for the morphological study.

We investigated the impacts of different dialysis solutions for post-treatments on the structures of polyampholyte hydrogel. Figure A1 shows the SEM images of DIW dialyzed hydrogel of D-PA-10-2.1. The morphology of D-PA-10-2.1 turns into a macroscopic cellular structure of polymeric networks with pore size of ~ 20 μm after dialysis. The SEM result suggests that salt ions are essential to screen charges of the polymer chains and thereby prevent electrostatic attraction between the polymer chains. DIW dialysis leaches out the salt ions and as a result highly charged polymer chains with opposite charges collapse together in an irreversible way.[1] In other words, the polyampholyte chains are 'zipped' and the water and the polyampholyte phase separate in the hydrogel, resulting in the macroscopic structure in Figure A1.[2] According to the mechanism, one can hypothesize that dialysis in a high ionic strength neutral salt solution may prevent the 'zipping' of the collapsed chains. Moreover, the structure change of dialyzed polyampholyte hydrogel in DIW can also support our finding in Chapter 5 that the DIW dialyzed hydrogels cannot prevent freezing of water molecules due to the irreversible collapse of the polyampholyte chains, resulting in most water molecules behaving as they do in the bulk.

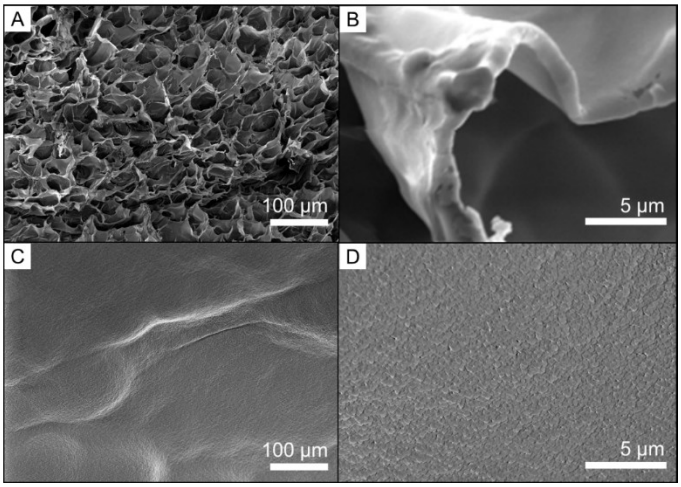

Figure A1. The SEM image of (A) freeze-dried D-PA-10-2.1 and (C) freeze-dried K-PA-10-2.1. (B) and (D) are the zoomed-in images of (A) and (C).

In a parallel study, we used KOH as the solution for dialyzing as-prepared hydrogel as gel electrolyte in the electrochemical storage device.[3] The result of quenched and freeze-dried K-PA-10-2.1 was shown in Figure A1C and A1D. A homogeneous distribution of fine nanostructures is found in the freeze-dried K-PA-10-2.1. The macroscopic cellular structure shown in Figure A1 is

not observed when the polyampholyte is dialyzed in a 6 M KOH solution, possibly indicating ion exchange behavior without 'zipping'. Moreover, the trimethylammonium groups in the polyampholyte chains may associate with hydroxide groups in the base environment.[4,5] If this happens, the polyampholyte chain is no longer charge-balanced and net charge on the chain becomes negative. The effect of hydroxyl ion association may result in a fundamental structure and property change of the polymer chains, which requires future studies.

A2. SAXS/WAXS Results of Polyampholyte Hydrogel

Small Angle X-Ray Scattering Characterization. SAXS samples were made by irradiating beeswax sealed glass capillaries (Charles Supper, US) containing a precursor solution with UV as shown in Table A2. The shaded samples were not measured due to limited beam time. The SAXS experiments were performed with the beamline 12-ID-B of the Advanced Photon Source at the Argonne National Laboratory in the US. The 14 keV X-ray beam was exposed to the 1.5 mm diameter capillary sample with an exposure time of typically 0.1 s. Scattered X-ray photons were measured with a Pilatus 2M (Dectris Ltd.) detector located about 2 m downstream of the sample. Ten images per sample were collected and averaged to confirm that no beam damage had occurred and to increase counting statistics. Background scattering from a capillary containing water was subtracted from sample data. Ten images per sample were collected and averaged to confirm that no beam damage had occurred and to increase counting statistics. Background scattering from a capillary containing water was subtracted from the sample data. In the temperature-dependent SAXS/WAXS measurements, the following thermal history was programmed: (i) held at 5 °C for 10 min, (ii) cooled from +5 to –40 °C at a rate of 10 °C/min, (iii) held at –40 °C for 10 min, (iv) heated up to 70 °C at a rate of 10 °C/min.

Table A2 Samples prepared for SAXS/WAXS measurement.

#	Sample Name	NaSS	MPTC (mL)	DMAEA-Q (mL)	NaCl	MBAA	Dialysis	T-Range (°C)	Comments
1	NaCl Solution	-	-	-	0.87	-	-	–40/70	Control Solution
2	PNM Control	2.29	4.2	-	0.29	-	-	–40/70	
3	PND Control	2.29	-	2.14	0.29	-	-	-40/70	
4	PNM/1:1/2.0	2.29	4.2	-	0.58	-	-	–40/70	
5	PNM/1:1/1.0	2.29	4.2	-	0	-	-	–40/70	Poly(NaSS-co-MPTC)
6	PNM/1:1/1.5	2.29	4.2	-	0.29	-	-	–40/70	Salt concentration
7	PNM/.5:.5/2.0	1.145	2.1	-	0.87	-	-	–40/70	Poly(NaSS-co-MPTC)
8	PNM/.75:.75/2.0	1.7175	3.15	-	0.725	-	-	–40/70	Polymer concentration
9	PND/1:1/2.0	2.29	-	2.14	0.58	-	-	–40/70	
10	PND/1:1/1.0	2.29	-	2.14	0	-	-	–40/70	Poly(NaSS-co-DMAEA-Q)
11	PND/1:1/1.5	2.29	-	2.14	0.29	-	-	–40/70	Salt concentration
12	PND/.5:.5/2.0	1.145	-	1.07	0.87	-	-	–40/70	Poly(NaSS-co-DMAEA-Q)
13	PND/.75:.75/2.0	1.7175	-	1.605	0.725	-	-	–40/70	Polymer concentration
14	PNMD/.8:.2	2.29	3.36	0.428	0.29	-	-	–40/70	
15	PNMD/.6:.4	2.29	2.52	0.856	0.29	-	-	–40/70	Poly(NaSS-co-MPTC-
16	PNMD/.4:.6	2.29	1.68	1.284	0.29	-	-	-40/70	DMAEA-Q)
17	PNMD/.2:.8	2.29	0.84	1.712	0.29	-	-	–40/70	
18	PNM/1:1/1.5-1C	2.29	4.2	-	0.29	0.0306	-	–40/70	
19	PNM/1:1/1.5-.5C	2.29	4.2	-	0.29	0.0153	-	–40/70	Poly(NaSS-co-MPTC)
20	PNM/1:1/1.5-.3C	2.29	4.2	-	0.29	0.0092	-	–40/70	Cross-linker concentration
21	PND/1:1/1.5-1C	2.29	-	2.14	0.29	0.0306	-	-40/70	
22	PND/1:1/1.6-.5C	2.29	-	2.14	0.29	0.0153	-	-40/70	Poly(NaSS-co-DMAEA-Q)
23	PND/1:1/1.7-.3C	2.29	-	2.14	0.29	0.0092	-	-40/70	Cross-linker concentration
24	PNM/1:1/1.5-.3C	2.29	4.2	-	0.29	0.0092	KOH 6M	–40/20	Chemically crosslinked
25	PND/1:1/1.7-.3C	2.29	-	2.14	0.29	0.0092	KOH 6M	-40/20	polymer with KOH dialysis
26	PNM/1:1/1.5	2.29	4.2	-	0.29	-	KOH 6M	–40/20	Polymer with KOH dialysis
27	PND/1:1/1.5	2.29	-	2.14	0.29	-	KOH 6M	-40/20	Sample 27 dissolved.
28	PNM/1:1/1.5	2.29	4.2	-	0.29	-	DIW	–20/70	
29	PND/1:1/1.5	2.29	-	2.14	0.29	-	DIW	-20/70	Polymer with DIW dialysis
30	KOH solution (6M)								Control Solution

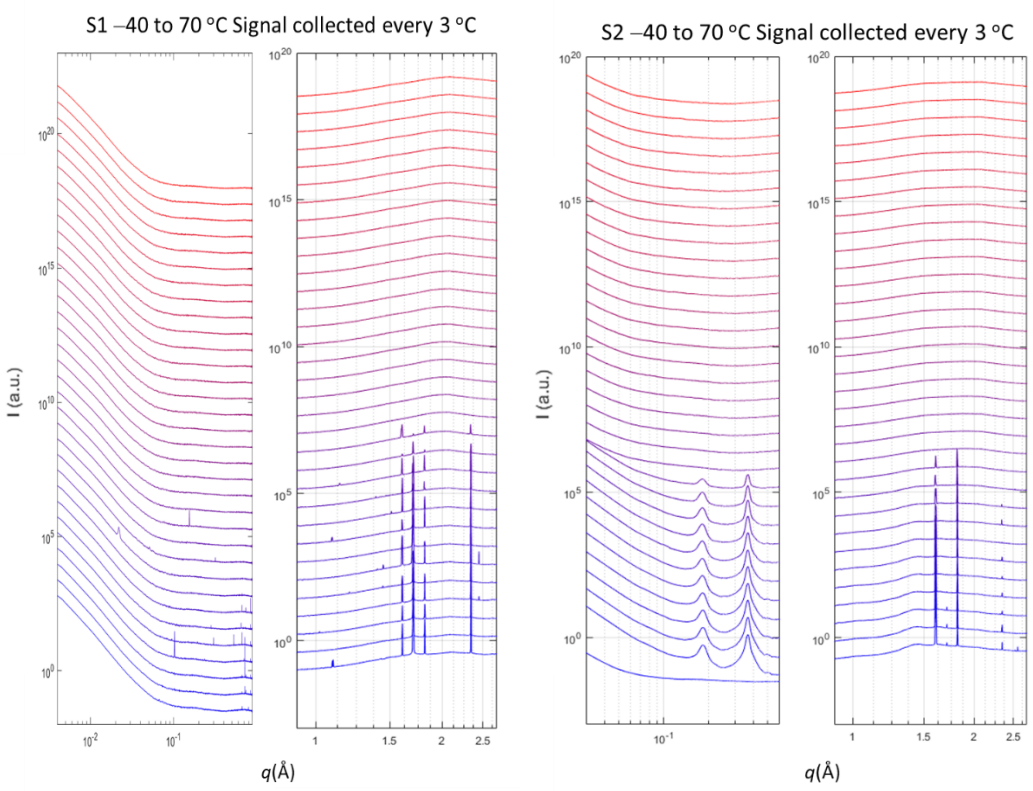
S1 –40 to 70 °C Signal collected every 3 °C
S2 –40 to 70 °C Signal collected every 3 °C
I (a.u.)
q(Å)

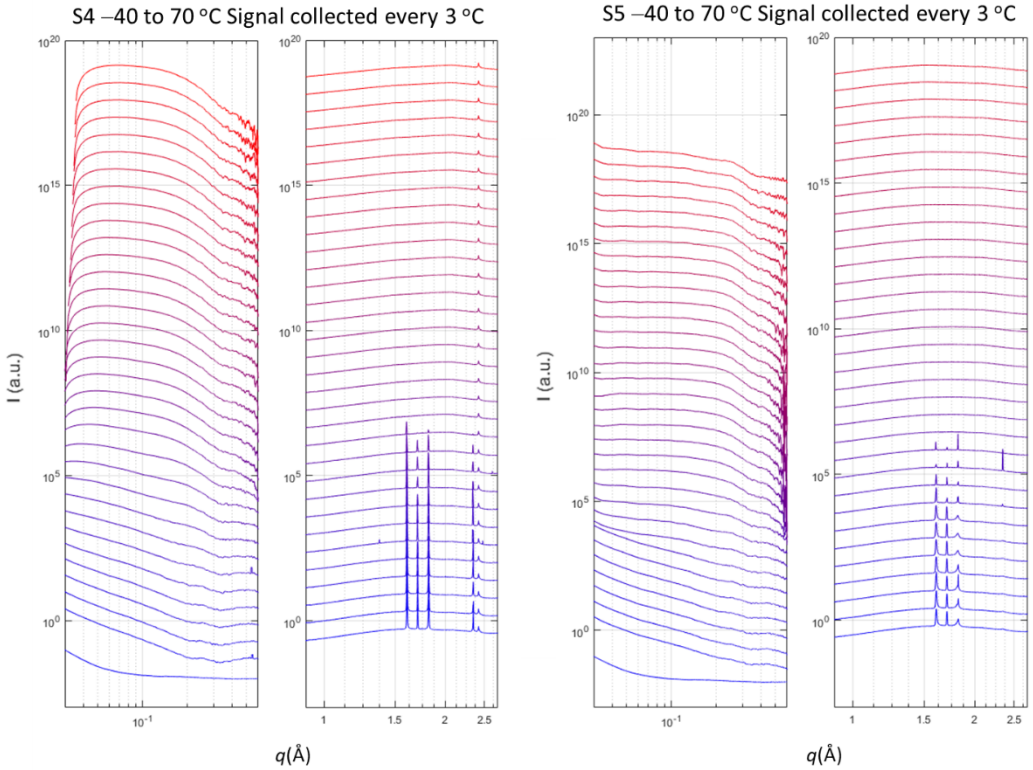
S4 –40 to 70 °C Signal collected every 3 °C
S5 –40 to 70 °C Signal collected every 3 °C
I (a.u.)
q(Å)

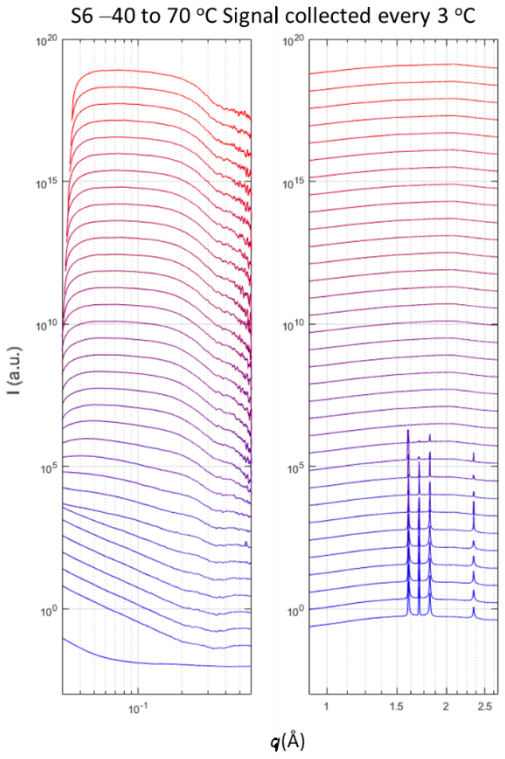
S6 –40 to 70 °C Signal collected every 3 °C
I (a.u.)
q(Å)

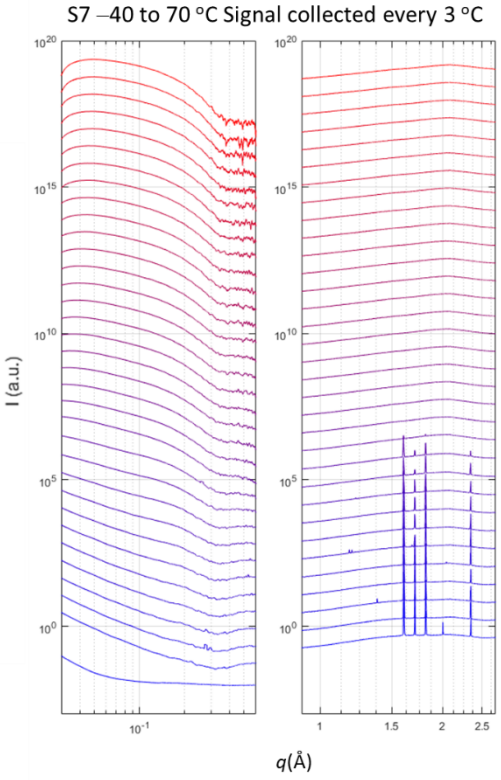
S7 –40 to 70 °C Signal collected every 3 °C
I (a.u.)
q(Å)

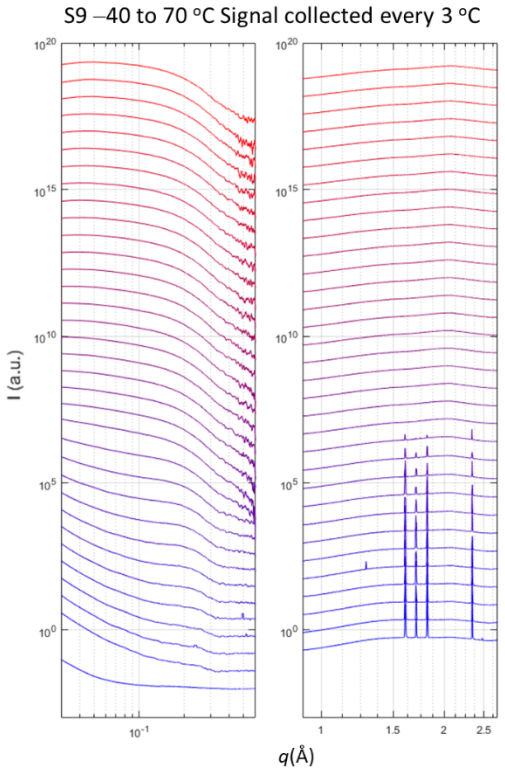
S9 –40 to 70 °C Signal collected every 3 °C
I (a.u.)
q(Å)

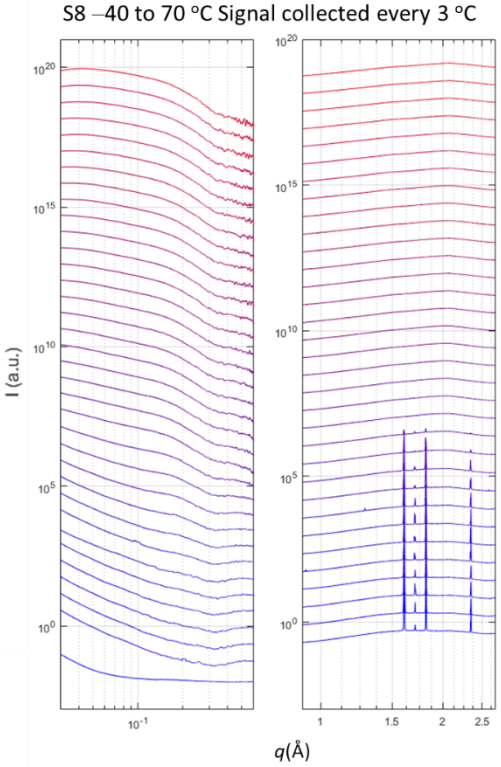
S8 –40 to 70 °C Signal collected every 3 °C
I (a.u.)
q(Å)

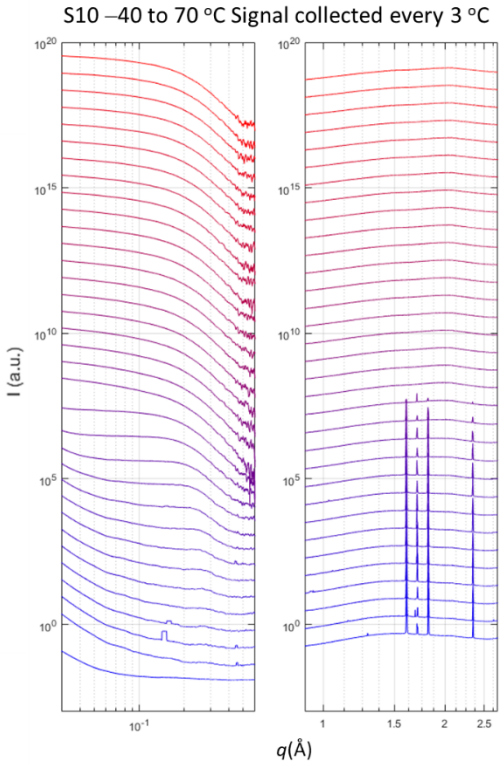
S10 –40 to 70 °C Signal collected every 3 °C
I (a.u.)
q(Å)

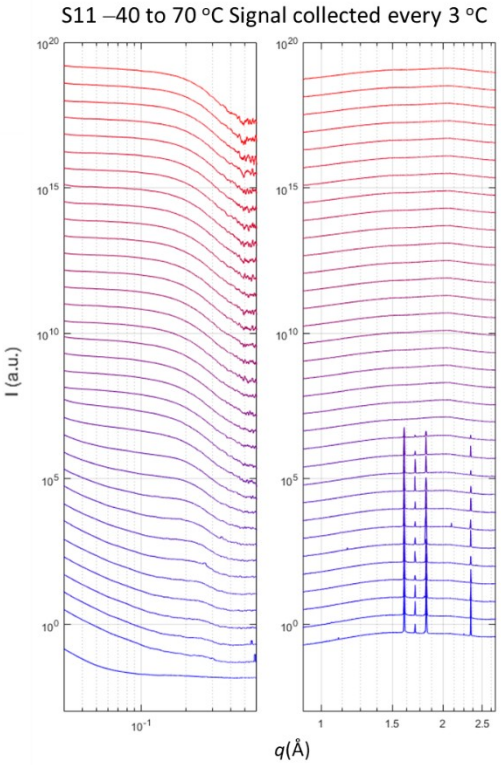
S11 –40 to 70 °C Signal collected every 3 °C
I (a.u.)
q(Å)

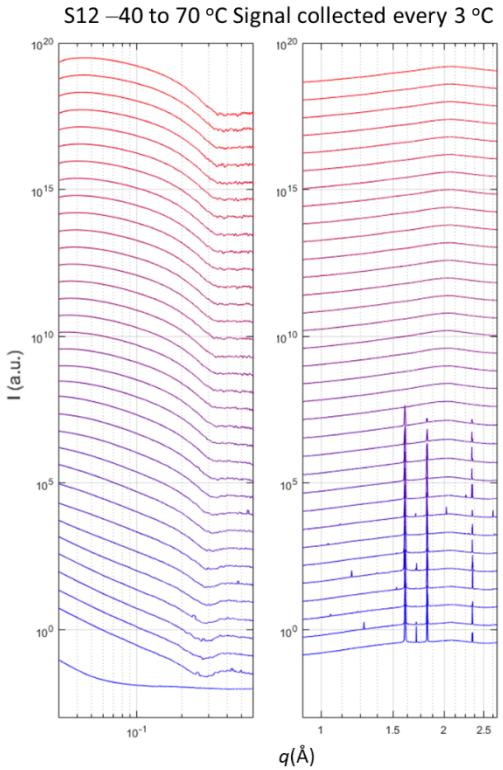
S12 –40 to 70 °C Signal collected every 3 °C
I (a.u.)
q(Å)

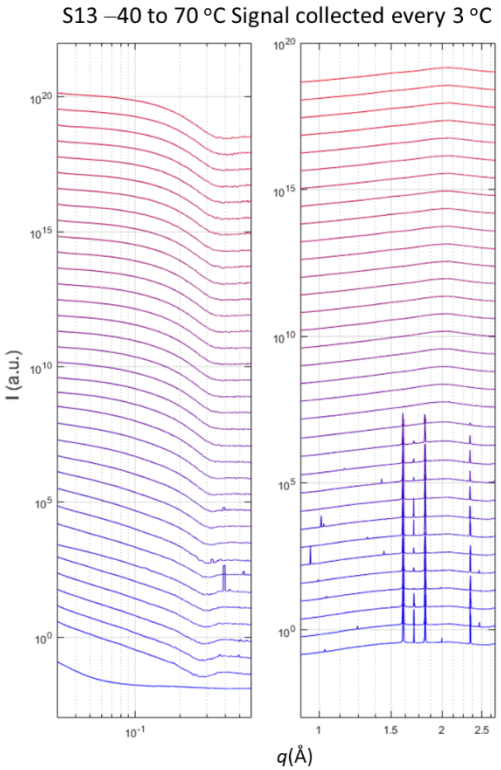
S13 –40 to 70 °C Signal collected every 3 °C
I (a.u.)
q(Å)

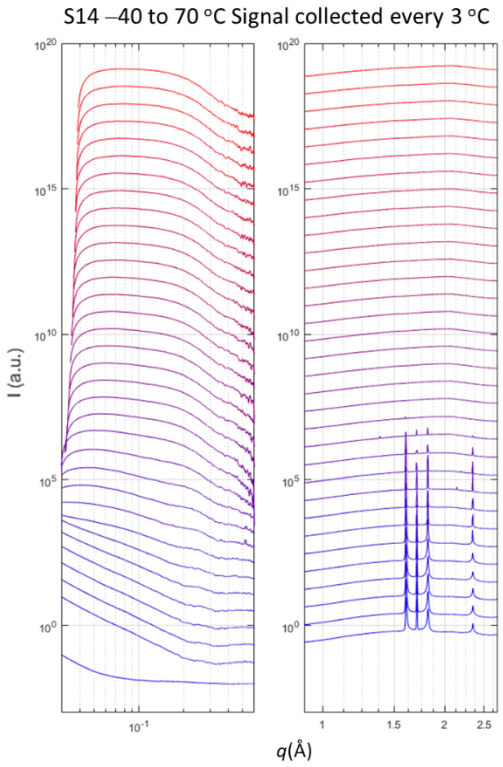
S14 –40 to 70 °C Signal collected every 3 °C
I (a.u.)
q(Å)

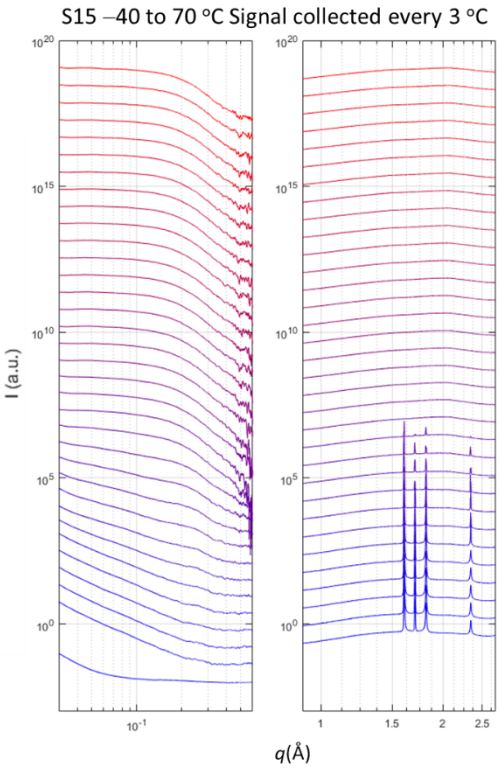
S15 –40 to 70 °C Signal collected every 3 °C
I (a.u.)
q(Å)

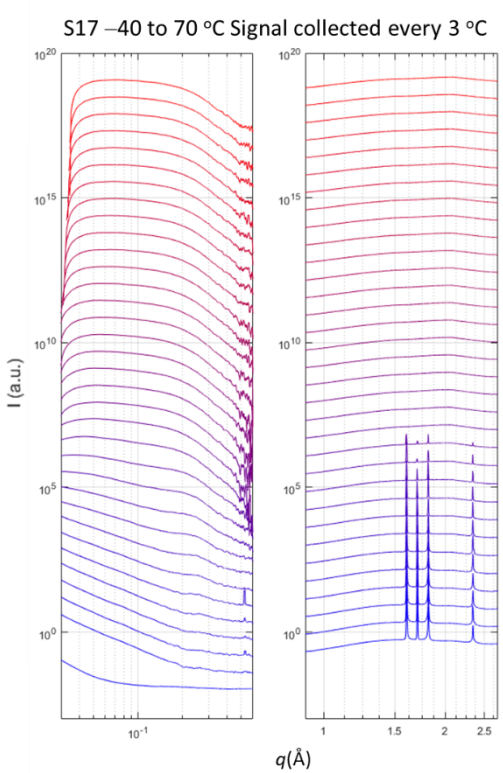
S17 –40 to 70 °C Signal collected every 3 °C
I (a.u.)
q(Å)

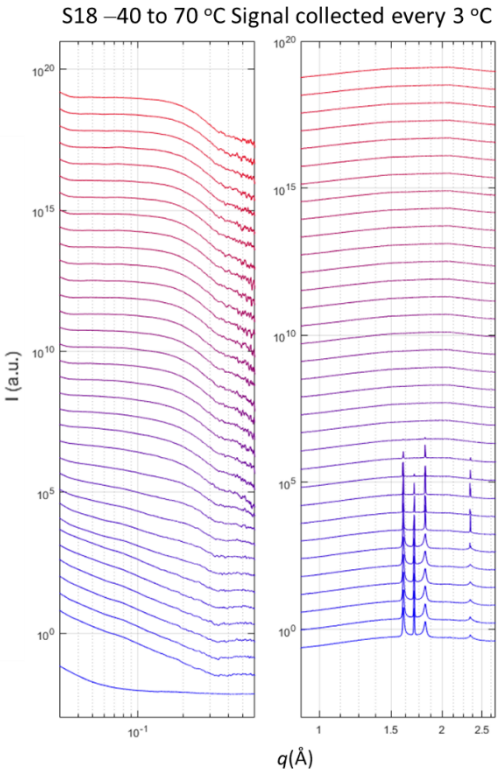
S18 –40 to 70 °C Signal collected every 3 °C
I (a.u.)
q(Å)

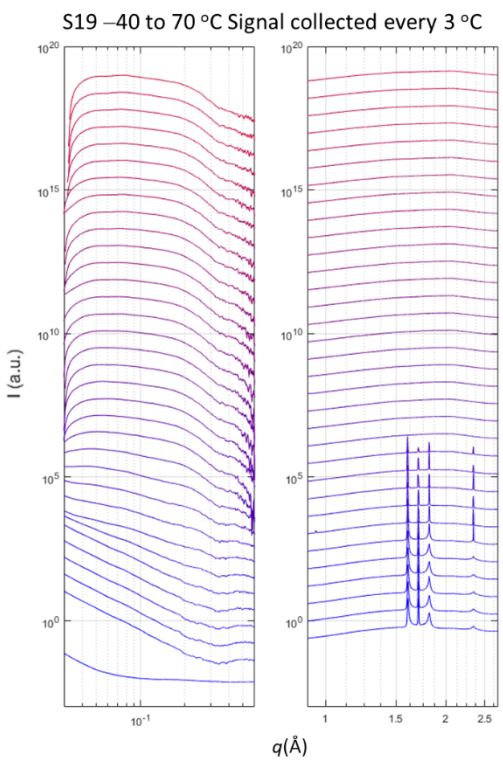
S19 –40 to 70 °C Signal collected every 3 °C
I (a.u.)
q(Å)

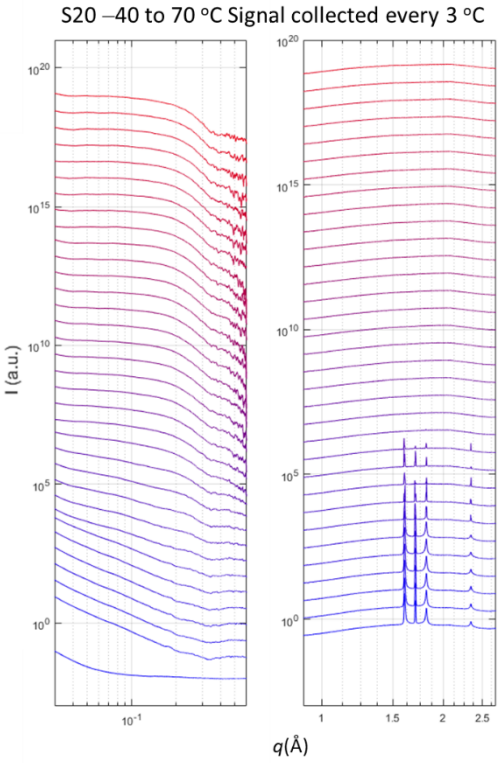
S20 –40 to 70 °C Signal collected every 3 °C
I (a.u.)
q(Å)

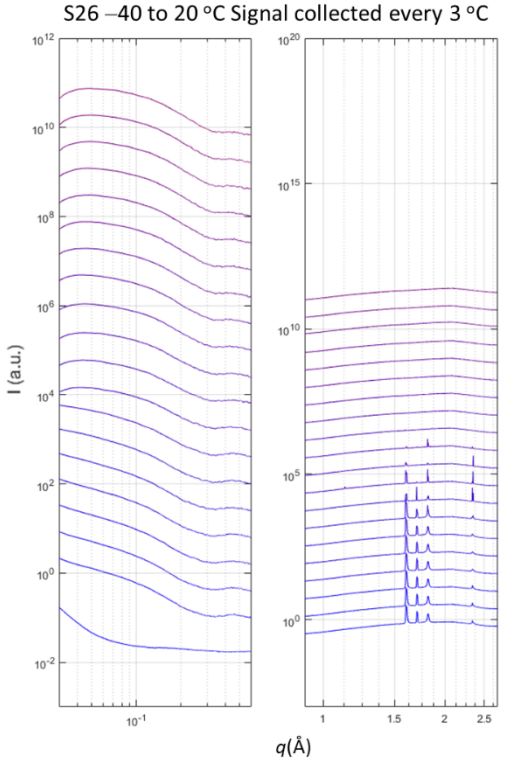
S26 –40 to 20 °C Signal collected every 3 °C
I (a.u.)
q(Å)

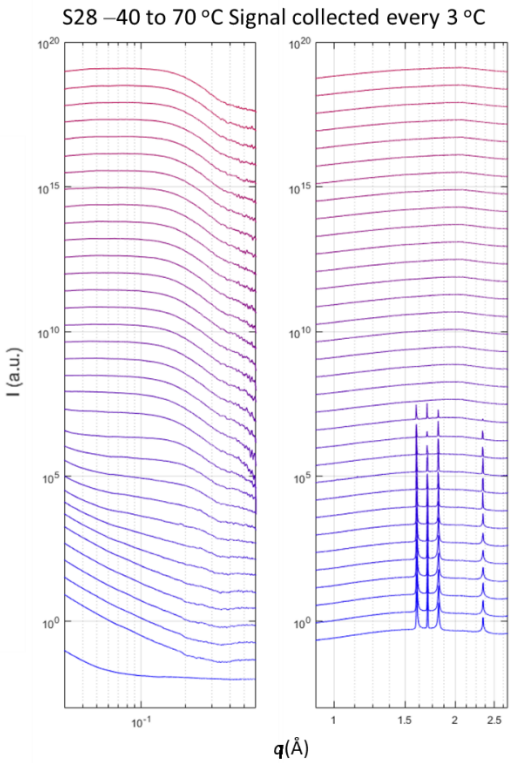
S28 –40 to 70 °C Signal collected every 3 °C
I (a.u.)
q(Å)

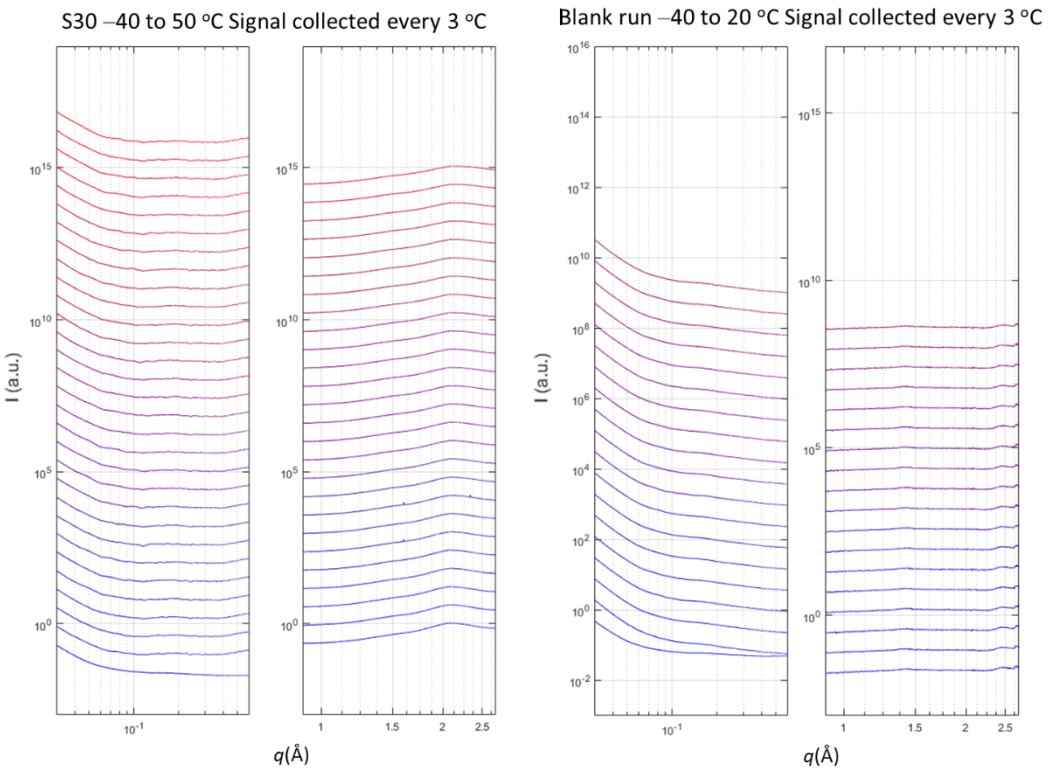

References for Appendices

1. Kumar, R.; Fredrickson, G. H., Theory of Polyzwitterion Conformations. *The Journal of Chemical Physics* **2009,** *131*, 104901.
2. Deek, J.; Chung, P. J.; Kayser, J.; Bausch, A. R.; Safinya, C. R., Neurofilament Sidearms Modulate Parallel and Crossed-Filament Orientations Inducing Nematic to Isotropic and Re-Entrant Birefringent Hydrogels. *Nature communications* **2013,** *4*, 2224.
3. X. Li , L. L., X. Wang , Y.S. Ok , J.A.W. Elliott, S.X. Chang, H.-J. Chung, Flexible and Self-Healing Aqueous Supercapacitors for Low Temperature Applications: Polyampholyte Gel Electrolytes with Biochar Electrodes. *Scientific reports* **2017**, *7*, 1685.
4. Kolthoff, I.; Chantooni Jr, M., Calibration of the Glass Electrode in Acetonitrile. Shape of Potentiometric Titration Curves. Dissociation Constant of Picric Acid1. *Journal of the American Chemical Society* **1965,** *87*, 4428-4436.
5. Dolman, D.; Stewart, R., Strongly Basic Systems. Viii. The H− Function for Dimethyl Sulfoxide–Water–Tetramethylammonium Hydroxide. *Canadian Journal of Chemistry* **1967,** *45*, 911-924.